Thèse n° 10 108

A Cavity-Microscope for Quantum Simulations with Locally-Controllable All-to-All Interactions

Présentée le 19 avril 2024

Faculté des sciences de base
Chaire Fondation Sandoz en physique des gaz quantiques
Programme doctoral en physique

pour l'obtention du grade de Docteur ès Sciences

par

Nick Jacob SAUERWEIN

Acceptée sur proposition du jury

Dr F. Blanc, président du jury
Prof. J.-Ph. Brantut, directeur de thèse
Prof. J. Léonard, rapporteur
Prof. A. De Luca, rapporteur
Prof. J. Home, rapporteur

École
polytechnique
fédérale
de Lausanne

2024

A CAVITY-MICROSCOPE FOR QUANTUM SIMULATIONS WITH LOCALLY-CONTROLLABLE ALL-TO-ALL INTERACTIONS

Abstract

This thesis presents the development, construction, and benchmark of an experimental platform that combines cold fermionic ^{6}Li atoms with locally controllable light-matter interactions. To enable local control, a new device, the cavity-microscope, was created. This device combines a high-finesse cavity with an on-axis high numerical aperture microscope. The cavity allows for strong interactions between photons and atoms, while the microscope enables high-resolution spatial engineering of the optical properties of the atoms. This is achieved by coupling the excited state of the effective two-level system to an auxiliary state with the help of a control laser beam that is focused to a small spot by the cavity-microscope.

We provide an overview of our experimental apparatus, with a particular focus on the design and fabrication process for the cavity-microscope. This includes the vibration-damping platform of the cavity-microscope, which helps to reduce the mechanical resonances of the mounting structure. Additionally, we discuss the progress of our newly developed next-generation cavity-microscope, which simplifies the optical design and improves the performance of our current device.

We provide a comprehensive description of the Hamiltonian that governs our laboratory system with a particular focus on the various measurement techniques that enable us to analyze the atom-cavity system. In particular, we demonstrate that the measurement of the cavity's dispersive shift can be used to infer in real-time different properties of the atomic cloud, such as atom count, temperature, and internal-state occupation.

We demonstrate the capability of our cavity-microscope to manipulate the interactions between light and matter by inferring the 3D density profile of the trapped atom cloud using the scanning probe technique. In detail, the control is achieved by a combination of Floquet and wavefront engineering of the control beam. With a spatial light modulator, we correct optical aberrations of the cavity-microscope based on a Hartmann–Shack scheme directly on the atomic cloud.

In our experiment, we realize an all-to-all interacting, disordered spin system by subjecting the atomic cloud in our cavity to controllable quasi-random light shifts. By spectroscopically probing the low-energy excitations of the system, we explore the competition of interactions with disorder and show disorder-induced breaking of the strong collective coupling.

Finally, we investigate the essential requirements for achieving control over high-rank cavity-mediated all-to-all interaction in our system. This control is crucial for enabling accurate quantum simulations of quantum gravity using the holographic duality of the Sachdev–Ye–Kitaev (SYK) model. To validate our findings, we performed two separate numerical experiments that demonstrate the robustness of our results.

Keywords: cold atoms, cavity qed, quantum simulation, cavity-microscope, random spin models, syk model

Laboratory for Quantum Gases
_ _ _ _ _

Résumé

Cette thèse présente le développement, la construction et l'évaluation d'une plateforme expérimentale qui combine des atomes froids fermioniques ^{6}Li avec des interactions lumière-matière contrôlables localement. Pour permettre le contrôle local, un nouveau dispositif, le microscope à cavité, a été créé. Ce dispositif combine une cavité de grande finesse avec un microscope à grande ouverture numérique dans le même axe. La cavité permet de fortes interactions entre les photons et les atomes, tandis que le microscope permet une ingénierie spatiale à haute résolution des propriétés optiques des atomes. Cela est effectué en couplant l'état excité du sytème à deux niveaux effectifs à un état auxiliaire à l'aide d'un faisceau laser de contrôle qui est focalisé sur un petit point à travers la cavité-microscope.

Nous présentons une vue d'ensemble de notre dispositif expérimental, en mettant l'accent sur la conception et le processus de fabrication du microscope à cavité. Cela inclut la plate-forme d'amortissement des vibrations du microscope à cavité, qui permet de réduire les résonances mécaniques de la structure de montage. En outre, nous discutons de l'avancement du développement de notre microscope à cavité nouvelle génération, qui simplifiera la conception optique et améliorera les performances de notre dispositif actuel. Nous fournissons une description complète de l'hamiltonien qui régit notre système, en mettant l'accent sur les différentes techniques de mesure qui nous permettent d'analyser l'ensemble atome-cavité. En particulier, nous démontrons que la mesure du déplacement de la cavité par effet dispersif peut être utilisée pour mesurer en temps réel différentes propriétés du nuage atomique, telles que le nombre d'atomes, la température et l'occupation de l'état interne.

Nous démontrons la capacité de notre microscope à cavité à manipuler les interactions entre la lumière et la matière en déduisant le profil de densité 3D du nuage d'atomes piégés à l'aide de la technique de la sonde à balayage. Au niveau microscopique, le contrôle est obtenu par une combinaison d'ingénierie de Floquet et de front d'onde du faisceau de contrôle. Avec un modulateur spatial de lumière, nous corrigeons les aberrations optiques de la cavité-microscope sur la base d'un schéma Hartmann–Shack directement sur le nuage atomique.

Grâce au montage expérimental décrit précédemment, nous réalisons un système de spin désordonné en interaction totale en soumettant le nuage atomique dans notre cavité à des décalages lumineux contrôlables quasi-aléatoires. En sondant spectroscopiquement les excitations de basse énergie du système, nous explorons la compétition des interactions entre les atomes avec le désordre et montrons la rupture, dans le régime de fort désordre, du couplage collectif fort.

Enfin, nous explorons les conditions nécessaires dans lesquelles notre système permet le contrôle de l'interaction tout-à-tout de haut rang médiée par la cavité. Ce contrôle est crucial pour permettre des simulations quantiques précises de la gravité quantique en utilisant la dualité holographique du modèle Sachdev–Ye–Kitaev (SYK). Pour valider nos conclusions, nous avons réalisé deux expériences numériques indépendantes qui démontrent la robustesse de nos résultats.

Mots clés : atomes froids, qed en cavité, simulation quantique, microscope en cavité, modèles de spin aléatoire, modèle syk

Acknowledgments

I started my Ph.D. in November 2018, and since then much time has passed (5 years, to be precise). Setting up a new lab from scratch was an extremely fun experience. I really enjoyed the variety of different components of my work, starting with the design of the setup, manufacturing different optical, mechanical, and electrical components, and finally having fun with the atoms. This has allowed me to gather a lot of experience and to work with many different people.

First, I would like to thank my supervisor Prof. Jean-Philippe Brantut, the master mind behind the setup. Not only is he an excellent researcher with great scientific know-how, intuition, and vision, but he is also a very welcoming and friendly person. This makes working in the laboratory for quantum gases an extremely stimulating and pleasant experience. Furthermore, Jean-Philippe gave me the opportunity to take four months of parental leave and then reduce my workload to 80 %, making becoming a father a very joyful and relaxed experience (as far as this can be relaxed ;)). Thank you sooo much for this!

Setting up an apparatus on the scale presented in this thesis has to be an enormous teamwork. In the scope of my thesis, I had the privilege of working with many extremely smart and talented people at different stages of their scientific career. First, I would like to thank Tigrane Cantat-Moltrecht, who worked as a postdoc on the setup. Starting with an empty lab, he designed many of the different components of the machine. His experience and knowledge in the field of cold-atom experiments were very valuable to me! At this point, I would like to mention Nicola Reiter. In the scope of her master thesis, she helped us trap the first cloud of atoms and subsequently perform the first cavity-based measurements. Nicola, thanks for your excellent work! Right after Nicola, Francesca Orsi had joined the lab. She started in the scope of her master thesis and is currently a Ph.D. student working on the experiment. The main scientific result of my thesis, the random spin paper [1], was measured, analyzed and written together with her. Francesca, I had a lot of fun working with you. Conversations with you are always very motivating, stimulating and fun. Thanks for the great time! Right after, Rohit Bhatt and Jonas Faltinath joined the team. In the scope of a one-year internship, Jonas contributed primarily to the design of the SLM setup and participated in the measurement presented in Chapter 4. Jonas, it was super nice and relaxed to work with you. I enjoyed the precision of your solutions to problems in the lab. Rohit is still working on the experiment in the scope of his postdoc. Rohit, thanks for managing the team in the last two years. Your positivity and motivation are really valuable and allowed us Ph.D. students to cope better with the frustrations related to the atoms not behaving as they should ;). In the last year of my Ph.D., I had the pleasure of working with Gaia Bolognini. In the scope of her master thesis, she designed the next-generation cavity-microscope. Gaia, I enjoyed it sooo much working with you! I love that you are so motivated, organized and happy all the time. This is just great! I would also like to thank the 'next-generation' Ph.D. students Katya Fedotova and Michael Eichenberger. It is really cool to see such motivated and talented people taking over my work! #nopressure , but I really hope you will get the quantum simulations of the SYK model done one day! Finally, I would like to mention all the interns who worked

on various topics during my Ph.D.: Daniel Ortuño, Camille Nesson, Ioana Grigoras, Samantha Koretsky, Nada Alghamdi, Xinyu Si, thanks a lot to you!

Many of the theoretical analyses presented in this thesis are the result of collaboration with theory groups. In particular, we worked together with Guido Pupillo and Francesco Mattiotti on the random spin paper [1]. I found this collaboration super helpful and efficient. Thanks for that! We also worked with Philipp Hauke, Soumik Bandyopadhyay and Philipp Uhrich. They helped us establish the theoretical basis for the SYK model quantum simulations and the random spin model paper. The SYK model theory was developed during multiple COVID zoom sessions. This made the lockdown super productive and fun. Philipp Uhrich wrote his Ph.D. thesis on the theoretical aspect of our experiment [2]. Thanks for your amazing work! It is sometimes funny to see how small the world is ;). Finally, I would like to thank the Julian Sonner group. The meetings in Lausanne, Zürich and Geneva were always super cool. It was a great interdisciplinary experience! A particular thanks to Rahel Baumgartner and Pietro Pelliconi for going through the theory chapters of my thesis. Thanks for the amazing feedback!

The microscope experiment, which was developed as part of my thesis, represents the second setup in the quantum gases laboratory overseen by Jean-Philippe Brantut. It bears a strong resemblance to the initial apparatus, known as the Fermi gas experiment, which involves Fermi gases composed of ultra-cold ^{6}Li atoms within a high-finesse cavity. Many of the principles employed in our experiment are derived from this original configuration. I wish to express my gratitude to the team behind the Fermi gas experiment for their valuable discussions and insights. In particular, I am thankful to Kevin Roux, Victor Helson, Hideki Konishi and Barbara Cilenti, who established the infrastructure for the Fermi gas experiment from scratch. The experiment is now run by the motivated and joyful ’next-generation’ team (Timo Zwettler, Tabea Bühler, Gaia Bolognini and Aurélien Fabre). Especially during lunch and coffee breaks, I made extensive use of your positive vibes =). Thanks for that!

A significant portion of the microscope experiment’s components were created and produced at EPFL, thanks to the outstanding facilities available at the physics institute. The mechanical and electrical workshops played a crucial role in producing the intricate parts needed for our experiment. Interacting with skilled engineers and tackling laboratory challenges not only helped me acquire advanced machining and assembly skills, but also enormously facilitated the development of our professionally designed apparatus. In particular, I am grateful to Gilles Grandjean who leads the mechanical workshop. Thanks for taking the time to discuss the numerous iterations of the different components! And of course, thanks to Adrien Grisendi, Daniel Clément, Luc Chevalley for manufacturing many of the key components. I thank Daniel Godat for teaching me the basics of milling. A particular thanks goes to Claude Amendola, who is an expert in essentially everything mechanical. Your help was outstanding! I thank José Grandjean and Philippe Cuanillon for realizing the numerous different electrical circuits! I thank Baptiste Le Gentil and Primo Locatelli for helping me with all computer problems. Last but not least, I thank Gabriella Fuchs, Anh Eymann, and Nadja Dekumbis for the excellent administrative support. Your work is very special!! Thanks for your help!

Finally, I would like to thank my family and friends. This starts, of course, with my parents. Thanks for supporting me in achieving my dream =). I would like to thank Jeremy Stevens, Sven Wang, Brennan de Neeve, Sophie Christe, Manon Cuixeres, Jenny Sülzle, Amirali Arabmoheghi, Mohammad Bereyhi, my friends from the CTT Montriond-Ouchy and the Lausanne-Sports aviron for all the fun activities together during these years. The most extreme thank you goes to my girlfriend Nina Urfer. You made the evenings and weekends of my Ph.D. amazing and thanks for listening to my constant frustrations ;P. We made it! Especially the last year with Léon was beautiful, happy and sometimes a bit tough. I really hope that we are not sick for the next 10 years straight ;). A special thanks goes to the Urfer Family (Nathalie, Daniel, Sora and Luigi).

Thanks for the great times together and thanks for the moral support, especially towards the end of my thesis =).

Thanks to everyone I met at EPFL and to everyone I forgot in this acknowledgment in the stress of these last weeks!

Contents

Abstract **iii**

Acknowledgments **v**

Contents **ix**

Introduction **1**

1 Design of Cavity-Microscope System **5**
- 1.1 Motivation for Cavity-Microscope 6
  - 1.1.1 Strong Interaction Between a Photon and an Atom 6
  - 1.1.2 Spatial Engineering the Atom-Cavity Coupling using Locally-Controlled Light Shifts 8
  - 1.1.3 Overview over Different Cavity-Microscope Designs 10
- 1.2 Key Design Parameters for the Cavity-Microscope and their Limitations 10
- 1.3 The Optically-Contacted cavity-microscope 13
  - 1.3.1 Optical Layout 14
  - 1.3.2 Performance and Characteristics of Final Assembly 14
  - 1.3.3 Details on the Components 16
  - 1.3.4 Assembly of the Cavity-Microscope 17
  - 1.3.5 Discussion 19
- 1.4 Design of Vibration Damping Platform 19
  - 1.4.1 Design Criteria 21
  - 1.4.2 Mechanical Assembly 22
  - 1.4.3 Performance Characterization 22
  - 1.4.4 Conclusion 24
- 1.5 Development of the Next-Generation Cavity-Microscope 24
  - 1.5.1 Optical Layout 25
  - 1.5.2 Performance and Characteristics of the Prototype Cavity-Microscope . . . 26
  - 1.5.3 Details on the Components 27
  - 1.5.4 Summary of Assembly Procedure 28
  - 1.5.5 Discussion and Outlook 30

2 The Cold-Atom Experiment **31**
- 2.1 Experimental Apparatus 32
  - 2.1.1 Ultra-High Vacuum System 32
  - 2.1.2 System of Electromagnets 34
  - 2.1.3 Laser System 35

2.1.4 Computer control 37
2.2 Preparation of Atomic Sample 39
2.3 Imaging the Atomic Cloud 42
2.3.1 Two-Photon Imaging Through the Cavity-Microscope 43
2.4 Cavity Probe Setup 45
2.4.1 Cavity Response Spectroscopy 46
2.4.2 Precision of Cavity Resonance Measurement 47
2.5 Conclusion 47

3 Basic Principles and Methods of Cavity QED 49
3.1 Detailed Description of the Hamiltonian of the Atom-Cavity System 50
3.1.1 Hamiltonian of the Multi-Level Fermionic Atoms 50
3.1.2 Hamiltonian of a Multi-Mode Cavity 51
3.1.3 Atom-Cavity Interaction Hamiltonian 51
3.1.4 Level-Structure of ^{6}Li and Simplification of Hamiltonian 52
3.1.5 Discussion on Spatial Structure of Atom-Cavity Hamiltonian 53
3.1.6 Incoherent Loss Processes: Cavity Loss and Spontaneous Emission 54
3.2 Susceptibility Spectroscopy of Atom-Cavity System 54
3.2.1 Measurement of Atomic Susceptibility: The Depumping Technique 55
3.3 Measurement of Dispersive Shift of the Cavity: The Swiss Army Knife of Measurements 57
3.3.1 Signal-To-Noise Ratio of Dispersive Shift Measurement 58
3.3.2 Repeated and Continuous Measurement of Number of Atoms 58
3.3.3 Temperature Measurement Using Differential Cavity Mode Shift 62
3.3.4 Cavity-based Detection of Raman Transitions 65
3.4 Conclusion 67

4 Shaping Light-Matter Coupling in Space and Time 69
4.1 Experimental Setup 70
4.2 Local Floquet Engineering of the Light-Matter Coupling 70
4.2.1 Single-Atom Model 71
4.2.2 Generalization to Many Thermal Atoms 72
4.2.3 Experimental Observation of Control over Atom-Cavity Interaction 72
4.3 Aberration Correction of Cavity Lens with Atoms 73
4.3.1 Procedure of Wavefront Reconstruction and Optimization 73
4.3.2 Measured Aberrations of Cavity Lens 75
4.4 Scanning Probe Imaging of Atomic Cloud 75
4.5 Discussion and Outlook 76

5 Collective Effects in Disordered Spin Systems with All-to-All Interactions 79
5.1 Fragmenting Eigenstates with Disorder in Atomic Transition Frequencies 80
5.2 Two-Atom Toy Model 81
5.2.1 Cavity-Mediated Flip-Flop Interactions Emerging in the Dispersive Regime 84
5.2.2 Dissipation and the Measurement Scheme 86
5.3 Many-Atom Model 87
5.4 Experimental Configuration 88
5.4.1 Implementation of the Disorder through Light-Shift Technique 89
5.5 Experimental results 91
5.5.1 Signature of Strong Coupling: Atom-Cavity Anticrossing 91

5.5.2 Near-Resonant Regime and Gray States . . . 93
5.5.3 Large-Detuning Regime and Lipkin–Meshkov–Glick model . . . 95
5.5.4 Localization of Atomic Excitations . . . 98
5.6 Conclusion . . . 99

6 Towards Experimental Realization of the SYK Model 101
6.1 Definition of SYK Model . . . 102
6.1.1 Variable-Rank SYK Model Decomposition . . . 102
6.2 Experimental Scheme . . . 103
6.2.1 Experimental Implementation of High-Rank Interactions . . . 105
6.3 Tunable Motion-Changing Interactions between Fermions in a Cavity Microscope 106
6.4 Rank-Scaling in 1D Model . . . 109
6.4.1 Analytic Structure of Atom-Cavity Coupling . . . 109
6.4.2 Decomposition of Interaction in Elementary Components . . . 110
6.4.3 Numerical Analysis of Rank-Scaling . . . 111
6.5 Simulation of Hamiltonian Dynamics of Random Interactions in Multi-Mode Cavity 113
6.5.1 Randomness of Two-Body Interactions . . . 113
6.5.2 Comparison to SYK Model Dynamics . . . 114
6.6 Experimental Requirements and Challenges . . . 118
6.6.1 Matching of the Disorder, Cavity-Mode and Trap Length Scales . . . 118
6.6.2 Implementation of Random Interaction using Speckle Pattern . . . 118
6.7 Discussion . . . 119

Conclusion and Outlooks 121

Bibliography 123

A Layout of Experiment 135
A.1 Layout of the Room . . . 135
A.2 Layout of Laser System . . . 136
A.2.1 Laser Beam Setup around Vacuum Chamber . . . 136
A.2.2 Master Laser: From the Source to the Atoms . . . 140
A.3 Layout of Imaging Setup . . . 144
A.4 PID Loops in the Experiment . . . 145
A.4.1 Detailed Overview of Feedback Systems . . . 145
A.4.2 RedPitaya for PIDs . . . 148
A.4.3 Feed-forward Scheme . . . 148

B Design and Construction of the MOT coils 149
B.1 Design of Coils . . . 149
B.2 Difference to Published Design . . . 150
B.2.1 Assembly Procedure . . . 150
B.3 Mistakes and Possible Improvements of the Design . . . 152

C Assembly of the Optically-Contacted Cavity Microscope 153
C.1 Step I: Optical Contact Between Mirror and Lens . . . 153
C.2 Step IV: Cavity Alignment . . . 155

CURRICULUM VITAE 157

Introduction

The discovery of new physics is achieved through either experimentation or theoretical predictions. For example, the particle zoo that led to the identification of quarks was discovered through experimentation [3, 4], while the Higgs particle was predicted decades before it was found in proton-proton collisions at the Large Hadron Collider (LHC) [5]. However, in the end, it is the constant dialogue and mutual confirmation between theoretical and experimental physics that leads to the development of highly successful theories, such as the standard model of elementary particles.

In the realm of quantum gravity, which seeks to combine quantum mechanics and general relativity, this dialogue is out of balance. There are numerous successful theories that can make predictions about the quantum behavior of black holes and other intense forms of gravity, yet testing these effects in the real world remains impossible. In the future, we may be able to gain insight into the quantum nature of gravity by using our ability to image black holes [6] and detect gravitational waves emitted from the merging of two black holes [7]. However, these experiments are limited to observations of nature, and it would be beneficial to create a controllable system in the laboratory, which would enable us to investigate properties of quantum gravity under a variety of different conditions that are perhaps not existent or accessible in nature. One such system could be the experimental realization of holographic quantum matter, a hypothesized form of strongly correlated many-body systems that has a holographically dual interpretation in terms of a quantum theory of gravity [8, 9]. A first step in this direction would be the quantum simulation of the Sachdev–Ye–Kitaev (SYK) model, which is believed to host the simplest known form of holographic duality [10]. It describes N fermionic modes with random, infinite-range two-body interactions. The random nature of these interactions necessitates a large number of independent couplings, making it difficult to approach the problem. In particular, in the large-N limit, which is relevant for the quantum gravity duality, there has not been a successful experimental realization of the SYK model. This presents an exciting challenge, which we address in this thesis.

In recent years, researchers have managed to create deeply degenerate Fermi gases with tens to hundreds of ultra-cold ^{6}Li atoms [11]. This has allowed for the direct observation of Cooper pairing between very few fermions [12]. These mesoscopic fermionic systems are an ideal platform for the realization of a quantum simulation of the SYK model. However, in such systems, the interactions between particles become weaker as the distance between them increases and are thus finite-range. This prevents these systems from achieving full connectivity between the particles, which is a necessary condition for quantum simulation of the SYK model. In cavity quantum electrodynamics (cQED), the interactions that are mediated by cavity photons are all-to-all in nature. This allows the realization of systems with perfect indistinguishability between particles, effectively creating interactions with an infinite range [13]. Such cavity-mediated interactions have been realized in cQED experiments with large clouds of ultra-cold fermionic atoms [14]. There, increasing the interaction strength leads to formation of a self-organized phase of matter, where the atomic density inherits the spatial structure of the interaction, which is dictated by the cavity mode. To realize the number of independent couplings necessary for the SYK model, one needs to randomize the cavity-mediated interaction by introducing local variations in the atom-cavity coupling.

This thesis presents the development of an experimental platform that unites fermionic ^{6}Li atoms with locally controllable cavity-mediated interactions, thus creating the necessary conditions for the quantum simulation of the SYK model. The core of the experiment is a high-finesse cavity that is combined with a high-resolution optical microscope in a single optical device, referred to as the cavity-microscope.

In the following, we present the outline of the thesis, which is divided into six chapters.

In Chapter 1 we explain the rationale and design of our cavity-microscope. We list key design parameters and provide an overview of the optical device and its vibration damping platform that were used in the atom experiments described in this thesis. To improve the coherence times in future experiments, we began the development of a next-generation cavity-microscope. We describe the properties and design of this new device at the end of the chapter.

In Chapter 2 we detail the infrastructure and procedures that allow us to prepare and probe small atomic samples between the mirrors of our cavity-microscope. The experimental apparatus features an ultra-high vacuum system, a set of electromagnets, and a system of frequency-stabilized lasers which are controlled using a computer control system. The prepared atomic sample can be imaged using different techniques. In particular, we developed two-photon absorption and fluorescence imaging through the cavity-microscope, the results of which are detailed in this chapter. Finally, we provide an overview of the techniques for measuring the properties of our optical resonator using a weak on-axis probe.

In Chapter 3 we explore the fundamentals of cavity quantum electrodynamics (cQED). We provide a comprehensive description of the Hamiltonian that governs our laboratory system, and then focus on the various measurement techniques that enable us to analyze the atom-cavity system. In particular, we explain the susceptibility spectroscopy using the depumping approach. Additionally, we demonstrate that the measurement of the cavity's dispersive shift can be used to measure properties of the atomic cloud in real time, such as the atom count, temperature, and even to detect transitions between different hyperfine ground states of the atoms.

In Chapter 4 we experimentally show the capability of our cavity-microscope to manipulate the interactions between light and matter in both space and time. We illustrate our capacity to alter the spectral properties of the atoms by using an amplitude-modulated control beam that produces spectrally distinct Floquet sidebands of their excited state. To shape the wavefront of the control beam, we use a spatial light modulator. This, combined with cavity-based measurement techniques, has enabled us to compensate for the aberrations of our cavity lenses using a purely atomic signal. We provide a description of the reconstruction algorithm and the results obtained. Lastly, we demonstrate the spatial resolution of our cavity-microscope by inferring the 3D density profile of the trapped atomic cloud using a scanning probe technique.

In Chapter 5 we explore the collective effects that arise in systems with homogeneous atom-cavity coupling and demonstrate experimentally how disorder in the atomic transition frequencies leads to the fragmentation of eigenstates. We begin by introducing the theoretical concepts with the aid of a two-atom model. In the experiment, the disorder in the atomic spins is generated through quasi-random light shifts of the excited state. After providing a thorough description of the experimental setup, we present our findings in both the near-resonant and large-detuning regimes. In the near-resonant regime, we observe the emergence of gray states in the normally dark Rabi gap. In the large-detuning regime, our experiment effectively simulates a spin system with all-to-all interactions. We observe a disruption of the ferromagnetic structure of the excitations with an increasing effective inhomogeneous magnetic field created by the atomic disorder.

In Chapter 6 the final section of this thesis, we investigate the conditions that make it possible to simulate the SYK model in our experiment. We define the SYK model in a way that is suitable for our experimental system. We show how the idea of locally engineering the atom-cavity coupling can be used to create adjustable interactions between fermions. We use two independent numerical studies to demonstrate that locally adjustable all-to-all interactions, which are present in cavity QED systems, can generate the conditions necessary for a successful quantum simulation of the SYK model. We finish the chapter by summarizing the key experimental requirements.

Chapter 1

Design of Cavity-Microscope System

Outline of the current chapter

1.1 Motivation for Cavity-Microscope 6
  - 1.1.1 Strong Interaction Between a Photon and an Atom 6
  - 1.1.2 Spatial Engineering the Atom-Cavity Coupling using Locally-Controlled Light Shifts 8
  - 1.1.3 Overview over Different Cavity-Microscope Designs 10

1.2 Key Design Parameters for the Cavity-Microscope and their Limitations 10

1.3 The Optically-Contacted cavity-microscope 13
  - 1.3.1 Optical Layout 14
  - 1.3.2 Performance and Characteristics of Final Assembly 14
  - 1.3.3 Details on the Components 16
  - 1.3.4 Assembly of the Cavity-Microscope 17
  - 1.3.5 Discussion 19

1.4 Design of Vibration Damping Platform 19
  - 1.4.1 Design Criteria 21
  - 1.4.2 Mechanical Assembly 22
  - 1.4.3 Performance Characterization 22
  - 1.4.4 Conclusion 24

1.5 Development of the Next-Generation Cavity-Microscope 24
  - 1.5.1 Optical Layout 25
  - 1.5.2 Performance and Characteristics of the Prototype Cavity-Microscope 26
  - 1.5.3 Details on the Components 27
  - 1.5.4 Summary of Assembly Procedure 28
  - 1.5.5 Discussion and Outlook 30

At the heart of our experimental setup is a device that unites a high-finesse cavity and a high-resolution microscope in one unit, the cavity-microscope. The optical resonator amplifies the interactions between atoms and photons, while the microscope is used to shape the atom-cavity coupling on a micrometer scale. This chapter outlines the design and fabrication of our cavity-microscope.

This chapter is structured as follows: We provide a motivation for the construction of our cavity-microscope in Section 1.1. The key parameters and constraints that guided the design of our device are discussed in Section 1.2. Our optically contacted cavity-microscope is described in Section 1.3, which includes a comprehensive description of the design, fabrication process, and performance. The cavity is mounted on a vibration damping platform, which is detailed in Section 1.4. We also discuss ways to improve the design, leading to the development of a more advanced high-resolution cavity-microscope in Section 1.5. This next-generation device will enable us to achieve higher finesse for the cavity and better spatial resolution for the microscope.

1.1 Motivation for Cavity-Microscope

In this section, we develop the motivation behind the construction of our cavity-microscope. In particular, in Section 1.1.1, we illustrate the physics of strong coupling with a simple Gedanken experiment, motivating the use of a high-finesse optical resonator. The microscope is used to enhance the spatial resolution of cavity-based measurements, a concept that is novel to our experiment. In Section 1.1.2, we present the mechanism that allows us to shape the atom-cavity coupling in space. In Section 1.1.3, we provide a summary of different experiments that combine a high-finesse cavity with a high-NA microscope.

1.1.1 Strong Interaction Between a Photon and an Atom

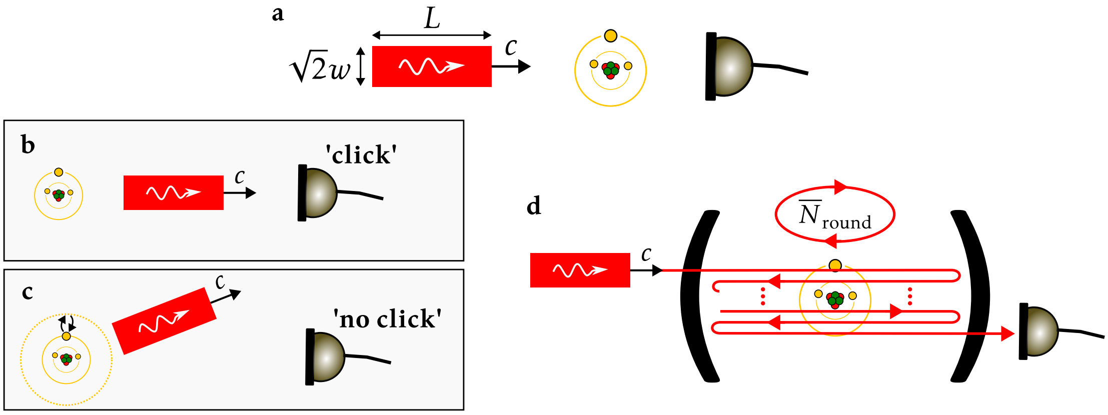

Figure 1.1: **Interaction Between Atom and Cylindrical Photon.** **a**, Setup of Gedanken experiment. Cylindrical photon is sent through a single atom onto a detector. **b**, If the detector 'clicks', the photon has not interacted with the atom. **c**, If the detector does not 'click', the atom has scattered the photon. **d**, The effect of the cavity is to increase the interaction probability by circulating the same photon many times ($\overline{N}_{\text{round}}$) over the atom.

In this section, we develop a simple Gedanken experiment that allows us to illustrate the physics of strong coupling between atoms and photons. The results motivate the use of an optical resonator to enhance the interaction. The experiment we imagine is a photon that is sent onto an atom. Behind the atom, we install a single-photon counter. In Figure 1.1**a** an illustration of the setup is shown. If the photon does not interact with the atom, it flies through it and makes a 'click' on the detector (see Figure 1.1**b**). However, as soon as the atom interacts with the photon, it absorbs it and re-emits it in any direction, reducing the probability of a 'click' on the detector (see Figure 1.1**c**). Therefore, the probability of a click on the detector is a measure of the interaction strength between the photon and the atom. This defines the goal of this section, which is to calculate the probability of a click on the detector and therefore to find a measure of the interaction strength between a single photon and an atom.

For the whole analysis, we assume that the photon oscillates at the frequency of the atomic transition ω. Furthermore, we assume that the size of the photon can be described by a cylindrical photon of radius $w/\sqrt{2}$ and length L. In general, a more sophisticated transverse and longitudinal profile of the photon electric field could be used [15], but this does not change the results presented in this section.

The amplitude of the electric field of our cylindrical photon E_{ph} can be calculated from the energy of the photon $\hbar\omega$ as

$$\begin{aligned}\hbar\omega &= \frac{\epsilon_0}{2}\int E_{\text{ph}}^2 + c^2 B_{\text{ph}}^2 dV = \epsilon_0 \int E_{\text{ph}}(\vec{x})^2 dV = 2\epsilon_0 E_{\text{ph}}^2 \left(L\pi w^2/2\right)\\ \rightarrow E_{\text{ph}} &= \sqrt{\frac{2\hbar\omega}{\epsilon_0 V}},\end{aligned}$$

where $V = Lw^2\pi/2$ is the volume the photon occupies in space. Sometimes people refer to this as the mode volume.

The photon interacts with the atom due to its electrical dipole moment μ. The Rabi frequency of the single photon in free space g_{fs} can be calculated as

$$g_{\text{fs}} = \mu E_{\text{ph}}/\hbar = \mu\sqrt{\frac{2\omega}{\hbar\epsilon_0 V}}.$$

It measures the rate of Rabi flops of the atom due to the single photon.

If we stay in the low saturation regime of the atom, $g_{\text{fs}} \ll \Gamma$*, the scattering rate of the photon can be quantified by $R_{\text{scattering}} = \Gamma(g_{\text{fs}}^2/\Gamma^2)$. Here, Γ is the spontaneous emission rate of the atom. So, to calculate the probability that the photon ends up in the detector, we have to multiply the scattering rate by the interaction time between the atom and the photon, $\tau = L/c$, resulting in

$$P_{\text{click}} = \exp\Big(-R_{\text{scattering}}\tau\Big) = \exp\left(-\frac{g_{\text{fs}}^2}{\Gamma}\tau\right) = \exp\left(-\frac{6}{k^2w^2}\right). \tag{1.1}$$

In the last step, we used the fact that the atomic linewidth and the electric dipole moment are linked, $\Gamma = k_0^3\mu^2/(3\pi\epsilon_0\hbar)$. The expression above motivates the definition of the free-space cooperativity.

$$\eta_{\text{fs}} = \frac{6}{k^2w^2},$$

which is a purely geometrical factor as the dependence on the dipole moment of the atom vanished. It depends only on the waist of the focused beam w and the wave vector of light k.

Equation (1.1) suggests two ways to increase the likelihood of an atom and a photon interacting. The first is to increase the coupling strength by increasing the electric field strength of the photon, and the second is to extend the interaction time between the atoms and the photon. However, it is not the electric field strength of the photon that determines the interaction probability, but rather the mode area at the location of the atom, as seen in Equation (1.1), since the final expression is independent of the length of the photon. This means that if we use a short pulse of light, which has a higher peak electric field, this increases the interaction strength g. However, this also reduces the interaction time, making it less likely to interact. In the end, these two processes cancel each other out. The only solution is to focus the light at the smallest possible area, which is limited by diffraction.

---

*If we would include the non-linearity resulting from saturation of the atom transition, interesting physics like the photon switch would emerge [16]. However, this is not the regime for which we are interested in working.

An alternative way to increase the probability of interaction that is not limited by diffraction is to modify the interaction time τ. As previously mentioned, in free space, the interaction time is directly related to the peak electric field. However, if an optical resonator is used, the same photon can pass through the atom multiple times. This leads to an enhancement of the interaction probability, which is determined by the number of round trips a photon makes before exiting the resonator (see Figure 1.1**d**). In fact, in a cavity, the average number of round trips is proportional to the finesse of the resonator $\mathcal{F}$, as $\overline{N}_{\text{round}} = \mathcal{F}/\pi$. Plugging this into Equation (1.1) yields

$$P_{\text{click}} = \exp\Big(-R_{\text{scattering}}\tau(4\overline{N}_{\text{round}})\Big) = \exp\Big(-\frac{24\mathcal{F}/\pi}{k^2w^2}\Big). \tag{1.2}$$

Note that the factor 4 that multiplies the number of round trips is motivated by the interference of the forward and backward propagating light in the resonator. For ring cavities, where light propagates only in one direction, this factor is equal to 1. Similarly to before, the expression motivates the single-atom cooperativity

$$\eta = \frac{24\mathcal{F}/\pi}{k^2w^2} = \frac{4g^2}{\kappa\Gamma}\ . \tag{1.3}$$

Here w is the waist of the cavity mode at the location of the atom. The right-hand side of the equation comes from the analogy with the typical cavity QED definition of cooperativity. However, both expressions are entirely equivalent, as can be seen from the derivation in Equation (1.2).

This motivates to use the cooperativity as a measure of the probability of interaction between a single atom and a photon. If $\eta > 1$, the strong coupling regime, the probability of measuring a click on the photon counter is significantly reduced.

An example of this effect is the transmission of the cavity. If the atom is placed in resonance with the resonator, the transmitted power drops by $1/(1+\eta)^2$, which can be a large factor*. Therefore, in cavities that operate in the strong-coupling regime, single atoms significantly change the optical properties of the cavity. This makes the cavity a useful tool to perform precise measurements of the presence of atoms within the cavity mode at the single-photon level [17–19]. An overview of the different cavity-based measurement techniques used in our experiment is presented in Chapter 3.

1.1.2 Spatial Engineering the Atom-Cavity Coupling using Locally-Controlled Light Shifts

We have previously shown that a single atom can significantly modify the optical properties of a cavity. This can be used to measure atomic properties with a cavity-based approach, but the spatial resolution of these measurements is restricted by the shape of the cavity mode. To address this, we present a method that allows us to customize the atom-cavity coupling with a focused laser beam, the control beam. This provides the foundation for the development of our cavity-microscope, a device that combines a high-finesse cavity and a high-resolution microscope.

---

[*] The equation of the cavity transmission differs from the result of our Gedanken experiment. This is a result of the approximation of the cavity as an object that makes the photon pass over the same atom $\overline{N}_{\text{round}}$ times. However, to first order in η the two expressions agree. See Ref. [15] for more details.

The strength of the interaction between an atom and a cavity is determined by the characteristics of both the cavity and the atom. The form of the cavity mode is fixed by its geometry and cannot be altered dynamically. However, the optical properties of the atom can be adjusted locally. For example, we can adjust the transition frequencies of the atom using light shifts. Specifically, we can use a focused laser beam, the control beam, to shift the excited state of the atom $|e\rangle$ in proportion to the beam intensity. The light shift is a consequence of off-resonantly coupling the excited state $|e\rangle$ to a control state $|c\rangle$. This mechanism is illustrated in Figure 1.2.

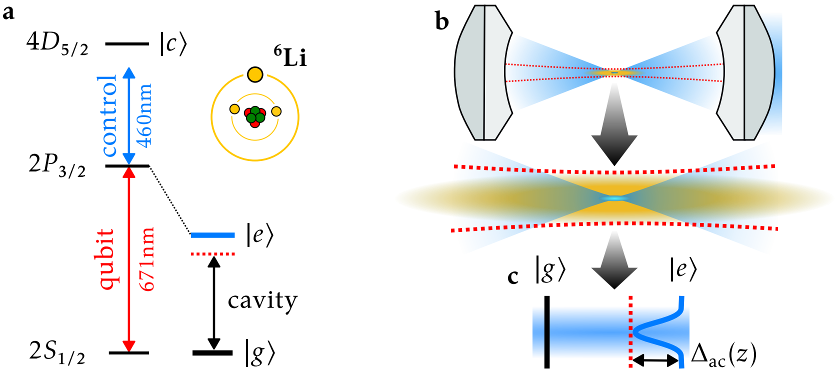

Figure 1.2: **Illustration of Focusing Effect.** **a**, Simplified level diagram of ^{6}Li showing the two major transitions used during the scope of the thesis: D2 line at 671 nm to encode the atomic qubit, and the $2P_{3/2}$–$4D_{5/2}$ transition at 460 nm for the control beam. **b**, Illustration of local control over atom-cavity coupling. The waist of the cavity mode is drawn as a red dashed line. The control beam (blue focused cone) changes the properties of the atomic cloud (yellow shaded blob) in a small region of space, much smaller than the waist of the cavity mode. The zoom-in below shows the same scenario magnified. **c**, Local control illustrated in a level diagram. In the focus of the control beam, the excited state $|e\rangle$ becomes shifted so that the atomic qubit ($|g\rangle$–$|e\rangle$) is locally resonant with the cavity. This is illustrated by a space-dependent atom-cavity detuning $\Delta_{\mathrm{ac}}(z)$

The panel **a** of the diagram displays a simplified level of ^{6}Li to illustrate the qubit and control transitions. The diagram shows the effect of the control beam at 460 nm on the energy of the excited state. Instead of the bare state $2P_{3/2}$, the dressed excited state $|e\rangle$ is the one that couples with the cavity, and thus the atom-cavity coupling inherits the local structure of the control beam. This three-level scheme is not exclusive to ^{6}Li, making it a very general concept. Alternatively, one can also use a Λ–system instead of the ladder system of states $|g\rangle$, $|e\rangle$, and $|c\rangle$ [20, 21].

Figure 1.2**b** shows the geometry of our cavity-microscope and the control beam. The waist of the cavity mode is depicted by the dashed red line, while the atomic cloud is completely contained within the cavity mode (green ellipse). The control beam (blue cone) is focused on a small area (much smaller than the cavity waist and the atomic cloud). This leads to a local alteration in the detuning between the atomic and cavity resonances $\Delta_{\mathrm{ac}}(z)$ (see Figure 1.2**c**) on a length scale that is no longer determined by the shape of the cavity mode, but rather by the spot size of the control beam.

We can gain insight into the location of atoms with high spatial resolution by using local control over the atom-cavity coupling. By applying a light shift similar to the one shown in Figure 1.2**c**, the dressed atomic transition is resonant with the cavity if the atom is located at the focal point of the control beam. Thus, if a decrease in cavity transmission is observed, this indicates that an atom is present at the focus of the control beam, providing us with information about the atom's location. The resolution of this measurement is no longer limited by the shape of the cavity mode, but rather by the spot size of the control beam.

The core of this thesis is the physics of controlling atom-cavity couplings locally. This concept is explored in various chapters, such as Chapter 4, which demonstrates the cavity-microscope as a high-precision imaging device, and Chapter 6, which examines cavity-mediated interactions and proposes their local controllability to simulate the SYK model.

1.1.3 Overview over Different Cavity-Microscope Designs

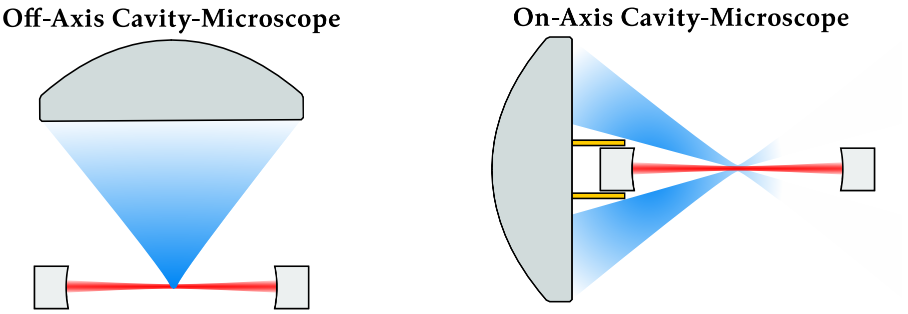

Figure 1.3: **Off- and On-Axis Cavity-Microscope.**

Several experiments have combined high-finesse cavities with high-resolution microscopes, with different configurations for the placement of the microscope relative to the cavity axis (see Figure 1.3). Most often, the microscope is placed 90° off-axis from the cavity, allowing longitudinal imaging of the cloud and the generation of optical tweezers to trap atoms [22–26]. This arrangement also enables adjustment of the atom-cavity coupling [22].

An alternative configuration is an on-axis microscope, which is less common [27]. This setup may be more complex to construct, as the cavity and the microscope share the same optical axis, but it has some advantages. Firstly, it allows for high-resolution manipulation and imaging in both directions transverse to the cavity mode. Secondly, the combination of the cavity and the microscope in a single optical device improves the mechanical stability of the relative alignment. This, combined with a cavity-enhanced dipole trap, can achieve good overlap with the cavity mode that does not drift over time, reducing the precise alignment requirement imposed by the cavity lattice structure in the off-axis configuration. For these reasons, this configuration was chosen for my thesis.

1.2 Key Design Parameters for the Cavity-Microscope and their Limitations

In the preceding section, we provided basic examples to demonstrate the utility of a cavity-microscope for cold-atom experiments. This section is more specific and outlines the key parameters and constraints that were taken into account when designing our cavity-microscope. These parameters are outlined in Figure 1.4 and discussed in further detail below.

	Requirement	Solution
a) Strong atom-cavity coupling $\eta > 1$	• high finesse $\mathcal{F}$ • small mode waist w 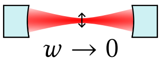 $w \to 0$	• super-polishing, coating • near-concentric geometry 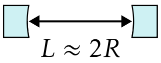 $L \approx 2R$
b) Focusing Effect	High-resolution microscope	high NA 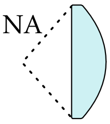
c) Cold-Atom Experiment ^{6}**Li** 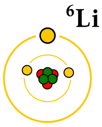	• high-finesse cavity • focusing beam • cavity dipole trap • optical tweezers	• HR: 671 nm, 1342 nm • HT: 460 nm, 780 nm (, 671 nm) 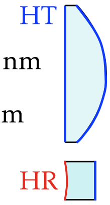
d) Optical access & UHV	• MOT, atoms, viewport • vacuum compatible • non-magnetic	• geometry • materials 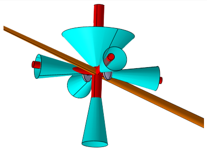
e) Fast and Precise Tuning of Resonance Frequency	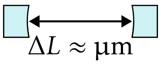 $\Delta L \approx$ µm	• piezoelectric actuators • cavity holder design

Figure 1.4: **Table of Experimental Requirements.**

a) Strong Atom-Cavity Coupling As visible in Equation (1.3), achieving the strong coupling regime between atoms and photons requires a high-finesse cavity which requires a small mode waist.

The finesse of a cavity is limited by the finite transmissivity of the mirrors and the scattering losses resulting from the roughness of the mirror surfaces. Ideally, the cavity should be overcoupled, which means that transmission losses dominate scattering losses. To reduce scattering losses, special attention must be paid to the coating, polishing, and handling of the mirrors. The scattered losses can be quantified by [28]

$$L_{\text{scattering}} = \left(\frac{4\pi\sigma}{\lambda}\right)^2,$$

where σ is the RMS surface roughness. Therefore, scattering losses of the order of 3.5 ppm require a surface roughness below $1\,\text{Å}_{\text{rms}}$ which is the limit of superpolishing techniques. This means that a cavity finesse of the order of 1×10^6 at the wavelength of lithium, 671 nm, is the state of the art. As the scattering losses scale quadratically with wavelength, higher finesses can be reached in the infrared.

In our experiment, we chose a centimeter-long symmetric Fabry-Perot interferometer as the cavity. This configuration provides for large optical access, which we use to directly laser cool the atoms between the cavity mirrors. This reduces cycle times and simplifies the experiment. When operating close to the concentric configuration, the smallest mode waist can be achieved, which is required for achieving high cooperativities (see Equation (1.3)). This means that the cavity length is only slightly less than double the radius of the mirrors. In particular, the centers of the spheres defined by the surface of the mirrors almost coincide. In this case, the mode waist can be expressed as $w = \sqrt{\lambda/\pi}\,(\zeta R)^{\frac{1}{4}}$, where $\zeta = 2R - L \ll R$ is the deviation of the cavity length from the concentricity condition, R is the radius of curvature of the mirror surface and L is the distance between the two mirrors, the length of the cavity.

The equation shows that small cavity modes can be achieved for small concentricity parameters ζ. However, as the difference between the centers of the two mirrors decreases, the cavity becomes more sensitive to the positioning of the mirrors, restricting the smallest possible waist of the mode. This is due to a mechanical lever amplification between the distance of the centers of the spheres defined by the mirror and the length of the cavity. As the centers of the spheres define the orientation of the cavity mode, a small displacement of the mirrors and therefore their centers leads to a large change of the cavity axis. The effect is illustrated in Figure 1.5.

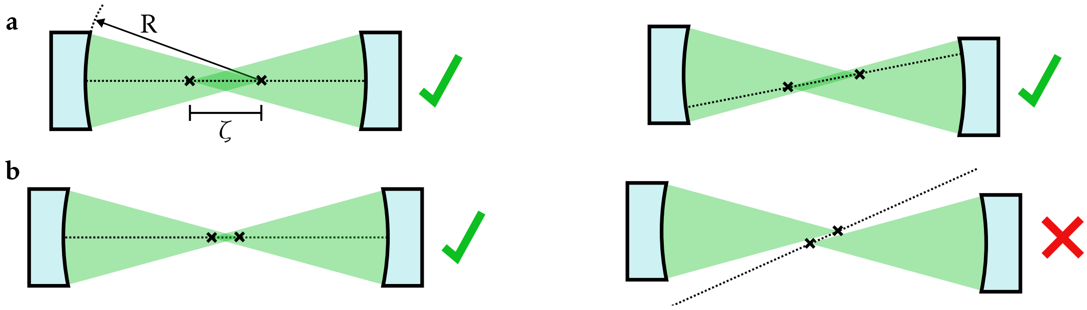

Figure 1.5: **Illustration of Sensitivity to Misalignment.** The axis of cavity mode (dashed line) is defined by the two origins of the mirrors (black crosses). A cavity can sustain a cavity mode, if it impinges on the mirror surface. The cone in which a mirror can capture the mode is marked in green. For the same misalignment, a cavity that is further from the concentric configuration (**a**) can sustain a mode, while a near-concentric cavity (**b**) cannot.

For centimeter-long cavities and millimeter-wide mirrors operating on the order of 100 µm from concentric, as in our case, this requires long-term stability in the position of the cavity mirror on the order of 1 µm. Cavities operating even closer to the concentric configuration require active stabilization of the mirror position, not only in the longitudinal direction (as is the case in our cavity), but also transverse to the cavity mode [29], which significantly increases the experimental complexity.

b) High-Resolution Microscope Local control over the interaction between the atoms and the cavity (see Section 1.1.2) allows us to enhance the spatial resolution of the cavity-enhanced measurements. The resolution of these measurements is determined by the resolution of the microscope. The spatial resolution of a microscope is limited by diffraction, the Abbe limit being $\lambda/(2\mathrm{NA})$, where λ is the wavelength of light and NA is the numerical aperture of the microscope.

In our experiment, we opt for a single-lens microscope design. To reach the diffraction limit, the front surface must have an aspherical shape. To reduce the curvature of the front surface, a glass with a higher refractive index can be used. State-of-the-art diffraction-limited aspheric lenses reach a numerical aperture of up to 0.6.

c) Fermionic ^{6}Li Our experiment is designed for ^{6}Li. The choice of atom determines the design wavelengths for our cavity-microscope. Atoms need to be trapped in optical dipole traps, which introduces wavelength requirements in addition to those imposed by the atom-cavity interaction and the focusing effect (see Section 1.1.2). Here is a short list of wavelengths and what they are used for:

- 671 nm: Cavity QED (cavity-based measurements and cavity-mediated atom-atom interactions), laser cooling (MOT and Zeeman slower, Raman transitions), imaging (absorption and fluorescence)
- 460 nm: Focusing effect (Light shift and Floquet driving), 2 photon imaging (absorption and fluorescence)
- 1342 nm: Cavity-enhanced optical dipole trap, PDH lock
- 780 nm: Optical tweezers trap

Following these requirements, our high-finesse cavity must support light at 671 nm and 1342 nm. The microscope must operate at 460 nm and 780 nm. Optionally, it could also be used to image the cloud at 671 nm. This was not possible for the optically-contacted design (see Section 1.3), as the same optical surface is used for both the microscope and the cavity. In the updated version (see Section 1.5), which separates the beams for imaging and the cavity, this feature was added.

d) Ultra-High Vacuum Environment and Optical-Access The cavity-microscope is designed for operation in an ultra-high vacuum (UHV) environment, which limits the choice of materials [30]. Furthermore, the materials used are non-magnetic as the atoms are very sensitive to stray magnetic fields. The shape of the device is optimized for large optical access. This is essential for our experiment, as we perform the laser cooling directly between the mirrors. In Figure 1.4 we show a diagram that illustrates the access requirements for the different viewports and laser beams.

e) Precise and Fast Adjustment of Cavity Length and Vibration Isolation Our experiments require adjusting the resonance frequency of the cavity. We use piezoelectric actuators under the mirrors to precisely tune the cavity length. Feedback acting on the piezo actuators is used to stabilize the length of the cavity. Particular care was taken in our experiment to optimize the mechanical response of the cavity, allowing us to reach high-bandwidth feedback on the cavity. Furthermore, cavities are very sensitive to mechanical vibrations. Therefore, we have designed a vibration isolation system that prevents acoustic noise from disturbing the cavity in the laboratory.

This concludes the list of requirements for our cavity-microscope. In the following section, we will describe the optical layout and features of the cavity-microscope currently installed in our vacuum chamber.

1.3 The Optically-Contacted cavity-microscope

In this section, the design and characteristics of the cavity-microscope currently used in the setup are discussed. All of the measurements presented in this thesis have been taken with this device. We are currently working on an upgraded design, which is discussed in Section 1.5.

This section is organized as follows: In Section 1.3.1, we provide an overview of the properties of the assembled cavity-microscope currently installed in the experiment. A more detailed description of the characteristics of each component that makes up the assembly is given in Section 1.3.3. A summary of the assembly process is given in Section 1.3.4. More details of the process can be found in Appendix C.

1.3.1 Optical Layout

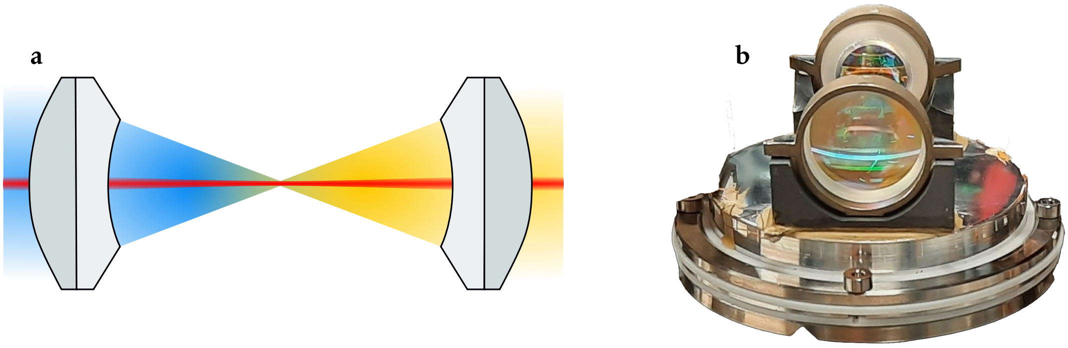

Figure 1.6: **Design of Optically-Contacted Cavity-Microscope. a**, Schematic of optics including the main laser beams. The cavity mirror (light gray) and the aspheric lens (dark gray) are optically contacted together. The cavity mode is shown in red. The focused beams at 460 nm and 780 nm are drawn in blue and orange. **b**, Picture of final assembly. An open-access online 3D model of the cavity is shown in Ref. [31]. Click here for quick access.

The cavity-microscope used in the setup is based on an optical contact design, as illustrated in Figure 1.6. This design combines a cavity mirror with an aspheric lens in a single optical element, the cavity lens. A special dielectric coating applied to its inner concave spherical surface enables the mirror to have a high reflection rate at 671 nm while at the same time providing a high transmission rate at 460 nm. The combination of the two cavity lenses forms a high-finesse optical resonator at the wavelength of the D2 line of lithium. The same element is used for the projection of patterns with high resolution at the control beam wavelength. This combination enables us to investigate the physics of locally tunable atom-cavity interactions (see Section 1.1.2), which is the core of this thesis. Furthermore, our cavity-microscope is used for atom trapping. It has a high reflection coating at 1342 nm that allows the operation of a cavity-enhanced dipole trap, which is used to keep the atoms in the middle of the cavity. Furthermore, the lenses can be used at 780 nm to trap atoms with optical tweezers.

1.3.2 Performance and Characteristics of Final Assembly

The properties of the device installed in our experiment are summarized in this section.

Cavity The properties of the assembled cavity are summarized in Table 1.1. From the mode structure of the cavity, we deduce that it is 105 µm shorter than the concentric configuration. This allows us to calculate a mode waist of 13.3 µm in the center. Combined with a measured finesse of 12 800, this gives a single-atom single-photon cooperativity of 6.5. Although the coating was designed for higher finesse at 671 nm, a higher finesse of 60 000 was observed at the trapping wavelength (1342 nm). The reduced finesse at 671 nm is probably due to scattering losses, as the shorter wavelength is more sensitive to surface roughness. This is in agreement with our cavity transmission measurements, which allowed us to estimate the cavity loss rates (see Figure 2.13). The losses caused by the scattering off the mirrors were found to be ten times greater than the losses due to transmission through the mirrors, leading to an extraction efficiency of photons from the cavity of 10 %. Since the cavity is symmetric, the detection efficiency of photons on each detector (single-photon counter and heterodyne detector, see Section 2.4) is limited to below 5 %.

Wavelength	671 nm	1342 nm
Cav. length	25.895 mm (2R – 105 µm)	
Free Spectral Range	5.79 GHz	
Transverse Mode Spacing	230 MHz	
Mode waist	13.3 µm	18.8 µm
Transmissivity (design)	25 ppm	100 ppm
Finesse (exp)	12 800	59 300
$\kappa/2\pi$ (exp)	451 kHz	98 kHz
η	6.5	
$g_0/2\pi$	2.7 MHz	

Table 1.1: **Characteristics of Cavity Part of the Cavity-Microscope Installed in Experiment.**

Being nearly concentric, the cavity assembly shows a mechanical amplification of the misalignment by a factor of approximately 130. A mirror displacement of only 10 µm in the transverse direction leads to a cavity mode displacement of approximately 1.3 mm on the mirror surface. As a result, the cavity is very sensitive to temperature fluctuations. In combination with mechanical hysteresis resulting from thermal stress relaxation in the cavity holder and epoxy glue, temperature changes can lead to irreversible misalignment of the cavity[*].

Wavelength	460 nm	780 nm
NA	0.37	
Focal length	16.68 mm	17.83 mm
Beam waist (theory)	0.52 µm	0.88 µm
Aberrations (theory)	$1.5\lambda_{\mathrm{RMS}}$ (spherical)	diffraction-limited
Strehl Ratio (exp)	N.A.	0.6

Table 1.2: **Characteristics of Microscope Part of the Cavity-Microscope Installed in Experiment.**

Microscope The cavity lenses have a numerical aperture of 0.37, which corresponds to a diffraction limited beam waist as small as 0.52 µm at 460 nm and 0.88 µm at 780 nm. The aspheric surface of the cavity lenses was optimized for 780 nm light, so the best optical performance can be seen at this wavelength. We measured a Strehl ratio of 0.6 at 780 nm, which is limited by imperfections in the shape of the aspheric lens surface and the imperfect relative alignment between the mirror and the lens*. The measured point spread functions of both of our cavity lenses are presented in Figure 1.7. The data were obtained by imaging light emitted from an SNOM tip using cavity lenses. With a modified Gerchberg-Saxton algorithm, we estimate the optical aberration of the lens [32]. The effective reconstructed wavefront in the Fourier plane is shown as an inset in Figure 1.7**a**.

---

[*] Unfortunately, we had left the MOT coils running for an entire weekend, which caused the two mirrors to become misaligned and the finesse to decrease to 6000. This occurred after the data presented in Chapter 5. The results in Chapter 4 were obtained with the deteriorated cavity.

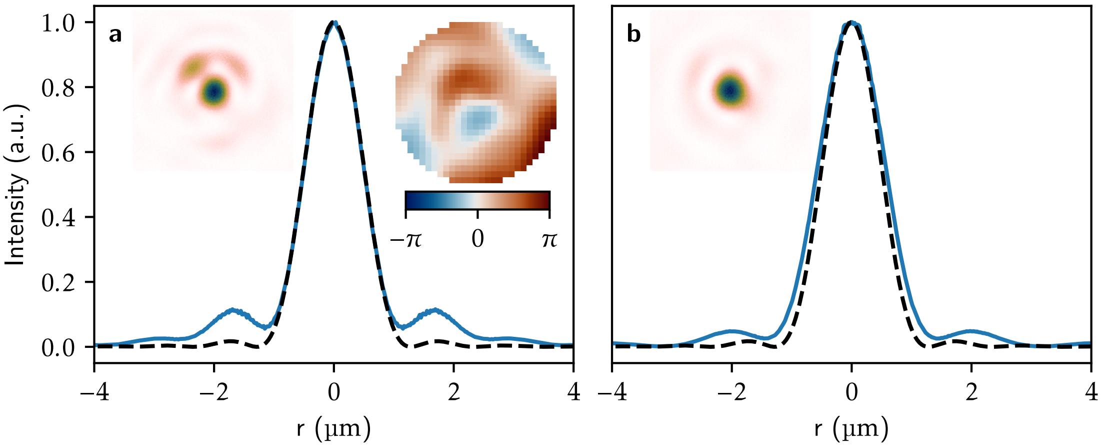

Figure 1.7: **Point-Spread-Function of Installed Cavity Lenses.** **a**, Measured and simulated point-spread-function (PSF) of the cavity lens we use for control pattern projection. **b**, Measured and simulated point-spread-function of the second lens. The blue line in the graph displays the measurement data, while the black dashed line indicates the theory. Both of these have been azimuthally averaged. The inset on the left of the graph is a false color image of the PSF measured on the camera. We used a modified Gerchberg-Saxton algorithm to reconstruct the wavefront, which is shown to the right of the graph.

Due to chromatic variations in the refractive index of the glass, the lenses exhibit a chromatic shift of 1.2 mm. In our experiment, we compensate for the change in focal length by diverging the input beam at 460 nm (see Appendix A.2.1). After compensating for the chromatic shift, simulations predict large spherical aberrations of around $1.5\lambda_{\mathrm{RMS}}$ at 460 nm. This is confirmed by measurements of the wavefront using the atomic cloud as a target. In Section 4.3, we demonstrate that a spatial light modulator (SLM) placed before the lens can be used to significantly reduce aberrations of the lens.

1.3.3 Details on the Components

In this section, the characteristics of each of the components of the cavity-microscope are summarized.

Cavity Mirror The cavity mirror is made of standard N-BK7 glass. Its thermal expansion rate is matched to the glass of the lens (S-LAH99). The optical element has a maximum diameter of 16 mm, which is also the diameter of the flat surface. Its diameter conically reduces towards the concave spherical mirror surface, which has a reduced diameter of 10 mm and a radius of curvature of 13 mm. The mirror has been superposlished over an aperture of 5 mm at the center of the mirror. In the superpolished region, the roughness of the mirror surface was specified to be below 1.5 Å outside this region, it was specified below 5 Å. The curved surface was measured by the manufacturer and reported an irregularity of quarter-wave peak-valley over 50 % of the clear aperture and half-wave peak-valley over 90 % of the clear aperture. The flatness of the planar side of the mirror was specified to 1/10 wave, which is necessary for good optical contact. The mirrors were manufactured and superpolished by *Perkins Precision Developments* [33].

---

*We ordered six lenses and post the two which showed the best Strehl ratio.

A coating was applied to the spherical surface by *fivenine optics* [34]. Its transmissivity was specified at 25(7) ppm for 671 nm and 75(10) ppm for 1342 nm. The reflectivity was minimized at 460 nm and 780 nm. The transmission measurements provided by the manufacturer show a transmission of 99 % at 460 nm and a transmission of 97 % at 780 nm.

Aspheric Lens The custom aspheric lens is made of high refractive index glass (S-LAH99), which allows it to be thin and simplifies the manufacturing process. It has a diameter of 16 mm and a clear aperture of 14.4 mm. The shape of the aspheric surface was adjusted to provide the best optical performance at 780 nm for the cavity lens assembly. *OSLO* [35], a lens design tool that combines advanced ray tracing, analysis, and optimization methods, was used to simulate the cavity lens and optimize the aspheric surface.

The lenses were manufactured by *Asphericon* [36] using CNC diamond milling. An antireflection coating was applied to the aspheric surface. The reflectivity was specified below 0.5 % for all wavelengths used in our setup. To reduce reflections at the interface between the lens and the mirror, an antireflection coating was applied to the flat surface of the lens, which matched the two refractive indices. The reflectivity was specified below 0.3 % for angles of incidence from 0–40°. The same as for the mirror, the flatness of the plano side of the mirror was specified as 1/10 wave.

Piezo Actuator The design uses flat piezoelectric shear actuators glued under the cavity mirror assembly to change the cavity length. They were supplied by *PI Ceramics* [37] and have a thickness of 0.5 mm. These actuators have a stroke greater than 1 µm when a voltage of 500 V is applied. They were cut to their final shape using a laser cutting machine.

Cavity Support Structure The cavity holder is made up of multiple layers of different materials, layered on top of each other. This structure helps decrease the mechanical resonance of the support structure. Its design is the subject of Section 1.4. The cavity lenses are mounted on top of the holder, allowing for large optical access from the side for various laser beams. The cavity lenses are held by a silicon carbide adapter. The high specific stiffness of silicon carbide improves the stiffness of the assembly and, therefore, pushes the resonance frequency of the flapping motion of the cavity lenses to a higher frequency. The silicon carbide adapters were provided by *Fraunhofer IKTS*[38].

1.3.4 Assembly of the Cavity-Microscope

This section outlines the procedure for assembling the cavity-microscope. An overview of the different steps is presented in Figure 1.8. More details of the procedures can be found in Appendix C.

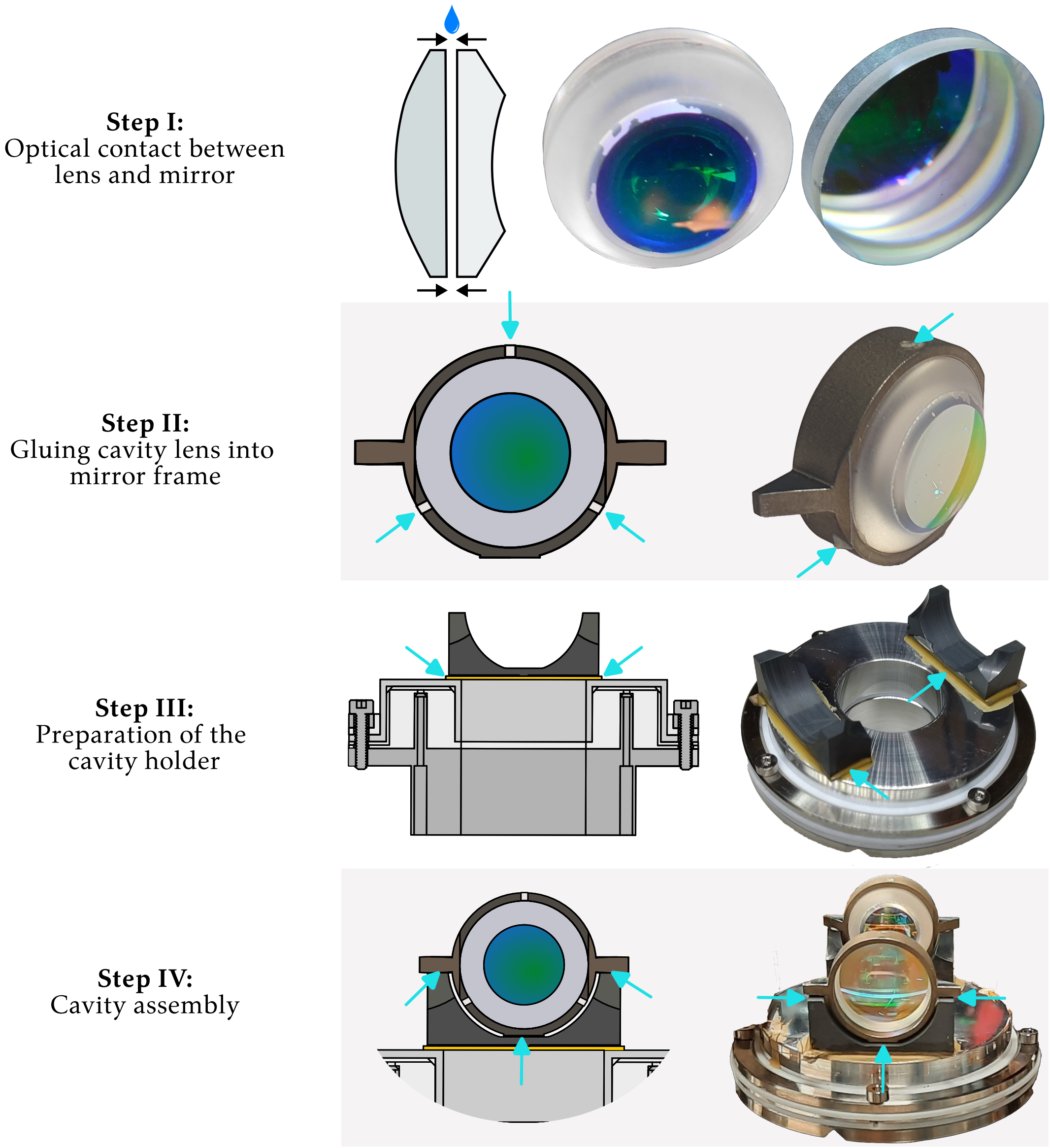
Step I:
Optical contact between lens and mirror
Step II:
Gluing cavity lens into mirror frame
Step III:
Preparation of the cavity holder
Step IV:
Cavity assembly

Figure 1.8: **Assembly Procedure for Cavity-Microscope Installed in Experiment.** (left) 2D schematic drawing of the assembly step. (right) Picture of the result of the assembly. The green arrows point to the locations where glue as applied.

Step I: Optical Contact between Lens and Mirror The assembly process begins by attaching two optical components, the mirror and lens, together. The assembly process based on optical contact bonding starts with cleaning the flat surfaces of the mirror and lens using the drag-and-wipe technique. Then, we mounted them in an optical alignment setup to make sure that they were concentric with a pilot beam. To initiate the optical contact process, we placed a drop of water in the gap between the two optical elements, which attracted them together. After most of the water had evaporated, we removed the cavity lens assembly from the alignment setup and heated it to 70 °C for 1 h under vacuum. In Appendix C.1 more details are provided on the setup and procedure used for optical contact between the two elements.

Step II: Gluing Cavity Lens into Mirror Frame The cavity lens was attached to a titanium frame with Masterbond EP21TCHT-1 adhesive. The two pieces were carefully aligned using a v-shaped Teflon tool. The wings and bottom of the titanium mirror frame were rounded to ensure good contact with the cavity holder during the final gluing process.

Step III: Preparation of the Cavity Holder The different components of the cavity support structure were manufactured using standard milling techniques. The elements are designed to fit tightly on top of each other. In fact, a manual press is needed to assemble the holder. The upper surface of the support structure was polished because this improves the outgassing characteristics of the aluminum under vacuum. Shear piezoelectric actuators, which allow an accurate adjustment of the cavity length, were attached between the holder and the u-shaped silicon carbide mirror mount. Electrical cables were adhered to the actuator using conductive adhesive.

Step IV: Cavity Assembly The last step of the assembly process is to combine two cavity lenses and the cavity holder to form the final cavity-microscope. This required a precise positioning of the mirrors. After the cavity was properly aligned and its performance was satisfactory, the cavity support structure was attached to the mirrors using a vacuum-compatible room temperature cure adhesive (Masterbond EP21TCHT-1). A special optical setup was designed to complete the cavity assembly, and more details can be found in Appendix C.

1.3.5 Discussion

The assembled cavity-microscope is installed in the vacuum chamber of our cold-atom experiment. Its optical performance is sufficient to achieve the strong coupling between the atoms and the cavity (see Section 5.5.1). We have shown that the combination of high-finesse cavity and high-resolution microscope allows the tuning of the atom-cavity interaction at the micrometer scale, making it a very sensitive measurement device with high spatial resolution (see Chapter 4).

However, there are many issues with the presented design that are addressed by the next generation cavity-microscope, which is presented in Section 1.5. During the design of this cavity-microscope, special care was taken to suppress the mechanical resonances of the cavity support structure. In the following section, we present the key arguments leading to the cavity support currently installed in the vacuum chamber.

1.4 Design of Vibration Damping Platform

In this section, we will present the key features of the mechanical mounting platform that supports our cavity-microscope. The content of this section follows closely our publications [39].

High-finesse optical interferometers, as the one installed in our experiment, are among the devices most sensitive to vibrations: Displacements of the mirrors at the picometer scale lead to significant changes in the cavity transmission. This sensitivity can be exploited for sensing [40, 41], but for most applications this leads to significant disturbances, in particular for cavity quantum electrodynamics (cQED) experiments that require absolute stability of the cavity length. Although shielding against external disturbances can be achieved efficiently through the use of well-established techniques [42], the need for active stabilization of the cavity length implies the use of actuators on the mirrors for continuous feedback, triggering vibrations in the structure. In particular, sharp vibration resonances severely limit the bandwidth of feedback loops and ultimately represent the main limitation to cavity stability. This is especially relevant for new generations of cQED experiments employing long cavities or complex geometries [25, 29, 43–49], where mechanical resonances can occur at low frequencies.

Damping and mounting strategies have been implemented for cavity systems, for example, in the context of laser stabilization or interferometers [50–54]. However, the constraints of an ultrahigh vacuum (UHV) environment have prevented their direct use in cQED applications. Therefore, advanced signal filtering methods have been developed to cancel mechanical resonances within feedback loops [55]. In this Letter, we present the design of a composite cavity holder that features efficient passive damping while maintaining UHV compatibility. Compared to a bulk platform with the same geometry, our composite platform shows efficient suppression of all mechanical vibration modes up to 100 kHz and a smooth phase response compatible with high-bandwidth feedback loops.

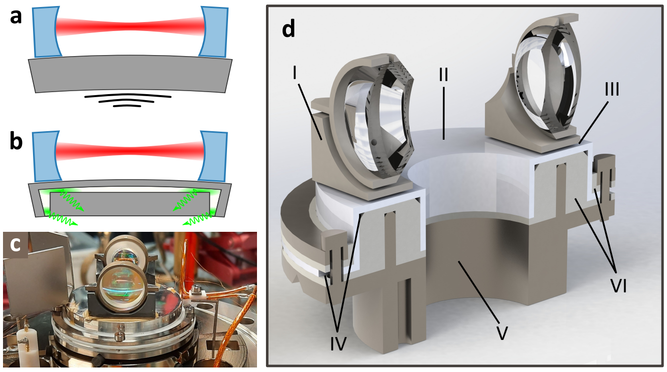

Figure 1.9: **Principle and Design of the Cavity Holder.** Schematic **a** shows the fundamental mode of vibration of a bulk cavity holder which leads to a shift of the optical resonance frequency. The holder in **b** is damped (dissipation in green), suppressing mechanical vibrations. Picture **c** of the final assembly of the optical cavity was taken before the system was installed inside the vacuum chamber. Rendering **d** represents a section of the cavity holder. The roman number annotations are referenced in the main text.

The cavity holder consists in a toroidal platform, hosting two shear piezoelectric actuators (see Figure 1.9d III) onto which the cavity mirrors (Figure 1.9d I) are glued. Its geometry is chosen to maximize optical access from all directions. The motion of the mirrors caused by the cavity length stabilization loop drives the mechanical vibration modes of the holder, as illustrated in Figure 1.9**a**. With a cavity mirror spacing of roughly 2.5 cm, the lowest vibration mode frequency lies in the 10 kHz range, weakly dependent on the choice of materials among vacuum compatible and machinable metals.

To damp these resonances, we designed the holder as a composite core-shell structure comprising three different pieces: (i) a rigid u-shaped shell maintaining the alignment of the cavity mirrors (Figure 1.9**d** II), (ii) a soft and thick damper that fills most of the shell's volume (Figure 1.9**d** VI) and (iii) a high-rigidity base pressed inside the damper (Figure 1.9**d** V). The general operation principle is illustrated in Figure 1.9**b**: the vibration mode driven by the piezoelectric actuators deforms the shell, which transmits the deformation to the damper. The damper is thus compressed against the base, efficiently dissipating energy within its volume.

1.4.1 Design Criteria

Materials

The simple mass-spring model presented in Figure 1.10**a** helped us extract the main figures of merit for choosing the materials. In this model, the mirrors (red) are connected to the holder (gray) through the springs of strength k_m. The distance from the mirror to the mount is tuned by a piezoelectric actuator (orange). The holder is attached to the damper (green), which has a damping coefficient η_d. A simple calculation shows that in the limit of stiff and light mirrors, the resonance frequency of the ensemble is proportional to $\sqrt{\widetilde{k_h}/\widetilde{m}}$, the square-root of the effective specific stiffness, where $\widetilde{k_h} = k_h + k_d$ is the combined elastic modulus of the holder and damper, and $\widetilde{m} = m_m + m_h + m_d$ is the combined mass of the mirror, holder, and damper. The quality factor Q of this resonance is proportional to $\sqrt{\eta_d \widetilde{m}}$.

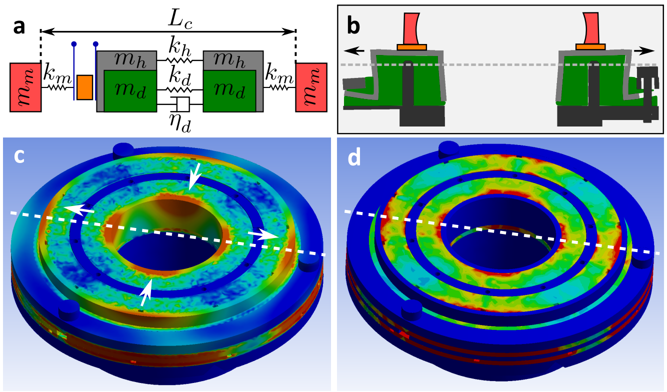

Figure 1.10: **Model and Simulation Results.** Drawing **a** depicts a simple spring model of the cavity assembly. Drawing **b** shows the exaggerated displacement of the cavity holder under the main mechanical resonance (colors as in **a**). In **c** and **d** respectively, the total displacement and the von Mises strain in the holder assembly are shown, in a section taken along the gray dashed line in **b**. The white dashed lines indicate the cavity axis and the white arrows represent the direction of deformation.

Minimizing the effect of mechanical vibrations requires high resonance frequencies, to allow for higher stabilization bandwidth, and low Q-factors, implying the use of materials with high specific stiffness and high damping. Unfortunately, all common stiff materials intrinsically have low damping coefficients, hence the use of a composite structure.

For the top shell, we chose aluminum as a compromise between machinability and high specific stiffness [*]. For the damper, we chose Teflon (PTFE) for its high mechanical loss tangent of 0.2 at room temperature, due to two first-order crystal-crystal transitions at 19 °C and 30 °C [57–59]. It can be machined easily and is UHV compatible, as opposed to most rubber materials commonly used as dampers. Additionally, it can be baked at temperatures exceeding 150 °C. For the base, we chose titanium for its high stiffness, machinability, and UHV compatibility.

---

[*] Taking simple precautions, its UHV compatibility can be ensured [56].

Geometry

We optimized the geometry of the holder using finite element (FE) simulations [60]. With a modal analysis, the shape of the top plate was optimized for high resonance frequencies (>20 kHz) and low weight. The mode that most affects cavity length is the fundamental stretch mode (see Figure 1.10**b**,**c** and **d**). A cylindrical u-shaped top plate was found to maximize its frequency, making it similar to that of a bulk holder while significantly reducing weight.

Because damping is proportional to the time-variation of strain, a key parameter here is the efficient coupling of the motion of the top plate to the compression of the damper. To achieve maximal deformation of the damper for a given deformation of the holder, we use a rigid base pressed inside the bulk of the damper. In this way, the deformation of the top plate compresses the damper against the base, as illustrated in Figure 1.10**b**. To validate the design principle, we calculated the distribution of the absolute value of the total deformation of our cavity holder for the stretch mode using a FE simulation, as presented in Figure 1.10**c**. The largest deformations appear on the outer shell and leave the base (blue circle in the middle) fixed, illustrating the compression mechanism of the damper between the shell and the base. The corresponding strain distribution is presented in Figure 1.10**d**, confirming the efficient strain transfer to the damper and validating our the design criteria. The simple model can thus be used for future designs of cavity holders without the need of a complete FE simulations.

1.4.2 Mechanical Assembly

The top plate consists of a 1 mm thick aluminum shell that encapsulates the PTFE damper, which is pressed against the titanium base. The parts are fastened together using titanium screws at the outer edges (see Figure 1.9**d**). There is no direct, rigid contact between the top plate and the base thanks to a damping PTFE ring on the outside. Apart from the piezoelectric actuators for cavity length stabilization, there are no moving parts, minimizing the risk of spurious vibrations. The assembly itself rests on a stack of two non-magnetic stainless steel rings separated by Viton rods for isolation [42], themselves sitting on the bottom flange of a vacuum chamber, as shown in Figure 1.9**c**. A network of venting channels in the damper and base (see Figure 1.9**d** IV) prevents virtual leaks for UHV operation.

1.4.3 Performance Characterization

Mechanical Response Measurements

We measured the frequency-dependent mechanical response of the holder by exciting harmonic vibrations and measuring them with a Michelson interferometer, using a mirror glued to the holder (see Figure 1.11**a**). With a slow feedback loop (200 Hz bandwidth), the interferometer was stabilized to a half-fringe configuration. Harmonically driving the piezoelectric actuator and demodulating the interference signal allowed retrieving the complex transfer function relating the relative mechanical displacement of the mirror with respect to a reference mirror to the actuator voltage. To evaluate the performance of our damped cavity holder, we compared its response with that of a geometrically identical holder made of bulk stainless steel.

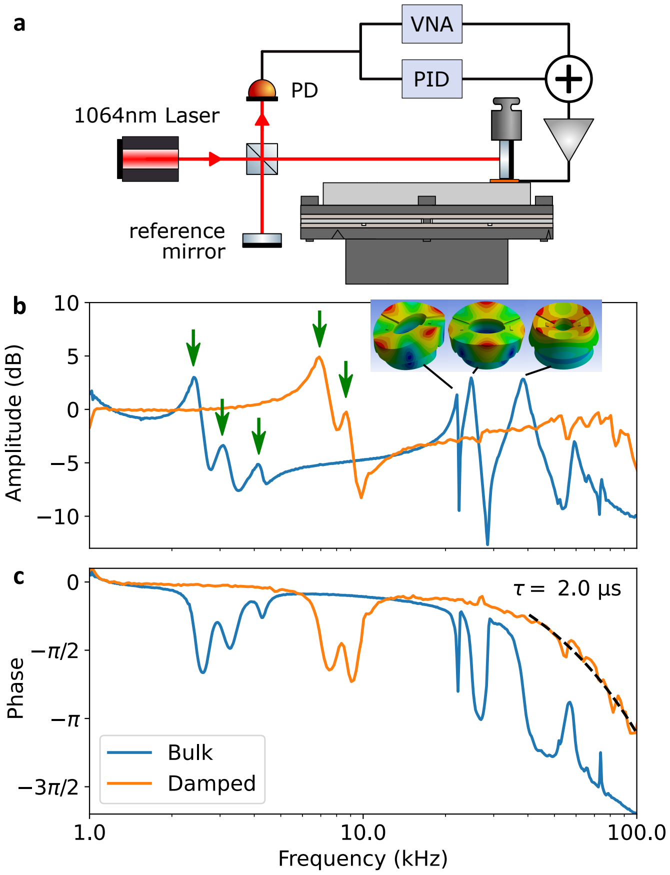

Figure 1.11: **Mechanical Response Functions.** Schematic **a** illustrates the mechanical, optical and electrical layout of the Michelson interferometer setup used to measure the mechanical response of the holders. In order to pull down the resonance frequency of the mirror from 20 kHz to below 10 kHz, we glued a weight on top of the test mirror. The graphs **b** and **c** present the amplitude and phase of mechanical response functions for two different holder designs, a damped holder in orange, and a geometrically identical bulk stainless steel version presented in blue. The weight on the stainless steel version is larger, hence the lower mirror resonance frequencies. The inset shows the exaggerated deformations of the bulk holder for the the indicated resonances.

The results are presented in Figure 1.11**b** and **c**. For both holders, a set of isolated resonances at frequencies lower than 10 kHz, indicated by arrows in Figure 1.11**a**, results from the flexure modes of the mirror itself. We have confirmed this first by an ab-initio FE calculation which we expect to be quantitatively accurate for such a simple homogeneous part, and second by changing the weight of the mirror, which led to a change of the mirror resonance frequencies. We did this by gluing small stainless steel weights on top of the mirrors (see Figure 1.11**a**). In the two cases, the weights were not identical. Therefore, the mirror resonances appear at different frequencies for the two different holders. Without any weight, the resonance frequency of the test mirrors itself was independently measured to be 20 kHz.

A second set of resonances at higher frequencies, insensitive to changes of the mirror mass, results from the modes of the holder itself. These resonances are very prominent in the bulk stainless-steel holder, appearing as sharp peaks and abrupt phase jumps by about $-\pi$. A comparison with the mode frequencies calculated from the FE model allows us to identify them as flexure and stretch modes of increasing order.

In contrast, the composite holder is essentially resonance-free up to 100 kHz. In particular, except at the mirror resonances, the phase of its mechanical response stays above $-\pi/2$ up to 60 kHz, and smoothly rolls with a typical timescale of 2 µs [*], making the platform, when used with small mirrors, suited for high-bandwidth regulation of the cavity length. At these higher frequencies, vibration modes become dense and overlapping, making electronic filtering challenging [55], while the damping properties of our composite holder do not degrade.

Vacuum Compatibility

The holder has been integrated into a cQED setup, with a pair of large mirrors (14 mm diameter) forming a high-finesse cavity ($\mathcal{F} = 6\times10^4$ at 1342 nm). After thorough cleaning and prebaking of the different parts of the holder at their maximum allowed temperature and under vacuum, the holder was assembled with cavity mirrors under ambient conditions and installed in a standard cold-atom UHV system. In our experiment, we use a nearly-concentric cavity, 100 µm away from the stability limit, which is sensitive to misalignment at the micrometer scale. Therefore, to prevent thermal deformation, the aligned cavity system was not baked after installation. Nevertheless, we measured a pressure in the low 10^{-11} mbar range, and a lifetime of laser-cooled atoms of 32 s at the center of cavity which increased to 68 s after less than a year of operation, demonstrating the full UHV compatibility of the holder and its suitability for the most demanding quantum gas experiments.

1.4.4 Conclusion

Due to its composite core-shell structure, our cavity holder efficiently damps the mechanical resonances within its structure, compromising neither optical access nor UHV compatibility. The materials are inexpensive, widely available, and can be easily machined using standard mechanical tools. This concept is generic and can be applied to a wide variety of systems, in particular to experiments requiring long cavities that are highly sensitive to vibrations. In our situation, where cavity mirrors are rather large, the mechanical modes of the mirrors themselves remain unchanged by the holder properties and lead to isolated resonances in the low 10 kHz range. These isolated resonances should be easily handled via electronic filtering. We expect that our mechanical approach, combined with electronic techniques, will allow for the use of long, ultra-narrow cavities in future quantum simulation systems without the risks associated with vibrations.

1.5 Development of the Next-Generation Cavity-Microscope

The cavity-microscope currently installed in our experiment has several issues, which led us to develop a new high-resolution cavity-microscope with a stacked optical design. Our aim is to enhance the optical performance of both the cavity and the microscope, thus enabling us to achieve higher cooperativity and spatial resolution while at the same time simplifying its design.

The section is organized as follows: In Section 1.5.1, we discuss the optical design of this prototype and how it addresses the problems encountered by the cavity-microscope currently used with the atoms. The optical performances of both the cavity and the microscope are summarized in Section 1.5.2. Section 1.5.3 provides a comprehensive list of the properties of each individual component of the cavity-microscope. Lastly, Section 1.5.4 describes the various stages of the assembly process. More details on the development process can be found in Gaia Bolognini's master thesis [61].

---

[*] We attribute this delay to the acoustic wave propagation in the mirrors and to delay in various parts of the electronic systems, in particular the high-voltage amplifier.

1.5.1 Optical Layout

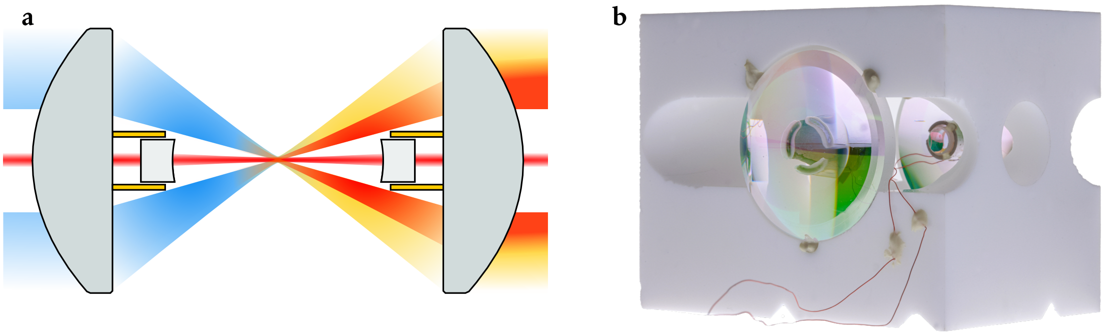

Figure 1.12: **Design of Next-Generation Cavity-Microscope. a**, Schematic of optical assembly and principle laser beams. The cavity mirror (light gray) and the aspheric lens (dark gray) spaced with a ring piezo (orange). The cavity mode is shown in red. The focused beams at 460 nm and 780 nm are drawn in blue and orange. The lenses can also image 671 nm light as illustrated in red. **b**, Picture of final assembly. TAn open-access online 3D model of the cavity is shown in Ref. [62]. Click here for quick access.

The next generation cavity-microscope has a separate optical layout, as illustrated in Figure 1.12. It is made up of two small mirrors that form a high-finesse cavity. These mirrors are combined with two large aspheric lenses. In this new design, light entering the cavity passes through the center of the lens, while light used for the microscope passes around the cavity mirror, thus simplifying both the cavity and the microscope design. This design is different from the optically contacted one, which uses a single optical surface for both the microscope and the cavity laser beams.

In particular, the cavity mirror coating is designed only for 671 nm and 1342 nm, since the need for high transmission at 460 nm and 780 nm is eliminated. Furthermore, the complexity of the optical design of the microscope is significantly reduced. The microscope light passes through the aspheric lens only, which means that off-the-shelf diffraction-limited lenses can be used for the assembly. This is in contrast to the optically contacted design, where a custom lens had to be developed in order to be able to focus through the cavity mirror. As a result of this disentanglement of both properties of the cavity-microscope, independent optimization of the optical properties of each component can be performed.

The small cavity mirrors are glued to the center of the aspheric lenses. A piezoelectric tube actuator is placed between the cavity mirror and the lens. This allows for the tuning of the cavity's length. Compared to the optically contacted device, the weight of the cavity mirror is significantly reduced, meaning that the forces needed to move the cavity mirrors are much smaller. This eliminates the need for a complex vibration-dampened cavity support structure, as the coupling to the mechanical resonances of the holder is strongly suppressed.

1.5.2 Performance and Characteristics of the Prototype Cavity-Microscope

The properties of our first prototype are summarized in this section.

Cavity The key characteristics of the cavity are summarized in Table 1.3. It is shorter than the concentric configuration of 46 µm, resulting in a small waist of 10.1 µm in the center. This, combined with a measured finesse of 9900, gives a single-atom, single-photon cooperativity of 8.5, which is slightly higher than the cavity currently in use. Although the coating was designed to achieve higher finesse at 671 nm, a higher finesse of 44 000 was observed at the trapping wavelength (1342 nm). The reduced finesse at 671 nm is likely due to scattering losses, as shorter wavelengths are more sensitive to surface roughness.

Wavelength	671 nm	1342 nm
Cav. length	19.954 mm (2R – 46 µm)	
Free Spectral Range	7.52 GHz	
Transverse Mode Spacing	230 MHz	
Mode waist	10.1 µm	15.7 µm
Finesse (exp)	9900	44 000
$\kappa/2\pi$ (exp)	750 kHz	170 kHz
η	8.5	

Table 1.3: **Characteristics of Cavity of Next-Generation Cavity-Microscope.**

Microscope The key properties of the single lens microscope are summarized in Table 1.4. The mirror located in the center of the lens blocks the view of the microscope, thus reducing its collection efficiency. In fact, the solid angle of light collected by the cavity lenses is decreased by 20 % due to the mirror. Despite this, the lens can still be used for high-resolution imaging. Its point spread function, which is an obscured airy pattern [27, 63], actually displays a smaller spot size than the original lens. The obscured airy pattern is characterized by the annular aperture obscuration ratio, which is 0.4 in our system.

Wavelength	460 nm	780 nm
NA	0.52	
Focal length	19.39 mm	20 mm
Beam waist (theory)	0.37 µm	0.63 µm
Aberrations (theory)	N.A.	diffraction-limited
Strehl Ratio (exp)	N.A.	0.55

Table 1.4: **Characteristics of Microscope of Next-Generation Cavity-Microscope.**

By blocking the center of the lens, we eliminate the low spatial frequencies of the imaging system. The high spatial frequencies that are necessary to obtain a high spatial resolution remain. We have tested this both theoretically and experimentally, and the results are shown in Figure 1.13. We observe that the spot size[*] decreases from 0.61 µm to 0.56 µm when inserting the mirror. The difference between the experiment and the theory is probably caused by chromatic aberrations that are a result of the spectral width of the LED used to light up our target.

---

[*] This quantity is the waist of a Gaussian fitted to the central fringe.

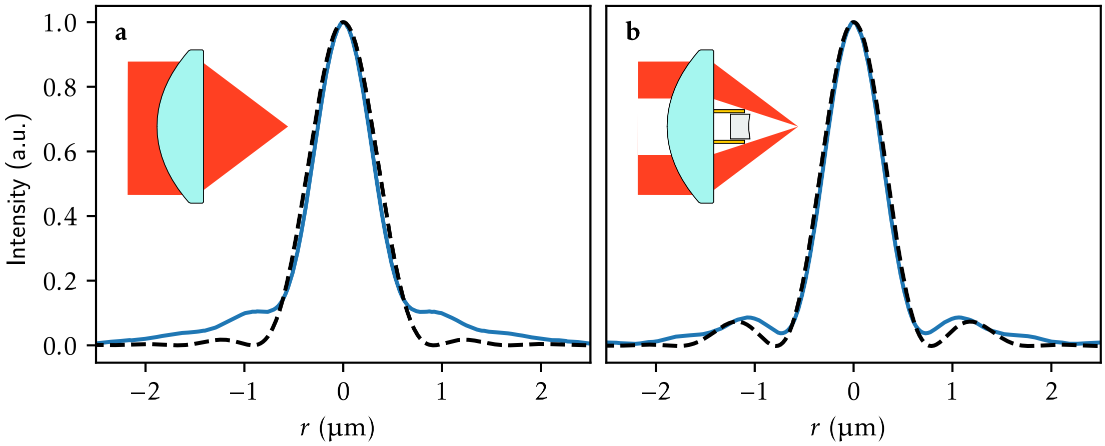

Figure 1.13: **Effect of Mirror on Imaging Performance. a**, Measured and simulated point-spread-function of bare lens. **b**, Measured and simulated point-spread-function of lens with mirror glued to the center. The measurement data is shown in blue and the theory in black dashed lines. In both cases, the measurements are azimuthally averaged. More details on the measurement setup can be found in the thesis of Gaia Bolognini [61].

1.5.3 Details on the Components

In this section, the characteristics of each of the components of the cavity-microscope are summarized.

Cavity Mirrors The mirror has a diameter of 4 mm. The manufacturer (Perkin Precision Optics [33]) measured that the roughness of the spherical surface is less than $1\,\text{Å}_{\text{RMS}}$ in the middle of the mirror. The mirror coating was done by *LaserOptics* [64]. They specified that the transmission of the mirror coating would be as low as 15 ppm for 671 nm, but the measured finesse of the cavity assembly was as low as 10 000. This is likely due to light scattering losses from contaminants in the coating or the substrate being too rough.

Aspheric Lens Standard diffraction-limited lenses (Thorlabs AL2520H) with a numerical aperture of 0.52 were used for the microscope. They are designed for 780 nm light, which is the same wavelength as our optical tweezers. According to the datasheet, these lenses are diffraction-limited in the wavelength range from 720 nm to 870 nm. At 671 nm a Strehl ratio of 0.3 is specified. Lenses are coated with an anti-reflective coating on both sides. The coating is specified at 671 nm, 460 nm, 1342 nm and 780 nm.

Piezo Actuator To adjust the length of the cavity, we use tube piezoelectric actuators. They were custom-made by *PI ceramics* [37] and have a length of 5 mm, an inner diameter of 4.5 mm and a wall thickness of 0.5 mm. The two electrodes (outer and inner) are silver coated. We cut small grooves at both ends of the actuator (see Section 1.5.4). These are used for venting and as a feed-through for the wire attached to the inner electrode.

Cavity Support Structure The support structure is custom-machined from Macor ceramic (see Figure 1.12**b**), which is similar to other cavity holder designs[22, 65, 66]. Unlike our former design, which had the mirrors placed on top of the holder, the lenses are embedded into the cavity holder. Cutouts that are precisely located in the holder enable optical access to the middle of the cavity. This is necessary for both the MOT beams and the Zeeman slower beams. This holder structure has the benefit of reducing the flapping mode of the large cavity lenses, which would otherwise lead to a strong connection between mechanical resonances and the cavity length. As a result, no additional design optimization was required to dampen mechanical vibrations.

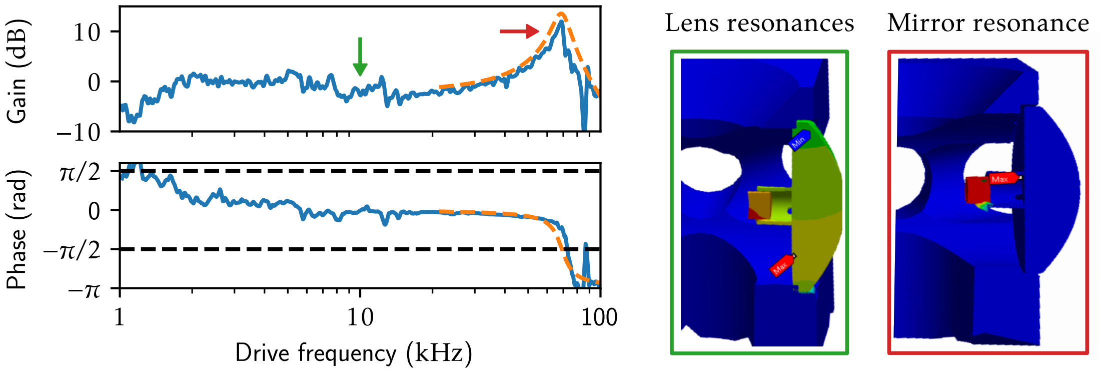

Figure 1.14: **Frequency Response of Piezoelectric Actuators.** Measured Bode response of piezoelectric actuators on cavity length. The data was measured by locking the cavity to the laser with a side-of-fringe lock and modulating the piezo voltage at different frequencies. Demodulating the cavity transmission reviled both the phase and the amplitude of the oscillations of the cavity length. The resonances in the 10 kHz range correspond to the resonances of the lens (see finite-element simulation on the left, green frame). The isolated resonance that strongly couples to the cavity length at 68 kHz corresponds to the mirror oscillating on top of the piezo (see finite-element simulation on the right, red frame).

We have measured the response of the cavity to changes in the voltage applied to the piezoelectric actuators. The measurements presented in Figure 1.14 confirm that small mirrors reduce the coupling of changes in cavity length with mechanical resonances of the cavity support structure. The response curve shows only a weak coupling to the resonances of the mount and lenses at frequencies below 100 kHz. Finite element simulations confirm that the first resonance at 70 kHz, which is strongly coupled to changes in cavity length (phase excursion greater than $\pi/2$), is due to oscillation of the mirror in the piezotube actuator. This shows that by using small mirrors, the need for a complex vibration-damping structure, as presented in Section 1.4 can be eliminated.

1.5.4 Summary of Assembly Procedure

This section presents a short summary of the assembly procedure for the cavity-microscope. A more detailed description of the assembly procedure can be found in the master thesis of Gaia Bolognini [61].

A summary of the different steps is provided in Figure 1.15. To protect the high-finesse mirrors from contamination or damage during handling, a protective film (*FirstContact* [67]) was applied to them throughout the process. The protective film was only removed for the final step, the cavity assembly.

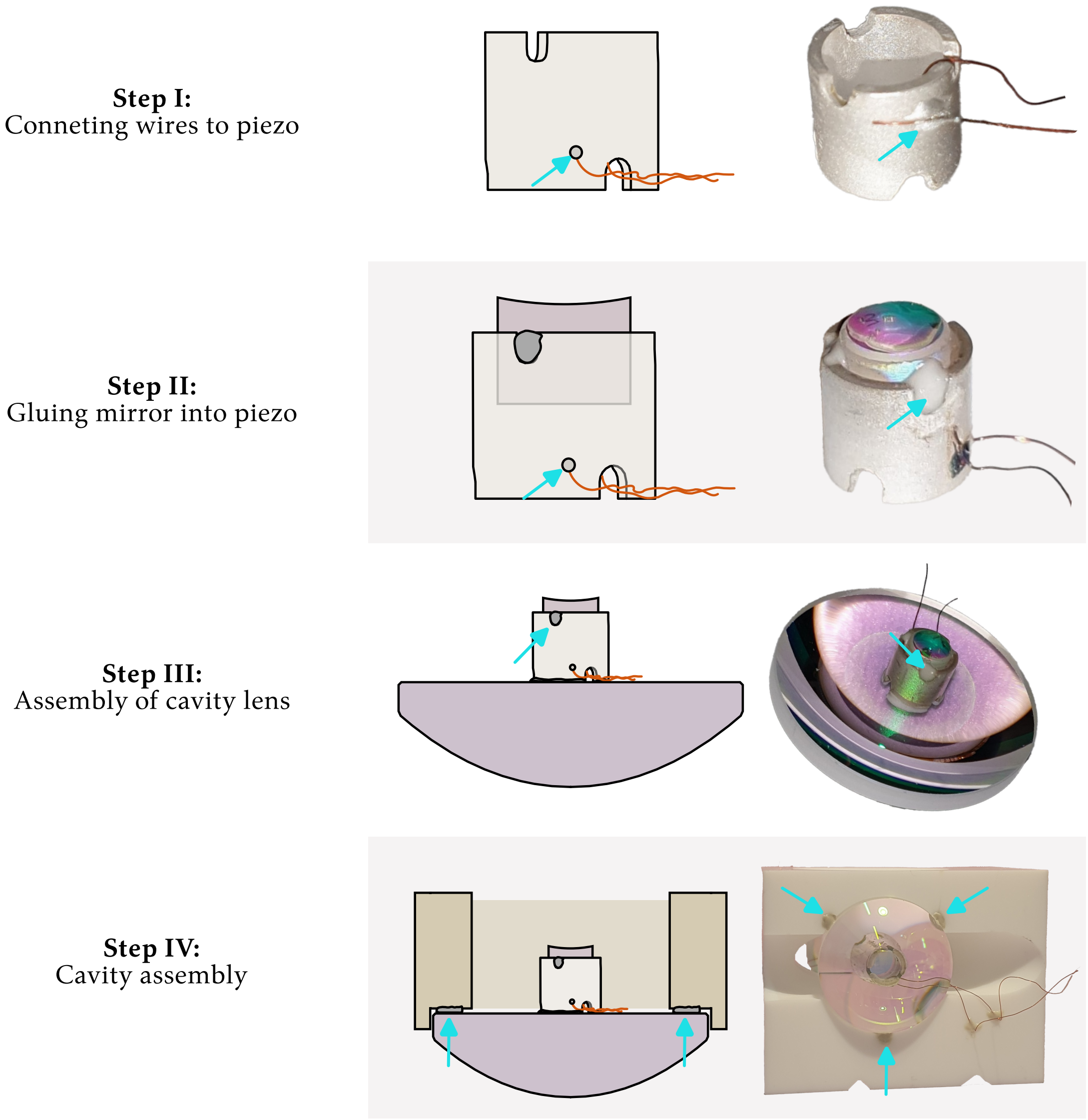
Step I:
Conneting wires to piezo
Step II:
Gluing mirror into piezo
Step III:
Assembly of cavity lens
Step IV:
Cavity assembly

Figure 1.15: **Assembly Procedure of Next-Generation Cavity-Microscope.** (left) 2D schematic drawing of the assembly step. (right) Picture of the result of the assembly step.

Step I: Connecting Wires to Piezo Actuators A conductive vacuum compatible adhesive was used to attach two wires of 0.1 mm in diameter to the inner and outer electrodes of the piezoelectric tube actuator. The wire from the inner electrode passes through the u-shaped openings in the piezotube.

Step II: Gluing Mirror to Tube Piezo Our high-finesse mirrors were glued to the tube piezo using Masterbond EP21TCHT-1 adhesive. A microscope was used to ensure the concentricity of the assembly.

Step III: Assembly of the Cavity Lens With a thin layer of Masterbond EP21TCHT-1 adhesive, the piezo-mirror assembly was glued to the center of the lens. The concentricity of the assembly was ensured by a custom alignment tool made from Teflon.

Step IV: Cavity Assembly The last step in cavity construction involves aligning the two cavity lenses to each other and then attaching them to the ceramic holder with Masterbond EP21TCHT-1 adhesive. We have developed an optical setup to perform this operation.

1.5.5 Discussion and Outlook

The second version of the cavity-microscope discussed in this thesis was able to address many of the issues associated with the optically contacted cavity-microscope. Its straightforward stacked optical design made the construction process easier and enabled independent optimization of the cavity and microscope parameters. Additionally, it enabled the use of smaller cavity mirrors, which are lighter and thus cause less vibrations in the cavity holder, as well as a faster response of the cavity length to changes in the voltage applied to the piezo. This eliminated the need for a complex damped cavity holder.

Nevertheless, there are still two issues with the current design that need to be resolved:

- This prototype has been found to have a much lower finesse than expected, leading to a low rate of photon extraction from the cavity. To enhance the optical performance of the cavity, more research is needed. At the conclusion of my thesis, a batch of highly polished substrates was ordered, which should address this problem.
- We observed a strong misalignment of the cavity mode during the curing process of the glue. In one of the two prototypes we assembled, this leads to the loss of the cavity signal. Being so close to concentric, this prototype has a mechanical amplification factor of approximately 217, making it even more sensitive to any misalignment of the mirrors than the existing cavity. To prevent this problem from occurring again, the design of the lens mounts and the gluing process must be improved. One potential solution is to divide the final cavity assembly into two gluing steps. The first step would involve adjusting the cavity length, and the second step would involve adjusting the relative alignment between the cavity mirrors. This would allow for a smaller gap between the lens and the cavity holder, thus reducing the chance that the lens position is changed due to deformations of the glue resulting from stress release during the curing process. Furthermore, the temperature cycling of the assembled cavity can help to release stress within the glue [68, 69].

Chapter 2

The Cold-Atom Experiment

Outline of the current chapter

2.1 Experimental Apparatus **32**
  2.1.1 Ultra-High Vacuum System 32
  2.1.2 System of Electromagnets 34
  2.1.3 Laser System 35
  2.1.4 Computer control 37
2.2 Preparation of Atomic Sample **39**
2.3 Imaging the Atomic Cloud **42**
  2.3.1 Two-Photon Imaging Through the Cavity-Microscope 43
2.4 Cavity Probe Setup **45**
  2.4.1 Cavity Response Spectroscopy 46
  2.4.2 Precision of Cavity Resonance Measurement 47
2.5 Conclusion **47**

The cavity-microscope has been designed to carry out quantum simulations with cold atoms. In this section, we discuss the experimental setup and techniques that allow us to capture and investigate a cloud of ^{6}Li atoms trapped within the optically connected cavity-microscope.

The chapter is organized as follows: In Section 2.1, we provide an overview of the different components of our experimental apparatus. In particular, this includes the ultra-high vacuum chamber (see Section 2.1.1), the system of electromagnets (see Section 2.1.2), and the laser system (see Section 2.1.3). In Section 2.2, the typical process of preparing the atomic samples is presented. The trapped atoms can be imaged with multiple cameras. In Section 2.3, we provide an overview of the different imaging techniques used in our experiment. Last but not least, the cavity probe setup that allows us to measure the optical properties of the cavity is discussed in Section 2.4.

2.1 Experimental Apparatus

This section provides a brief overview of the components of our experimental setup. Further details regarding the exact configuration of the system can be found in Appendix A.

2.1.1 Ultra-High Vacuum System

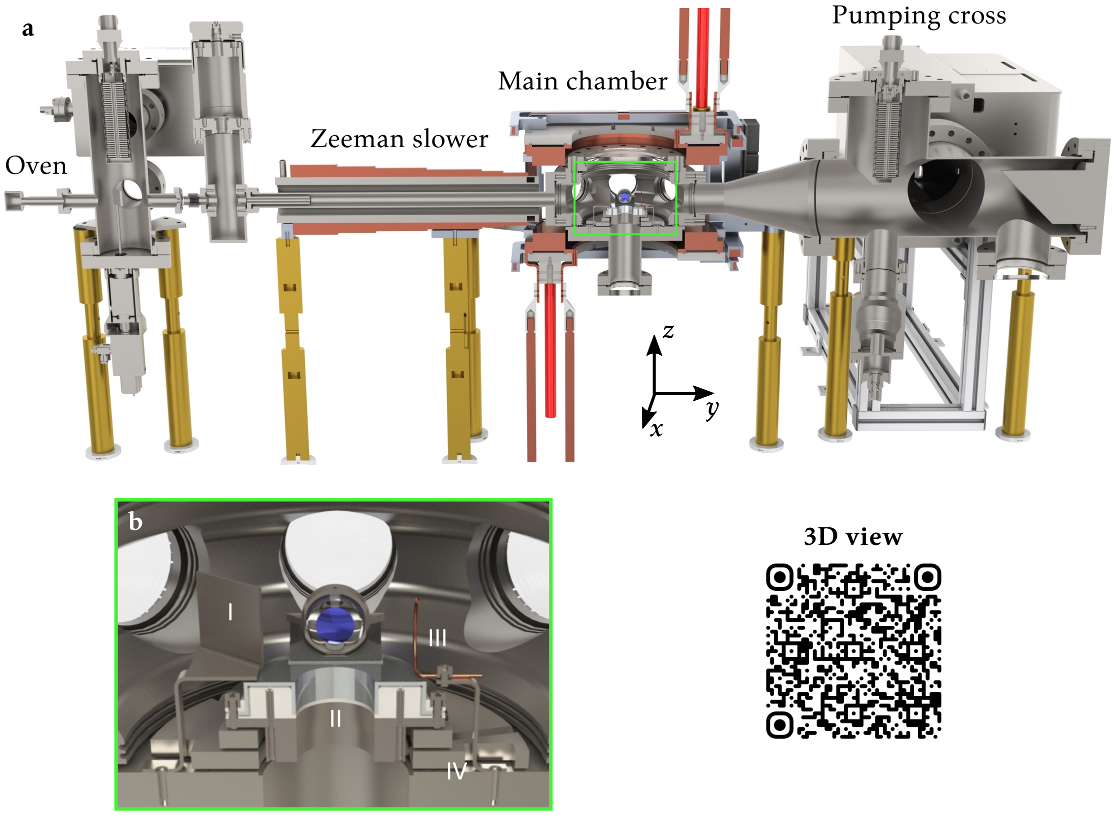

Figure 2.1: **Rendering of Vacuum System.** **a**, Section of complete vacuum system. **b**, Zoom into main chamber. **I**, Shield to protect mirrors from ^{6}Li. **II**, Cavity assembly, **III**, RF antenna to drive hyperfine transitions. **IV**, Vibration isolation system.

The vacuum system is composed of three components: the oven chamber, the main chamber, and the pumping cross (see Figure 2.1). The oven chamber houses the ^{6}Li oven, which is heated to 400 °C. The main chamber, located between the oven chamber and the pumping cross, is where the cavity-microscope is situated, which is the core of the experiment. To achieve pressures as low as 1×10^{-11} mbar in the main chamber, a combination of ion and non-evaporable getter pumps (NEG) is connected to it through the pumping cross. The connection between the oven and the main chamber, where the Zeemann slower coils are located, is very narrow, allowing differential pumping, and thus prevents contamination of the main chamber with gas flowing from the oven chamber. A gate valve located between the two chambers can be closed during the filling of the oven with lithium[*].

The entire vacuum system is supported by eight adjustable posts, four under the oven chamber, and four under the pumping cross[†]. There are no posts supporting the main chamber as it is firmly attached to the pumping cross with a conical adapter. The four additional posts visible in Figure 2.1 hold the electromagnets (see Section 2.1.2). Two vacuum gauges are used to monitor the pressure of the oven chamber and the pumping cross. The latter allows an estimation of the pressure in the main chamber, but ultimately the atom lifetime in the MOT quantifies the quality of vacuum in the main chamber. After one year of continuous operation of the vacuum system, we have measured a MOT lifetime of 66 s.

Preparation and Assembly of Vacuum Pieces Before the vacuum system was assembled, each of the stainless steel chambers was heated to 400 °C for 3 h to reduce hydrogen outgassing [70]. We ensured that all pieces put into the vacuum chamber were made of material contained in the LIGO Vacuum Compatible Materials List [30]. For all pieces, we followed the cleaning procedures explained in Ref. [71].

Non-Evaporative Getter (NEG) Coating In cooperation with the SLS vacuum group at the Paul Scherrer Institut (PSI) in Villigen, a non-evaporative getter coating was applied to the interior of the pumping cross, the conical adapter between the pumping cross and the main chamber, and the tube at the bottom of the main chamber [72]. This surface treatment transforms the vacuum chamber into a pump, allowing it to absorb the residual gas present in the chamber. To activate this coating under vacuum, it must be heated to 200 °C for 2 h.

Pumping Procedure We describe the process used to pump the chambers down. Initially, the chamber was evacuated with a molecular turbo pump to pressures as low as 1×10^{-8} mbar. We performed a bake-out of the chambers at 150 °C for almost a week. Once hydrogen dominated the residual gases in the chamber, the NEG pump activation procedure was performed. This was followed by the activation of the ion getter pump and isolation of the chamber from the turbo pump. Special attention was paid to the primary chamber during the bake-out, as even a slight increase in temperature could cause permanent misalignment of the cavity. In fact, powerful cooling fans were used to keep the main chamber at room temperature, while the pumping chamber and Zeeman tube were heated. To ensure that no contaminates were present in the main chamber, the whole system was pumped and baked without the cavity and then vented with pure nitrogen to insert the cavity-microscope.

---

[*] During the coarse of the operation of the experiment (3 years) the oven had to be refilled only once.

[†] The vacuum chamber is electrically isolated from the optical table to prevent ground loops. This is done with plastic caps at the end of the posts.

2.1.2 System of Electromagnets

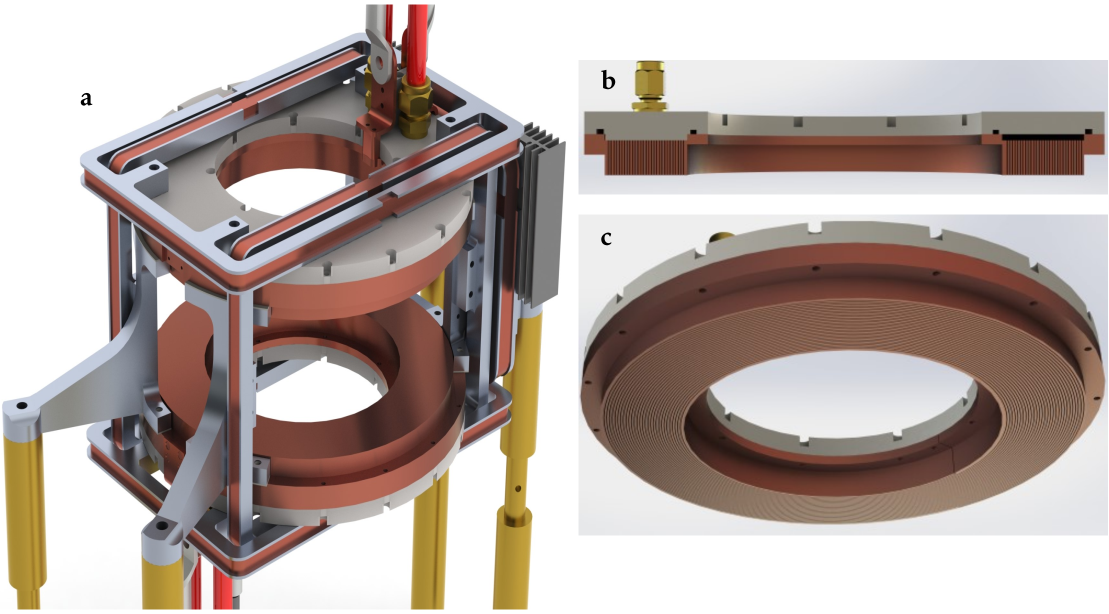

Figure 2.2: **Coil System Installed Around Main Chamber. a**, Rendering of coil stack hosting the MOT coils and five compensation coils. **b**, Rendering of section through the MOT coil showing the water channel between the PEEK cap and the cooper coil. **c**, Bottom view onto MOT coil showing the spiral cut into the bulk copper.

The coil system of the experiment consists of three components: A long conical coil for the Zeeman slower, a pair of strong electromagnets for the MOT, and a set of five compensation coils. We ensured that none of the coils come into contact with the vacuum chamber. This prevents vibrations caused by switching the coils to reach the cavity. Furthermore, the air gap between the coils and the chamber reduces heat transfer. This is essential because the cavity is very sensitive to temperature variations. The key characteristics of the coils are presented in Table 2.1.

Coil	**Field**	**Field (max)**
MOT coils (quadrupole config.)	$33.4 \times 10^{-2}\,\mathrm{G\,cm^{-1}\,A^{-1}}$	$134\,\mathrm{G\,cm^{-1}}$
MOT coils (dipole config.)	$2.56\,\mathrm{G\,A^{-1}}$	1024 G
x-compensation coil (pair)	$2.5\,\mathrm{G\,A^{-1}}$	50 G
z-compensation coil (pair)	$1.5\,\mathrm{G\,A^{-1}}$	29 G

Table 2.1: **Properties of Coils.**

MOT Coils The MOT forms combined with the compensation coils a single unit, the coil stack (see Figure 2.2**a**). The two large electromagnets used for the MOT are designed to handle currents of 400 A, allowing us to generate magnetic fields of up to 1000 G at the location of the atoms. Their compact design is based on a bulk-machined copper spiral that is glued together using epoxy glue in a vacuum injection molding process [73]. A rendering of the cross section of the electromagnets is shown in Figure 2.2**b**,**c**). The cooling water flows through a channel between the copper and a PEEK-made plastic cap. The seal is created with two o-rings placed in the two small trenches of the PEEK cap. A H-bridge based on insulated-gate bipolar transistors (IGBTs) is used to switch the MOT coils from the quadrupole configuration to the dipole configuration under full current.

Compensation Coils Two pairs of compensation coils are capable of producing offset magnetic fields in the vertical and cavity directions. Each coil is manufactured by winding a Kapton-coated wire with a cross section of $1 \times 2\,\mathrm{mm}$ around a custom aluminum frame. In the experiment, these coils are used to adjust the center of the MOT to the center of the optical resonator by shifting the zero crossing of the quadrupole field. Furthermore, these coils can be used to create a quantization axis that stops the mixing of spin states during our experiments. The last and largest of the compensation coils is used to counter the Zeeman slower field. Cooling radiators are used to dissipate heat during operation. The characterization of the magnetic field generated by each of the coils can be found in the master thesis of Nicola Reiter [32].

Zeeman Slower Coils The electromagnet for the Zeeman slower was manufactured by winding a Kapton-coated wire with a cross section of $1 \times 2\,\mathrm{mm}$ around a water-cooled stainless steel cylinder. The number of transverse windings is reduced from the oven chamber to the main chamber to match the magnetic field smoothly to the MOT field. A detailed description of a similar design can be found in the Ph.D. thesis of Kevin Roux [74]. The Zeeman slower coil is mounted on two adjustable posts, as visible in Figure 2.1.

2.1.3 Laser System

This section provides a concise overview of the lasers used in our experiment. We will also discuss the frequency stabilization scheme of the optical resonator and the lasers. For more information on the laser system and electronics, please refer to Appendix A.

Master Laser (1342 nm & 671 nm) A unique feature of our experiment is that a single frequency-doubled laser system (the master laser) is used for the MOT, Zeeman slower, absorption, and fluorescence imaging, the cavity-enhanced dipole trap, and finally probing of the cavity. The laser is based on a Toptica TA-SHG system, which outputs both 1342 nm light and frequency-doubled light at 671 nm. The infrared component is used for the dipole trap, while the red component is used to address the D2 transition of ^{6}Li.

Spectro Laser (671 nm) The spectro laser, which is based on a Toptica DL pro operating at 671 nm, serves as an absolute frequency reference. Its frequency is stabilized to the crossover with the help of a saturated absorption spectroscopy on the D2 line of ^{6}Li.

Blue Laser (460 nm) In our experiment, a blue Toptica DL pro laser operating at 460 nm is utilized for the control beam allowing us to shape the atom-cavity interactions. This laser is frequency-stabilized with a high-precision wavemeter.

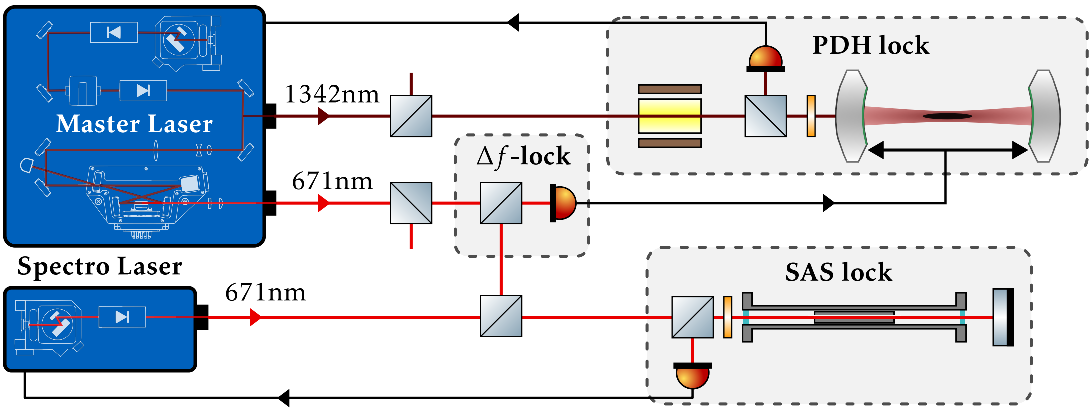

Figure 2.3: **Frequency Stabilization Scheme of Master Laser.** Schematic of locking scheme of master laser and cavity resonance frequency. The beamline is drawn in a simplified manner to highlight the locking scheme. For more details on the exact implementation, we refer to Appendix A.2 and Appendix A.4

Locking Scheme of the Cavity and the Master Laser A schematic overview of the locking system is shown in Figure 2.3. As mentioned previously, the master laser is used for both laser cooling and cavity probing. The former requires adjusting the absolute frequency of the laser in relation to the D2 transition of ^{6}Li with an accuracy of approximately 1 MHz, while the latter requires relative frequency stability between the cavity and the master laser with a precision of less than 20 kHz.

The master laser frequency is stabilized to the cavity resonance using a Pound-Drever-Hall (PDH) scheme at 1342 nm. The lock has a high bandwidth of 1.8 MHz*, which allows us to meet the stringent frequency requirement between the master laser and the cavity. Due to the intrinsic stability of the frequency-doubling process, there is a fixed frequency relation between the cavity mode and the laser at 671 nm. As a consequence, the cavity and the master laser form a combined frequency unit, the laser-cavity unit, and adjusting the length of the cavity alters both the cavity and the master laser frequency simultaneously. The frequency relation is illustrated in Figure 2.4.

An offset lock between the spectro laser and the master laser ensures the absolute frequency stability of the laser-cavity unit and fixes the cavity to the desired length. Due to the intrinsic frequency stability of the cavity resulting from mechanical isolation, it is sufficient to use a low-bandwidth lock (below 1 kHz†) on the piezo actuators of the cavity to stabilize the laser-cavity unit.

---

[*] Frequency of oscillation at large gain.

[†] This is limited by the flapping mode of the cavity mirrors.

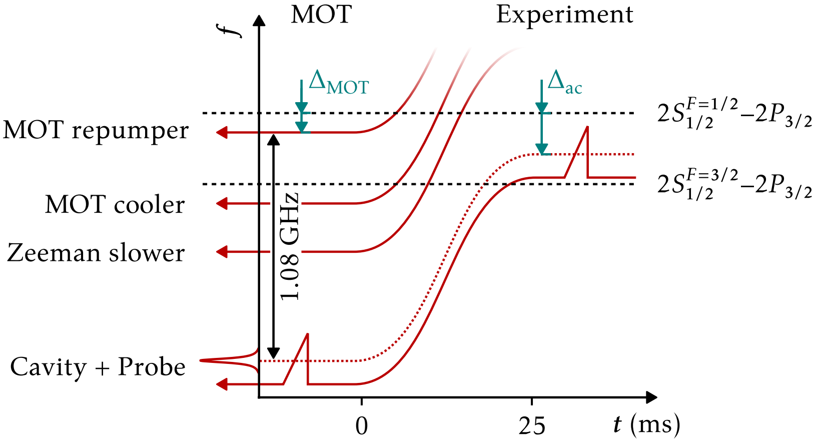

Figure 2.4: **Fast Tuning of Atom-Cavity Detuning.** Illustration of frequencies of different beamlines during experimental sequence. During the MOT phase it is the MOT detuning Δ_{MOT} that determines the frequency of the laser and cavity. During the experiment, it is the atom-cavity detuning Δ_{ac} that determines the frequency of the laser and cavity. The sweeps of the cavity probe over the cavity resonance show the moments of cavity response measurements (see Section 2.4).

As mentioned in Section 2.2, the cloud of atoms is confined in a cavity-enhanced dipole trap during the experimental sequence. This requires the master laser to remain locked to the cavity. The preparation of the atomic sample is based on the 671 nm component of the master laser for laser cooling, resulting in an atom-cavity detuning Δ_{ac} of -1.08 GHz during the MOT stage. To measure the atom-cavity system at different atom-cavity detunings Δ_{ac}, the frequency of the laser-cavity unit is adjusted after the preparation of the atomic sample. Figure 2.4 shows a typical curve of the cavity and laser frequency during the modification of the atom-cavity detuning Δ_{ac}. We have developed a feedforward system that enables us to modify the cavity length and thus the master laser with speeds up to 0.1 GHz ms^{-1} without losing the atoms trapped in the cavity dipole trap.

2.1.4 Computer control

In this section, a brief overview of the computer control systems of the experiment is given.

Labscript Our system is built around the *Labscript Suite*. It is a powerful and extensible platform for creating, controlling, executing, and analyzing experiments. It was originally developed for quantum science and engineering, but it can also be applied to optics, microscopy, materials engineering, biophysics, and any other field that requires the repetition of experiments with adjustable parameters and hardware-timed operations [75]. Due to its vibrant community and the fact that many different devices can be controlled using Python, it is highly flexible and versatile. The *Labscript Suite* has a comprehensive documentation and there are numerous studies that discuss its characteristics [76].

Our experimental cycles are much shorter than those of the usual cold-atom experiments (~ 200 ms), so we made a few changes to speed up the *Labscript Suite*. We used subsequences to reduce the overhead of communication with the different devices. Instead of sending one sequence for each experiment, we loop over multiple repetitions of the same experiment (subsequence) per *labscript* sequence, allowing us to reach effective repetition rates of up to 5 Hz. The bottleneck then becomes live plotting of the experimental data, which is usually done with *matplotlib*, the standard Python plotting library. To accelerate plotting, we created the *analysis plot panel* tool, which is available online [77]. This tool is based on the fast Python-based graphing library *pyqtgraph* [78]. Our tool is integrated into the *Labscript Suite* through a multishot routine.

Interlock and Data Logging We have developed a safety system in our laboratory, the interlock, that monitors the state of many of the devices and the environment. It is designed to turn off any device if abnormal conditions are detected. This is especially important in our experiment because we use powerful electromagnets, lasers, and RF-electronics that require continuous water cooling. The interlock is based on a *Raspberry Pi* minicomputer. People can interact with the device via a touchscreen or remotely through a Web interface (see Figure 2.5**a**). The instructions for the interlock system are available online [79], and the code can be downloaded from GitHub.

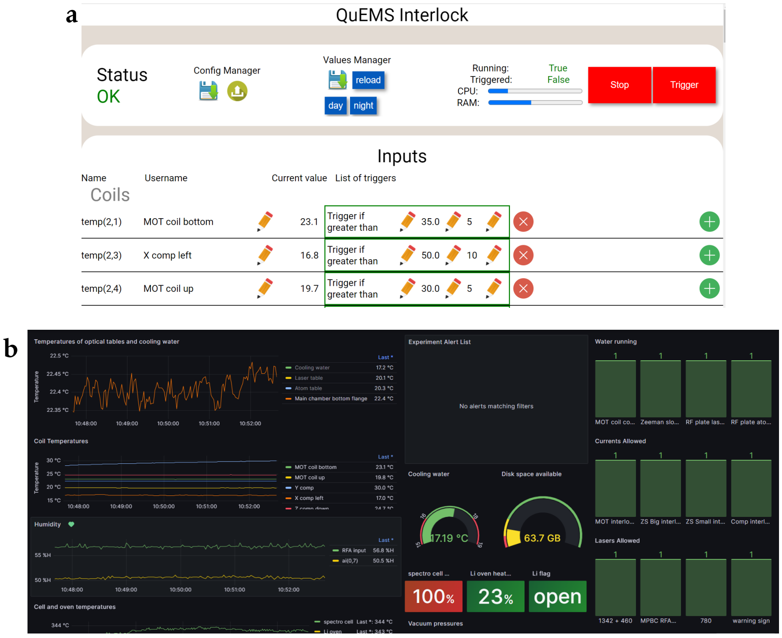
a
b
Config Manager
Values Manager
reload
day
night
CPU:
RAM:
Stop
Trigger
Temperatures of optical tables and cooling water
Temperature
22.5 °C
22.45 °C
22.4 °C
22.35 °C
10:48:00
10:49:00
10:50:00
10:51:00
10:52:00
Coil Temperatures
30 °C
25 °C
20 °C
15 °C
Humidity
55 %H
50 %H
Cell and oven temperatures
344 °C
Experiment Alert List
Cooling water
15
16
18
19
17.19 °C
Disk space available
63.7 GB
spectro cell ...
100%
Li oven heat...
23%
Li flag
open
Vacuum pressures
Water running
1
MOT coil co...
Zeeman slo...
RF plate las...
RF plate ato...
Currents Allowed
MOT interlo...
ZS Big interl...
ZS Small int...
Comp interl...
Lasers Allowed
1342 + 460
MPBC RFA...
780
warning sign

QuEMS Interlock

Status OK

Running: True
Triggered: False

Inputs

Name	Username	Current value	List of triggers		
Coils					
temp(2,1)	MOT coil bottom	23.1	Trigger if greater than	35.0	5
temp(2,3)	X comp left	16.8	Trigger if greater than	50.0	10
temp(2,4)	MOT coil up	19.7	Trigger if greater than	30.0	5

	Last *
Cooling water	17.2 °C
Laser table	20.1 °C
Atom table	20.3 °C
Main chamber bottom flange	22.4 °C

	Last *
MOT coil bottom	23.1 °C
MOT coil up	19.8 °C
Y comp	30.0 °C
X comp left	17.0 °C
Z comp down	24.7 °C

	Last *
RFA input	56.8 %H
ai(0,7)	50.5 %H

spectro cell Last *: 344 °C
Li oven Last *: 343 °C

No alerts matching filters

Figure 2.5: **Screenshot of Web interface** of Interlock (**a**) and Grafana (**b**).

Data from the interlock system are stored in a time series database (InfluxDB). We use Grafana to display the data in the web browser (see Figure 2.5**b**). Additionally, we sync key parameters and measurements, such as atom numbers, with Grafana, which enables us to compare and analyze experiments over a long period.

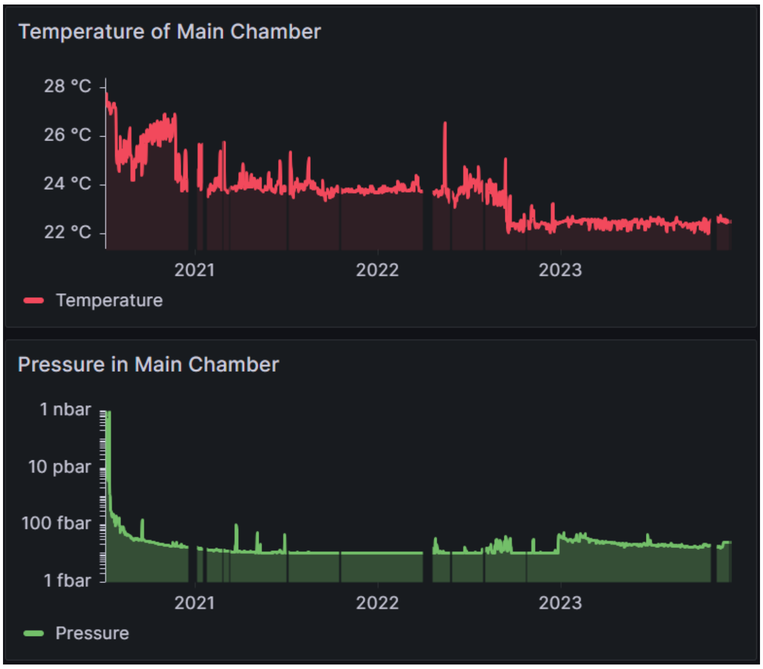

Figure 2.6: **Temperature and Pressure of Main Chamber** measured from the closing of the chamber to the end of the thesis. In mid 2022, a temperature regulation was installed on the main chamber. This resulted in a slight decrease of the measured temperature.

2.2 Preparation of Atomic Sample

A typical experiment consists of a sequence of many experimental stages. For our experiment, these stages can be grouped into two major parts: the preparation of the atomic sample and the probing of the atom-cavity system. Once the experimental sequence is completed, the atoms are released from the trap and the cycle restarts. In this section, the essential steps of preparation of the atomic sample are discussed. The remainder of the thesis is devoted to experiments and measurements conducted with the atom-cavity system, the main part of the sequence.

In the following, we go through the different experimental stages that allow us to get an atomic cloud. A timeline of the experimental sequence is shown in Figure 2.7.

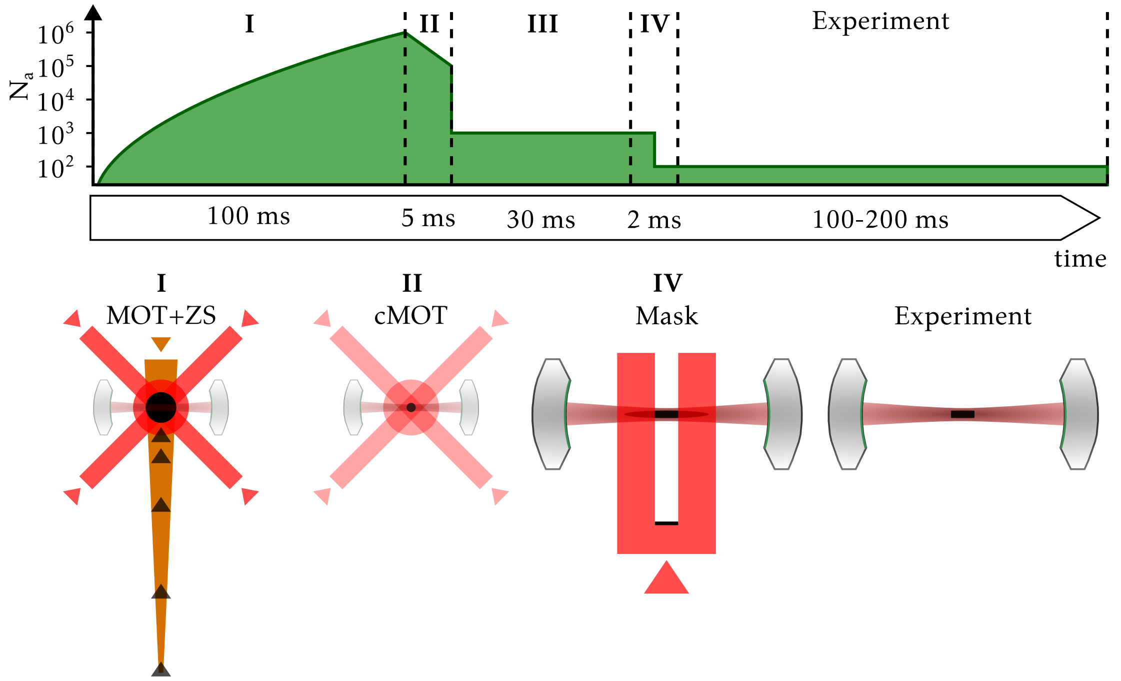

Figure 2.7: **Layout of a Typical Experimental Sequence.** The graph on the top shows the number of trapped atoms as a function of time during the four steps of preparation of an atomic sample (**I** MOT loading, **II** MOT compression, **III** Coil switching, **IV** Application of mask). A schematic plot of the laser configurations shown below. During the hole process the cavity-enhanced dipole trap is switched on. **I**: MOT inside the cavity is loaded by atoms (black arrows) decelerated by the Zeeman slower (orange beam). **II**: MOT is compressed (less laser power, smaller cloud). **IV**: Mask is applied to cloud so that longitudinal size of cloud is reduced during the experiments.

I: Zeeman Slower and Magneto-Optical Trap (MOT) A sequence starts with the loading of the atoms from the oven into a magneto-optical trap (MOT) located directly between the cavity mirrors (see Figure 2.7**I**). During this process, the atoms are cooled from 400 °C in the oven to a fraction of mK using laser cooling. In our case, we use standard cooling techniques in the D2 transition of ^{6}Li. The first step of the cooling process is done with a Zeeman slower, which helps to increase the capture velocity of the MOT, thus increasing the atom flux during loading. The second step, the magneto-optical trap, takes place directly between the cavity mirrors, eliminating the need to transport the atoms and thus making the experiment faster. Our MOT is created by combining a strong magnetic-field gradient with three back-reflected laser beams (two in the horizontal plane and one vertical) for trapping and cooling. A detailed map showing the location of the MOT beams is presented in Appendix A.2. At the end of the MOT stage, which usually takes less than 100 ms, we trap roughly 1×10^6 atoms at a temperature of a fraction of a millikelvin. The lifetime of the atoms in the MOT is 66 s.

II: Compressed Magneto-Optical Trap (cMOT) Once enough atoms are loaded, they are transferred from the MOT to a cavity-enhanced optical dipole trap that operates at 1342 nm. This can be done with a compressed MOT stage, where the detuning between the MOT lasers and the cooling transition is decreased. Note that it is also important to reduce the power of the laser beams, as this reduces the residual heating. A critical factor to achieve efficient transfer is the power ratio between the cooler and the repumper light. Just before turning off the MOT beams, we measure roughly 1×10^5 atoms in the trap.

III: Cavity-Enhanced Optical Dipole Trap (cODT) We transfer roughly 1×10^3 atoms to the cODT. The low transfer efficiency is due to the narrow linear geometry of the cavity-enhanced dipole trap. Due to the intense power build-up in the cavity mode, which is a consequence of its high finesse, we have achieved longitudinal trapping frequencies of up to 1.8 MHz with a low laser input power of around 10 mW. In this setup, we have observed a transverse trapping frequency of approximately 17 kHz. These values were determined by measuring the loss of atoms resulting from parametric heating at twice the trapping frequency. For these measurements, we modulated the trap intensity. The temperature of the cloud strongly depends on the depth of the dipole trap [32]. This is likely due to suboptimal Doppler cooling conditions at high trap depth that result from differential light shifts between the ground and excited state (see Figure 2.8). In a typical experiment, we measure temperatures on the order of 300 µK, which is more than double the theoretical limit of 140 µK, the Doppler temperature of ^{6}Li. The best lifetime of the atoms in the cODT measured during my Ph.D. was 4 s. However, it strongly depends on the linewidth of the laser*. Typical measured lifetimes are on the order of 500 ms.

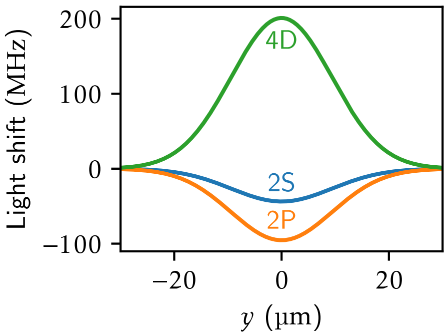

Figure 2.8: **Theoretical Estimation of State-Dependent Trap Profile.** The plots show a theoretical estimate of the transverse profile of the cODT. The light shifts are calculated using the different transitions of lithium cataloged in Ref. [80]. The light shift of the excited state is about 2.2 higher than the ground state. The 4D state is anti-trapped which leads to fast losses of atom in the $4D$ state.

In the cODT the atoms are maximally coupled to the optical resonator, meaning that they are trapped at the anti-nodes of the standing wave cavity field. This is illustrated in Figure 2.9, which shows the geometry of a typical atomic sample used for our experiments. The precise alignment of the trap and the cavity field is ensured by the symmetry of the cavity and the fact that we use double the wavelength of the cavity field, 1342 nm, for the dipole trap. A similar configuration is discussed in Ref. [81]. Depending on the experiment, at this point we employ a procedure that allows us to prepare a deterministic number of atoms based on the cavity transmission signal (see Section 3.3.2).

IV: Application of Mask The cloud loaded from the MOT into the standing wave dipole trap extends up to 1 mm in the cavity direction. We reduce the size of the cloud for our experiments by expelling atoms at the wings of the trap using resonant light. We image the shadow of a metal-coated tapered fiber (the mask) to protect a short section of the atomic cloud from the resonant expelling light. This reduces the number of atoms trapped by a factor of five and produces a cloud with a length of approximately 120 µm. An absorption picture of the cloud loaded into the dipole that includes the mask shadow is shown in Figure 2.10**c**.

---

*Regular tuning of the laser cavity is necessary to have optimal performance.

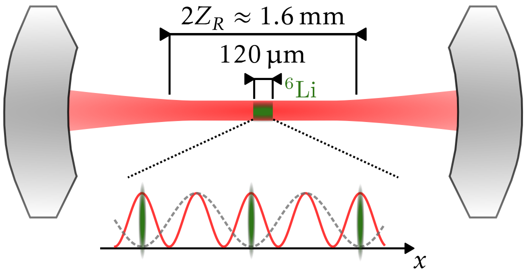

Figure 2.9: **Schematic of Typical Atomic Sample in Cavity.** The atoms are trapped in the center between the two cavity mirrors. The extent of the atomic cloud (120 µm) is much shorter than the Rayleigh range of the cavity mode (0.8 mm). The zoom-in below shows the shape of the cloud with respect to the cavity field. The atoms (green blobs) are trapped in the cavity-enhanced dipole trap, forming a lattice (trapping potential in dashed gray line). Due this trap shape, the density of the cloud forms pancakes with equal size that are spaced by 671 nm in the cavity direction (green ellipses). Due to the symmetry of the mirrors, the cloud density is peaked precisely at the anti-nodes of the 671 nm cavity field (red sine wave).

After each of the different preparation steps, we measure the dispersive shift of the cavity, which gives us information about the number of atoms and the temperature of the cloud. More details on these cavity-based measurement techniques are shown in Chapter 3.

2.3 Imaging the Atomic Cloud

We complement our cavity-based measurements with imaging. Our experiment utilizes two distinct types of imaging: absorption and fluorescence imaging. Absorption imaging produces high-contrast rapid images for a large number of atoms, while fluorescence imaging is more sensitive, allowing the measurement of smaller amounts of atoms, possibly even single atoms [82].

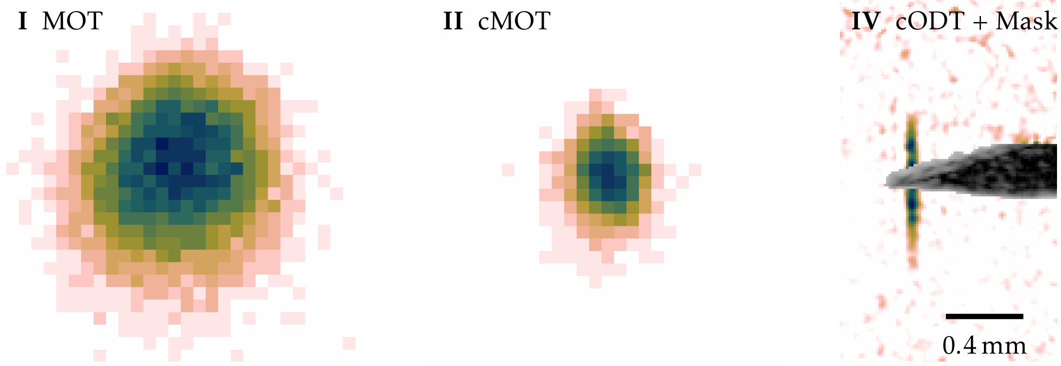

Figure 2.10: **Images of the Atomic Cloud during Different Preparation Stages.** Fluorescence images of the cloud during the MOT (**I**) and cMOT (**II**) stage. **IV**, Absorption image of cloud trapped in cavity-enhanced dipole trap. The gray cone in the center shows the mask used during the preparation stage of the experiment. All three images are in-scale, see scale bar on bottom right. The labels of the images corresponds to the labels of the different preparation stages (see Figure 2.7).

In our experiment, we use two cameras for fluorescence imaging and one for absorption imaging. Their location is detailed in Appendix A.2. Figure 2.10 displays images of the cloud at various points during the experimental sequence, which were created using absorption and fluorescence imaging on the D2 line. The image of the atoms in the MOT (Figure 2.10**a**) and the compressed MOT (Figure 2.10**b**) illustrates the size change during the compression process. Once loaded into the dipole trap, we imaged the atoms using the absorption technique. A typical image is shown in Figure 2.10**c**. Note that all three images are shown with the same magnification, demonstrating the small size of the final atomic sample, which is obscured by the mask compared to the initial size of the cloud trapped in the MOT.

2.3.1 Two-Photon Imaging Through the Cavity-Microscope

The imaging setup of our experiment only allows for low resolution due to the numerical aperture of the imaging lenses. However, if we use the lenses of our cavity-microscope (see Section 1.3.2), we can achieve a much higher resolution. Due to the reflective coating, these lenses are not compatible with standard D2 imaging techniques[*]. Therefore, we have developed a two-photon imaging technique that relies on the consecutive scattering of a 671 nm and a 460 nm photon. The latter is efficiently transmitted through the cavity lenses, allowing for high-resolution imaging only limited by the aberrations of the cavity lenses.

We have developed two distinct approaches for imaging through our cavity lenses. The first, two-photon fluorescence imaging, is based on fluorescence in a two-colored MOT, similar to the method described in Ref. [83]. The second, two-photon absorption imaging, involves the absorption of 460 nm photons by the excited atoms during standard D2 absorption imaging. Schematics that illustrate two techniques and the resulting images are shown in Figure 2.11.

---

[*] The newer version of the cavity, presented in Section 1.5, would make this possible.

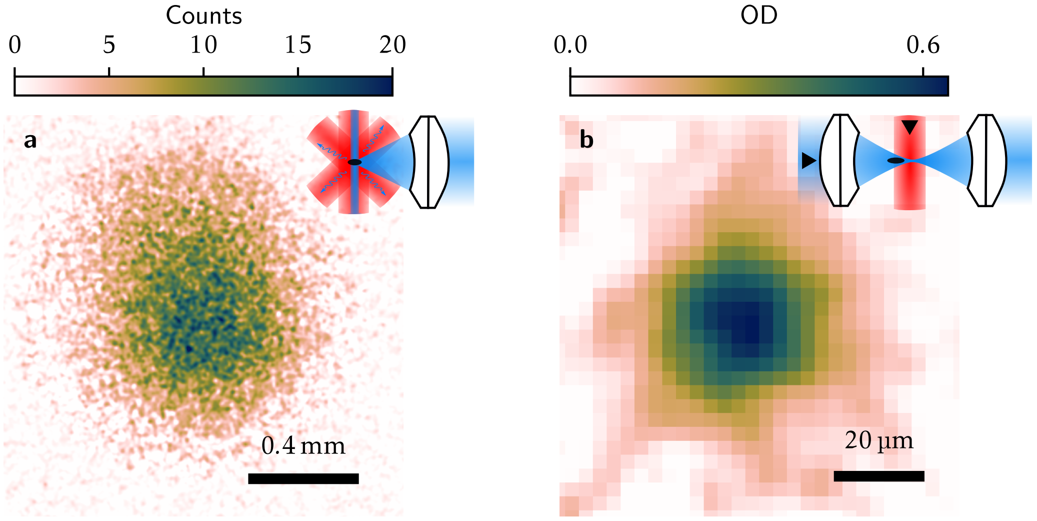

Figure 2.11: **Two-Photon Fluorescence and Absorption Imaging.** **a**, Fluorescence images of the cloud of 30 atoms trapped in a two-colored MOT. **b**, Absorption image of cloud trapped in cavity-enhanced dipole trap. The cloud is off-centered with respect to the cavity (see illustration on top right).

Fluorescence Imaging in a Two-Colored MOT Fluorescence imaging in a magneto-optical trap (MOT) is a highly sensitive technique that can detect single atoms with great precision [84, 85]. The MOT beams sent from six directions can cause scattering from the viewports or other components in the vacuum chamber, leading to noise in the measurements. To avoid this, a two-colored MOT can be employed [83]. This involves a pair of smaller counterpropagating laser beams that are directed at the center of the standard MOT, producing the fluorescence. A color filter in front of the camera eliminates direct light from the standard MOT, allowing for measurements with a high signal-to-noise ratio. In our experiment, we used two counterpropagating blue beams in the vertical direction to excite the atoms from the MOT to the $4D$ manifold. The blue fluorescence was then captured by the cavity lens and imaged onto a camera. The blue laser was 5 MHz red detuned from the main $2P_{3/2}$–$4D_{5/2}$ transition to achieve the best results.

Two-Photon Absorption Imaging An alternative two-photon imaging technique is based on the absorption of 460 nm light. This method works by sending blue light through the cavity lenses during regular absorption imaging on the D2 line. If the frequency of both beams is adjusted correctly, the excited atoms in the $2P$ state can absorb a blue photon, bringing them to the $4D$ manifold, which creates a shadow at the location of the atoms that can be seen on a camera. This is similar to regular absorption imaging, except that the atoms are initially in the excited $2P$ state. To ensure that the cloud only absorbs a small section of the beam[*], the atoms are displaced by 1 mm along the cavity axis, as shown in the inset of Figure 2.11**b**. This imaging process is not very efficient, as the momentum kick and heating are increased by the two-photon process. However, it can be used to align the focus of the 460 nm light with the cavity axis, which was beneficial during the alignment of the focusing beam.

---

[*] The 460 nm light is focused in the center of the cavity.

2.4 Cavity Probe Setup

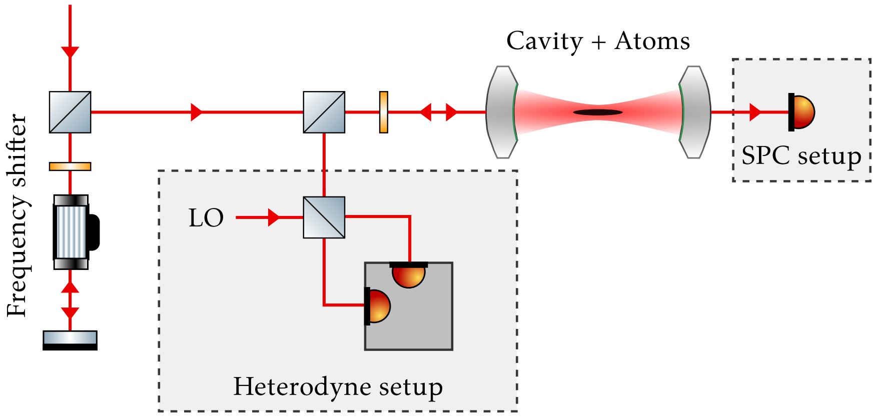

Figure 2.12: **Cavity Interrogation Setup.** The red lines indicate the path of the 671 nm cavity probe light. It first passes through a double-pass AOM, allowing for frequency sweeps over the cavity resonance. Then it impinges on the cavity. The reflected light gets detected in a heterodyne setup where it gets mixed with a local oscillator (LO). The transmitted photons get detected on a single-photon counter (SPC).

In the final section of this chapter, we outline the design of the cavity probe setup and explain how it can be used to measure the frequency response of the optical resonator. A simplified illustration of the setup is shown in Figure 2.12. More realistic drawings can be found in Appendix A.2. A double-pass acousto-optic modulator (AOM) is used to shift the frequency of the light from the master laser, allowing us to set the probe cavity detuning. A second double-pass AOM, not shown in the drawing, is used to adjust the power of the cavity probe beam sent into the cavity. The reflected light is mixed with a local oscillator and detected on a balanced photodiode, implementing a heterodyne detection scheme. The light transmitted through the cavity is detected on a single-photon counter.

The light beams at both detectors can be used to gain insight into the cavity field. The single-photon counter transforms photons into electrical pulses that contain precise data on the times of arrival of photons on the detector. Each click coming from the detector is linked to a photon that has escaped the cavity, and thus contains information about quantum jumps of the cavity field. For an efficient detector, these data allow the reconstruction of single quantum trajectories [86]. The heterodyne detector measures the light field that is reflected off the cavity. Its signal contains information on both quadratures of the field, meaning that we can measure both the phase and the amplitude of the reflected light. Furthermore, these data can be used to extract the power spectral density of light that leaks from the cavity.

2.4.1 Cavity Response Spectroscopy

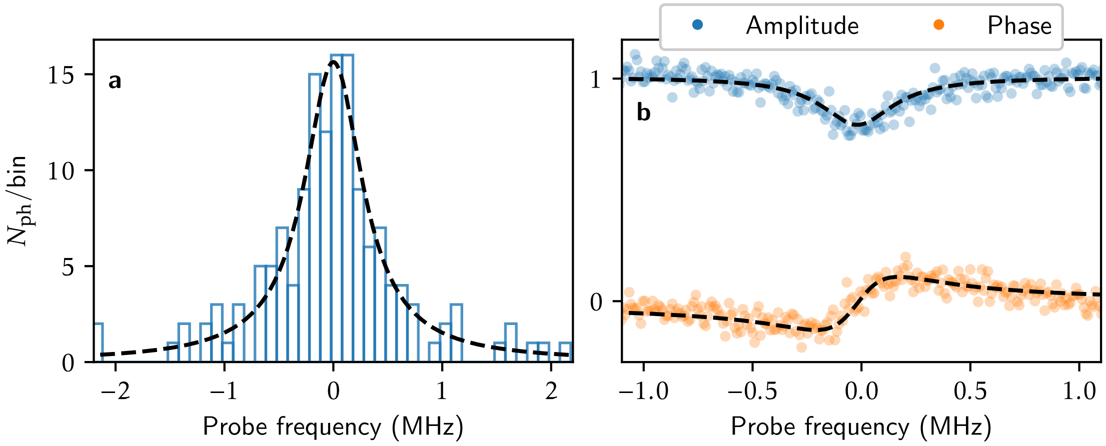

Figure 2.13: **Cavity Response Measurement for a Single Shot. a**, Histogram of single-photon events transmitted through the cavity as a function of probe frequency. The dashed line shows a fit using a Lorentzian function. **b**, Phase and amplitude of light reflected off the cavity measured by the heterodyne detector. The dashed line shows a fit with a linear response model. Both measurements were taken during the same cavity sweep, allowing us to compare the signal strengths.

A typical measurement that we perform several times in the sequence is cavity response spectroscopy. It is performed by sweeping the probe frequency over the cavity resonance using the frequency shifter and correlating the signal on the detectors with the probe frequency. This allows us to extract a frequency-resolved cavity reflection and transmission response of the cavity. A typical signal is shown in Figure 2.13. The signal on the single-photon detector is referred to as cavity transmission spectroscopy. Fitting a Lorentzian to the measurement results allows us to extract the linewidth and resonance frequency of the cavity. These parameters are modified in the presence of atoms in the resonator. In the following Chapter 2, we discuss how cavity spectroscopy can be used to extract information about the atomic cloud confined in the resonator.

2.4.2 Precision of Cavity Resonance Measurement

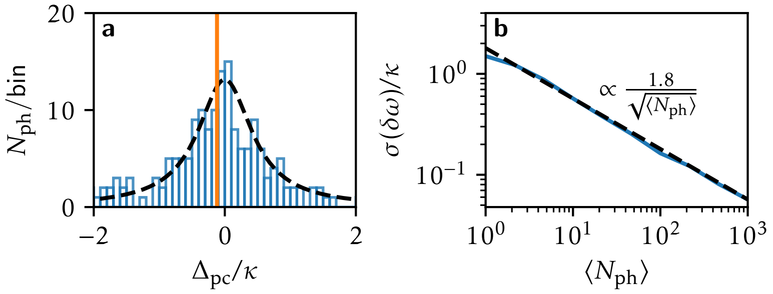

Figure 2.14: **Error of Cavity Resonance Measurement.** **a**, Simulated cavity transmission experiment. The dashed black line shows the Lorenzian shape of the cavity transmission. From these data, we estimate the resonance frequency using the center-of-mass (see orange vertical line). **b**, Plot of normalized error as a function of the mean total photon count detected during a single cavity transmission spectrum. The data follow the empiric model of $\sigma(\delta\omega)/\kappa = 1.8/\sqrt{N_{ph}}$.

The main parameter that determines the precision of the cavity resonance frequency measurement $\delta\omega$ is the total number of photons observed in a cavity probe sweep N_{ph}. This is illustrated in Figure 2.14**b**, where we plot the error of the dispersive shift measurement $\sigma(\delta\omega)$ normalized by the linewidth of the cavity. As expected from statistics, the error scales as the square root of the number of detected photons. The results were obtained from a numerical experiment including the poissonian nature of the measurement.

2.5 Conclusion

In this chapter, we explored the experimental setup and techniques that enable us to capture a tiny cloud of ^{6}Li atoms in our cavity-microscope. The subsequent chapters present the results of our measurements of the atom-cavity system in various configurations. Further details of the individual configurations are discussed in the relevant chapters.

Chapter 3

Basic Principles and Methods of Cavity QED

Outline of the current chapter

3.1 Detailed Description of the Hamiltonian of the Atom-Cavity System **50**
  3.1.1 Hamiltonian of the Multi-Level Fermionic Atoms 50
  3.1.2 Hamiltonian of a Multi-Mode Cavity 51
  3.1.3 Atom-Cavity Interaction Hamiltonian 51
  3.1.4 Level-Structure of ^{6}Li and Simplification of Hamiltonian 52
  3.1.5 Discussion on Spatial Structure of Atom-Cavity Hamiltonian . . . 53
  3.1.6 Incoherent Loss Processes: Cavity Loss and Spontaneous Emission . 54
3.2 Susceptibility Spectroscopy of Atom-Cavity System **54**
  3.2.1 Measurement of Atomic Susceptibility: The Depumping Technique 55
3.3 Measurement of Dispersive Shift of the Cavity: The Swiss Army Knife of Measurements **57**
  3.3.1 Signal-To-Noise Ratio of Dispersive Shift Measurement 58
  3.3.2 Repeated and Continuous Measurement of Number of Atoms . . . 58
  3.3.3 Temperature Measurement Using Differential Cavity Mode Shift . 62
  3.3.4 Cavity-based Detection of Raman Transitions 65
3.4 Conclusion **67**

In Section 1.1, we demonstrated through a Gedanken experiment that a cavity can increase the interaction between atoms and photons by prolonging the interaction time. In Section 3.1 of this chapter, we discuss a more detailed microscopic model that describes our atom-cavity system, which serves as the theoretical basis for the rest of the thesis[*]. In the remainder of the chapter, we illustrate the model by presenting cavity-based measurement techniques that allow us to extract information from the atom-cavity system. In particular, Section 3.2 presents techniques for measuring the susceptibility of the atom-cavity system with weak on-axis drive. Additionally, we provide an overview of various cavity-based measurement techniques that enable us to quantify different properties of the atomic cloud, such as the number of atoms (see Section 3.3.2), the temperature of the cloud (see Section 3.3.3) or their spin state (see Section 3.3.4).

---

[*] For the theoretical derivations we assume $\hbar = 1$.

3.1 Detailed Description of the Hamiltonian of the Atom-Cavity System

In this section, the theoretic basis of our experiment, the Hamiltonian of the atom-cavity system, is presented. In its complete form, the Hamiltonian is very complex, as in reality our system consists of a cloud of multilevel fermionic atoms strongly coupled to a multimode cavity. The goal of this section is not to frighten the reader, but rather to set the stage for the remainder of the thesis, where we develop different sectors and regimes of the Hamiltonian. Presenting the Hamiltonian in its full form will allow us to define a notation in terms of the Feynman diagram, which significantly simplifies the theoretical discussions in the remainder of my thesis.

The Hamiltonian of the atom-cavity system can be decomposed in three components, like

$$\hat{H} = \hat{H}_{\text{atoms}} + \hat{H}_{\text{cavity}} + \hat{H}_{\text{atom-cavity}}.$$

The first component $\hat{H}_{\text{atoms}}$ describes the dynamics of the atoms, the second component, the dynamics of the optical resonator and the final component specifies the structure of the atom-cavity coupling. In the following, we describe step by step the different constituents of the full Hamiltonian.

3.1.1 Hamiltonian of the Multi-Level Fermionic Atoms

A fermionic atom, like ^{6}Li in our experiment, is described by its position and its internal state (spin of the electron, the nucleus, and the energy level of the electron). In case of a cloud of many atoms, this positional and internal degree of freedom can be modeled in the second quantization formalism by a multicomponent field operator $\hat{\Psi}(\vec{x}) = \sum_i \hat{\Psi}_i(\vec{x})|i\rangle\langle i|$ that describes a vector of independent field operators for each of the internal states of the atom. Often, this complex structure can be simplified by isolating only a few internal states of the atoms. In many cases, it suffices to model the atoms by only two components, which describes a fermionic field of two-level systems (pseudo-spin 1/2). However, it should be noted that this is only an approximation and, in general, all components are necessary to fully describe the dynamics of a gas of ^{6}Li atoms. More details on the typical level structure used in our experiment are given in Section 3.1.4.

Having defined the field operators, we can write the atom Hamiltonian as

$$\hat{H}_{\text{atoms}} = \int \hat{\Psi}^\dagger(\vec{x})\hat{E}_{\text{kin}}\hat{\Psi}(\vec{x})\,dV + \int \hat{\Psi}^\dagger(\vec{x})\hat{\mathbf{V}}(\vec{x})\hat{\Psi}(\vec{x})\,dV + \hat{H}_{\text{interactions}}.$$

The first term of the equation is the kinetic energy of the atomic gas, which is independent of the internal state of the atoms. This is represented by the kinetic energy operator $\hat{E}_{\text{kin}} = -\hbar\nabla^2_{\vec{x}}/(2m)$. However, the second term describes the trapping potential, which depends on the internal state of the atoms and is represented by the position-dependent matrix $\hat{\mathbf{V}}(\vec{x})$ that acts on the internal states of the atom. This term also includes the transition frequencies between the different internal states. The last term describes the interaction between the atoms, which includes the physics of contact interactions that can be adjusted by an external magnetic field using Feshbach resonances. In the remainder of the thesis, we will drop this interaction term. However, by doing so, we neglect interesting physics that emerges in the competition between cavity-mediated interactions and contact interactions [14]. In the case of a thermal gas, the atoms become distinguishable, and the integral over the field operators can be approximated by a sum over the positions of the individual atoms*.

3.1.2 Hamiltonian of a Multi-Mode Cavity

Compared to the atomic Hamiltonian, the Hamiltonian of a multimode cavity is rather simple. Instead of allowing for a continuous spectrum of modes as is possible in free space, in a cavity a discrete set of modes is present. In experimental terms, three indices are generally used to describe the structure of different longitudinal and transverse modes of a cavity and the polarization of the cavity field. To simplify the notation, this structure is absorbed into the multi-index m. In this case, the cavity Hamiltonian then reads

$$\hat{H}_{\text{cavity}} = \sum_m \omega_c^{(m)}\, \hat{a}_m^\dagger \hat{a}_m\,,$$

where $\hat{a}_m$ and $\hat{a}_m^\dagger$ are the creation and annihilation operators for a photon in cavity mode m, with corresponding resonance frequency $\omega_{\text{c}}^{(m)}$. Note that the spatial structure of the cavity modes is not contained in the cavity Hamiltonian but rather shows itself in the atom cavity coupling. Nevertheless, we can better understand the structure of the cavity field by writing down the form of the electric field in the cavity.

$$\vec{E}_{\text{c}}(\vec{x}) = \sum_m \vec{E}_m(\vec{x})\ (\hat{a}_m^\dagger + \hat{a}_m)$$

Here, $\vec{E}_m(\vec{x})$ describes the spatial profile and polarization of a single photon in the cavity mode m.

3.1.3 Atom-Cavity Interaction Hamiltonian

The last term of the full Hamiltonian, the atom-cavity interaction, contains the physics that we are most interested in. There are two Hermitian conjugate processes that are described by this term: An atom either emits or absorbs a cavity photon, thereby changing its internal state. In the dipole approximation, which is a very good approximation for the atoms trapped in our resonator, the interaction between the electric field $\vec{E}(\vec{x})$ and the atoms can be determined by the Hamiltonian

$$\hat{H}_{\text{atom-cavity}} = \int \hat{\Psi}^\dagger(\vec{x}) \Big(\vec{\mathbf{d}} \cdot \vec{E}(\vec{x})\Big) \hat{\Psi}(\vec{x})\, dV \tag{3.1}$$

$$\overset{\vec{E}=\vec{E}_{\text{c}}}{=} \sum_m \left(\int \hat{\Psi}^\dagger(\vec{x})\ \mathbf{g}_m(\vec{x})\ \hat{\Psi}(\vec{x})\, dV \right) \times \left(\hat{a}_m^\dagger + \hat{a}_m\right). \tag{3.2}$$

Note that any external electric fields, such as driving the atoms from the side using a pump laser, are inserted into Equation (3.1). Here, we have assumed that the only electric field present is the cavity field. This equation appears rather simple, but much of the complexity of multilevel atoms and the multimode cavity has been absorbed into the space-dependent atom-cavity coupling

---

[*] This approximation was helpful for modeling cavity cooling of many hot atoms.

matrix $\mathbf{g}_m(\vec{x})$. It describes the transition strength between any of the internal atomic states depending on the mode index m and the coordinate $\vec{x}$. Note that the scalar product between the dipole transition moment $\vec{\mathbf{d}}$ of the atom and the electric field $\vec{E}(\vec{x})$ is in 3D space. It describes the effect of polarization of the electric field, which has also been absorbed into the definition of the space-dependent atom-cavity coupling matrix $\mathbf{g}_m(\vec{x})$.

Despite the complex structure underlying the dependent atom-cavity coupling matrix $\mathbf{g}_m(\vec{x})$, the total Hamiltonian describing our system can be summarized in a sum over simple Feynman diagrams

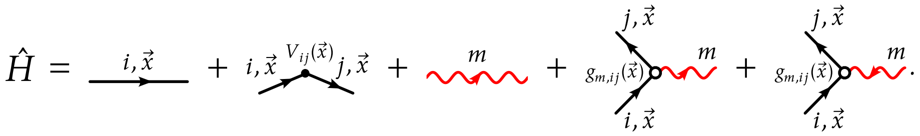

(3.3)

In the diagrams the indices i and j refer to the internal state of the atoms and the index m to the cavity mode. In the diagrams above, we were very explicit about the dependence on $\vec{x}$, which we will simplify in the future. In what follows, we will keep only the notation for the potential $V(\vec{x})$ and the atom cavity coupling term $g(\vec{x})$, since dependence is important for future analysis.

3.1.4 Level-Structure of ^{6}Li and Simplification of Hamiltonian

The discussion in the previous chapters is very general. Here, we concretely adapt it to the structure of ^{6}Li that we make use of for the rest of the thesis. In Figure 3.1 a simplified level diagram with the transitions considered in the thesis is shown*.

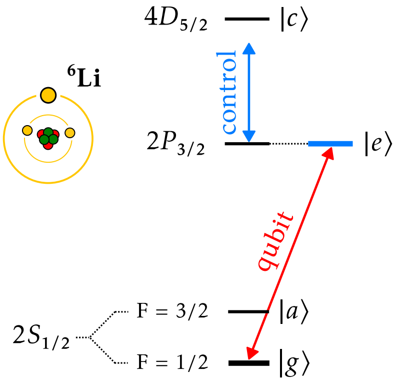

Figure 3.1: **Simplified Level Scheme of ^{6}Li.** We encode the atomic qubit in the $2S_{1/2}^{F=1/2}$ ($|g\rangle$) and $2P_{3/2}$ ($|e\rangle$) states. The coupling between the excited state $|e\rangle$ and a higher-lying control state $|c\rangle$ ($4D_{5/2}$) induced by the control laser is used to dress the excited state, therefore changing the properties of the atomic qubit $|g\rangle$–$|e\rangle$. The auxiliary ground state $|a\rangle$ ($2S_{1/2}^{F=3/2}$) is used for the detection of atomic excitations (see Section 3.2.1).

Taking into account only the atomic qubit in the coupling to the cavity, the notation simplifies significantly. In this notation the Feynman diagrams simplifies to

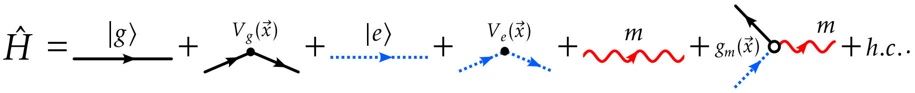

---

[*] All of the presented levels are actually manifolds that consist of many close-to-degenerate states. Under the conditions considered in our experiments, this substructure does not change the observed results. For more details on the structure of the electronic states of ^{6}Li, we refer to Ref. [80, 87]. In particular, special care was taken with respect to the polarizations of the laser beams. The $F = 1/2$ ground-state manifold consists of two different states. However, if linear polarization is used for the control and cavity probe beam, their behavior is exactly identical, and therefore the approximation of a two-level system is valid.

Note that we have removed the counter rotating terms that were still present in the full description of Equation (3.3). In many experimental cases, the cavity can be approximated by a single-cavity mode. In our notation, we will just drop the index m if this is the case. The effects of the control laser, which we used to locally change the optical properties of the atoms, are encoded in the state-dependent potential $V_e(\vec{x})$ and the local profile of the atom-cavity coupling $g_m(\vec{x})$.

3.1.5 Discussion on Spatial Structure of Atom-Cavity Hamiltonian

At this point, it is interesting to look at the spatial structure of the different parts of the Hamiltonian.

The cavity field is totally delocalized; its creation and annihilation operators are independent of space. The space dependence of the electric field is decoupled from the operators and is entirely contained in the amplitude of the single-photon field $\vec{E_m}(\vec{x})$, which is locally determined by the profile of the cavity mode. This is the origin of the all-to-all nature of cavity-mediated interactions. All atoms in the cavity field instantaneously feel the presence of a photon, independently of their position[*]. This is in stark contrast to the atomic excitations. The atomic field operators $\hat{\Psi}(\vec{x})$ explicitly depend on space, giving the fermionic field a local degree of freedom. This suggests that acting on the local properties of the atoms, such as their internal state structure, allows for local tunability of atom-cavity interactions.

Interestingly, the atom-cavity coupling is also local in origin. Atoms interact with the local strength of the electric field. However, since the field is totally delocalized, all the different local degrees of freedom present in the fermionic field operators are averaged out in the interaction term. The round brackets in Equation (3.2) highlight this structure. In fact, for a single-mode cavity, the atom-cavity coupling can be factorized into a tensor product between an operator acting on the atom density and an operator acting on the cavity field.

It is precisely this interference of the couplings of the many atoms into one cavity mode that gives rise to collective phenomena. For example, in the case of pinned atoms (neglecting the motional degree of freedom), this property leads to isolation of the cavity coupling to the collective fully exchange-symmetric Dicke spin states to the cavity. This is in one-to-one correspondence with the isolation of the center-of-mass motion of the atomic cloud when considering the coupling between the motion of the atoms and the cavity field. Furthermore, it is precisely this property that limits the rank of cavity-mediated interactions (for more details, see Chapter 6).

In more naive words, one can think of the cavity as a very sparse degree of freedom that can be simply described by its occupation of the photon states. On the other hand, the atomic Hilbert space is very large. In the approximation of two-level atoms, looking only at the internal structure, the number of available states 2^N already scales exponentially with the number of atoms. If the motion of the atoms is included, the size increases even further. It is precisely this mismatch in the different sizes of the cavity and the atomic Hilbert space for a given number of excitations that enforces the strong symmetry of the atom-cavity coupling[†]. A symmetry that needs to be broken to realize arbitrary all-to-all interactions as required for the quantum simulation of the SYK model (for more details, see Chapter 6). In Chapter 5, we experimentally investigate the breaking of collective symmetry in the atom-cavity interaction by studying the effects of atom disorder on the structure of the eigenstates of the atom-cavity system.

---

[*] These considerations neglect the short time dynamics of the cavity field resulting from the finite speed of light.

[†] As an example: In the single-excitation regime, there are N atomic states, but only one photonic state.

3.1.6 Incoherent Loss Processes: Cavity Loss and Spontaneous Emission

The Hamiltonian discussed in the preceding sections describes the coherent dynamics of our atom-cavity system; however, it is not a closed system. There are two pathways through which excitations can escape: the mirrors of the cavity can cause a loss of cavity photons, and the excited state of the atoms can spontaneously decay, emitting a photon into free space. The loss rate through both channels is measured by the linewidth of the cavity, κ, and the linewidth of the excited state of the atoms, Γ, respectively.

The advantage of cavity photon losses is that some of the lost photons can be detected on a single-photon counter, giving us information about the state of the cavity. This is in contrast to the photons emitted spontaneously by the atoms, which are sent in a random direction and therefore difficult to detect. We have developed a technique that can capture these spontaneous emission events and imprint the information on the atomic ground state. This is made possible by the presence of spontaneous Raman scattering in transitions that are not closed. Specifically, these measurement techniques are the topic of the next section.

3.2 Susceptibility Spectroscopy of Atom-Cavity System

In this section, we discuss techniques for measuring the excitations of the atom-cavity system. We focus on two types of excitation: those of the internal state of the atoms and those of the photons in the cavity. In this section, we consider pinned atoms, therefore, neglecting the effects of the motion of the atoms. In particular, we explore how the cavity transmission signal can be used to measure the susceptibility of the atom-cavity system to weak driving of the cavity, which will give us insight into the photonic and atomic weights of the eigenstates. This is especially important to understand the experiments conducted in Chapter 5, as it allows us to analyze the linear response of random spin coupled to the cavity.

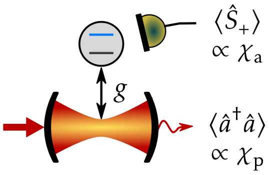
$\langle \hat{S}_+ \rangle$
$\propto \chi_a$
g
$\langle \hat{a}^\dagger \hat{a} \rangle$
$\propto \chi_p$

Figure 3.2: **Probing Scheme of Susceptibility Measurement.** The excitations are injected into the system by probing the cavity (red arrow). From the cavity the photons can leak out and get detected on a single-photon counter, which allows us to estimate the mean photon number in the cavity which is proportional to the photonic susceptibility χ_p. The photons in the cavity excite the atoms which can spontaneously decay into a different electronic ground state. Using the depumping technique, we can measure $\langle S_+ \rangle$ which is proportional to the atomic susceptibility χ_a.

When probing the cavity using an on-axis beam, we inject excitations into the atom-cavity system through the cavity. These excitations are lost from the atom-cavity system through two channels: the cavity mirrors (transmission and scattering) and the atoms (spontaneous emission). The schematic in Figure 3.2 illustrates the two loss processes. When the rate of losses is measured through the different loss channels, we can gain information about the structure of the eigenstates of the atom-cavity system. In particular, losses through the cavity mirrors measure the strength of the cavity field and therefore contain information about the photonic susceptibility χ_p, the ease of injecting photons into the cavity using a weak on-axis drive. Quantifying the rate of losses through the atoms measures the average number of excitations of the atoms. This contains information on the atomic susceptibility χ_a of the atom-cavity system, the ease of excitation of atoms using a weak on-axis cavity drive.

Measuring the photonic susceptibility in our system is straightforward, since photons leaving the resonator are detected directly on the single-photon counter. The rate of photons hitting the detector is a direct measure of the cavity field and therefore of the photonic susceptibility. However, measuring the atomic susceptibility requires detecting the photons that are lost through spontaneous emission of the atoms. Detecting these photons using fluorescence imaging is very inefficient, since the photons are emitted in all directions. In the remainder of this section, we describe a cavity-based method to measure the atomic susceptibility that does not require detecting the scattered photons, the depumping technique.

3.2.1 Measurement of Atomic Susceptibility: The Depumping Technique

The depumping technique for measuring the atomic susceptibility is based on the precise detection of spontaneous Raman transitions using the cavity. In our case, the transition that couples to the cavity is not closed, which means that excited atoms can decay into a ground state different from that with which they started. As a result, the population of the different ground states contains information on atomic excitations. In other words, only if an atom was excited can it change its ground state by spontaneous emission. Therefore, changes in the ground state population can be directly linked to the excitation of atoms in the atom-cavity system.

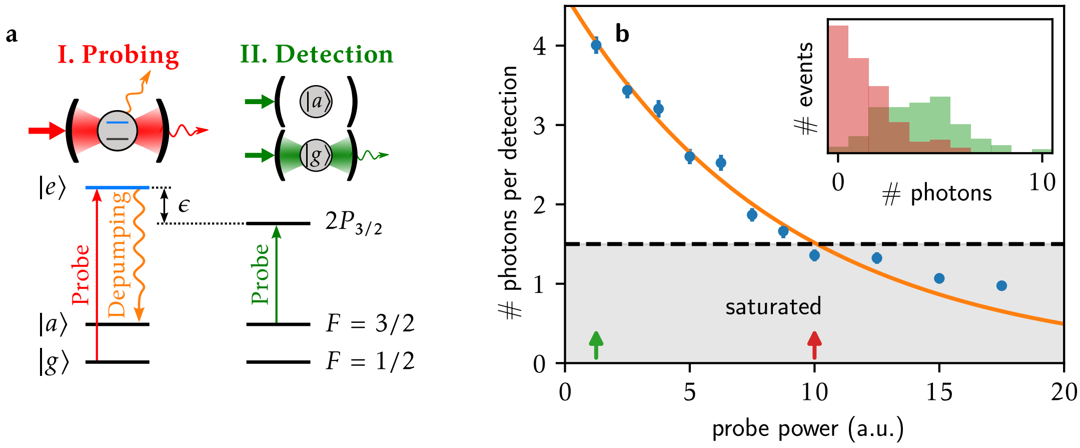

Figure 3.3: **Depumping scheme and calibration.a**, Illustration of the probe configurations during interrogation and depumping detection. **I**, When probing the disordered system, the excited state of the atoms is dressed with the light-shifting laser, indicated by the blue color of the level and the shift ϵ. Photons entering the cavity from the probe have two decay channels. Either they leak out of the cavity on the other side (red wiggled arrow) where they will be detected by a single photon counter, or they can be lost by free-space spontaneous emission of an atomic excitation (orange wiggled line). At zero-magnetic field, the transition from $|g\rangle$ to $|e\rangle$ is not closed; therefore, spontaneous emission events can depump the atom into the $|a\rangle$ state. **II**, These depumped atoms can be detected by measuring the cavity transmission. If the cavity is on resonance with the $|a\rangle$–$|e\rangle$ transition, a single atom in state $|a\rangle$ leads to a strong suppression of the cavity transmission. **b**, Calibration of the depumping signal. The mean number of photons transmitted during the depumping detection is plotted against the probe power during the interrogation of the disordered system. The error bars of the data represent the standard error that comes from statistical fluctuations. The orange line shows a fit of the theoretically expected relation. The inset shows a histogram of detected photons for low (green) and high (red) probe powers (see arrows on x-axis for configuration).

We make use of this concept in our system to measure the atomic susceptibility. A schematic illustrating the measurement procedure is shown in Figure 3.3**a**. At zero magnetic field, the transition between $|g\rangle$ and $|e\rangle$ is not closed, and an atom in state $2P_{3/2}$ can decay into the $F = 3/2$ ground state manifold, denoted as an auxiliary state $|a\rangle$. This state is only weakly dispersively coupled to the cavity field because of the large hyperfine splitting. Since decay can occur only from the state $|e\rangle$, the population accumulated in the $F = 3/2$ state is directly proportional to the excited state population $\langle \hat{S}_z \rangle$ integrated over the duration of the probe pulse. For weak and short probing, only very few atoms are excited; therefore, saturation and effective atom loss effects can be neglected. In this regime, normalizing the excited-state population by the power of the probe beam directly measures the atomic susceptibility χ_{a}, the linear response of the atoms to a weak cavity drive. In equations this reads

$$\chi_{\mathrm{a}}(|\Psi\rangle) = |\langle \Psi | \hat{S}^{+} | G \rangle|^2 \, .$$

A detailed derivation of the correspondence to the experimental measurement scheme, is presented in the thesis of Philipp Uhrich [2].

The sensitivity of this measurement technique depends on the branching ratio during spontaneous emission events and the detection efficiency of atoms in the auxiliary state, which can be very efficient using cavity-based absorption. In particular, in the strong atom-cavity coupling regime, cavity transmission is significantly altered by the presence of a single atom. As a result, cavity transmission can be used to detect atoms in the auxiliary state with single-atom sensitivity. In fact, the population of the $F = 3/2$ state can be measured after interrogation of the atom-cavity system (see Figure 3.3**a, I**) using cavity transmission spectroscopy, with the cavity tuned in resonance with the $F = 3/2$ to $2P_{3/2}$ transition (see Figure 3.3**a, II**). In this configuration, the transmission of the cavity is suppressed by $1/(\eta+1)^2$ in the presence of a single atom in the $F = 3/2$ state, yielding a single atom level sensitivity for the detection of the atomic response.

In practice, we implement the detection by sweeping the frequency of the on-axis probe over the cavity resonance, yielding an average photon count of 4 photons per sweep for the empty $|a\rangle$ manifold (see green histogram in the inset of Figure 3.3**b**). The frequency sweep is essential, as it removes the systematic effects of dispersive shifts on the detection of depumping resulting from the presence of atoms in the $|g\rangle$ state. Figure 3.3**b** shows the dependence of the number of transmitted photons on the laser power during interrogation, showing the expected exponential trend, allowing for the characterization of the atomic susceptibility. At large probe powers, we observe a deviation from the exponential model that is due to saturation effects and atom losses.

3.3 Measurement of Dispersive Shift of the Cavity: The Swiss Army Knife of Measurements

The previous section discussed measurement techniques that allow for the characterization of resonant excitations of the atom-cavity system. In this section, we develop the complementary regime of dispersive atom-cavity coupling. A particular focus is on the measurement of the dispersive shift of the cavity, which is a very versatile technique that allows us to extract various properties of the atomic cloud with minimal heating.

The regime of large detunings between the atomic and cavity resonance frequencies, $\Delta_{\mathrm{ac}} \gg g\sqrt{N}$, is known as the dispersive regime. In this regime, the effect of the atoms on the properties of cavity resonance can be treated perturbatively. In particular, its resonance frequency is modified by a small parameter $\hat{\delta\omega}_{\mathrm{c}}$, leading to the effective Hamiltonian

$$\hat{H}_{\mathrm{disp}} = \hat{\delta\omega}_c \hat{a}^\dagger \hat{a}.$$

Here, the dispersive shift operator $\hat{\delta\omega}_{\mathrm{c}}$ acts on the atomic sector of the Hamiltonian and is a result of a purely coherent process, which can be calculated directly from Hamiltonian dynamics.

The diagram describing the dispersive shift is

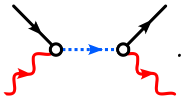

It describes the process of a photon virtually exciting an atom, the first-order correction of the photon field. In the dispersive regime, the atomic excitation instantaneously responds to a weak oscillating electric field. Its Green's function is approximated by $1/\Delta_{\mathrm{ac}}$, which stems from the tail of the Lorentzian in the optical Bloch equations. Therefore, any of the excited-state branches in the Feynman diagrams (blue dashed lines) can be replaced by $1/\Delta_{\mathrm{ac}}$.

We can interpret the diagram in terms of equations, which results in an expression of the dispersive shift operator

$$\hat{\delta\omega}_{\mathrm{c}} = -\int \frac{g^2(\vec{x})}{\Delta_{\mathrm{ac}}}\,\hat{\rho}(\vec{x})dV = \int \delta\omega_{\mathrm{c}}(\vec{x})\,\hat{\rho}(\vec{x})dV\,, \tag{3.4}$$

which describes the L^2-inner product between the local dispersive shift $\delta\omega_{\mathrm{c}}(\vec{x})$, resulting from a single atom located at $\vec{x}$, and the atomic density operator $\hat{\rho} = \hat{\Psi}^{\dagger}\hat{\Psi}$. Here, we assumed a two-level atom coupled to a single cavity mode; however, for many-level atoms coupled to a multimode cavity, the shape of the final Hamiltonian is very similar (see Section 3.3.3 and Section 3.3.4 for more details).

3.3.1 Signal-To-Noise Ratio of Dispersive Shift Measurement

There are two parameters that we would like to optimize for dispersive shift measurements: The signal-to-noise ratio of the measurement and the heating of the atom cloud. In this section, we demonstrate that they are actually linked and that optimization of one can only be done at the expense of the other.

The signal-to-noise ratio of the dispersive shift measurement is determined by the ratio between the value of dispersive shift and the precision of determining the cavity resonance frequency measurement using cavity response spectroscopy. In Section 2.4.2, it is shown that the precision of cavity response spectroscopy scales like the square root of the total photon number N_{ph} during measurement.

The heating of the atomic cloud is proportional to the number of incoherent photon scattering events during the measurement, which scales linearly with the number of photons detected during the measurement. More precisely, the scattering rate can be quantified by the additional photon losses of the cavity owing to the atoms,

$$\kappa_{\mathrm{a}} = \frac{Ng^2}{4\Delta_{\mathrm{ac}}^2}\Gamma\,.$$

Here, N refers to the number of atoms trapped in the resonator and Γ is the linewidth of the atomic transition. The expression shows that the scattering rate scales with $1/\Delta_{\mathrm{ac}}^2$, which means that for very large detunings between the cavity and the atoms, the dispersive shift $\delta\omega_{\mathrm{c}}$ becomes the dominant effect of the atoms on the optical resonator, and additional photon loss can be neglected due to scattering light off the atoms.

At this point, it is important to note that losses cannot be neglected when considering the signal-to-noise ratio of the dispersive shift measurement. In fact, if detuning is increased, the dispersive shift decreases with $1/\Delta_{\mathrm{ac}}$. To obtain the same signal-to-noise ratio, the photon count N_{ph} has to increase proportional to Δ_{ac}^2. Taking this into account, the number of incoherent processes during measurements with the same signal-to-noise ratio is independent of Δ_{ac}, but rather proportional to a dimensionless parameter, the cooperativity η [88, 89].

In the remainder of this chapter, we explore how the dispersive shift can be used to measure properties of the atomic cloud, such as the number of atoms and their temperature, and to detect Raman transitions between different hyperfine ground states.

3.3.2 Repeated and Continuous Measurement of Number of Atoms

The most fundamental technique used to measure the number of atoms trapped in the resonator is based on the measurement of the dispersive shift of the cavity. Assuming an atomic cloud that is completely contained within the cavity mode ($g(\vec{x}) = g$ for the support of $\langle\hat{\rho}\rangle(\vec{x})$), the dispersive shift in Equation (3.4) simplifies to

$$\delta\hat{\omega}_{\mathrm{c}} = -\frac{g^2\hat{N}}{\Delta_{\mathrm{ac}}} , \tag{3.5}$$

where $\hat{N} = \int\hat{\rho}(\vec{x})dV$ counts the number of atoms. As the dispersive shift in Equation (3.5) is proportional to the number of atoms, measuring it with a cavity spectroscopy (see Section 2.4) provides information on the instantaneous number of atoms trapped inside the resonator without significant heating of the atomic cloud. As a result, many measurements of the atom number can be performed during one experimental sequence, which is a feature we make extensive use of in our experiment.

In fact, it is even possible to continuously measure the dispersive shift to keep track of the number of atoms trapped in the resonator. In our experiment, we implemented two techniques that provide continuous temporal information about the number of atoms. We have used these techniques to track the atom count and prepare a deterministic sample of atoms, reducing the fluctuation of the atom count. Both techniques are based on continuous measurement of cavity response (see Figure 2.13).

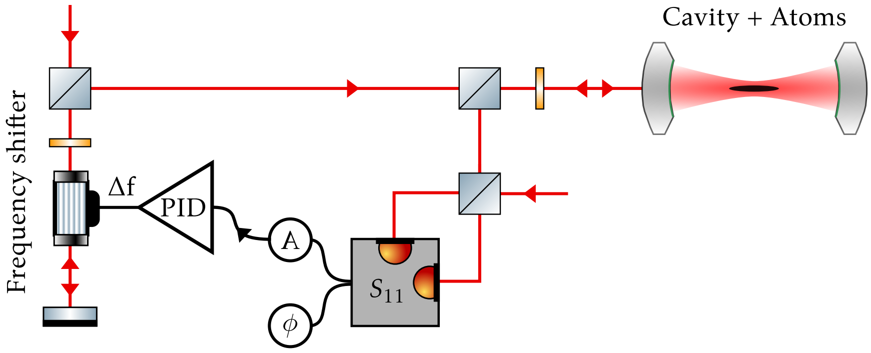

Figure 3.4: **Schematic of Atom Number Tracking Setup.**

Feedback-based Atom Number Tracking The first technique that we implemented in our system utilizes a side-of-fringe lock on the cavity probe frequency to continuously measure the dispersive shift. A schematic of the feedback loop is shown in Figure 3.4. With the heterodyne setup, we monitored the amplitude of light reflected from the cavity. A PID unit based on an FPGA (see Appendix A.4.2) acted on the frequency of the cavity probe to stabilize the amplitude of the cavity reflection to half the maximum. We solely used the integrator to achieve stabilization. Figure 3.5 shows four typical time traces of the dispersive shift. The normalized slope of a linear fit (see the dashed line in Figure 3.5) allows us to calculate the lifetime in the trap during interrogation as $\tau = (97 \pm 5)\,\mathrm{ms}$. The measurements are offset from each other due to variations in the initial number of atoms present in the trap after loading.

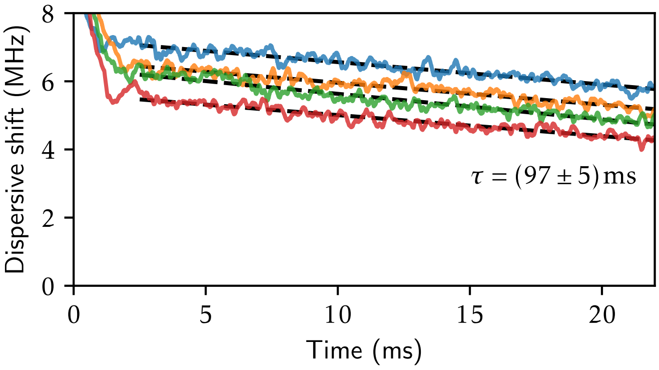

Figure 3.5: **Continuous Measurement of Atom Number.** Time traces of dispersive shift of cavity extracted from cavity probe frequency Δf for four different experiment cycles. The dashed black line shows a linear fit to the data.

The traces in Figure 3.5 show that it is possible to measure the dispersive shift of the cloud over a long period of time. Additional particle losses may result from both the heating and spontaneous formation of molecules (photoassociation).

Deterministic Preparation of Atom Number The second technique was developed to reduce variations in the atom count of our experiment. This was done to reduce the noise in our measurements, as the total number of atoms has a direct influence on many of our observables. The technique allows for the preparation of a deterministic number of atoms. In the following, we first describe the sources of variation in atom number and then detail our cavity-based preparation technique.

The loading of atoms from a magneto-optical trap (MOT) into a dipole trap is a Poisson process that can be characterized by a loading rate. This process can lead to fluctuations in the number of atoms because of two distinct sources. First, variations in the experimental parameters (laser detunings, polarizations, timings, oven temperature, alignment, etc.) can cause changes in the loading rate, thus resulting in a different mean number of loaded atoms. Second, even when the loading rate is constant, fluctuations in the number of atoms are still observed due to the Poissonian nature of the loading process, which is inversely proportional to the square root of the atom number. As a result, experiments involving only a few atoms are subject to large relative fluctuations in the number of atoms.

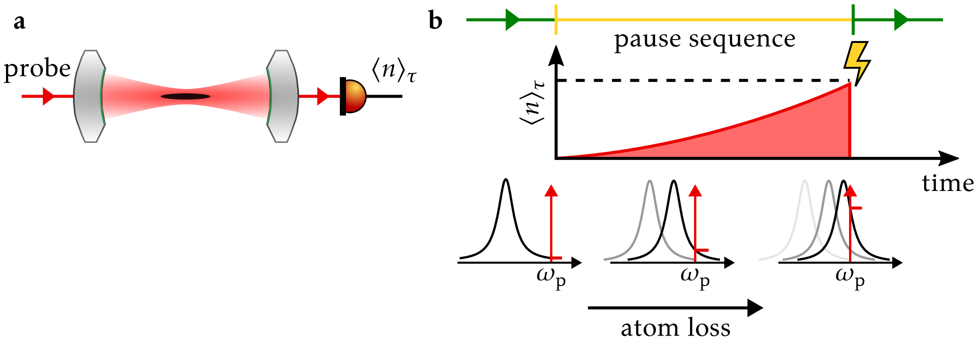

Figure 3.6: **Principe of Deterministic Loading.** **a**, Scheme of optical setup. The transmission of the probe laser at fixed frequency ω_p is monitored on the single photon counter. **b**, Flow diagram of sequence. The cavity probe and molasses are switched on right before the sequence is temporarily halted (marked by a yellow vertical line). When the average photon flux $|n|_\tau$ surpasses a predetermined limit, a trigger signal is sent and the sequence resumes (shown by a yellow flash and a green vertical line). The three frequency digrams below, show the evolution of the cavity resonance frequency at different times of the preparation process.

The diagram in Figure 3.6**b** illustrates the working principle of the deterministic preparation mechanism. After loading the atoms from the MOT into the dipole trap, weak molasses cooling beams are activated to maintain the cloud close to Doppler temperature, leading to atom loss due to light-assisted collisions [90]. Our technique is to stop the molasses and thus the atom losses when the desired atom number is reached. This is done by sending a weak cavity probe beam that is blue-detuned with respect to the dispersively red-shifted cavity mode. Note that, in contrast to the first technique, this technique is based on continuous measurement of the transmission signal (see Figure 3.6**a**) on the single-photon counter, not the reflection signal on the heterodyne detector. As the dispersive shift decreases over time due to atom loss, the rate of transmitted photons increases. By detecting the photon signal on the single-photon counter, we can estimate the photon flux and then trigger the termination of the molasses process. Specifically, the pulse train signal of the single-photon counter is digitized and processed in an FPGA unit, allowing for a real-time estimate of the photon rate averaged over a variable time scale. We use the *WaitMonitor* infrastructure implemented in the Labscript suite to achieve the triggered termination of the molasses process. The detuning of the cavity probe beam can be used to set the dispersive shift at which the process terminates and thus the desired atom number.

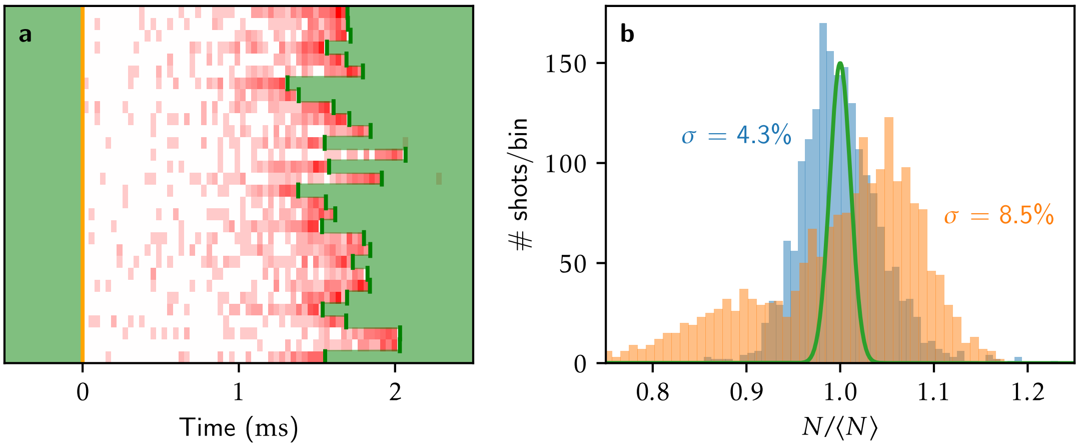

Figure 3.7: **Performance of Deterministic Loading.** **a**, Vertical stack of photons traces for different experimental cycles. The orange vertical line, indicates the time when the wait monitor is activated, meaning that the sequence is paused. It resumes when photon rate (red shading) has reached the critical value. The vertical green bar marks the time when the trigger is send and the sequence resumes. **b**, Histogram of relative atom number $N/\langle N\rangle$ before (orange) and after (blue) deterministic loading. The distribution of poissonian atom loading is shown in green. For these measurements we used an average number $\langle N\rangle = 1200$ atoms.

The experimental results of the preparation process are shown in Figure 3.7. Histograms in Figure 3.7**b** illustrate the measured distribution of the normalized number of atoms before and after the preparation process. It is evident that the distribution of atom numbers before the deterministic loading was not Poissonian, as it has two peaks. This implies that there are fluctuations in the loading rate of the atoms that are caused by changes in the experimental parameters. The distribution of atom number after the preparation process is single-peaked, indicating that most of the systematic variations have been eliminated. In addition to the distribution of atom numbers, we plot the ideal distribution resulting from the Poissonian nature of the loading. The discrepancy between the two distributions reveals that our technique was not preparing a sub-Poissonian distribution. Ultimately, the precision of the atom number preparation is limited by photon shot noise, which can be improved by increasing the probe power. However, for our experiments, the observed improvements were sufficient to improve the noise of our measurements.

3.3.3 Temperature Measurement Using Differential Cavity Mode Shift

In general, the exact expression of the dispersive shift $\delta\omega_c$ depends on the positions of the atoms, that is, the overlap of the atomic density with the cavity mode (see Equation (3.4)). In this section, we use the dependence on the size of the atomic cloud to perform temperature measurements.

The most widely used technique for measuring the temperature of an atomic cloud is time-of-flight thermometry. It consists of measuring the size of the cloud after expansion for a short time interval after releasing it from the trap. Once the size of the cloud is dominated by ballistic expansion because of its initial momentum spread, the temperature becomes proportional to the square root of the final size. Because this method relies on the release of the cloud from the trap, the atoms cannot be used further in the experiment. In this section, we demonstrate how the ratio of dispersive shifts of two consecutive longitudinal cavity modes can be used to measure the *in situ* size of the cloud and therefore estimate its temperature with minimal heating, allowing temperature measurements within the experimental sequence.

Taking a look at the formula in Equation (3.4), we see that the average dispersive shift is proportional to the overlap integral between the average density profile of the atoms $\langle\hat{\rho}\rangle(\vec{x})$ and the shape of the cavity mode $g^2(\vec{x})$ which depends on the total number of atoms and the size of the cloud. For a harmonic trap potential, the size of the cloud is directly proportional to the square root of the temperature. As a result, the dispersive shift can be used to estimate the temperature of the trapped gas. The problem with the dispersive shift is that it measures a quantity that is proportional to both the number of atoms in the cloud and its temperature. However, the dependence on the total number of atoms can be eliminated by considering the ratio of dispersive shifts of two consecutive longitudinal cavity modes, which is the technique developed in this section.

As mentioned in Section 2.2, our atomic sample is made up of a series of pancakes, trapped at the maximums of the cavity field. In fact, this is only true for even cavity modes, which we will refer to as the subscript a, since the atoms are trapped in the antinode*. For odd longitudinal modes, which will be termed the subscript n (node), the atoms are trapped at the nodes of the cavity field.

The longitudinal shape of two consecutive cavity modes, spaced by one free-spectral range (FSR), is

$$g_a^2(x) = g^2\cos^2(kx)$$
$$g_n^2(x) = g^2\sin^2(kx).$$

Due to the boundary conditions on the mirror surface; these two modes are separated by $\lambda/2$. As a result, they are shifted by $\lambda/4$ in the center of the cavity. In this analysis, we assume the atoms to be trapped at positions $x = n\lambda$, which is equivalent to considering one pancake located at $x = 0$. In Figure 3.8**a**, we plot the thermal distribution of a gas trapped in a harmonic potential and the mode functions of two consecutive longitudinal cavity modes. In this example, the trap frequency is 2 MHz and the temperature is 250 µK, which are typical for our experiment after loading from the MOT.

The average dispersive shifts of two consecutive longitudinal cavity modes is

$$\delta\omega_{\mathrm{a}} = \int \frac{g_{\mathrm{a}}^2(x)}{\Delta_a}\rho(x)dV, \quad \delta\omega_{\mathrm{n}} = \int \frac{g_{\mathrm{n}}^2(x)}{\Delta_n}\rho(x)dV.$$

Here, Δ_{a} and Δ_{n} are the atom-cavity detunings of the two different cavity modes.

There are two different relations involving the two dispersive shifts that allow us to estimate the total number of atoms and the temperature of the atomic cloud independently.

- To measure the total number of atoms, independent of the temperature of the atomic cloud (neglecting transverse effects), we can define $g^2 N_{\mathrm{atoms}} = \delta\omega_{\mathrm{n}}\Delta_{\mathrm{n}} + \delta\omega_{\mathrm{a}}\Delta_{\mathrm{a}}$. The fact that $\cos^2 + \sin^2 = 1$ makes this rescaled dispersive shift independent of the longitudinal shape of the cloud.

- To measure the temperature of the cloud, independent of the atom number, we define the ratio of the dispersive shifts as
$$\alpha = \frac{\delta\omega_{\mathrm{n}}\Delta_{\mathrm{n}}}{\delta\omega_{\mathrm{a}}\Delta_{\mathrm{a}}},$$

---

[*] All of the experiments presented in the thesis, only use the antinode configuration.

the dependence on the total number drops out of the relation. In fact, if we assume a Gaussian profile of the cloud, we can find a closed for $\alpha = \tanh\left(k^2\sigma^2\right)$ and as a result a linear relationship between α and the thermal occupation number of the trap n_{th} can be observed for small sizes*. This is illustrated in Figure 3.8**b**.

With this we conclude that α can be used as a direct method to measure the temperature of the trapped cloud without releasing the atoms from the trap. A similar analysis can be performed for transverse cavity modes, allowing us to measure the temperature in transverse directions.

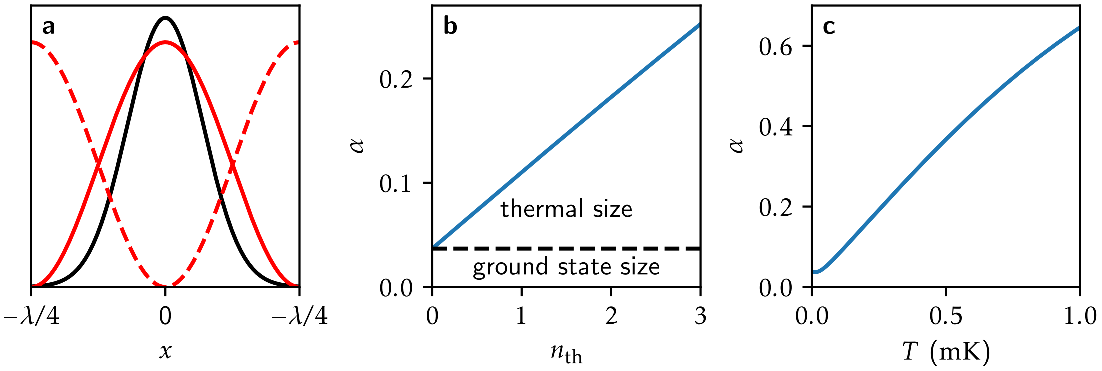

Figure 3.8: **Theory of Cavity-Based Temperature Measurement.** **a**, Density distribution ρ (black) of thermal cloud and mode functions of two consecutive longitudinal cavity modes (solid: anti-node, dashed: node). **b**, Plot of dispersive shift ratio α as a function of thermal occupation of the trap n_{th}. The offset at $n_{\mathrm{th}} = 0$ is due to the finite size of the ground state of the trap. **c**, Plot of dispersive shift ratio α as a function of the temperature of the cloud.

In our experiment, we can measure the dispersive shifts of two successive longitudinal modes with a single cavity spectrum†. The experimental results are summarized in Figure 3.9. The two consecutive longitudinal cavity modes have an atom-cavity detuning of $\Delta_a/2\pi = -1\,\mathrm{GHz}$ and $\Delta_n/2\pi = 4.8\,\mathrm{GHz}$. Cavity transmission spectra as a function of different numbers of atoms are plotted in Figure 3.9**a**,**b** (blue few atoms, red many atoms). The normalized ratio of dispersive shifts α is independent of atom number and measures the temperature of the cloud (see Figure 3.9**c**). The average value of α corresponds to a longitudinal temperature of approximately 0.8 mK. This value is significantly higher than what we expect from time-of-flight measurements. The discrepancy is probably due to the anharmonicity of the lattice trap, as this leads to larger cloud sizes for the same temperature.

---

[*] Note that the presented analysis assumed a harmonic trapping potential, which is a valid approximation of our system at low temperatures. At high temperatures, this approximation breaks down. However, α remains an indicator of relative temperature changes.

[†] This is realized with the sidebands generated from a high-bandwidth fiber electro-optical modulator in the cavity probe beam path.

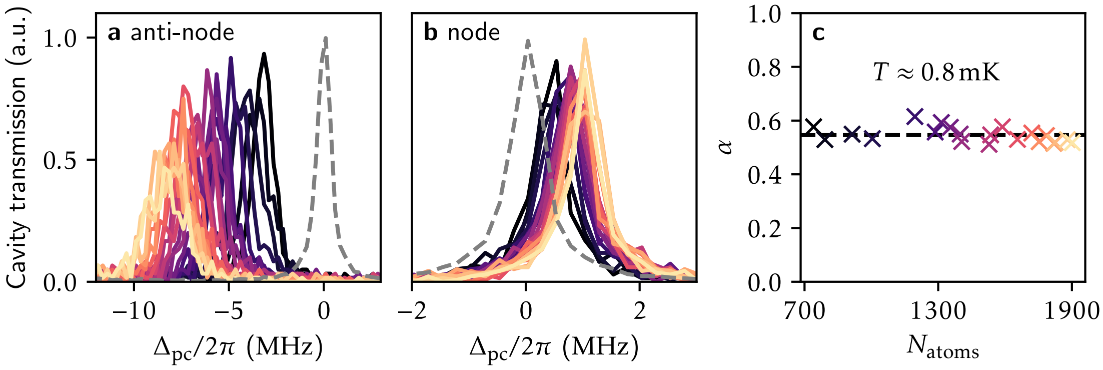

Figure 3.9: **Experimental Comparison of Dispersive Shifts.** Cavity transmission spectrum of anti-node (**a**) and node (**b**) cavity mode for different MOT loading times. The bare cavity resonance is plotted in both cases as a black dashed line. **c**, Plot of normalized ratio of dispersive shifts, α, as a function of atom number N_{atoms}. In all three graphs the colors indicate the number of loaded atoms (black: few, yellow: many).

The data presented in Figure 3.9 show that the dimensionless parameter α can be used to estimate the temperature of the cloud. The advantage of this technique is that it does not depend on the release of the atoms from the dipole trap, and therefore several temperature measurements can be performed during one experimental cycle. However, the presented technique only works for an atomic sample that is trapped in equally spaced pancakes, precisely overlapping with the nodes and antinodes of the cavity field. This is the case for our standing wave cavity-enhanced dipole trap, but for a trap that is not a lattice, the parameter α always averages to 1 and can therefore not be used to measure the temperature of the cloud.

Most importantly, this section illustrates that the dispersive shift of the cavity depends on the shape of the atomic cloud and can be used to extract information about the spatial distribution of atoms trapped inside the resonator. This measurement is based on the spatial distribution of the cavity mode. In Chapter 4, we show that this limit can be overcome by using a focusing beam, which allows us to shape the atom-cavity coupling on the micrometer scale.

3.3.4 Cavity-based Detection of Raman Transitions

Last but not least, the measurement of the dispersive shift can be used to extract properties about the internal-state population of the atoms. This allows for the detection of Raman transitions, which is usually done with state-resolving fluorescence. In this section, we explore how the measurement of the dispersive shift can be used to detect changes in the ground-state population of the atoms.

The formula of the dispersive shift presented in Equation (3.5) is valid for two-level atoms coupled to the cavity by a homogeneous coupling strength of g. For multi-level atoms, the coupling strength varies between different atomic transitions, which is due to the different dipole moments (see Equation (3.3)). As a result, the dispersive shift depends on the internal state of the atoms.

Therefore, if Raman transitions are driven, the internal state of the atoms changes, leading to a modification of the dispersive shift. We have verified this experimentally by driving transitions from the $F = 1/2$ manifold to the $F = 3/2$ manifold of the $2S$ state of the ^{6}Li atoms using a set of copropagating laser beams detuned by $228\,\mathrm{MHz} + \Delta_{\mathrm{raman}}$.

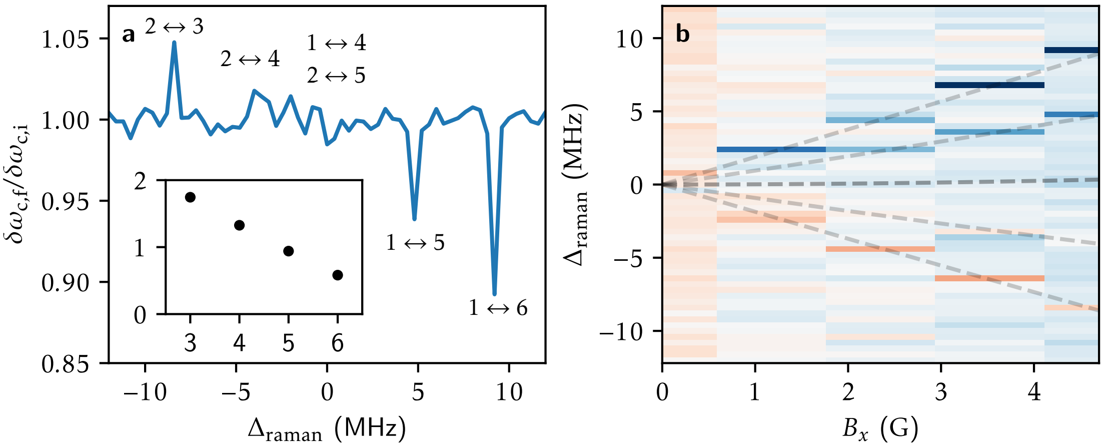

Figure 3.10: **Detection of Raman Transitions.** **a**, Ratio between the final and initial dispersive shifts, $\delta\omega_{\mathrm{c},f}$ and $\delta\omega_{\mathrm{c},i}$, as a function of the detuning between the Raman beams. The transitions are driven between the $F = 1/2$ and $F = 3/2$ manifold. The relative strengths of the dispersive shifts are plotted in the inset. The states are numbered after their order at high magnetic fields starting at the energetically lowest state. The values are normalized to the dispersive shift of spin state 2. Since we use σ_- light to probe the cavity, the dispersive shift is maximal for spin state 3 and smallest for spin state 6. **b**, Raman spectrum as a function of magnetic field. The levels are split according to the Zeeman effect. The theoretically expected shifts are shown with the black dashed lines.

For more details on the placement of the laser beams in the setup, see Figure A.3. In Figure 3.10**a**, we plot the relative change in the dispersive shifts as a function of the detuning between the two Raman beams. The inset in Figure 3.10**a** shows the theoretical relative differences in the dispersive shift depending on the internal spin state. The data qualitatively agree with the measurements. Additionally, when the magnetic field is varied, we observe the expected Zeeman splitting of the levels (Figure 3.10**b**). Furthermore, we can observe Rabi oscillations when driving the Raman transitions resonantly (see Figure 3.11). The measurements demonstrate that the dispersive shift is dependent on the ground state population of the atoms and that this dependence can be used to detect Raman transitions during the experiment with high-fidelity.

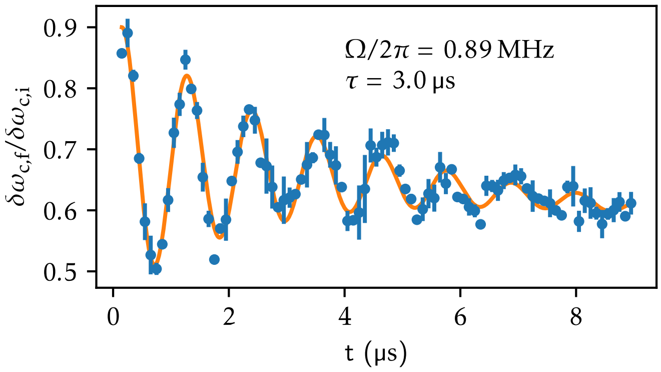

Figure 3.11: **Detection of Rabi Oscillations.** Relative change of dispersive shift as a function of Raman pulse duration. These measurements have been made at $\Delta_{raman} = 0\,\mathrm{MHz}$, driving the transitions between the 1 ↔ 5 and 2 ↔ 4 spin states simultaneously. The magnetic field was oriented along the z axis (up) with a strength of 10 G. The two laser beams had a power of 0.2 mW. The data were fitted with a model that takes into account decoherence and particle losses. The fitted Rabi frequency was 0.89 MHz with a coherence time of 3.0 µs. The lifetime of the particles in the trap during the driving of Raman transitions was estimated to be 69 µs, which is much longer than the decoherence period. The error bars represent the standard error that results from fluctuations in the measurement of the dispersive shift.

Together with the previous two sections, this demonstrates the utility of dispersive shift-based measurements in our cavity QED system.

3.4 Conclusion

In this chapter, we have constructed a model that explains the atom-cavity system. We have demonstrated that the cavity can be used to measure many of the significant characteristics of the atom-cavity system. In particular, we have demonstrated that the dispersive shift of the cavity is a very useful tool that can be used to acquire information about the spatial distribution of atoms in real-time with great accuracy. However, the resolution of these cavity-based techniques is restricted by the size of the cavity mode. In Chapter 4, we experimentally prove that this limitation can be surpassed with the aid of a laser beam that locally modifies the optical properties of the atoms.

Chapter 4

Shaping Light-Matter Coupling in Space and Time

Outline of the current chapter

4.1 Experimental Setup **70**
4.2 Local Floquet Engineering of the Light-Matter Coupling **70**
  4.2.1 Single-Atom Model 71
  4.2.2 Generalization to Many Thermal Atoms 72
  4.2.3 Experimental Observation of Control over Atom-Cavity Interaction 72
4.3 Aberration Correction of Cavity Lens with Atoms **73**
  4.3.1 Procedure of Wavefront Reconstruction and Optimization 73
  4.3.2 Measured Aberrations of Cavity Lens 75
4.4 Scanning Probe Imaging of Atomic Cloud **75**
4.5 Discussion and Outlook **76**

Our cavity-microscope is a device that combines a high-finesse cavity with a high-resolution microscope in a single optical device. In Section 1.1.2, we argued that a control beam focused through the cavity lens can be used to increase the spatial resolution of cavity-based measurements.

In this chapter, we investigate the method that allows us to modify the atom-cavity coupling in both space and time. We present two experiments to demonstrate this. The first experiment is the correction of the aberrations of our cavity lens. The second experiment focuses on the micrometer resolution reconstruction of our atomic cloud.

In this chapter, we provide a general summary rather than a comprehensive explanation, as our work is still ongoing. We are currently working on a publication that further develops our findings.

The chapter is organized as follows: We start by discussing the experimental setup in Section 4.1. Then, in Section 4.2, we demonstrate the Floquet technique that enables us to adjust the atom-cavity interactions both theoretically and experimentally. The results of the lens aberration correction are shown in Section 4.3. Finally, in Section 4.4, we demonstrate the capacity to reconstruct the 3D density distribution with our system.

4.1 Experimental Setup

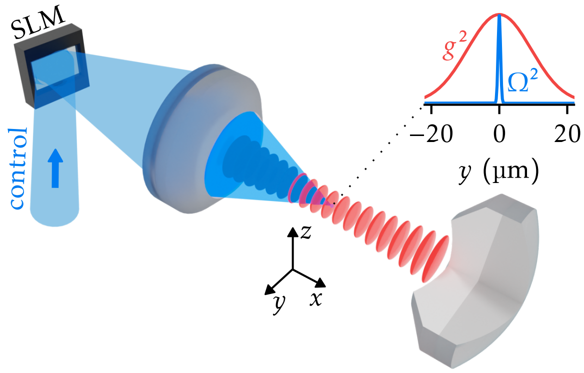

Figure 4.1: **Shaping the Control Beam.** Our cavity-microscope supports a high-finesse cavity mode, which forms a standing wave (red blobs). The control beam is focused by the cavity lens to a small spot, much smaller than the size of the cavity mode. This is illustrated in the inset on the top right. A spatial light modulator (SLM) in the beam path of the focusing beam is used to generate arbitrary intensity patters at the location of the atoms.

A rendering of the experimental configuration is shown in Figure 4.1. We send a blue control beam through the cavity lens, where it is tightly focused at the location of the atomic cloud. The resulting spot size is much smaller than the cavity mode (see the inset in Figure 4.1). A spatial light modulator in the beam path allows for wavefront engineering of the control light. In Appendix A.2.1, more details on the layout of the SLM setup are shown. We use the spatially resolved phase shifts to generate arbitrary intensity patterns of the control beam in the center of the cavity.

4.2 Local Floquet Engineering of the Light-Matter Coupling

To change the atom-cavity coupling in space, we engineer the spectrum of the atomic transition that couples to the cavity field ($|g\rangle$–$|e\rangle$) by altering the properties of the excited state. This is achieved by using a laser beam that passes through the cavity lens and is focused to a small spot in the center of the atomic cloud (see Figure 4.1). This control beam resonantly drives a transition from the excited state to a higher-lying control state, $|e\rangle$–$|c\rangle$. The beam is amplitude-modulated with frequency ω_m which leads to the formation of the Floquet sideband in the excited state (Figure 4.2**a**). For our experiments, we chose a modulation frequency of 110 MHz.

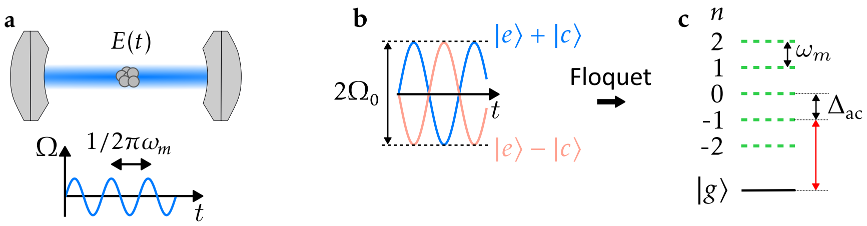

Figure 4.2: **Theory of Floquet Engineering.** **a**, Schematic of amplitude modulated control beam. The Rabi frequency Ω get modulated in time. **b**, Illustration of Frequency modulated Autler–Townes doublet. **c**, Illustration of Floquet sidebands on $|g\rangle$–$|e\rangle$ transition split by ω_m. The red arrow indicates the frequency of the cavity.

4.2.1 Single-Atom Model

In the following, we illustrate the effect of modulating the excited state of a single atom (Figure 4.2**a**). The Hamiltonian describing the space-dependent driving with an amplitude modulated oscillating electric field is

$$H_{\mathrm{m}}(t) = \Omega_0(\vec{x})\cos(\omega_{\mathrm{m}}t)\left(|e\rangle\langle c| + |c\rangle\langle e|\right) ,$$

where $\Omega_0(\vec{x})$ measures the peak drive Rabi frequency and therefore inherits the spatial dependence from the control beam focused by the cavity lens.

A constant drive resonant with the $|e\rangle$–$|c\rangle$ transition generates an Autler–Townes splitting between the states $(|e\rangle + |c\rangle)/\sqrt{2}$ and $(|e\rangle - |c\rangle)/\sqrt{2}$, where the splitting is twice the drive Rabi frequency. The effect of amplitude modulation is to modulate the energy of both these states in time (Figure 4.2**b**). Using the identity

$$\left|\psi(t)\right\rangle = \exp\left(i\frac{2\Omega_0(\vec{x})}{\omega_{\mathrm{m}}}\sin(\omega_{\mathrm{m}}t)\right)\left|\psi_0\right\rangle = \sum_{n=-\infty}^{\infty} J_n\left(\frac{2\Omega_0(\vec{x})}{\omega_{\mathrm{m}}}\right)\exp(i\,n\,\omega_{\mathrm{m}}t)\left|\psi_0\right\rangle,$$

we see that a modulation of the energy of a state results in a spectral distribution into a comb of discrete resonances spaced by the modulation frequency ω_{m}. These effective energy levels are called Floquet sidebands. In our case of resonant driving, two of those combs are generated, one for each of the states in the Autler–Townes doublet. Summing these combs of opposite driving amplitudes together results in interference, so that every even sideband couples directly to $|e\rangle$ and every odd to $|c\rangle$.

In fact, the cavity couples to transitions from the ground state to each sideband individually, as described in

$$H_{\mathrm{int}} = \hat{a}\sum_{n=2k} g_n(\vec{x})\sin\left(n\omega_{\mathrm{m}}t\right)|e\rangle\langle g| + \hat{a}\sum_{n=2k+1} g_n(\vec{x})\sin\left(n\omega_{\mathrm{m}}t\right)|c\rangle\langle g| + \mathrm{H.c.}$$

with the coupling strengths $g_n(\vec{x}) = g(\vec{x})J_n\left(\frac{\Omega_0(\vec{x})}{2\omega_{\mathrm{m}}}\right)$ given by the Bessel function of order n. This structure of spectrally isolated transitions allows for precise targeting of the sidebands for cavity-based detection of atoms that are exposed to control light.

4.2.2 Generalization to Many Thermal Atoms

The above analysis can be generalized to the case of many thermal atoms by introducing the local density of the cloud $\rho(\vec{x})$. This allows us to calculate the effect of a gas on the transmission of the cavity. The analysis is similar to Section 3.3.3, where we used the dispersive shift to estimate the temperature of the atomic cloud.

In particular, when the cavity is on resonance with the n^{th} atomic sidebands, the transmission of the cavity on resonance drops by $1 = 1/(1+\eta_{\text{eff}}^{(n)})^2$, where

$$\eta_{\text{eff}}^{(n)} = \int \rho(\vec{x}) \frac{4g_n^2(\vec{x})}{\kappa\Gamma} d^3x$$

is the effective cooperativity of atoms located at the focus of the control beam*. This equation shows that the cavity transmission depends on the convolution of the control beam intensity with the atomic density. It is precisely this feature that allows us to estimate the local atomic density with a cavity-enhanced absorption measurement. In fact, shaping the intensity patterns of the control beam with the SLM allows for programming of the spatial distribution of the atom-cavity couplings.

4.2.3 Experimental Observation of Control over Atom-Cavity Interaction

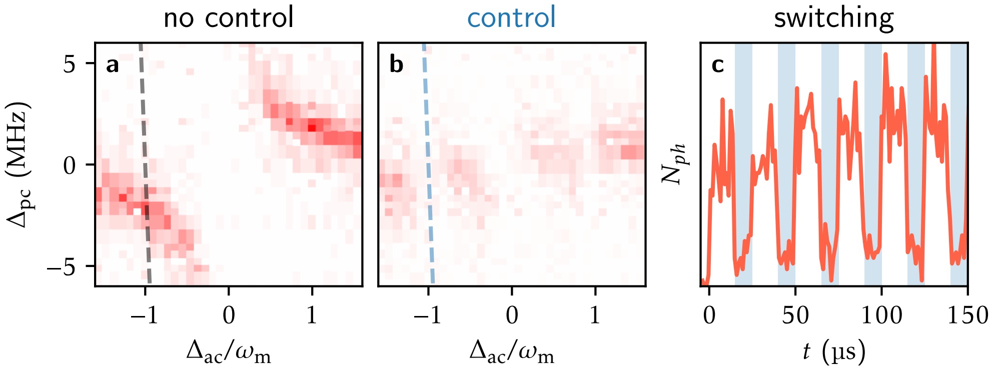

Figure 4.3: **Switching of Atom-Cavity Interactions.** **a**, Measurement of cavity transmission without control beam showing typical avoided-crossing. **b**, Measurement of cavity transmission with control beam showing avoided crossing at $n = -1, 0, 1$ sidebands. **c**, Transmitted photon rate N_{ph} in arbitrary units as a function time. The blue shaded region shows the time intervals when the control beam is on. The corresponding configuration is marked by the gray and blue dashed lines in the two graphs on the left.

In Figure 4.3, we present the effect of the control beam on the cavity transmission spectrum. For this measurement, the spot size of the control beam is adjusted for homogeneous illumination of the atomic cloud (see Figure 4.2**a**). Without the control beam, we measure the expected avoided-crossing between the cavity field and the atomic transitions $|g\rangle$–$|e\rangle$(see Figure 4.3**a**). The size of the Rabi gap measures the collective coupling strength. Once the control beam is on, we observe gap openings at the modulation sideband frequency for $\Delta_{\mathrm{ac}} = \pm\omega_{\mathrm{m}}$ (see Figure 4.3**b**). This is a signature of the coupling of the modulation sideband to the cavity field.

---

*To this point, this formula is an educated guess. We are currently working on its mathematical proof. However, the formula is correct only in the large modulation frequency regime, as otherwise the levels sidebands will mix similar to the results presented in Chapter 5.

We can switch the coupling in time by turning on and off the control beam. This is demonstrated in Figure 4.3**c**, where we plot the transmission signal from the cavity as a function of time. For this measurement, the cavity is resonant with the $n = -1$ sideband (see gray and blue dashed line in Figure 4.3**a,b**). When the control beam is turned on (blue shaded background), we observe a drop in the transmitted photon rate.

These two measurements illustrate the spectral engineering of the atoms using Floquet techniques. We show that the interactions of the atoms with the cavity can change fast in time. The remainder of the chapter is focused on demonstrating the spatial tunability of the atom-cavity interactions.

4.3 Aberration Correction of Cavity Lens with Atoms

By design, the cavity lenses introduce a high degree of optical aberrations at 460 nm, which significantly deteriorates the spot size of the control beam. As a first demonstration of the controllability of the atom-cavity interactions, we perform an aberration correction of our cavity lenses using a cavity-enhanced Shack-Hartmann scheme directly on the atomic cloud. This scheme allows us to improve the spatial resolution of the control beam by directly probing the beam quality at the location of the atoms, similar to Ref. [91].

4.3.1 Procedure of Wavefront Reconstruction and Optimization

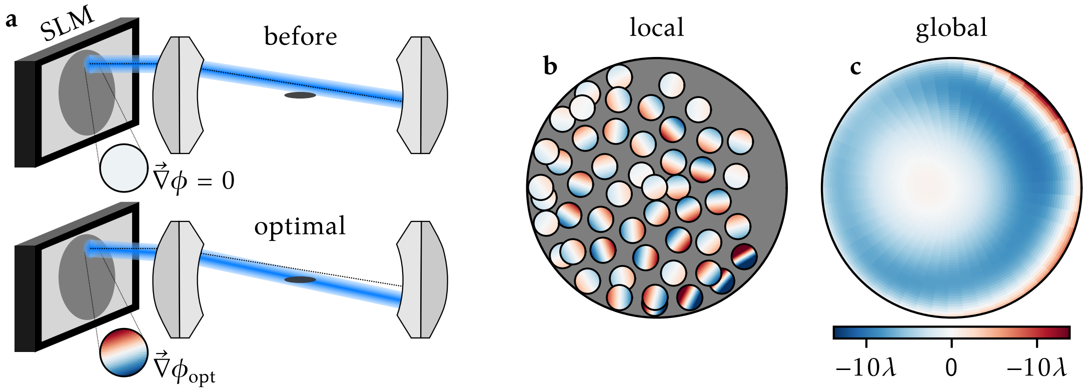

Figure 4.4: **Principle of Aberration Correction.** **a**, schematic of ray pointing optimization to extract local phase gradient. **b**, distribution of local phase gradients over the full beam diameter. **c**, reconstructed global wavefront correction applied to the SLM. Same as in the inset of Figure 4.6**b**.

We use an iterative procedure that estimates and corrects for aberrations in the cavity lens. In each interaction, we infer the global wavefront error from local measurements of the phase gradient (see Figure 4.4**b**). In particular, we divide the SLM area covered by the control beam into homogeneously distributed round patches with radii of approximately 1/10 of the total radius of the beam (see Figure 4.4**b**). For each patch, we adjust the local phase gradient to steer the ray originating from the patch into the atomic cloud (see Figure 4.4**a**). Using an algorithm that maximizes observed atom losses on the Floquet carrier ($n = 0$), we can estimate the local wavefront deviation at the patch position and deduce a global wavefront correction (see Figure 4.4**c**).

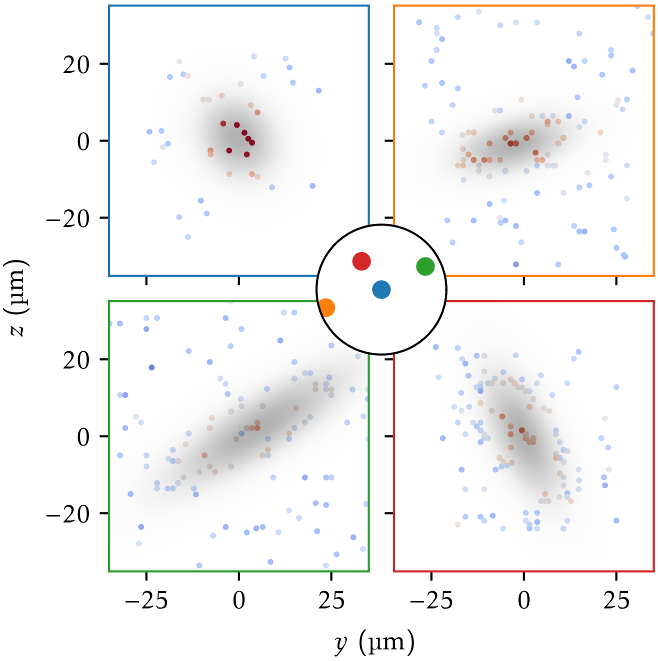

Figure 4.5: **Aiming at the Cloud.** The color of the scattered points in the figure illustrates the relative atom loss for different patches of the wavefront (blue: little atoms lost, red: many atoms lost). The position of the points indicates the amount of displacement of the ray. The gray shaded blob is a 2D Gaussian fit to the data. The fit is used to determine the optimal phase gradient (see Figure 4.4**a**). The inset in the center shows the location on the wavefront from which the ray originated. The color of the dot corresponds to the color of the subpanels.

We created a custom algorithm to direct the individual beams towards the atomic cloud (see Figure 4.5). Our algorithm is based on the Bayesian optimization approach [92]. Instead of utilizing a general Gaussian process to represent the cost function, we fitted a 2D Gaussian function model to the acquired data. This is motivated by the shape of our atomic cloud. From the fit we can extract the center of the Gaussian, which allows us to estimate the local phase gradient. The algorithm selects the next points to measure by maximizing the expected improvement. We expect the best improvement of the fit at the locations of maximum fit error. Our algorithm has the benefit of reducing the number of measurements required while at the same time allowing us to estimate the error on the local phase gradients.

4.3.2 Measured Aberrations of Cavity Lens

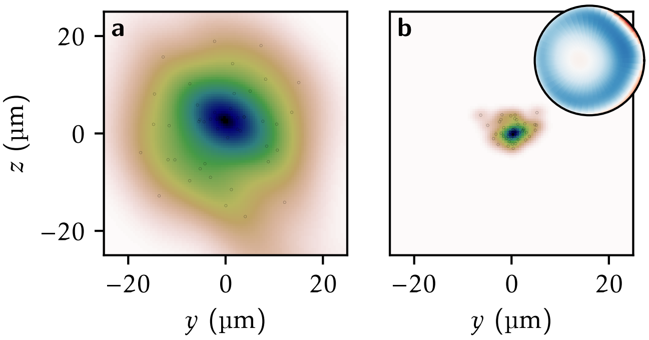

Figure 4.6: **Improvement of Ray Pointings.** **a**, Distribution of ray pointings (black dots) before aberration correction. The color shading estimates the density of rays using kernel density estimation. **b**, Distribution of ray pointings (black dots) after aberration correction. The inset on the top right shows the phase mask applied to the SLM to obtain the presented result. The darkest blue corresponds to a wavefront deviation of $-9.8\,\lambda$.

The performance of the aberration correction is summarized in Figure 4.6, where we compare the distribution of optimized ray pointings before and after the aberration correction. Merging the wavefront corrections of the different iterations results in an estimate of the total aberrations of the cavity lens (see the inset inFigure 4.6**b**). The wavefront error is circularly symmetric, which points to spherical aberrations. The measured wavefront error is $4.9\,\lambda$ peak-vally (PV), which matches well the theoretically expected value of $4.5\,\lambda$PV (see Section 1.2).

4.4 Scanning Probe Imaging of Atomic Cloud

We demonstrate the capability of our cavity-microscope by performing a cavity-based measurement of the atomic density with micrometer resolution. Similarly to a scanning probe microscope, which measures the properties of the sample at the location of a small tip, we estimate the atomic density at the focus of the control beam through cavity-enhanced absorption on the second Floquet sideband ($\Delta_{\mathrm{ac}} = 2\omega_{\mathrm{m}}$). Scanning the focal spot over the atomic cloud allows for a 3D reconstruction of the atomic density. The steering of the beam in all three directions was done by applying tip, tilt and defocus to the wavefront with the SLM (see Figure 4.7**a**).

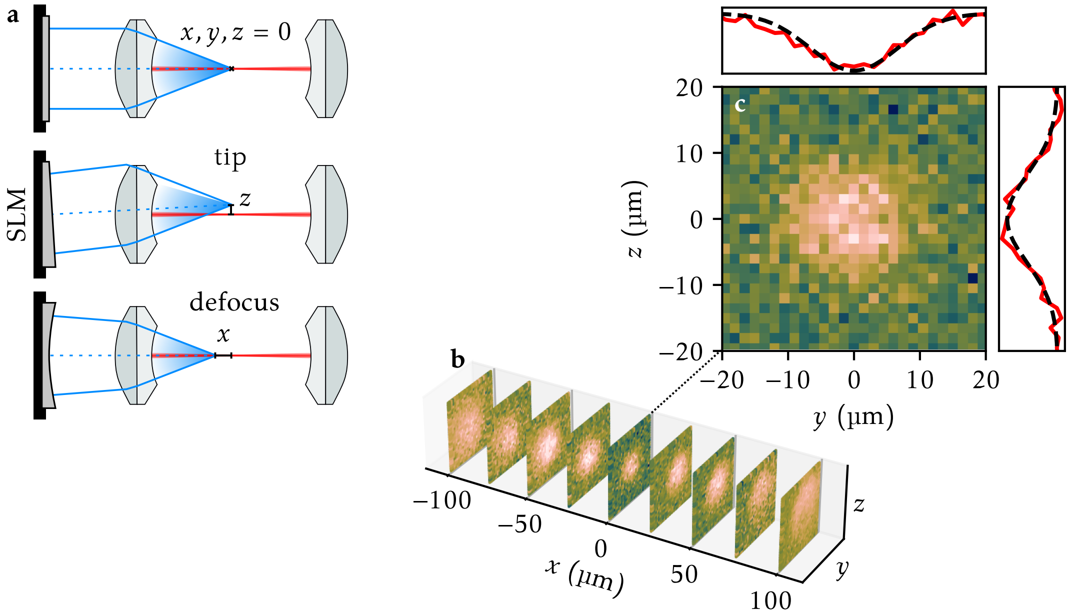

Figure 4.7: **Scanning Probe Measurement.** **a**, Schematic of effect of SLM on beam position. A flat wavefront defines the center. A tip of the wavefront leads to a displacement in the z direction. A spherical wavefront leads to defocusing and, therefore, to a shift in the x direction. **b**, Measurement of cavity transmission for different focus positions (green: high photon flux, white: low photon flux). **c**, 2D focus scan for $x = 0\,\mu\text{m}$. The insets on the right and top show the photon count rate averaged over z and y respectively.

In Figure 4.7**b**, the result of a 3D scan is shown. When the focus hits the atom cloud, the transmitted photon flux drops. Our atomic sample has a length of 120 µm (see Section 2.2) in the direction of the cavity. This can be seen in the 3D scan, as the transverse size of the signal increases for large x. This is a result of the focus of the control beam not hitting the cloud anymore, but rather the wings of the control beam, which have a much larger waist. Furthermore, we observe the tilt of the cloud (for positive x to the top and negative x to the bottom). This is due to a tilt between the cavity mode and the principal axis of the cavity microscope developed during the curing process of the glue (see Section 1.3.2).

The Figure 4.7**c** zoom in the center reveals the transverse profile at $x = 0\,\mu\text{m}$. The averages of the y and z coordinates demonstrate a decrease in cavity transmission. We compare the measurements with the theoretically expected cavity mode profile and observe very good agreement. This demonstrates the large transverse size of our atomic cloud because of the height temperature after loading into the dipole trap.

4.5 Discussion and Outlook

In this chapter, we have shown that our cavity-microscope can be used to shape the atom-cavity coupling both in space and in time. Using the flexibility of the SLM, we corrected the optical aberrations of the cavity lens directly with atomic signals. Additionally, we have shown that it is possible to perform cavity-enhanced measurements with micrometer resolution, which is sufficient to shape the atom-cavity coupling at length scales compatible with the size of the single-atom wavefunctions. Therefore, the presented scheme serves as a blueprint for the experimental realization of QND reconstructions of motional wave functions in systems with higher atom-cavity cooperativity [20, 21].

Moreover, cavity-mediated flip-flop interactions enable all-to-all couplings between atomic qubits [47, 93, 94]. Combined with fast programmable switching of the interactions, it allows for all-to-all connected two-qubit gates and can thus enhance the connectivity of atom-tweezer quantum computers [95, 96]. Furthermore, the fast local addressability allows mid-circuit readout of the atomic qubits, eliminating the need to move the atoms in the cavity field [97].

In the next chapter, we explore the all-to-all nature of cavity-mediated interactions. We analyze how disorder in the atomic transition frequencies disrupts the collective spin description and consequently removes the strong symmetry of the excitations caused by the indistinguishable atoms. By combining these cavity-mediated interactions with rapid local control of light-matter interactions, we can create systems with programmable cavity-mediated infinite-range interactions. This opens the door to experimental realization of holographic quantum matter in small samples of our ^{6}Li fermionic atoms, as proposed in Chapter 6.

Chapter 5

Collective Effects in Disordered Spin Systems with All-to-All Interactions

Outline of the current chapter

5.1 Fragmenting Eigenstates with Disorder in Atomic Transition Frequencies 80
5.2 Two-Atom Toy Model 81
  5.2.1 Cavity-Mediated Flip-Flop Interactions Emerging in the Dispersive Regime 84
  5.2.2 Dissipation and the Measurement Scheme 86
5.3 Many-Atom Model 87
5.4 Experimental Configuration 88
  5.4.1 Implementation of the Disorder through Light-Shift Technique . . 89
5.5 Experimental results 91
  5.5.1 Signature of Strong Coupling: Atom-Cavity Anticrossing 91
  5.5.2 Near-Resonant Regime and Gray States 93
  5.5.3 Large-Detuning Regime and Lipkin–Meshkov–Glick model 95
  5.5.4 Localization of Atomic Excitations 98
5.6 Conclusion 99

This chapter takes a closer look at the structure of the spin Hamiltonian in cavity QED systems. A particular focus is placed on resonant cavity-mediated flip-flop interactions that are naturally all-to-all in cavity QED systems. Using the results reported in [1], we study how disorder in atomic transition frequencies competes with collective effects emerging from flip-flop interactions. This is a crucial step towards the quantum simulation of the SYK model, which requires tunable all-to-all interactions between fermions (see Chapter 6).

This chapter focuses on the spin dynamics of the Hamiltonian that describes our system (see Equation (3.3)), meaning that all motional degrees of freedom are neglected. This is possible because of the high temperature of our atomic cloud and the fact that our cavity-enhanced dipole trap tightly localizes the atomic distribution onto the antinodes of the cavity. For more details on the exact experimental configuration, see Section 2.2 and Section 5.4. To study the SYK model, these interactions must be extended to the motional degree of freedom, which means the cavity-mediated momentum transfer that occurs during off-resonant photon exchanges, as discussed in more detail in Chapter 6. Even though these interactions act in a different Hilbert space (motion vs. internal states), their structure is similar.

This chapter is organized as follows: We start by providing a brief overview of the physical phenomena observed when disorder increases in the system in Section 5.1. This introduces the concept of fragmentation of the eigenstates. To illustrate these ideas, we present a two-atom toy model in Section 5.2. We then extend the concepts to the case of many atoms in 5.3. Our experimental findings, which support the theoretical discussion, are summarized in Section 5.5. The experimental setup and implementation of the tunable disorder that is based on pseudorandom light shifts are discussed in Section 5.4.

5.1 Fragmenting Eigenstates with Disorder in Atomic Transition Frequencies

In a cavity QED system, flip-flop interactions naturally emerge from photon exchange between the atoms [47, 93, 94]. In a homogeneous system, these interactions are all-to-all, meaning that a cavity photon coming from the deexcitation of one atom can be absorbed by any other atom. It is this exchange symmetry between the atoms that leads to the formation of collective Dicke states with enhanced atom-cavity coupling. In such systems, synchronization between atomic spins leads to Dicke superradiance. This has been demonstrated in many experimental systems [98, 99] and might in the future lead to the realization of a continuous superradiant laser for atomic clock applications.

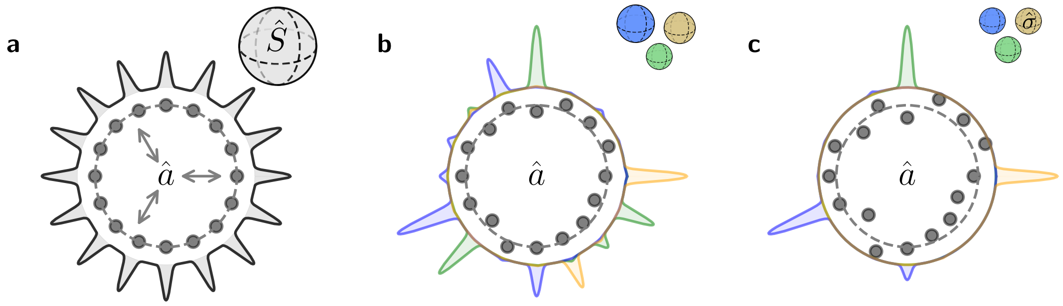

Figure 5.1: **Fragmentation of Eigenstates** The illustations show the structure of the typical eigenstates for homogeneous system (**a**), a system at intermediate disorder (**b**) and a large disorder system (**c**). In each diagram, the radial position of the dots with respect to the dashed circle represents the transition frequency of each spin. Left: Disorder-free system (all spins with the same energy) with all spins identically coupled to the central mode $\hat{a}$ provided by the cavity field, forming a collective symmetric Dicke state. The structure of the Hilbert space is characterized by a Bloch sphere for collective spin $\hat{S}$. Right: With disorder, the collective state fragments into few- or single-spin ensembles whose constituents are located at arbitrarily large distances, exchanging excitations through the cavity, sketched here for three excitation modes. The structure of the Hilbert space in this case, characterized by a Bloch sphere for single-atom excitations $\hat{\sigma}$.

In our study, we are interested in understanding how to tune the interactions between the atoms, which requires breaking the exchange symmetry of the system. Introducing disorder in the atomic transition frequencies disrupts the all-to-all character of cavity-mediated interactions by dividing the eigenstates of the atom-cavity system into states with fewer atoms that are closely resonant with each other. This is illustrated in Figure 5.1, which shows the structure of atomic excitations in typical eigenstates for different levels of disorder. For the homogeneous system (Figure 5.1**a**), the eigenstate is represented by the collective Dicke states, which have the same probability amplitude in all atoms. As the disorder increases, the excitations become more localized (two to three atoms in Figure 5.1**b**), and, eventually, at a very high level of disorder, they become completely localized in single atoms (Figure 5.1**c**). This summarizes the main effect of disorder, the fragmentation of spin excitations.

5.2 Two-Atom Toy Model

In this section, we will use a two-atom toy model to demonstrate the physics of eigenstate fragmentation. This helps us to understand the ideas necessary to interpret our measurements. We will expand on these concepts and apply them to a larger number of atoms in Section 5.3.

The system we consider in this section describes two atoms with different transition frequencies $\omega_{a_1} = -\epsilon + \overline{\omega_\mathrm{a}}$ and $\omega_{a_2} = \epsilon + \overline{\omega_\mathrm{a}}$ coupled equally with strength g to a single cavity mode. The detuning between the two atoms, which measures the disorder, is 2ϵ. In our model, the cavity is described by its resonance frequency ω_c and the creation and annihilation operators of photons in the cavity mode, $\hat{a}^\dagger$ and $\hat{a}$. In the frame rotating at the average atomic resonance frequency $\overline{\omega_\mathrm{a}}$, the Hamiltonian can be written as

$$\hat{H} = \hat{H}_\mathrm{a} + \hat{H}_\mathrm{c} + \hat{H}_\mathrm{i} = -\frac{1}{2}\epsilon\left(\hat{\sigma}_1^z - \hat{\sigma}_2^z\right) + \Delta_\mathrm{ac}\hat{a}^\dagger\hat{a} + g\hat{a}^\dagger\left(\hat{\sigma}_1^- + \hat{\sigma}_2^-\right) + \mathrm{H.c.},$$

where the first two terms describe the energy of the two atomic spins and the optical resonator and $\Delta_\mathrm{ac} = \bar{\omega}_\mathrm{a} - \omega_c$ is the relative detuning between the average atomic frequency and the resonance of the cavity.

The third term is the link between the atoms and the cavity mode. It explains the creation of a photon in the cavity due to the deexcitation of an atom and can be represented by a Feynman diagram as

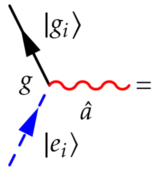

$$= g\,\hat{a}^\dagger\,\hat{\sigma}_i^- .$$

The total interaction is the sum of the two coupling terms of the two atoms. This results in only the coupling of the symmetric Dicke states ($|gg\rangle$, $\frac{1}{\sqrt{2}}(|eg\rangle + |ge\rangle)$, and $|ee\rangle$) with the cavity. We restrict our analysis to the single excitation manifold (SEM), thus disregarding collective phenomena such as Dicke superradiance that would arise from the synchronization of emission of photons into the cavity when both atoms are initially excited ($|ee\rangle$). We do this because the interactions of interest (SYK interactions) only require a virtual population of the cavity mode (see Chapter 6). However, exploring these collective effects in combination with disorder is of great interest, as it allows the investigation of phenomena related to BCS superconductivity [100]. Additionally, understanding the resilience of superradiance to inhomogeneous broadening is essential for the development of a superradiant laser atomic clock [101].

In the single-excitation regime, atomic excitations can be expressed in the basis of symmetric $|s\rangle = \frac{1}{\sqrt{2}}(|eg\rangle+|ge\rangle)$ and antisymmetic excitations $|a\rangle = \frac{1}{\sqrt{2}}(|eg\rangle-|ge\rangle)$ and the Hamiltonian becomes

$$\hat{H} = \frac{1}{2}\epsilon\,\hat{\sigma}_a^+\hat{\sigma}_s^- + \frac{1}{2}\Delta_{\mathrm{ac}}\,(\hat{\sigma}_s^z + \hat{\sigma}_a^z) + \sqrt{2}g\,\hat{a}^\dagger\,\hat{\sigma}_s^- + \mathrm{H.c.}. \tag{5.1}$$

In this basis, it is evident that the cavity only couples to the symmetric spin state. The disorder ϵ mixes the symmetric and antisymmetric spin states, localizing the eigenstates of the Hamiltonian on the single atom states $|eg\rangle$ and $|ge\rangle$.

In conclusion, the Hamiltonian describes the competition between the cavity coupling and the disorder in atomic energies. The former encourages completely delocalized spin excitations, whereas the latter binds the excitations to individual spins. With increasing disorder, a crossover from delocalized to localized can be observed. Even in the large-N limit, this remains a crossover and does not become a phase transition (see Section 5.3).

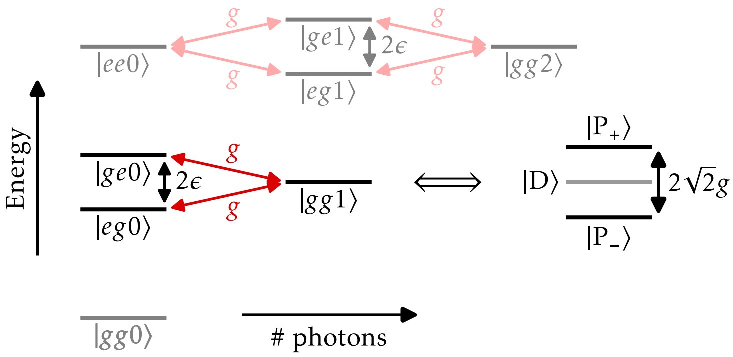

Figure 5.2: **Level Diagram of Two-Atom Hamiltonian.** In the diagram the cavity is on resonance with mean atomic transitions frequency ($\Delta_{\mathrm{ac}} = 0$). The ground state and the two-excitation manifold are marked in gray. We focus our analysis on the single-excitation manifold (solid black). The atomic excitations ($|eg\rangle$, $|ge\rangle$), split by 2ϵ and linked to the cavity excitation ($|gg0\rangle$) with strength g. The coupling form two bright polariton ($|\mathrm{P}_+\rangle$, $|\mathrm{P}_+\rangle$) and a dark state ($|\mathrm{D}\rangle$), whose coupling to the cavity depends on the disorder strength ϵ.

The level diagram of the two-atom Hamiltonian (see Figure 5.2) illustrates this crossover. In the large disorder regime, two independent atomic excitations are coupled to the cavity (left of Figure 5.2). When the cavity coupling is stronger than the disorder, the levels transform into two bright polaritons ($|\mathrm{P}_-\rangle$, $|\mathrm{P}_+\rangle$) with an increased Rabi gap of size $2\sqrt{g}$ and a dark state ($|\mathrm{D}\rangle$) in the middle. As the disorder increases, the coupling of the dark state to the cavity increases, and the state is called the gray state.

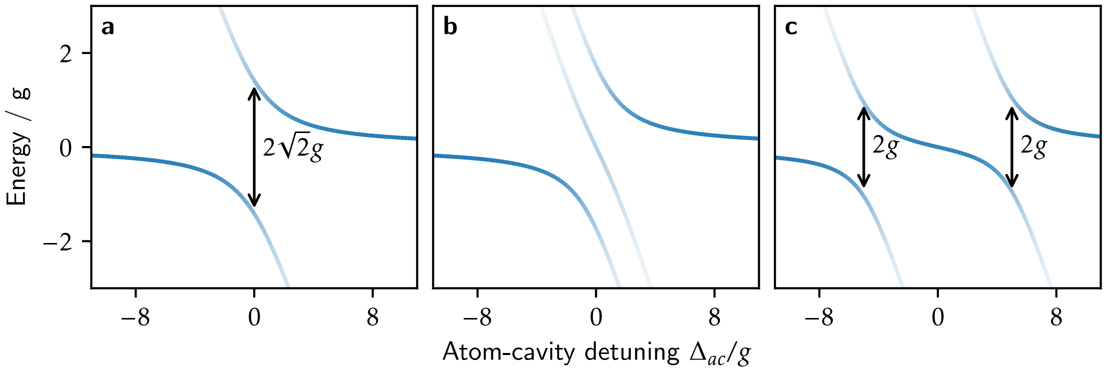

Figure 5.3: **Anticrossing in Two-Atom Spectrum.** Eigenstate spectrum as a function of atom-cavity detuning for different disorder strengths (**a**: $\epsilon = 0$, **b**: $\epsilon = g$, **c**: $\epsilon = 5g$). The transparency of the graph measures the photon weight of the eigenstate.

Small Disorder Regime ($\epsilon \ll g$) In the small disorder regime, we can neglect the first term of the Hamiltonian defined in Equation (5.1). As a result, the Hamiltonian describes two atomic transitions with frequency Δ_{ac}. However, only the symmetric state $|s\rangle$ is coupled to the cavity with an increase in Rabi frequency by a factor of $\sqrt{2}$. In contrast, the antisymmetric state vanished from the atom-cavity coupling, suppressing its excitation by cavity photons and rendering it dark. This results in the typical anticrossing, as shown in the spectrum in Figure 5.3**a**.

Large Disorder Regime ($\epsilon \gg g$) For large detunings between the two atoms, the atomic part of the Hamiltonian dictates the structure of the eigenstates. When the cavity is tuned to be resonant with either of the two atoms $\Delta_{\mathrm{ac}} = \pm\epsilon$, the effect of the other atom is dispersive in nature, changing the effective resonance frequency of the cavity. Neglecting this effect, the resulting Hamiltonian describes the coupling of two independent atoms to the cavity mode, creating anticrossings at their respective resonances (see Figure 5.3**c**).

Crossover Between Delocalized and Localized: Appearance of Gray States Between the two extremes of large and small disorder, a transition from delocalized to completely localized excitations can be observed. This is accompanied by the appearance of a gray state in the Rabi gap (see Figure 5.4**a**). The admixture of photonic excitations in the gray state, known as its photon weight, increases as the disorder increases (see Figure 5.4**b**). This is due to the mixing of symmetric and antisymmetric states caused by the first term in the Hamiltonian (5.1). The antisymmetric state does not directly couple to the cavity but is transformed into the symmetric state by the atomic disorder.

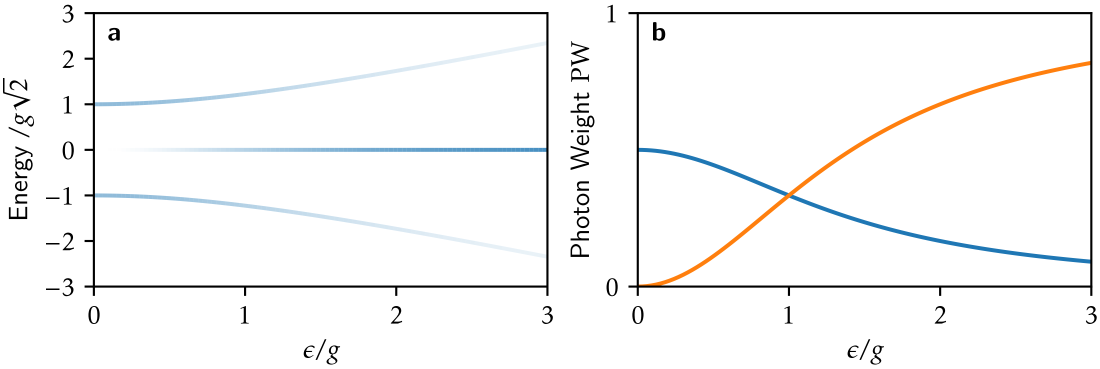

Figure 5.4: **Appearance of Gray States. a**, Eigenenergy spectrum of two-atom Hamiltonian. The transparency of the graph measures the photon weight of the eigenstate. **b**, Photon weight of bright (blue) and gray (orange) state as a function of disorder strength ϵ.

5.2.1 Cavity-Mediated Flip-Flop Interactions Emerging in the Dispersive Regime

The interaction term in the two-atom Hamiltonian describes the absorption (emission) of cavity photons that are accompanied by a flip (flop) of the atomic spin. The photon generated by an emission event in one atom can induce an absorption event in another atom. This photon exchange results in an effective flip-flop interaction between the atomic spins, which can be illustrated with a Feynman diagram

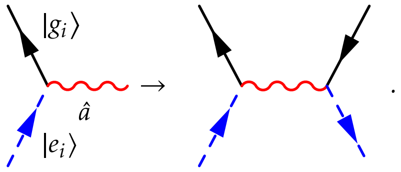

Generally, the probability of photon exchange is determined by the Green's function of the cavity (which has a Lorentzian shape and memory). However, when the atom-cavity detuning is much larger than the collective Rabi frequency ($|\Delta_{ac}| \gg g\sqrt{N}$), the cavity mode is only virtually populated, and the dynamics of the cavity becomes instantaneous and independent of frequency. There we can adiabatically eliminate the cavity mode from the Hamiltonian (5.1), which results in a spin-only Hamiltonian of the form

$$\hat{H} = \epsilon\hat{\sigma}_2^z - 2J\hat{S}^+\hat{S}^- + \text{H.c.}.$$

where $\hat{S}^{+(-)} = 1/\sqrt{2}(\sigma_1^{+(-)} + \sigma_2^{+(-)})$ are the creation and (annihilation) operators of the collective spin and $J = -g^2/\Delta_{ac} > 0$ measures the strength of the cavity-mediated flip-flop interactions. Note that the Hamiltonian has been expressed in the frame that rotates at the resonance frequency of the first atom $-\epsilon$. This Hamiltonian is analogous to an all-to-all interacting magnetic spin model with varying local magnetic fields. It illustrates the competition between ferromagnetic interactions (second term) that attempt to align the spins with each other and inhomogeneous magnetic fields (first term) that disrupt this symmetry.

The ferromagnetic character of cavity interactions is well illustrated by $\hat{S}^+\hat{S}^- = |\hat{S}|^2 - 1/2\hat{S}_z + \hat{S}_z^2$. The first term describes the length of the total spin, and the second term is a light shift of the atomic resonance due to the modified vacuum inside the cavity. It is the last term that favors an alignment of the two spins either up or down. It is also this term that creates spin-squeezing at the equator of the generalized Bloch sphere [102, 103]. The energy of the state of both spins pointing down $|gg\rangle$, the ground state, is reduced due to the ferromagnetic interaction. This results in the need for additional energy to flip one of the two spins. In other words, the system shows a ferromagnetic gap.

In the following, we show how disorder disrupts the ferromagnetic behavior of the system. We restrict our analysis to the single-excitation regime, restricting ourselves to small deviations from the ferromagnetic ground state. The resulting spin-only Hamiltonian is

$$\hat{H} = 2\epsilon\,|eg\rangle\langle eg| - J\,|eg\rangle\langle ge| + \text{H.c.}.$$

For readability, we have removed the light-shift of each atom by going into a frame rotating at J.

The eigenvalues of this two-level Hamiltonian are $E_\pm = \epsilon \pm \sqrt{\epsilon^2 + J^2}$ with corresponding eigenstates being

$$|-\rangle \propto \left(\epsilon + \sqrt{\epsilon^2 + J^2}\right)|eg\rangle + J\,|ge\rangle,$$
$$|+\rangle \propto -J\,|eg\rangle + \left(\epsilon + \sqrt{\epsilon^2 + J^2}\right)|ge\rangle.$$

Similarly to the quasi-resonant case, with zero disorder, the eigenstates are the symmetric and antisymmetric states $|s\rangle$ and $|a\rangle$, and for large disorder, the eigenstates approach the paramagnetic single-spin states $|eg\rangle$ and $|ge\rangle$. This is supported by the eigenenergy spectrum shown in Figure 5.5**a**. The splitting of the two eigenstates for zero disorder is equal to the spin interaction energy $2J$, forming a ferromagnetic gap of size J. For large disorder, the splitting is determined by the detuning parameter ϵ and the states are dictated by the inhomogeneous magnetic fields.

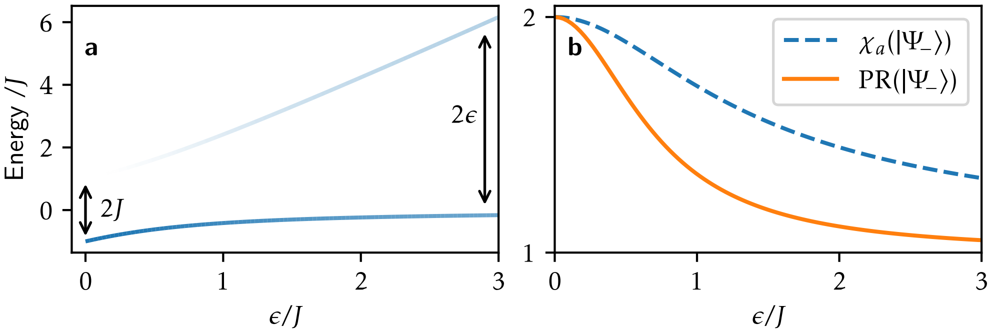

Figure 5.5: **Bound on Participation Ratio. a**, Eigenenergy spectrum of two-atom Hamiltonian as a function of disorder strength ϵ. The transparency of the graph indicates atomic susceptibility of the corresponding eigenstate.**b**, Participation ratio and atomic susceptibility of lower-lying eigenstate as a function of disorder strength ϵ.

Ferromagnetic interactions favor not only the alignment of the spins when the system is in the ground state $|gg\rangle$, but also during excitations, generating entanglement between the atoms by encouraging completely delocalized spin excitations. To quantify the delocalization of a spin state $|\Psi\rangle = \sum_{i=1}^{N} c_i \, |e_i\rangle$ in the single excitation manifold, one can define its participation ratio as

$$\mathrm{PR}(|\Psi\rangle) = \left(\sum_{i=1}^{N} |c_i|^4 \right)^{-1} \overset{\mathrm{N}=2}{=} \frac{1}{|c_1|^4 + |c_2|^4} \, . \tag{5.2}$$

For the symmetric state $c_i = 1/\sqrt{2}$ which is favored by the ferromagnetic interaction, the participation ratio can be evaluated as $\mathrm{PR}(|\Psi_b\rangle) = 2$, which equals to the total number of spins. For the localized single-atom states $|e_i\rangle$, the participation ratio is equal to 1. As the disorder increases, the participation ratio slowly decreases from 2 to 1. For theoretical analysis, the participation ratio is an important tool because it measures the number of contributing states. However, measuring it in the lab is usually very difficult.

In Figure 5.5, we can see graphically that the atomic susceptibility χ_{a} of the lower-lying collective spin state $|\Psi_{-}\rangle$ provides an upper limit to its participation ratio

$$\chi_{\mathrm{a}}(|\Psi_{-}\rangle) \geq \mathrm{PR}(|\Psi_{-}\rangle). \tag{5.3}$$

The atomic susceptibility measures the ease of flipping one spin in our system with an oscillating external magnetic field, which can be determined using the depumping technique (see Section 3.2.1). This, in turn, allows us to set a limit on the localization of the most energetically favorable excitation.

For a two-atom system, the atomic susceptibility of a state $|\Psi\rangle$ is defined as

$$\chi_{\mathrm{a}}(|\Psi\rangle) = |\langle \Psi | \hat{S}^{+} | G \rangle|^2 = |\sum_{i=1}^{N} c_i|^2 = |c_1 + c_2|^2 \, .$$

As the participation ratio (see Equation (5.2)), the atomic susceptibility equals to 2 for the collective symmetric excitation and 1 for the localized excitation $|e_i\rangle$, meaning that the bound in Equation (5.3) is exact for zero and infinite disorder. In Figure 5.5**b** both the participation ratio and the atomic susceptibility of energetically favorable excitation $|\Psi_{-}\rangle$ are plotted. As stated by the bound, the value of the atomic susceptibility lies above the participation ratio.

The mathematical proof of Equation (5.3) can be achieved by using the hierarchy of Rényi entropies. It is essential to note that the proof is dependent on the positivity of the coefficients c_i. This is only the case for the lowest energy excitation $|\Psi_{-}\rangle$. For the two-atom model, a counterexample is given by the dark state that has a zero total spin (paramagnetic) and is an eigenstate in the single-excitation manifold at zero disorder. As it is maximally delocalized (Bell state), its participation ratio is equal to 2. However, its atomic (magnetic) susceptibility is zero due to its asymmetry ($c_1 < 0$ and $c_2 > 0$), which is a consequence of its total spin being zero. The proof of the positivity of the coefficients for the lowest-lying excitation at any disorder in the case of many atoms is based on the Perron–Frobenius theory and can be found in Ref. [2].

5.2.2 Dissipation and the Measurement Scheme

Using the two-atom toy model, we can explore the dissipation pathways that are present in our experiment. This helps us to demonstrate the measurement procedure. Specifically, we discuss the methods used to measure the photonic and atomic susceptibilities. For an analysis of the case of multiple atoms, we refer to Section 3.2.

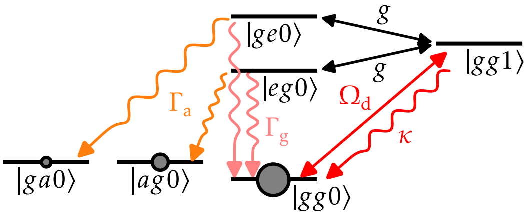

Figure 5.6: **Level Diagram including Driving Scheme and Dissipation.** Level diagram of the ground and single excitation manifold. The double headed solid arrows depict coherent coupling between different levels. The wiggly lines illustrate the dissipation channels. The population of the ground states after a short evolution of the system is depencited as circles.

The extended level diagram in Figure 5.6 illustrates the dissipation pathways and the driving scheme used in our experiments. We initially placed our system in the ground state $|gg0\rangle$. We then stimulate the cavity with a weak laser beam, which connects the ground state to the first excited state with one photon in the cavity $|gg1\rangle$. The photons in the cavity are lost at a rate κ, resulting in a dissipation channel back to the ground state. These photons are detected as signals on the single-photon counter, allowing us to measure the photonic susceptibility, which gauges the ease of generating cavity photons using an external drive.

The coherent atom-cavity coupling enables the reversible transfer of cavity photons into atomic excitations. These excitations can be lost through the emission of photons into the environment. In the case of ^{6}Li atoms, there are two dissipation channels connecting the excited state $|e\rangle$ to two different ground states. One of these channels returns the system to its initial state, while the other leads to the states $|ag\rangle$ and $|ga\rangle$, where it remains. By measuring the probability of ending up in these states after a short evolution of the system, it is possible to directly estimate the atomic susceptibility, which is a measure of the ease of exciting atoms with a cavity drive.

5.3 Many-Atom Model

The concepts developed in the two-atom model (see Section 5.2) can be extended to the case of N atoms. For a rigorous derivation of the theoretic results presented, we refer to the thesis of Philipp Uhrich [2]. Our system implements a paradigmatic model consisting of N Ising spins, mapped to internal atomic states, identically coupled to the central bosonic photon mode of the cavity. By exposing the i^{th} spin to a random energy shift ϵ_i, the model is described by the disordered Tavis–Cummings-type Hamiltonian

$$\hat{H}_{\text{TC}} = \Delta_{\text{ca}}\hat{a}^\dagger\hat{a} + g\sqrt{N}\left(\hat{S}^+\hat{a} + \hat{S}^-\hat{a}^\dagger\right) + \sum_{i=1}^{N}\epsilon_i\,\frac{\hat{\sigma}_i^z}{2}. \tag{5.4}$$

Here, $\hat{a}^\dagger$ and $\hat{a}$ are the creation and annihilation operators of photons in the cavity, $\hat{\sigma}_i^r$ are the r-Pauli operators acting on the Ising (pseudo-)spin-1/2 of the i^{th} atom, $\hat{S}^{+(-)} = \sum_{i=1}^{N}\hat{\sigma}_i^{+(-)}/\sqrt{N}$ are the collective spin-raising (lowering) operators, and Δ_{ca} is the detuning between the cavity and the bare atomic resonance.

Cavity excitations are coupled to the atoms with the collective spin operator. As a result, only the symmetric $N+1$ spin states couple to the cavity. In the absence of disorder, the model is described by the Tavis–Cummings Hamiltonian, and its eigenstates can be conveniently represented on a generalized two-dimensional Bloch sphere. The remaining $2^N - (N+1)$ states form a dark manifold that is decoupled from the cavity field. In the single excitation manifold, this structure reduces to two polaritons and $N-1$ dark states.

For many atoms, the collective coupling strength increases with $\sqrt{N}$, resulting in a larger Rabi gap between the two polaritons. This makes the anticrossing more resilient to disorder in the spins (homogeneous broadening). This phenomenon, known as cavity-protection, was investigated in an experiment conducted in parallel to our measurements [104]. The ferromagnetic gap that appears in the dispersive regime of Equation (5.4) is proportional to N. This is expected in a system with all-to-all ferromagnetic interactions, since the strength of the internally generated magnetic field is proportional to the number of participating spins. As a result, the amount of disorder required to disrupt the ferromagnetic dynamics also increases with the number of atoms.

In the two-atom model, we have seen that the collective ground state transitions into a localized spin state as the disorder increases. The same behavior is seen in the case of N atoms, where the ferromagnetic gap does not close. The localization of the excitations on a single atom is a finite-size effect; as the number of atoms increases, the chances of frequency coincidences become greater. Therefore, in the large-N limit, the structure of weak excitations remains neither localized nor delocalized, but rather semilocalized for all levels of disorder, and no level crossings or phase transitions can be seen [105].

5.4 Experimental Configuration

In our experiment, the Hamiltonian in Equation (5.4) is realized by an array of $N = 90$ to 800 thermal ^{6}Li atoms confined in about 160 trapping sites, positioned at the antinodes of the resonant cavity field (see Section 2.2). The spins are encoded in the $2S_{1/2}^{F=1/2}$ ($|g\rangle$) and $2P_{3/2}$ ($|e\rangle$) states of the ^{6}Li atoms (see Figure 5.7 and Section 3.1.4). The cavity resonance is tuned close to the $2S_{1/2}$–$2P_{3/2}$ transition at 671 nm, with the detuning given by Δ_{ca}. Our cavity is close to concentric, leading to a single-atom cooperativity of $\eta = (4g^2)/(\kappa\Gamma) = 6.4$ with $g/2\pi, \kappa/2\pi, \Gamma/2\pi = 2.05\,\mathrm{MHz}, 0.45\,\mathrm{MHz}, 5.8\,\mathrm{MHz}$ (see Section 1.3.2). Due to the cloud's temperature of $200\,\mu\mathrm{K}$, and the reduced dipole moment for linearly polarized light at zero magnetic field, the average cavity coupling experienced by the atoms is $\bar{g}/2\pi = 1.23\,\mathrm{MHz}$.

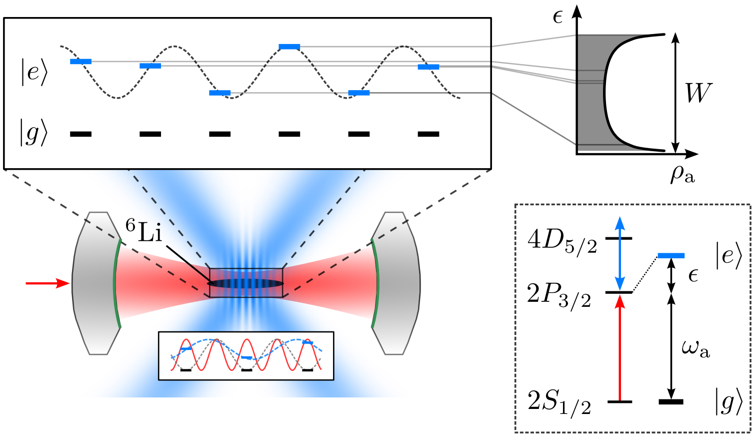

Figure 5.7: **Experimental Realization of Random Spin System.** Atoms are trapped in an optical resonator, forming an atom array commensurate with the cavity mode, ensuring identical atom–light coupling. Two crossed light-shifting beams (blue) illuminate the atoms with an incommensurate standing wave inference pattern, leading to a quasi-random intensity distribution ρ_a over the atoms (right). The inset below illustrates the positions of the atoms (black bars) with respect to the cavity field intensity (red wave), the optical dipole trapping potential (gray wave), and the intensity of the light-shifting lattice (blue wave). The inset on the bottom right shows a simplified level diagram of the ^{6}Li atoms. The light-shifting laser (blue arrow) off-resonantly couples the $2P_{3/2}$ manifold with the higher-lying $4D_{5/2}$ manifold, yielding a dressed state $|e\rangle$ (blue), with an energy shift proportional to the laser intensity.

The disorder is created by two laser beams that intersect at the position of the atoms, with a frequency slightly detuned from the $2P_{3/2}$–$4D_{5/2}$ transition at 460 nm (see Section 5.4.1), forming a light-shifting lattice with a period of 1.04 µm which is incommensurate with the trapping lattice, which has a period of 671 nm. This produces a quasi-random pattern of strong light-shifts of the $2P_{3/2}$ state, with negligible effect on atoms in the ground state, as illustrated in Figure 5.7. These light shifts result in quasi-disordered energy shifts ϵ_i, which translate into the spin language as random local longitudinal fields sampled from the distribution $\rho_a(\epsilon) = \left[\pi\sqrt{\epsilon(W-\epsilon)}\right]^{-1}$, where W is proportional to the intensity of the control laser (see Methods). We neglect the light shifts induced by the trapping light on the ground and excited states, as it is small compared to the light shift induced by the 460 nm beam.

We probed the system by weakly driving the cavity on-axis with a probe beam and measuring both the photon transmission proportional to $\langle \hat{a}^\dagger \hat{a}\rangle$, and the atomic excitations $\langle \hat{S}^z\rangle = \langle \sum_{i=1}^{N} \hat{\sigma}_i^z\rangle/(2N)$ using an optical pumping technique. In the linear response regime, this provides us with the frequency-dependent photonic and atomic (spin) susceptibilities, χ_p and χ_a. For a more detailed description of the different probing techniques used, we refer to Section 3.2.

5.4.1 Implementation of the Disorder through Light-Shift Technique

In our system, the transition frequency of the atoms can be tuned by light-shifting the excited state $|e\rangle$. In particular, this is achieved by dressing the $2P_{3/2}$ state with the higher-lying $4D_{5/2}$ manifold using a control laser at 460 nm detuned from resonance (see inset in Figure 5.7) by Δ_{blue}. We first calibrated the light shift of the excited state due to a single Gaussian beam of waist 120 µm, with Δ_{blue} =50 MHz—by performing an absorption spectroscopy of the D2 transition

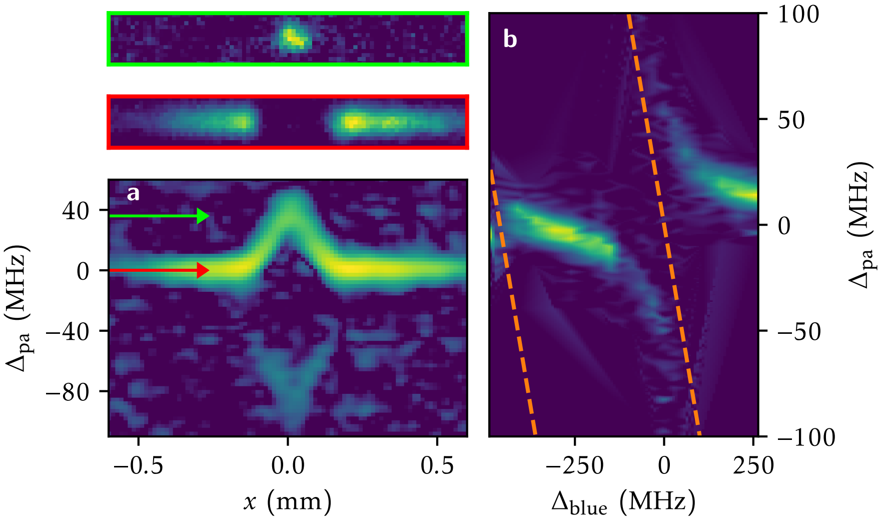

Figure 5.8: **Characterization of Light Shift of Excited State.** **a**, Spatially-resolved absorption spectroscopy of the D2 transition in the presence of a single lattice beam (Gaussian beam centered on $x = 0\,\mathrm{mm}$ with waist of $120\,\mu\mathrm{m}$). Each horizontal line of plot **a** is the y-integrated optical density. The absorption images with maximum shift (green arrow in **a**) and zero shift (red arrow in **a**) are show in the inset above. The light-shifting laser was 50 MHz blue detuned from the $2P_{3/2}$–$4D_{5/2}$ transition. We can observe both resonances of the Autler–Townes doublet, the strong light-shifted single-photon transition (top) and the faint two-photon transition (bottom). **b**, Absorption spectroscopy of the central cloud ($x = 0\,\mathrm{mm}$) for different control beam detunings Δ_{blue}.

similar to [106]. Taking absorption images of the cloud at different imaging frequencies, we reconstructed the spatial distribution of the light shift of one of the two identical beams that generate the light-shifting lattice when sent together, as presented in Figure 5.8**b**. We performed this spectroscopy both *in situ* and after releasing the atoms from the cavity dipole trap, allowing us to measure the trap-related shift of the $2P_{3/2}$–$4D_{5/2}$ transition to be 90 MHz[*]

Furthermore, we characterized the dependence of the cavity transmission spectrum on the detuning of the light-shifting laser, showing an avoided crossing for both states of the Autler–Townes doublet, in particular the light-shifted single-photon $2S_{1/2}$–$2P_{3/2}$ transition and the two-photon transition $2S_{1/2}$–$4D_{5/2}$ (see Figure 5.8**c**). We observed increased atom losses for small detunings of the light-shifting laser. These losses are due to radiation pressure that occurs when atoms are promoted to the $2P_{3/2}$ state during spectroscopic measurements and to antitrapping in the cavity-enhanced dipole trap, in which the atoms are promoted to the $4D$ manifold (see Figure 2.9). We minimized this effect by choosing the maximal detuning (400 MHz blue detuned from the $2P_{3/2}$–$4D_{5/2}$ transition), allowing us to go up to $W = 26\,\mathrm{MHz}$ for the maximal available power of the laser of 7.3 mW per lattice beam.

The light-shifting laser produces a dipole potential on the atoms in the ground state about 5×10^{-6} smaller than the light shift of the $2P_{3/2}$ state, negligible compared with the intra-cavity trapping potential.

Both light-shifting lattice beams are linearly polarized perpendicular to the cavity axis, and

---

[*] This shift due to the strong antitrapping of the $4D$ state in the cavity-enhanced dipole trap (see Figure 2.9). The main reason we lose atoms in the $4D$ state.

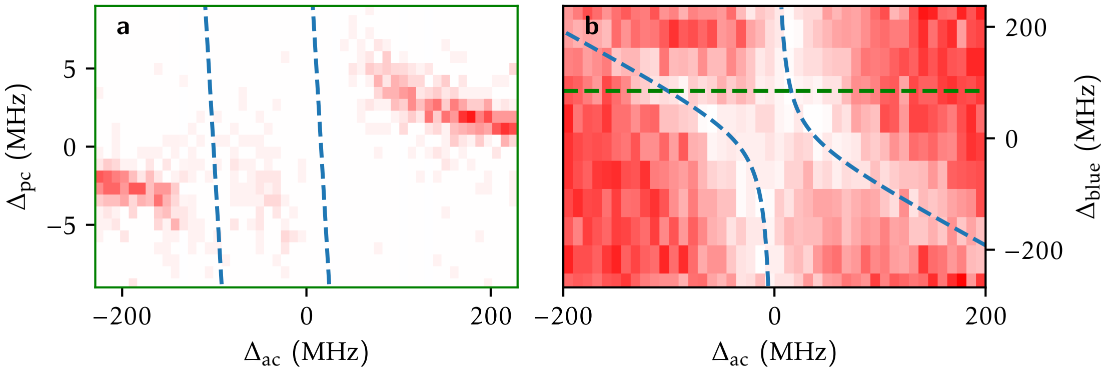

Figure 5.9: **Coupling of Autler–Townes Doublet to Cavity Mode.** **a**, Cavity transmission spectroscopy for cloud illuminated with homogeneous light-shifting beam. The dashed blue lines indicate the expected resonance frequencies of the Autler–Townes doublet. **b**, 2D map of cavity transmission spectra for different detunings of the light-shifting laser from the $2P_{3/2}$–$4D_{5/2}$ transition. Each horizontal line is a cavity transmission spectrum. The red color indicates a large number of photons transmitted through the cavity. The green line in panel **b** marks the detuning of the control beam during the measurement presented in panel **a** ($\Delta_{blue} = 75\,\text{MHz}$).

set the direction of the quantization axis. We probe the cavity using π-polarized light, to avoid any vector light-shift effect of the light-shifting beam. Because atoms reside in the $F = 1/2$ hyperfine manifold, the π transition used for cavity interrogation is free from tensor light-shift effects. As a result, even though our sample comprises an incoherent mixture of the two magnetic sublevels of the $F = 1/2$ manifold, the two components experience a strictly identical light shift and probe beam, contributing equally to the signal without further broadening effects. Cross-optical pumping between the two does not deteriorate the signal in the linear response regime explored in this work.

5.5 Experimental results

This section summarizes our experimental findings for both the near-resonant regime, where we observe the appearance of gray states in the presence of disorder (see Section 5.5.2) and the large-detuning regime, where the cavity-mediated spin-exchange interaction implements a Lipkin–Meshkov–Glick model (see Section 5.5.3).

5.5.1 Signature of Strong Coupling: Atom-Cavity Anticrossing

In this section, we discuss the properties of a special case of the Hamiltonian, the homogeneous system, where all atoms have the same transition frequency. In this case, the system can be described with the Tavis-Cummings model. The experimental consequence is illustrated in Figure 5.10 which shows the measured cavity transmission spectrum as a function of frequency detuning between the atomic and cavity resonance Δ_{ac} and probe-cavity detuning Δ_{pc}. More details of the setup that allowed us to obtain this measurement result are presented in Section 2.4. It reveals a sign of strong coupling, the avoided crossing between the cavity and atom excitations. In fact, because of the influence of the atoms on the cavity, the injection of photons into the resonator by a weak on-axis probe is strongly suppressed at its resonance frequency ($\Delta_{pc} = 0$).

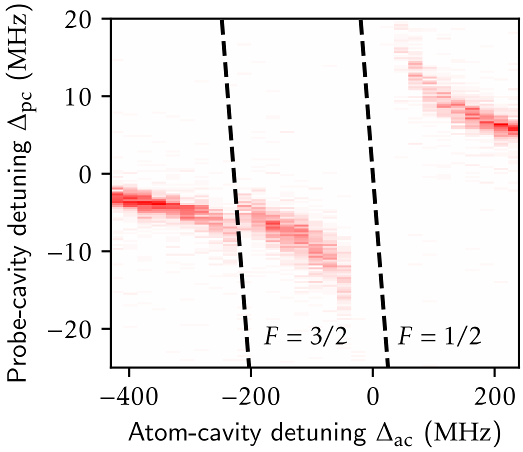

Figure 5.10: **Strong Coupling between Atoms and Cavity.** Cavity transmission spectrum as a function of atom-cavity detuning and probe-cavity detuning. The resonance condition for the two atomic transitions originating from the two hyperfine ground states are marked by dashed black lines.

This effect is particularly strong in the resonant regime, where the cavity resonance is tuned so that it overlaps with the atomic transition frequency ($\Delta_{ac} = 0$). Due to the strong coupling between the cavity photons and the atomic excitations, fast Rabi oscillations develop. In the spectrum, this presents itself by the formation of two normal modes, the polaritions, which are spit by a Rabi gap. The size of the Rabi gap measures the strength of the interactions, which in the case of many atoms is $2g\sqrt{N}$. The factor $\sqrt{N}$, which scales with the number of atoms, is the result of the enhancement of the coupling of collective Dicke states to the cavity. In Section 5.5.2, we experimentally study the breakdown of collective effects resulting from disorder in the atomic transition frequencies.

In the regime of large atom-cavity detuning, also known as the dispersive regime, the two polaritions turn into one more atom-like excitation (atomic polariton) and one more cavity-like excitation (cavity polariton). In the cavity transmission spectrum, the cavity polariton creates a stronger signal in the spectrum as it becomes more photonic. In this regime, the effect of the atoms on the cavity can be treated perturbatively. In particular, the two key parameters that characterize the cavity, its resonance frequency and its linewidth, are modified by the presence of the atoms. In Section 3.3, we study how we can use this feature to gain information about the atomic cloud. On the contrary, the atomic polariton fades out for large atom-cavity detunings. This is the result of the reduced photonic admixture of the state. It is precisely in this regime that cavity-mediated flip-flop interactions are observed. A more detailed experimental analysis of this regime is presented in Section 5.5.3.

A small but important detail of the anticrossing presented in Figure 5.10, is that anticrossings develop between the cavity and any of the atomic transition frequencies. The size of the Rabi gap developed depends on whether these transitions can be driven by light. In our case, we prepared the atoms in the $F = 1/2$ ground state, meaning that transitions from the $F = 3/2$ ground state are strongly suppressed. The presence of a small anticrossing in the $F = 3/2$ transition is only due to imperfect preparation of the cloud. In fact, this feature is what we use to detect atomic excitations and measure the atomic susceptibility as discussed in Section 3.2.1.

5.5.2 Near-Resonant Regime and Gray States

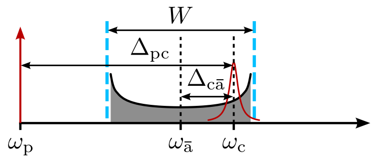

Figure 5.11: **Frequency Diagram in Near-Resonant Regime** illustrating the relative detunings between the atoms with average frequency $\omega_{\bar{a}}$ in a range W, the cavity at frequency ω_c, and the probe at ω_p.

We first investigate the regime at small $\Delta_{c\bar{a}}$ where the cavity resonance is close to the mean atomic resonances, $\Delta_{c\bar{a}} = \Delta_{ca} - W/2$ (see Figure 5.11). In the absence of disorder, we observe the canonical normal-mode splitting of width $2g\sqrt{N}/2\pi = 22\,\mathrm{MHz}$ expected from the Tavis–Cummings model, as shown in Figure 5.12**a**. As a result of this splitting, a Rabi gap forms at $\Delta_{c\bar{a}} = 0$, and direct atomic excitations at the bare resonance frequency are suppressed (see center of Figure 5.12**a**). Although there are $N-1$ eigenstates of the Hamiltonian lying within the gap, these are purely atomic, and the symmetry of the all-to-all atom–cavity coupling prevents their excitation, rendering them completely dark.

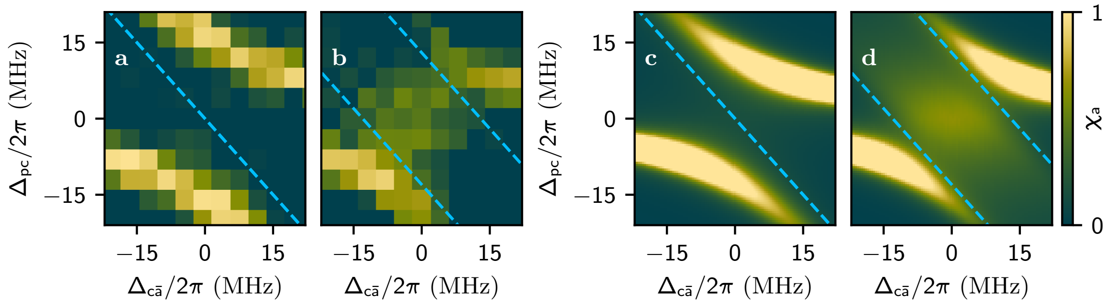

Figure 5.12: **Anticrossing in Homogeneous and Disordered Atom-Cavity System.** Measured (**a**, **c**) and simulated (**b**, **d**) atomic susceptibility maps as a function of atom–cavity and pump–cavity detunings (x- and y-axis, respectively), for the clean system (**a**, **c**) and at maximal disorder $W/2\pi = 26\,\mathrm{MHz}$ (**b**, **d**). For these measurements we trapped on average $N = 74$ atoms.

Upon introducing disorder, we observe the onset of a non-zero response around zero detuning, a manifestation of the increase of photon weight of the originally dark purely atomic states. A representative spectrum of χ_a for $W/(2\pi) = 26\,\mathrm{MHz}$ is presented in Figure 5.12**b**. We observe that the fading out of the Rabi splitting occurs via a redistribution of the spectral weight from the polaritons to a wide spectrum of midgap states. For $|\Delta_{c\bar{a}}| \gtrsim W$, a narrow dispersively shifted cavity resonance is restored around $\Delta_{pc} = 0$ (see Figure 5.12**b**).

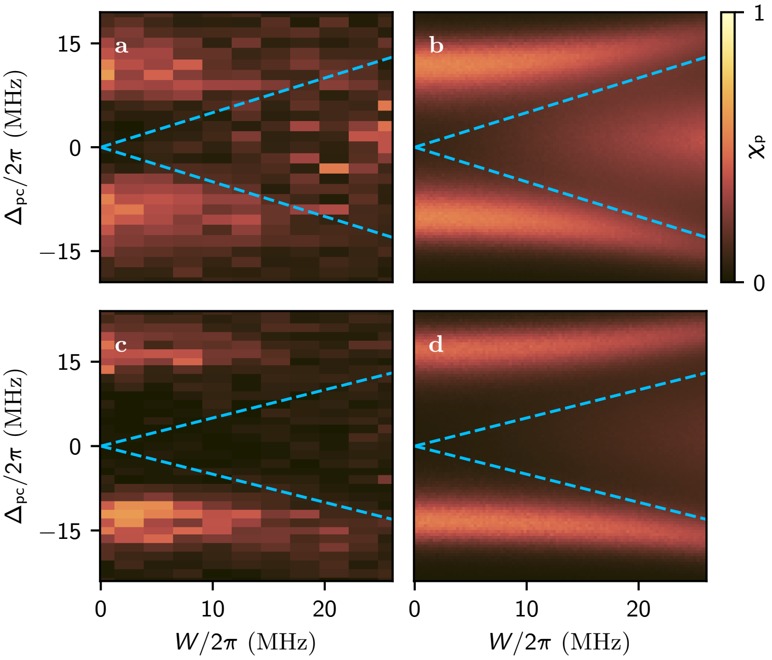

Figure 5.13: **Appearance of Gray States in the Rabi Gap.** Measured (**a**, **c**) and simulated (**b**, **d**) photonic susceptibility as a function of disorder strength W for different atom numbers: $N = 74$ (**a**, **b**) and $N = 145$ (**c**, **d**).

To better understand the evolution of the spectrum with disorder strength, we probe the photonic susceptibility at $\Delta_{c\tilde{a}} = 0$ as a function of disorder strength W and detuning Δ_{pc}. The results are presented in Figure 5.13**a**, **b** for different mean atom numbers N. For a weak disorder, the photonic susceptibility χ_{p} confirms the presence of the two bright polaritons and a manifold of degenerate dark states at the center of the Rabi gap.

As the disorder becomes comparable with the collective atom–cavity coupling, $W \sim g\sqrt{N}$, we observe a smooth increase of χ_{p} around $\Delta_{\mathrm{pc}} = 0$, signaling the onset of a finite coupling of a gray state manifold emerging from the originally dark states. Simultaneously, the polaritons' response weakens and fades away for the largest disorder, where the spectrum consists of a resonance centered at $\Delta_{\mathrm{pc}} = 0$ strongly broadened by the disorder.

The evolution of the spectrum with disorder is driven by the fragmentation of the eigenstates, from fully delocalized bright and dark states without disorder to randomly distributed isolated resonances for the largest disorder. To confirm this interpretation, we compare our observation (Figure 5.13**a**, **b**) with theoretical calculations (Figure 5.13**c**, **d**) of cavity transmission based on Green's function techniques (see Methods of our publication [1]). The model takes into account the experimental distribution of the spin energies, which is correlated and non-uniform, differently from the case studied in [105].

However, we have verified that the eigenfunctions are multifractal in the same way (see Supplementary Information, Sec. 1.1 of [1]). The simulations, which take into account the measured atom number fluctuation, the effects of the thermal motion on the atom–cavity couplings and both the losses of photons and the atomic decay, are in good agreement with the observations for the low disorder regime. For the strongest disorder, deviations appear in particular for the upper polariton, whose signal appears moderately weaker in the experiment.

We attribute this to losses induced by the control laser at 460 nm, which affect predominantly excited atoms with the largest admixture in the $4D_{5/2}$ manifold (see Section 5.4). For the largest disorder strength, we do not resolve the polaritons themselves, but we observe a clear signal from the gray states. These results are further confirmed in Figure 5.14**b**, which presents a direct comparison of experimental and theoretical data for the photonic susceptibility χ_p as a function of Δ_pc for representative values of the strength of the disorder W. The same simulation procedure reproduces also the atomic susceptibility χ_a measured as a function of detuning, as shown in Figure 5.13**a, b**.

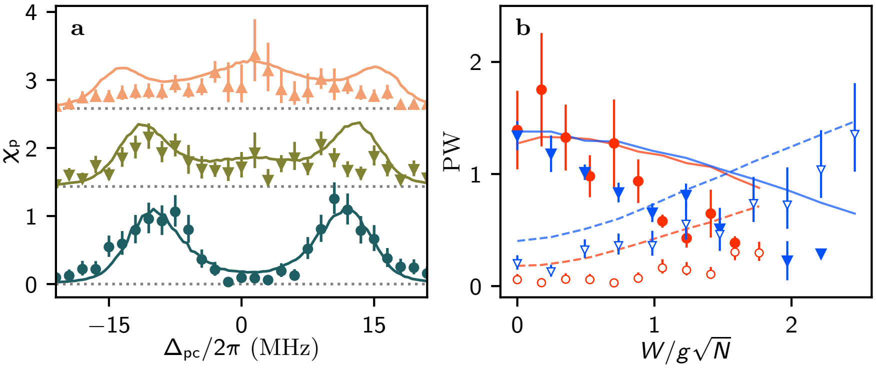

Figure 5.14: **Cascade Plot and Photonweight.** **a**, Vertical sections of panels Figure 5.13 **b** and **d** overlapped (curves are offset vertically for clarity) for $W/g\sqrt{N} = 0, 1, 2$. **b**, Photon weight PW of the gray states (empty markers, dashed lines) and the polaritons (filled markers, continuous lines) as a function of normalized disorder strength for $N = 145$ (circles) and $N = 74$ (triangles) atoms, indicating the disappearance of the polaritons and the appearance of the gray states. The photon weight of the gray states was measured by taking the average photonic susceptibility over the gray state region defined by $\Delta_\mathrm{pc} \in \{-\Gamma/2, \Gamma/2\}$, while the photon weight of the polariton was quantified by taking the height of the lower polariton, which is not affected by the radiation pressure of the light-shifting beam.

We quantitatively analyze the fading out of the polariton and the emergence of gray states by comparing the photonic susceptibility in the lower (respectively, middle) parts of the spectrum shown in Figure 5.12**a**–**d**. This yields the total photon weight of the polariton and gray states as a function of the normalized disorder strength shown in Figure 5.14**b**. The crossover between the light–matter interaction-dominated regime and the disorder-dominated regime manifests itself as smooth redistribution of spectral weight from the polariton to gray states, in qualitative agreement with the simulations.

5.5.3 Large-Detuning Regime and Lipkin–Meshkov–Glick model

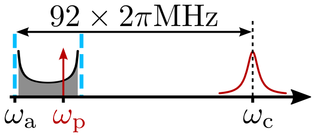

Figure 5.15: **Frequency Diagram in Large-Detuning Regime** depicting the detuning between the atomic disorder, the cavity and the weak cavity probe.

In the central mode model investigated so far, an essential role is played by the finite admixture of the spin excitations to the delocalized photon field. For large detuning $\Delta_{\mathrm{ca}} \gg g\sqrt{N}$, the cavity field is only virtually populated, giving rise to an all-to-all interaction between the spins, thus realizing an effective Lipkin–Meshkov–Glick (LMG) model [107–109] (see Figure 5.15, the Methods Section of [1] and the two-atom model, presented in Section 5.2). In the presence of a longitudinal random field, the Hamiltonian for these effective dynamics reads

$$\hat{H}_{\mathrm{LMG}} = \sum_{i=1}^{N} \epsilon_i \frac{\hat{\sigma}_i^z}{2} - JN\hat{S}^+\hat{S}^-, \tag{5.5}$$

a where $J = g^2/\Delta_{\mathrm{ca}}$ is the strength of the spin-exchange interactions. Equation (5.5) is a particular case of the class of exactly solvable Richardson–Gaudin models [110, 111] that are ubiquitous in quantum many-body systems [112].

Similar to the central mode model, in the absence of disorder ($W = 0$), Eq. (5.5) describes the dynamics of a collective spin within the Hilbert subspace of symmetric states. The nonlinearity inherited from the spin–cavity coupling favors a ferromagnetic ground state, protected by a finite gap of size JN. A striking manifestation of ferromagnetism is the strong suppression of the zero–frequency magnetic response.

To realize the model of Equation (5.5), we detune the cavity to the blue of the atomic transition by $\Delta_{\mathrm{ca}}/2\pi = 92\,\mathrm{MHz}$, and probe the system at a frequency ω_{p} in the vicinity of the bare atomic resonance ω_{a} (see Figure 5.15). In this regime, the transmission of the cavity is negligible such that $\chi_{\mathrm{p}} \sim 0$, and the atomic signal $\chi_{\mathrm{a}}(\Delta_{\mathrm{pa}})$ (see Section 3.2.1) directly measures the transverse spin susceptibility of the system at frequency $\Delta_{\mathrm{pa}} = \omega_{\mathrm{p}} - (\omega_{\mathrm{a}} + 2g^2/\Delta_{\mathrm{ca}})$.

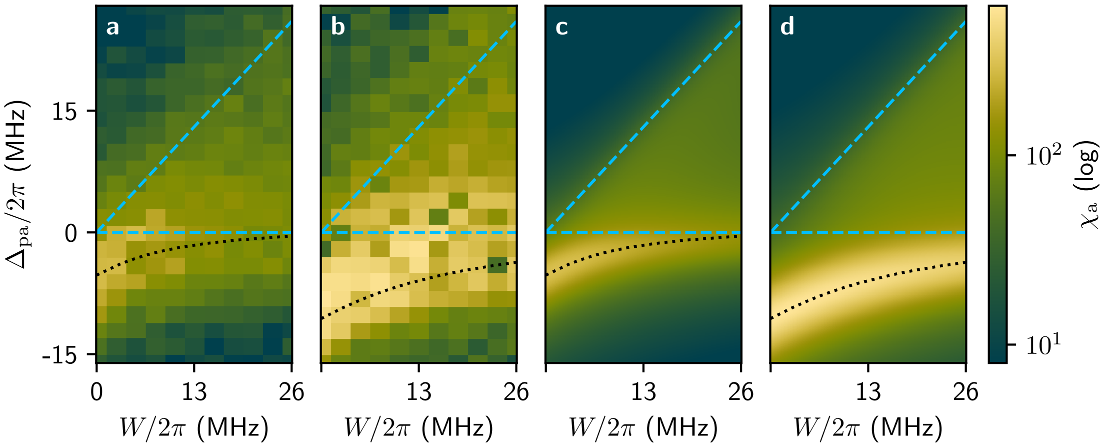

Figure 5.16: **Response of the Random LMG Model.** Measured (**a**, **b**) and simulated (**c**, **d**) atomic susceptibility for $N = 303$ (**a**, **c**), and $N = 610$ (**b**, **d**) atoms. The dashed blue lines mark the edges of the disorder distribution. The dashed black line marks the theoretically calculated location of the resonance of the collective spin state.

As shown in Figure 5.16**a** and **c**, in the absence of disorder, the frequency dependence of χ_{a} reveals the finite ferromagnetic gap of magnitude Δ_{FM}, which means that the atomic resonance is modified. As a result, the zero–frequency susceptibility at $\Delta_{\mathrm{pa}} = 0$ is reduced. The signal is broadened by the finite decay rate of the excited atomic states, which reduces to a convolution of the response with the linewidth of the atomic transition (see the Supplementary Information of [1], Sec. 1.2).

Now we investigate this model in the presence of disorder. Similar to the central-mode model, this breaks the description in terms of a collective spin, restoring the system's ability to explore the full Hilbert space. For a given strength of the disorder W, the susceptibility (see Figure 5.17) shows an asymmetric peak, corresponding to a collectively enhanced response superimposed with a weak and broad background whose width traces the strength of the disorder (see dashed blue line in Figure 5.16). This is a manifestation of the gradual fragmentation of the collective spin, as disorder renders the individual spins off-resonant with each other. The peak is located at $-\Delta_{\mathrm{FM}}$, and we denote its amplitude by $\chi_{\mathrm{a}}^{\mathrm{FM}}$.

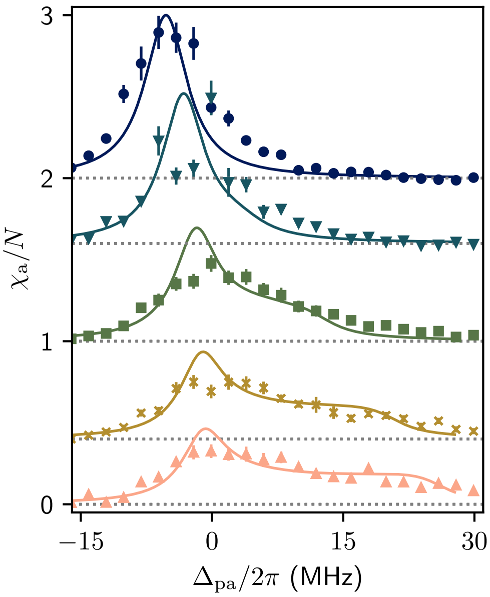

Figure 5.17: **Cascade plot of response of the random LMG model.** Cuts through Figure 5.16, illustrating the quantitative agreement between experiment (markers) and theory (solid lines). The cuts show data for different disorder strengths $W/2\pi = 0.0, 5.2, 13.0, 20.8, 26.0$ (MHz) (top to bottom), and are offset from one another according to $(26 - W/2\pi)/13$.

Tracking the location of this peak provides a measurement of the ferromagnetic gap as a function of W. Without disorder, this gap increases linearly with the number of atoms, as shown in Figure 5.18**a**. With increasing disorder, it gradually decreases to zero, as shown in Figure 5.18, where, for small atom numbers, the gap is zero within our error bars. This demonstrates the competition between the infinite-range cavity-mediated interaction J and the spectral disorder W for the dynamics of the effective model $\hat{H}_{\mathrm{LMG}}$. Our results agree very well with a simulation of the response χ_{a} of $\hat{H}_{\mathrm{LMG}}$ (see Ph.D. thesis of Phillip Uhrich [2]), over the entire parameter regime (see Figure 5.16**a**–**e**).

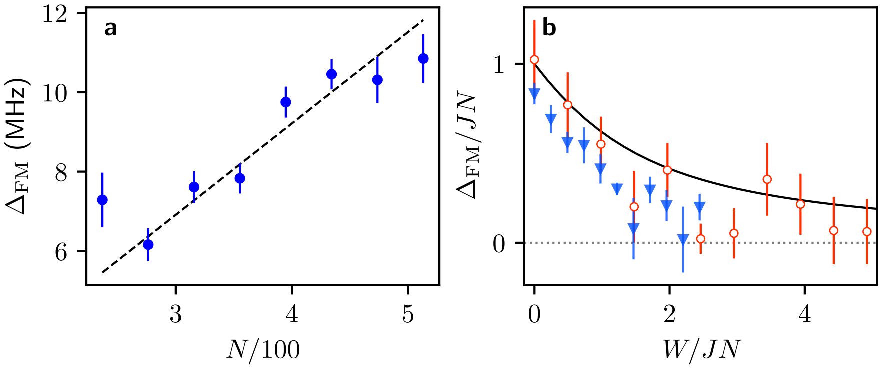

Figure 5.18: **Scaling of Ferromagnetic Gap with Atom Number and Disorder.** **a**, Scaling of the collective ferromagnetic gap $\Delta_{\mathrm{FM}} = JN$ at zero disorder $W = 0$ with mean atom number N. **b**, Behavior of Δ_{FM} as a function of disorder strength W for $N = 303$ (emtpy red circles) and $N = 610$ (blue triangles) atoms. To illustrate the scale invariance of the system, the axes are rescaled by the size of the zero-disorder ferromagnetic gap JN. The markers represent the experimental data with statistical error bars, and the lines show the theoretical results obtained by exact diagonalization.

The sizes of the simulated system were set as the mean number of atoms N realized in all experimental runs, and the effect of the thermal motion of the atoms on the atom–cavity coupling g has been taken into account, as in the near-resonant case. The decrease in the ferromagnetic gap (see Fig. 5.18**a**) indicates a drastic change in the properties of the system as the disorder increases. However, in the thermodynamic limit, the system is always ferromagnetic, and no paramagnetic phase transition should occur.

Indeed, intuitively, for any fixed disorder strength, increasing the number of atoms will always lead to an infinite number of close-to-resonance spins, enforcing ferromagnetism in the thermodynamic limit for an arbitrarily large disorder strength. However, for any finite number of atoms, there exists a disorder strength large enough to bring the ferromagnetic gap close to zero, rendering each spin essentially spectrally isolated from all the others, thus crossing the system over into a paramagnet. More precisely, our simulations show that finite systems display a minimal gap at a disorder strength $W^\star$ suggestive of critical behavior; however, the value of $W^\star$ diverges with increasing atom number (see Supplementary Information of [1], Sec. 1.3 and Supplementary Fig. 2).

5.5.4 Localization of Atomic Excitations

The distribution of energy resonances in disordered systems is the essence of Anderson localization. In our system, excitations can hop at arbitrarily large distances, provided that the spins are closely resonant. The disorder decimates the spins available for resonance by offsetting most spins from each other, but does not prevent long-distance propagation [105, 113].

Interestingly, while our spectroscopic probe does not yield spatially-resolved information, it does carry relevant insights about the localization of excitations. Indeed, general arguments based on the hierarchy of Rényi entropies show that a system's magnetic response may be used to bound the participation ratio of the excitations, i.e., the number of spins contributing to the wave function. The participation ratio PR_1 of the first excited state obeys

$$\chi_{\mathrm{a},1} \geq \mathrm{PR}_1, \tag{5.6}$$

at any $W \geq 0$, where $\chi_{a,1}$ is the contribution of the first excited state to the atomic susceptibility when the system is probed on resonance with the transition to this state, from the global ground state. The bound is reached for $W = 0$ where $\mathrm{PR}_1 = N$ corresponds to a uniformly distributed wave function on all spins, as well as in the limit $W \to \infty$ in which the excitation becomes localized on a single spin ($\mathrm{PR}_1 \to 1$). Our frequency-resolved measurement thus allows us to verify the fragmentation of the system's collective excitations into ever more localized wave functions, consistent with the expectations for eigenstates of the central-mode model [105, 113, 114].

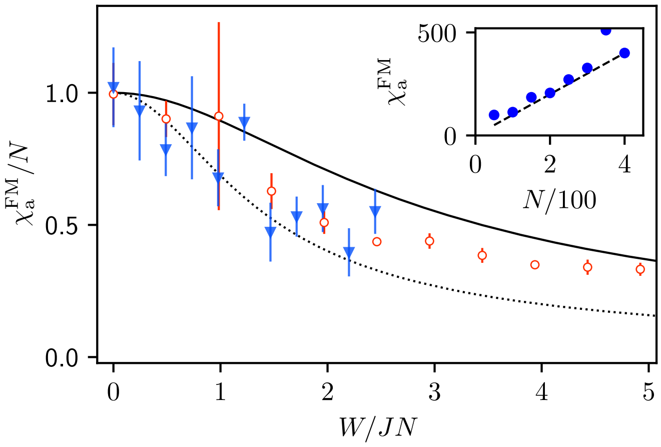

Figure 5.19: **Participation Ratio Bound from Atomic Susceptibility.** Normalized atomic susceptibility χ_a^{FM}, an upper bound to the participation ratio PR_1 of the first excited state, for $N = 303$ (empty red circles) and $N = 610$ (blue triangles) as a function of normalized disorder strength. The solid black line shows the corresponding simulation results for $\chi_{a,1}$ of Equation (5.6). The black dotted line is the directly simulated participation ratio of the first excited state, PR_1. Inset: Maximum value of the zero-disorder atomic susceptibility as a function of atom number, showing linear scaling expected from the definition of χ_a in Section 3.2.1.

Figure 5.19 shows the bound to the participation ratio deduced from our measurements, showing a decrease by more than a factor of two as the disorder reaches the highest values. Upon normalization of PR_1 by the mean atom number N and of W by the corresponding zero-disorder ferromagnetic gap JN, all the data collapse onto each other and agree with the simulations. The figure also shows the theoretically predicted value of PR_1, which obeys the bound observed in the data.

Similar to the ferromagnetic gap, suggestive as these findings are, they do not herald a transition from delocalized to localized. For a fixed disorder strength, increasing the number of atoms leads to an infinite number of close-to-resonance spins at arbitrary distances, preventing full localization but leading to a semilocalized regime similar to the critical regime of the Anderson transition [113].

5.6 Conclusion

Our ability to introduce controlled disorder in cavity QED offers many timely and exciting prospects for further investigations, such as the study of Bardeen–Cooper–Schrieffer superconductivity as proposed in Ref. [100, 115], where our atomic susceptibility measurements would directly map to the pairing gap. More broadly, Equation (5.5) allows the direct simulation of Richardson–Gaudin models that are relevant to a variety of many-body systems, from superconductivity in ultrasmall grains to quark physics and neutron stars. Furthermore, the capabilities demonstrated in our experiment could also be used to study the effect of inhomogeneous broadening for quantum optics applications, in particular for superradiant laser clocks [101]. The combination of disorder with cavity-mediated interactions could be used to study glassy phases of matter [116, 117]

Although the finite lifetime of the excited state employed limits current investigations to one excitation above the fully polarized state, higher excitations can be probed by encoding the spins in the ground-state manifold and coupling them via Raman transitions [47] or through the use of atoms with long-lived excited states [109].

Finally, using high-resolution optics of our cavity-microscope and time-resolved manipulation of the control light, as discussed in the previous chapter, it becomes possible to program the otherwise homogeneous long-range cavity-mediated interaction in space and time, lifting one of the most stringent restrictions for the use of cavities in quantum simulation applications. In combination with small ultra-cold samples of our fermionic ^{6}Li atoms, this allows the creation of random long-range interactions between fermionic degrees of freedom, one of the building blocks for holographic quantum matter, as discussed in the next chapter.

Chapter 6

Towards Experimental Realization of the SYK Model

Outline of the current chapter

6.1 Definition of SYK Model **102**
6.1.1 Variable-Rank SYK Model Decomposition 102
6.2 Experimental Scheme **103**
6.2.1 Experimental Implementation of High-Rank Interactions 105
6.3 Tunable Motion-Changing Interactions between Fermions in a Cavity Microscope **106**
6.4 Rank-Scaling in 1D Model **109**
6.4.1 Analytic Structure of Atom-Cavity Coupling 109
6.4.2 Decomposition of Interaction in Elementary Components 110
6.4.3 Numerical Analysis of Rank-Scaling 111
6.5 Simulation of Hamiltonian Dynamics of Random Interactions in Multi-Mode Cavity **113**
6.5.1 Randomness of Two-Body Interactions 113
6.5.2 Comparison to SYK Model Dynamics 114
6.6 Experimental Requirements and Challenges **118**
6.6.1 Matching of the Disorder, Cavity-Mode and Trap Length Scales . . 118
6.6.2 Implementation of Random Interaction using Speckle Pattern . . . 118
6.7 Discussion **119**

Finally, in this chapter, we bring together the concepts studied in previous chapters to demonstrate the possibility of a quantum simulation of the SYK model. We show that the combination of cavity-mediated interactions (as discussed in Chapter 5) and precisely adjustable atom-cavity couplings (as discussed in Chapter 4) leads to dynamics in our fermion-cavity system, which closely resemble those of the SYK model. Our aim is to identify an experimentally feasible parameter range in which fast scrambling can be observed.

The chapter is organized as follows: In Section 6.1, we introduce the SYK model and provide a theoretically and experimentally interesting redefinition in terms of variable-rank interactions in Section 6.1.1. This allows us to set criteria for the scaling of the rank to observe the SYK dynamics. Section 6.2 outlines the experimental configurations in which our cavity microscope can implement tunable variable-rank interactions between fermions. Two numerical studies are then conducted to demonstrate the effectiveness of the experimental configuration in mimicking the dynamics of the SYK model. The first study in Section 6.4 shows that extensive rank scaling can be observed in a 1D system. The second study in Section 6.5 simulates the full dynamics of a 2D model closely resembling our cavity QED system. This leads to a set of important experimental criteria, the feasibility of which is discussed in Section 6.6.

6.1 Definition of SYK Model

The SYK model[*] can be defined through the Hamiltonian

$$\hat{H}_{\text{SYK}} = \sum_{ijkl}^{N} \mathcal{J}_{ij,kl}\; \hat{c}_i^\dagger \hat{c}_j\, \hat{c}_k^\dagger \hat{c}_l,$$

which describes arbitrary four-point interactions between N fermionic modes which index i described by their creation and annihilation operators, $\hat{c}_i^\dagger$ and $\hat{c}_i$. The SYK model preserves the number of fermions, allowing its dynamics to be divided into sectors with different filling fractions. Mathematically, each real-valued[†] scattering amplitude $\mathcal{J}_{ij,kl}$ is randomly drawn from a Gaussian distribution with a standard deviation of J. Because of this high degree of randomness, all cross-correlators between couplings of different four-point interactions vanish. It is important to note that even though the scattering amplitudes are randomly chosen, for a particular realization of the SYK model, the coefficients themselves are constant in time. From an experimental point of view, the random character of the amplitudes implies a large degree of control over the interaction amplitudes. In fact, one can think of the SYK model as a special case for systems with arbitrarily tunable four-point interactions.

6.1.1 Variable-Rank SYK Model Decomposition

As mentioned above, the SYK model describes a system with arbitrary four-point interactions that are defined by the scattering amplitude tensor $\mathcal{J}_{ij,kl}$. In a cavity QED system, the structure of the interactions suggests a convenient decomposition of the four-point interaction in terms of the contraction of a set of two-index tensors $u_{ij}^{(m)}$. In terms of equations, this composition can be written as

$$\mathcal{J}_{ij,kl} = 1/2 \sum_{m=1}^{R} \lambda_m u_{ij}^{(m)} u_{kl}^{*\,(m)}.$$

Here, the index m refers to different channels through which the fermions can interact. More details about the experimental implementation of this structure can be found in Section 6.2.1. The rank of the tensor $\mathcal{J}$ is defined as the number of linearly independent $u^{(m)}$ that is required to decompose the tensor. In the previous equation, this was denoted by the limit of the sum R.

---

[*] Historically, the definition of the SYK model relies on Majorana fermions. Here, we use the definition proposed in Section VII of Ref. [118]. This choice is motivated by the structure of cavity-mediated interactions present in our system.

[†] The usual definition of the SYK model uses complex amplitudes. Here, we focus on real amplitudes motivated by the experiment.

This is analogous to the decomposition of a 2×2 matrix into the contraction of a set of linearly independent vectors.

In terms of Feynman diagrams, this decomposition can be written as

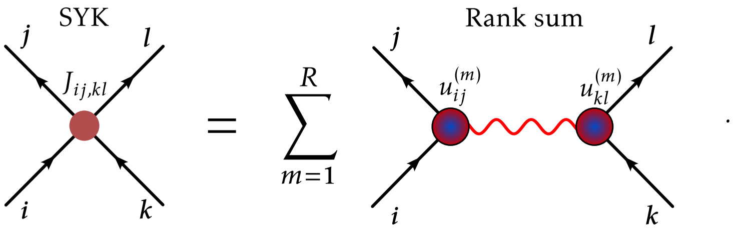

(6.1)

The Feynman diagram already suggests the physical implementation of the four-point interaction in our system. The four-point interaction can be decomposed into two consecutive motional-state changing atom-cavity interactions. The first term changes the motional state of one atom by emitting a photon in the cavity. This photon can induce a transition between different motion states in another atom, effectively leading to two correlated motion-changing interactions, a force. Here, the photon field acts as a bosonic mediator of this force. This makes the mechanism similar to the mechanism of Coulomb scattering between charged particles. In Section 6.3, the structure of motion-changing interactions present in our cavity QED system is discussed, which results in a microscopic model for the scattering amplitudes $u_{ij}^{(m)}$. A particular focus is placed on the tunability of these interactions, which is key to implementing the SYK model.

The complete SYK model has a rank of N^2, which scales with the square of the size of the system and is therefore called superextensive. However, models with reduced rank, known as low-rank SYK models, have been studied before [118]. Models with extensive rank scaling, meaning $R \propto N$, are particularly interesting, as the physics of the resulting model closely resembles that of the full-rank SYK model. However, the complexity of the models is significantly reduced compared to the full-rank SYK model.

6.2 Experimental Scheme

The experimental configuration required for the quantum simulation of the SYK model resembles that presented in Chapter 4, where the local tunability of the atom-cavity couplings was used to measure the properties of the atomic cloud with high spatial resolution. However, there are fine differences that allow us to obtain tunable momentum-changing cavity-meditated interactions, which are the topic of this section.

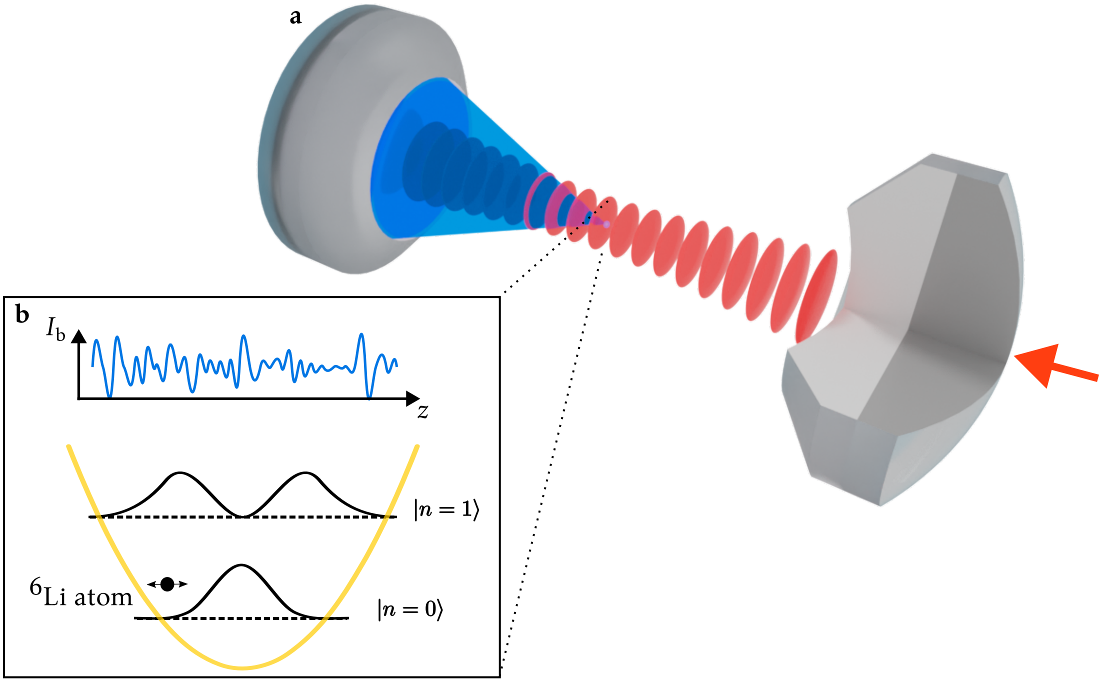

Figure 6.1: **Experimental Configuration for Quantum Simulation of SYK Model.a**, Rendering of cavity-microscope with cavity mode (red) and focused control beam (blue). The cavity is driven with a laser beam (red arrow). **b**, Illustration of atoms (black wavefunctions) in harmonic trap (yellow parabola). The graph on the top shows the locally varying intensity of the control beam $I_b(z)$.

In general, there are four important ingredients: Fermionic atoms, all-to-all couplings, local tunability, and high rank. In the following, we go step by step through these criteria and develop from this the experimental configuration.

Fermionic Atoms In our experiment, we trap a cloud of ^{6}Li atoms in a high-finesse cavity. To unlock the fermionic character of these atoms, they need to be trapped in a single trap such that their wave functions overlap spatially. This is contrary to our current configuration, where the atoms are confined in a lattice of pancake traps (see Section 2.2). This is illustrated by the inset in Figure 6.1.

Cavity-Mediated All-to-All Interactions All-to-all interactions naturally emerge from photon exchange between atoms in Cavity QED systems. For example, in Section 5.5.3, we experimentally studied the structure of cavity-mediated flip-flop interactions in the regime of large atom-cavity detunings. These interactions act on the spin degree-of-freedom. To promote the interaction to a motional degree of freedom, we need to operate in the dispersive regime, where the atoms remain in their ground state. The important parameter that describes the atom-cavity coupling is the single-atom dispersive shift $\delta\omega_c(\vec{x})$ (see Section 3.3). It describes the frequency shift of the cavity as a result of the presence of an atom in the location $\vec{x}$. The interaction requires a probe beam that introduces photons into the system. In Figure 6.1, this is illustrated by an on-axis probe beam (red arrow).

Tunability of Local Single-Atom Dispersive Shift We have shown two distinct ways to adjust the atom-cavity coupling locally: light shifts (see Section 5.4) and Floquet driving (see Section 4.2). The single atom dispersive shift $\delta\omega_c(\vec{x}) = g^2(\vec{x})/\Delta_{\mathrm{ac}}(\vec{x})$ can be modified by both of these techniques. By light-shifting the excited state $|e\rangle$, the atom-cavity detuning $\Delta_{\mathrm{ac}}(\vec{x})$ can be altered, while Floquet driving affects the spatial shape of the single-atom Rabi frequency $g(\vec{x})$ by dispersively coupling to a Floquet sideband. Schemes that allow for a local change in the single-atom dispersive shift are depicted in Figure 6.2.

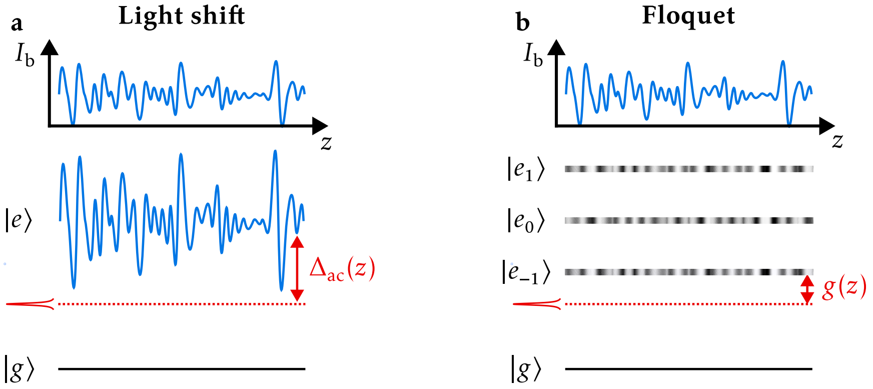

Figure 6.2: **Tunability of Single-Atom Dispersive Shift.** **a**, Light shift approach acting on $\Delta_{\mathrm{ac}}(z)$. Locally-varying intensity patterns of the blue control beam $I_{\mathrm{b}}(z)$, lead to local variations of the atomic transition frequency, which directly affects the atom-cavity Δ_{ac}. **b**, Floquet approach acting on $g(z)$. Locally-varying intensity patterns of the blue control beam $I_{\mathrm{b}}(z)$, lead to local variations in the strength of the Floquet modulation sidebands, which directly affect the atom-cavity $g(z)$.

6.2.1 Experimental Implementation of High-Rank Interactions

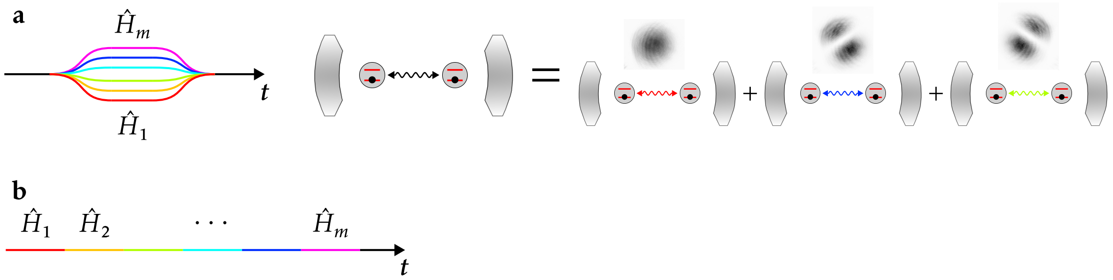

Figure 6.3: **Multiplexing of Rank-1 Interactions.** **a**, Schematic of multimode cavity approach. The total dynamics is the parallel evolution of many Hamiltonians indicated by the different colors. This is realized with different transverse cavity modes (see picture above cavity). **b**, Schematic of Trotter approach. The total dynamics is a sequence of many Hamiltonian evolution is time.

As discussed in Section 6.1.1, a quantum simulation of the SYK model requires high-rank four-point interactions. This requires many bosnic channels through which the atoms can interact. In our system, we envision two ways: Multimode cavity and Trotterization.

Multimode Cavity The first option is to implement this multiplexing using the multimode character of the optical resonator (see Figure 6.3**a**). With the use of multiple independent cavity modes through which the atoms can exchange photons, the variable-rank interaction becomes a sum over different transverse cavity modes. In this case, the index m describes the set of different transverse modes of the cavity.

Trotterization Another option is to multiplex the interaction over time, effectively generating a high-rank interaction using a Trotter scheme. In this configuration, the high-rank Hamiltonian is implemented by decomposing the time evolution in discrete steps with different rank-one Hamiltonians $\hat{H}^{(m)}$ (see Figure 6.3**b**). This approach requires only a single-mode cavity but relies on fast switching between different rank-one Hamiltonians to increase the complexity of the interaction. Note that here the index m does not correspond to the cavity mode index but rather to the configuration of the interaction in the m^{th} step. The rank of the interaction is controlled by the number of linearly independent Trotter steps.

6.3 Tunable Motion-Changing Interactions between Fermions in a Cavity Microscope

The rank decomposition in Section 6.1.1 suggests that a general four-point interaction can be divided into a sum of rank-one interactions, each consisting of two successive atom-cavity interactions that modify the motional state of the atoms. This section will concentrate on deriving the form of the rank-one interactions that naturally emerge in our cavity QED system. The rank of the resulting interactions can be increased with the techniques presented in Section 6.2.1.

As mentioned in Section 6.2, to implement motion-changing atom-cavity interactions on ground-state atoms, we need to operate in the dispersive regime of large atom-cavity detuning. In this regime, the mechanism underlying the atom-cavity interaction is the modification of the dispersive shift of the optical resonator due to the motion of the atoms. In Section 3.3, we show that the dispersive shift of the cavity can be used to collect information on the spatial distribution of the atom cloud. However, if interpreted from the atom direction, the dispersive shift Hamiltonian describes a cavity-field-dependent dipole force acting on the atoms. The combination of measurement of the spatial distribution of the cloud and cavity field-dependent dipole force is what leads to the elementary four-point interactions.

To implement cavity-mediated interactions between atoms, we must find a way to link the measurement of the atom's position with the strength of the dipole force. We can interpret the Hamiltonian that describes the dispersive shift (see Equation (3.4)) as the dipole force acting on the atoms that is directly proportional to the number of intracavity photons $\hat{a}^\dagger \hat{a}$. By using an on-axis drive that is detuned from the cavity resonance, a change in the cavity resonance frequency, caused by the redistribution of the atoms, is translated into a change in the intracavity photon number, which in turn alters the force acting on the atoms. This concept of a feedback mechanism is the basis of cavity optomechanics [40] and allows us to generate interactions between atoms at any distance.

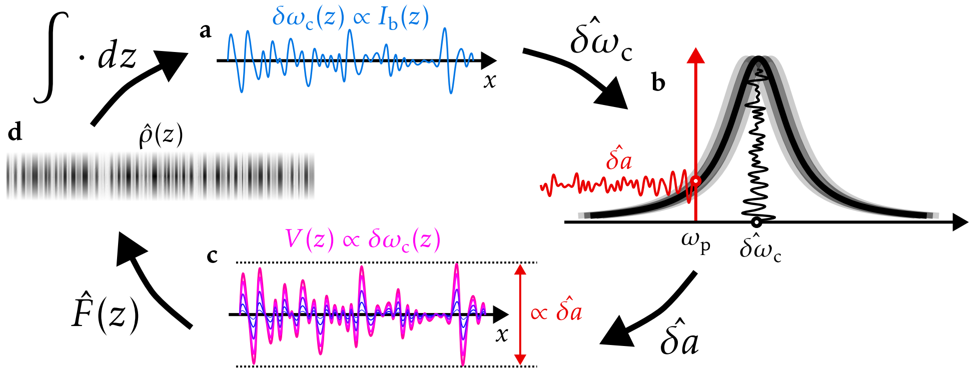

Figure 6.4: **Feedback Mechanism of Cavity-Mediated Interactions.** **a**, Illustration of locally varying dispersive shift. Using the mechanisms discussed in Section 6.2, the control beam is used to imprint a spatially varying local dispersive shift. **b**, Illustration of the transduction process induced by the cavity probe. Changes in the resonance frequency of the cavity, which are due to variations in the atomic density, are transduced into fluctuations of the intracavity photon field. **c**, Illustration of the cavity-field-dependent dipole potential. The fluctuations in the intra-cavity photon field result in variations of the dipole potential acting of the atoms. These affect the motion of the atoms and therefore the atomic density distribution. **d**, Illustration of one-dimensional density variations in the atomic cloud.

The feedback mechanism is illustrated in Figure 6.4. The total dispersive shift of the cavity is related to the density distribution of the atomic cloud by an integral (see Equation (3.4)). Instead of being a homogeneous integral, the local dispersive shift $\delta\omega_c(z)$ is modified by the intensity of the focusing beam $I_b(z)$, which can be modified by the pattern projected through the cavity lens (see Section 6.2). The convolution of the local dispersive shift and the cloud density results in the total dispersive shift. A cavity probe detuned from the cavity resonance directly transduces dispersive shift fluctuations into cavity field fluctuations. These fluctuations induce variations in the dipole force experienced by the atoms. This effect is visible in the dispersive shift Hamiltonian if interpreted as the intracavity field-dependent dipole force. This dipole force $\hat{F}(z)$, on the other hand, modifies the spatial distribution of the atomic density, which finally closes the feedback loop.

In the following, we will put these arguments into equations. The effect of the drive on the axis can be modeled in a mean-field decomposition. The total cavity field is decomposed into the sum of a constant classical cavity field characterized by its amplitude α and a small fluctuating cavity field $\hat{\delta a}$. This can be illustrated in terms of Feynman diagrams as

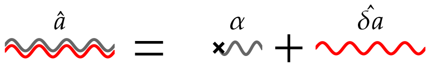

.

Inserting this decomposition into the Feynman diagram describing the dispersive shift Hamiltonian results in

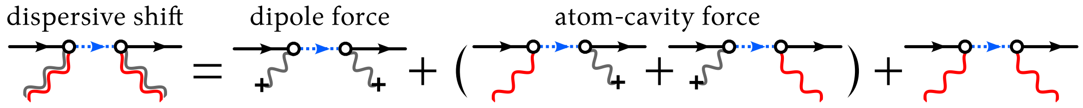

.

In this case, the atom-cavity interaction can be split in three components. The first term describes an effective atomic potential that is proportional to the absolute value of the classical cavity field. This can be understood as a classical dipole force acting on the atoms, which modifies the trapping potential. The second term leads to a linear coupling between the atomic motion and the fluctuations in the cavity field $\hat{\delta a}$. This coupling term is proportional to the strength of the classical drive and can therefore be tuned by changing the power of the drive laser. For high drive strength, the third term, which describes the nonlinear dynamics, can be neglected. In principle, the first term can be compensated for by the trapping potential. However, this requires exquisite control over the trapping field. In the supplementary information of our proposal [119], we describe a method based on a two-tone drive that potentially eliminates these dipole potentials.

It is the linear atom-cavity coupling that is observed when the cavity is driven by a classical field that gives rise to motional state-changing atom-cavity interactions. The Hamiltonian that describes these interactions can be written as

$$\hat{H}_{\text{int}} = \alpha \hat{\delta a}^{\dagger} \int \delta\omega_{\text{c}}(\vec{x})\ \hat{\rho}(\vec{x})\ dV + \text{H.c.} = \alpha\ \hat{\delta a}^{\dagger}\ \hat{\delta\omega}_{c} + \text{H.c.}$$

In words, it describes the linear change of the intra-cavity photon field $\delta\hat{a}$ as function of the local density of the atomic cloud. Here, $\delta\omega_{\text{c}}(\vec{x}) = g^2(\vec{x})/\Delta_{\text{ap}}(\vec{x})$ describes the dispersive shift of the cavity resonance due to the presence of a single atom at the location $\vec{x}$. The tunability of this Hamiltonian arises from a local control of the local dispersive shift (see Section 6.2).

The last step of the derivation is to include the cavity transduction process. In other words, we adiabatically eliminate the cavity field, as it directly follows the variations of the dispersive shift, $\hat{\delta a} = \alpha\hat{\delta\omega}_{\text{c}}/\Delta_{\text{pc}}$. This results in the final Hamiltonian

$$\hat{H} = 2\frac{|\alpha|^2}{\Delta_{\text{pc}}}\hat{\delta\omega}_{\text{c}}\hat{\delta\omega}_{\text{c}} = \frac{1}{2}\lambda\hat{\delta\omega}_{\text{c}}\hat{\delta\omega}_{\text{c}}. \tag{6.2}$$

The complex conjugate was dropped on $\hat{\delta\omega}_{\text{c}}$ as the dispersive shift is a hermitian operator. The scattering matrix u_{ij} arises from the dispersive shift operator $\hat{\delta\omega}_{\text{c}}$ once we choose a basis for the degree of freedom of motion. The factor $\lambda = 4|\alpha|^2/\Delta_{\text{pc}}$ in Equation (6.1) can be defined directly from Equation (6.2).

In the field of cavity optomechanics, the Hamiltonian in Equation (6.2) produces the well-known optomechanical spring effect, which is a change in mechanical resonance frequency due to the feedback mechanism imposed by coupling to the cavity field. This is evident when the optomechanical coupling is identified as $\delta\omega_{\text{c}} = G\hat{x}$. If the cavity is linearly connected to multiple mechanical oscillators $\delta\omega_{\text{c}} = G\sum_i \hat{x}_i$, the Hamiltonian describes a shift in the resonance frequency of the center-of-mass motion $\hat{X} = \sum_i \hat{x}_i$, which can be interpreted as a homogeneous all-to-all coupling of mechanical oscillators. This is analogous to the coupling of the collective spin state to the cavity in the Lipkin–Meshkov–Glick model (see Chapter 5). In the described scheme, the linear coupling property is lifted when the blue laser is used to generate density-density interactions with an arbitrary spatial distribution. Although this structure appears to be complex, Equation (6.2) can be interpreted as an effective optomechanical spring effect Hamiltonian. This is due to the integrability of rank-one interactions. As soon as the rank increases, the Hamiltonian is no longer separable and chaotic behavior emerges, a key feature of the SYK model. However, only if the rank is sufficiently high, ‘fast scrambling can be observed. This implies that the system displays the strongest chaotic behavior allowed by quantum mechanics.

6.4 Rank-Scaling in 1D Model

The interactions that arise naturally in a cavity QED system have a rank of one. As discussed in Section 6.1.1, a quantum simulation of the SYK model requires scaling the rank of interactions with the system size. Section 6.2.1 examines experimental methods for multiplexing interactions in our system. In this section, we discuss whether the experimental scheme of locally tuning the atom-cavity coupling can create enough linearly independent interaction channels. To this end, we derive the explicit form of the interaction matrices $u_{ij}^{(m)}$ for a 1D model and perform a numerical analysis on them. This helps us identify important experimental parameters, such as the gain size of the intensity pattern of the focusing beam, the trap size, and the cavity mode size, which can be used to define optimal conditions to simulate the SYK model.

6.4.1 Analytic Structure of Atom-Cavity Coupling

To obtain an explicit form of the atom-cavity coupling matrix, we decompose the motional degree of freedom of the atoms into the harmonic oscillator basis, meaning $\hat{\Psi}(z) = \sum_i \hat{c}_i \phi_i(z)$, where $\phi_i(z)$ are the Hermite–Gauss functions of order i. The decomposition is motivated by the harmonic trap shown in Figure 6.1. The shape of the trap dictates the size of the ground-state wave function.

The resulting atom-cavity coupling matrix is

$$u_{ij}^{(m)} = \left(\hat{\delta\omega}_{\mathrm{c}}\right)_{ij} = \int \delta\omega_{\mathrm{c}}^{(m)}(z)\ \phi_i(z)\ \phi_j(z)\ dx, \tag{6.3}$$

which describes the overlap integral between two motional states and the variable local single-atom dispersive shift[*].

To illustrate the structure of $u_{ij}^{(m)}$ we consider some analytic examples:

- If $\delta\omega_{\mathrm{c}}^{(m)}(z)$ is constant, the matrix reduces to $u_{ij}^{(m)} \propto \delta_{i,j}$, where $\delta_{i,j}$ is the Kronecker-Delta. The resulting interaction couples directly to the total number of atoms, regardless of their spatial distribution. This is similar to Section 3.3.2, where we found that homogeneous atom-cavity couplings lead to a dispersive shift that is directly proportional to the number of atoms.

- In the case of $\delta\omega_{\mathrm{c}}^{(m)}(z) \propto x$, which is linear in space, $u_{ij}^{(m)} \propto \delta_{i,j+1}$ describes jumps up and down the harmonic ladder, similar to the couplings obtained in a cavity cooling system in the Lamb-Dicke regime [120].

- In the case of $\delta\omega_{\mathrm{c}}^{(m)}(z) \propto H_m(z)$, where $H_m(z)$ is the order m Hermite polynomial, an explicit form of the interaction can be derived analytically, as

  $$u_{i,i+\delta}^{m} \propto \int H_m\ \phi_i(z)\ \phi_{i+\delta}(z)\ dx = \sum_{s=0}^{i} A_{i,s,\delta}\ \delta_{m,2s+\Delta}.$$

  To derive the exact expression for $A_{i,s,\delta}$, the multiplication relation of the Hermite polynomials can be used. In this general form, the formula demonstrates that a Hermite polynomial of order m allows the order of the harmonic ladder state to increase by a step of m. As a result, all interactions $u^{m}_{i,i+\delta}$ are linearly independent of each other, which is an important criterion for the SYK model (see Section 6.1.1).

---

[*] The complex conjugate on ϕ_i was dropped as it is a real function.

6.4.2 Decomposition of Interaction in Elementary Components

The analytical examples suggest that, by choosing the right shape of the local dispersive shift, linearly independent interactions can be achieved. To further quantify the scaling of the rank, we perform a numerical analysis. This section describes the numerical methods and presents the final results, which suggest the possibility of extensive rank scaling in a 1D system.

The coupling matrix $u^{(m)}_{ij}$ is crucially dependent on the distribution of the local dispersive shift $\delta\omega^{(m)}_{\mathrm{c}}(z)$. In general, the local dispersive shift can be decomposed into basis functions. Motivated by the structure of transverse cavity modes, we choose the bases of Hermite–Gauss functions $\phi_k(\zeta x)$ which results in the decomposition

$$\delta\omega^{(m)}_{\mathrm{c}}(z) = \sum_{k=0}^{N_k-1} X^{(m)}_k \, \phi_k(\zeta x) \, ,$$

where $X^{(m)}_k$ are the amplitudes of the decomposition. Here, we introduce the parameter ζ, which measures the mismatch of the relative length scale between the motional eigenstates and the basis of the disorder. This parameter allows us to investigate the importance of relative length scales of the disorder and fermion modes. Note that the decomposition contains only N_k basis elements. This truncation allows us to evaluate the scaling of the rank with the size of the basis decomposition. In the experiment, this measures either the number of transverse cavity modes or the number of Trotter steps required to achieve the necessary rank (see Section 6.2.1). Due to the linearity of the integral in Equation (6.3), this decomposition translates into the coupling matrix as

$$u^{(m)}_{ij}(z) = \sum_{k=0}^{N_k-1} X^{(m)}_k \, \tilde{u}^{(k)}_{ij}(z) \, .$$

In this section, we numerically analyze the structure of these elementary interaction matrices $\tilde{u}^{(k)}_{ij}(z)$. We restrict our numerical analysis presented in this chapter to a total of $N = 17$ fermionic modes. The basis interaction matrices $\tilde{u}^{(k)}_{ij}(z)$ are plotted in Figure 6.5.

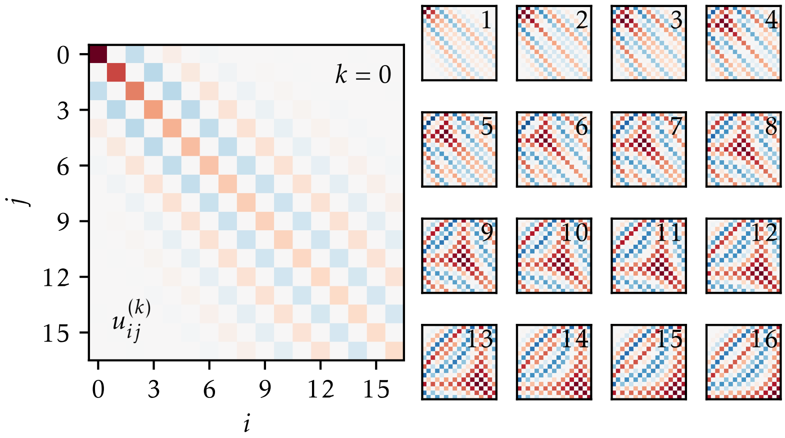

Figure 6.5: **Shape of Interaction.** Shape of elementary coupling matrix $\tilde{u}_{ij}^{(k)}(z)$ as a function of order k of the local dispersive shifts for $\zeta = 1$. In the color code, red corresponds to positive coefficients and blue to negative coefficients.

It is clearly visible that the $\tilde{u}_{ij}^{(k)}(z)$ are linearly independent for different orders k as the coefficients spread more and more into the off-diagonal sector, effectively allowing for larger jumps in the harmonic ladder of motion states. The $\tilde{u}_{ij}^{(k)}(z)$ display a checkerboard pattern, which is due to the symmetry of the Hermite-Gauss function. More precisely, any coefficient that satisfies $k + i + j = \text{odd}$ is zero.

6.4.3 Numerical Analysis of Rank-Scaling

As stated in Section 6.1.1, we would like to realize in our experiment the regime in which R scales extensively with N. To evaluate the scaling of the rank with the system size numerically, we define a quantity that we refer to as the effective rank $\tilde{R}$ of the set of $\{u_{ij}^{(k)}$ for $k = 0...(N_k - 1)\}$, where N_k is the number of basis interactions. The effective rank is defined as the participation ratio of the normalized singular values s_k of the matrix $A_{\alpha k} = u_{\alpha}^{(k)}$, where $\alpha = (ij)$ is the super index that flattens the coupling matrix. In particular,

$$\tilde{R} = \frac{1}{\sum_k s_k^4} \, .$$

with $1 = \sum_k s_k^2$. This definition is different from the mathematical definition of the rank, which counts the number of nonzero singular values. Motivated by the participation ratio of spin excitations (see Section 5.5.3), the effective rank measures the number of independent interaction channels with similar strength. For example, if one interaction component dominates the others in magnitude, the effective rank will tend to one even though mathematically the rank of the matrix could be full.

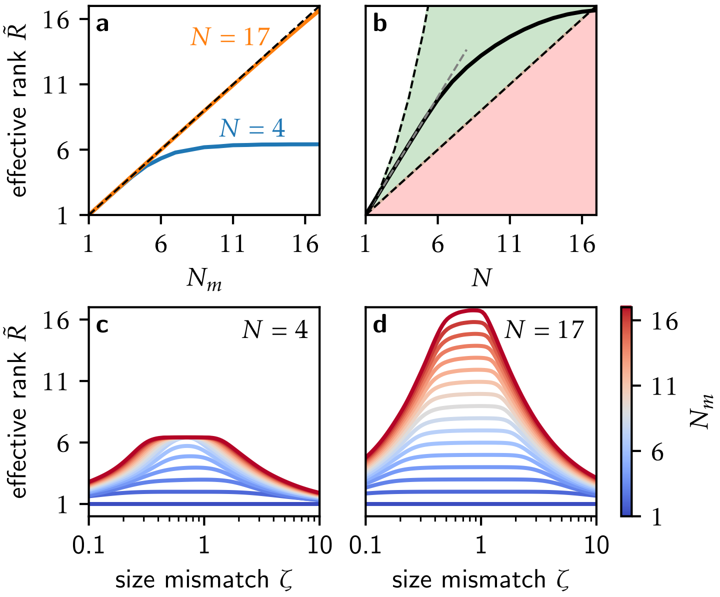

Figure 6.6: **Scaling of Effective Rank.** **a**, Scaling of effective rank with the size of disorder basis N_k for two different system sizes, $N = 4$ and $N = 17$. **b**, Scaling of effective rank with system size for a fixed number of configurations $N_m = 17$. The red area marks the region where the rank is smaller than the system size. The green area is between the maximal theoretical rank $N(N+1)/2$ and the system size N. **c,d**, Plot of effective rank as a function of the size mismatch between the focusing beam pattern and the motional states for two different system sizes, $N = 4$ (**c**) and $N = 17$ (**d**).

In Figure 6.6, the effective rank $\tilde{R}$ is plotted against important system parameters. In particular, in Figure 6.6**a**, the effective rank is plotted against the size of the disorder basis decomposition N_k for two different system sizes, $N = 4$ and $N = 17$. For $N = 17$, the effective rank closely follows the theoretical maximum of N_k. However, for high N_k, a small deviation can be seen, which is the start of a saturation of the rank. This saturation is more obvious for a smaller system size of $N = 4$ fermionic modes, where a maximum effective rank of $\tilde{R} = 7$ is observed.

In Figure 6.6**b**, the highest achievable effective rank (for $N_k = 17$ basis interactions) is plotted against the size of the system. It is important to note that all $\tilde{u}_{ij}^{(k)}$ are hermitian and real, a property inherited from the dispersive shift operator $\hat{\delta\omega}_c$. This symmetry limits the maximal possible rank to the size of the Hilbert space of symmetric matrices, which is $N(N+1)/2$. For small N, extensive scaling with a slope of $\gamma = 1.8$ is seen (see the dashed gray line). This scaling saturates for large systems, which is due to the limit on the total number of basis interactions to $N_k = 17$.

In Figure 6.6**c,d**, the effective rank is plotted against the size mismatch between the length scale of the local dispersive shift decomposition and the motion states ζ. Resonant behavior is observed, indicating that extensive scaling can only be achieved if both length scales are of similar size $\zeta \approx 1$. For the smaller system size of $N = 4$, a rank saturation of $\tilde{R} = 7$ is visible. For $N = 17$, this saturation is not yet apparent, since the number of basis vectors N_k was limited to 17 in our numerical analysis.

This analysis demonstrates that an extensive scaling of the rank with system size N is achievable in our system*. This suggests that SYK-like physics, such as fast scrambling, can be observed[118]. The resonant behavior observed in rank scaling as a function of size mismatch ζ places restrictions on the experimental setup. Specifically, it implies that the grain size of the disorder pattern must be equal to the size of the motional state. Further information on the experimental requirements is provided in Section 6.6.

6.5 Simulation of Hamiltonian Dynamics of Random Interactions in Multi-Mode Cavity

The analysis presented in the last section was based on the rank of the random four-point interactions present in our system. In this section, we go one step further and demonstrate numerically that the resulting dynamics of the system approaches that of the SYK model. The results are based on a proposal that we have written in collaboration with the Hauke group in Trento and Julian Sonner in Geneva [119].

The experimental configuration studied in the publication differs from the discussion in the previous chapters, since an off-axis drive is used to generate the scattering of photons between the atoms. In the supplemental information of the publication and the thesis of Philipp Uhrich[2], it is shown that both scenarios lead to the same effective Hamiltonian. The proposal is based on a multimode cavity approach to increase the rank of interactions (see Section 6.1.1). The important parameter is N_m, which measures the number of effective cavity modes. The random tuning of the interactions is achieved by randomly varying light shifts resulting from intensity speckle patterns of the focusing beam. This approach is experimentally easier to achieve than the decomposition of disorder in Hermite-Gauss modes, as proposed in the previous section. In fact, in Section 6.6 where the current experimental advances are discussed, we show a picture of a speckle pattern that was already projected onto the atoms in our experiment. Furthermore, the numerical calculations in this section have been performed in two dimensions. This is in contrast to the rank analysis in Section 6.4, which was performed in 1D. However, similar results in terms of experimental requirements are obtained.

The publication presents a derivation of a microscopic model for the four-point interactions present in our system. The derivation includes the multimode character of the cavity and is therefore more adapted to the proposed experimental scenario than the derivation presented in Section 6.3.

6.5.1 Randomness of Two-Body Interactions

Before studying the dynamics of the effective Hamiltonian we take a look at the structure of the random four-point interaction amplitudes $\mathcal{J}_{ij,kl}$ by numerically calculating the interactions $\mathcal{J}_{ij,kl}$ from first principles. Figure 6.7 shows the distribution for a single representative realization of the system. The distribution deviates from a Gaussian probability density and is better approximated by a Cauchy distribution. Interestingly, this feature is not unique to the setup considered here. In the proposal, we have found that some previous proposals [122, 123], which also

---

*At this point, it is important to note that the effective rank of the ensemble of interaction matrices $\{u_{ij}^{(k)}$ for $k = 0...(N_k - 1)\}$ not only tells us the maximal achievable rank of the four-point interaction tensor, but also limits the number of random degrees of freedom for each rank-one interaction. This becomes more concrete when we define the interaction matrices in the Trotter m step as $u_{ij}^{(m)} = \sum_k X_k \tilde{u}_{ij}^{(k)}$, where $\{X_k$ for $k = 0...(N_k - 1)\}$ is a set of random variables with uniform standard deviations. In this case, a high rank is related to a low number of correlations in the interaction matrix $\tilde{u}_{ij}^{(m)}$ and therefore points to a high controllability of the interaction Hamiltonian.

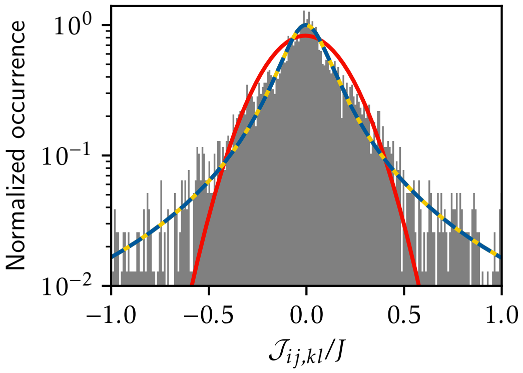

Figure 6.7: **Distribution of Two-Body Interaction Amplitudes** Representative distribution of $\mathcal{J}_{ij,kl}$, for $N = 14$ fermionic modes, $N_m = 10$ effective cavity modes, and $\zeta = 1$. Fitting the distribution by a (pseudo)Voigt profile [121] (blue dashed line), which interpolates between a Gaussian (red line) and a Cauchy probability density (yellow line), quantifies the deviation from Gaussian statistics.

numerically calculate interactions according to the microscopic description of their respective model, have also obtained non-Gaussian distributions. A possible reason for the failure of the central limit theorem may be the presence of correlations within each realization of the disorder, which could arise, for instance, between distinct interaction amplitudes that have one or more fermion modes in common and thus sample the spatial disorder in a similar way. The important question then arises of how far the deviating probability distribution modifies the physics of the SYK model, a question that is actively investigated for other probability distributions [124–127]. In supplementary information of our proposal, we compare the dynamics of an SYK model with Cauchy-distributed interactions to its Gaussian counterpart, finding that they are qualitatively the same.

6.5.2 Comparison to SYK Model Dynamics

In this section, we numerically probe the chaoticity of the dynamics present in our system and compare them to the dynamics of the SYK model [125, 128]. To this end, we simulate out-of-time-order correlators (OTOCs) and the spectral form factor (SFF) as probes of, respectively, early-time and late-time chaos [129–133]. We employ exact diagonalization methods, the limitation of which to small system sizes prevents one from accessing the maximal scrambling rate of the SYK model [134]. Thus, our goal is to use the dynamics of the SYK model for a given system size N as a benchmark against which we can compare the dynamics of our proposed system. This allows us to see how the experimental parameters can be tuned so that its dynamics approach those of the SYK model.

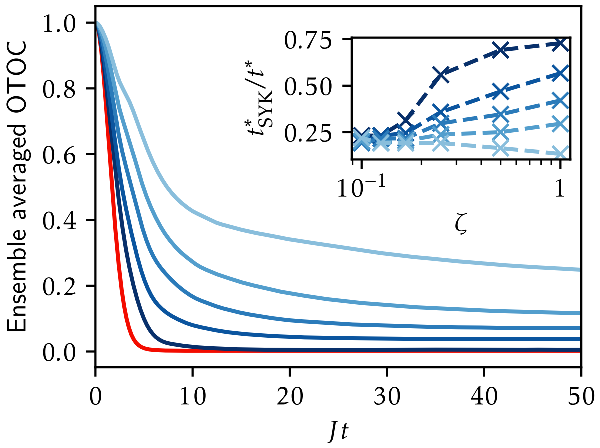

Figure 6.8: **OTOCs of Effective and Target model.** Dynamics of ensemble averaged out-of-time-order correlator for the proposed model (blue curves) for $\zeta = 1$, compared to those of the SYK model with real coefficients (red curve). Data are for $N = 10$ fermionic modes at half filling, and represent ensemble averages over 250(1000) disorder realizations of the proposed model (the SYK model). The shades of blue, from light to dark, correspond to $N_m = 3, 11, 21, 37, 107$. The inset shows the inverse times $1/t^*$, relative to that of the target model $1/t^*_{\mathrm{SYK}}$, at which the correlator has decayed to $1/e$, for each value of N_m (same shades of blue as the main figure), as a function of the transverse size ζ of the atomic cloud.

Out-of-Time-Order Correlators (OTOCs) Figure 6.8 shows the real part of the OTOC $F(t) = \mathrm{tr}\big(\rho_\beta W^\dagger(t) V^\dagger W(t) V\big)$, calculated with respect to the infinite temperature state $\rho_{\beta=0} \propto 1$, for an atomic cloud size matched to the cavity mode size $\zeta = 1$. In this example, we choose the unitary operators $W = 2c_i^\dagger c_i - 1$, $V = 2c_j^\dagger c_j - 1$, with $i = 0$ and $j = 1$.

The blue curves correspond to the disorder-averaged dynamics for the effective number of independent cavity modes N_m. As N_m increases, the OTOCs decay faster and finally approach those of the SYK model (red). This speed-up is more prominent for size mismatches close to unity, as shown in the inset. This dependence is due to the shape of the cavity mode functions: As they have a length scale (the waist of the cavity w_0), all interactions mediated by different transverse cavity modes become linearly dependent for small sizes, reducing the effective number of modes that mediate interactions. As a consequence, the convergence to the SYK model is slower. This indicates that the effective model resembles the SYK model on a length scale comparable to the waist of the cavity, $\zeta = 1$.

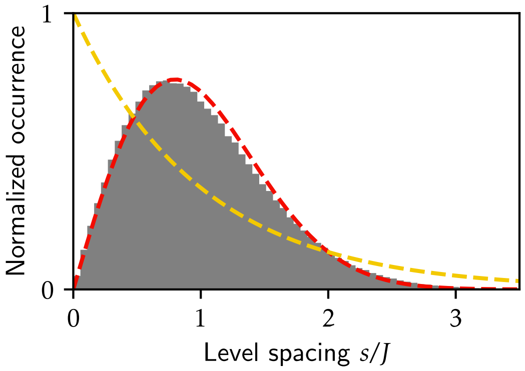

Figure 6.9: **Comparison of Level Statistics.** The level spacing distribution for $N_m = 100$, which agrees well with the Wigner surmise for the Gaussian orthogonal ensemble (red dashed line). Poisson level statistics (yellow dashed line) are shown for comparison.

Level Statistics and Spectral Form Factor (SFF) A typical diagnostic of quantum chaos is the distribution $p(s)$ of the spacings s of nearest-neighbor energy levels (see Figure 6.9), with integrable models displaying Poisson statistics (yellow dashed curve) and chaotic models following the Wigner surmise (red dashed curve, for the Gaussian Orthogonal Ensemble) [135]. In fact, the SYK model is known to follow the Wigner surmise [136], and we find that, also for our system, $p(s)$ matches the Wigner surmise very well for all the values considered in N_m. Unlike the OTOCs, there is no qualitative change in $p(s)$ as a function of the number of transverse cavity modes N_m. However, since $p(s)$ is a measure of short-range spectral correlations (nearest neighbor), it can only identify the presence of chaotic behavior at long timescales, on the order of $1/s$.

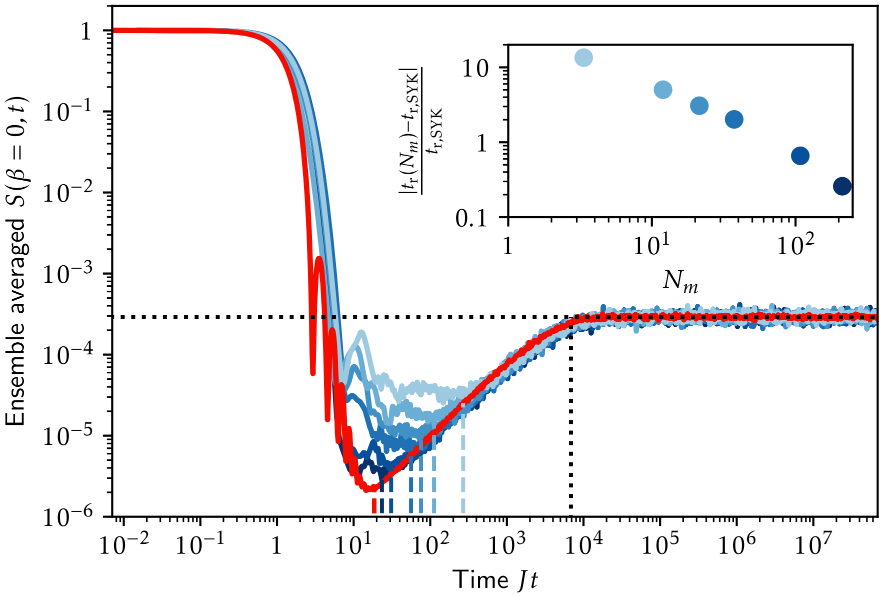

Figure 6.10: **SFF of effective and target model.** Disorder averaged SFF of effective model (blue curves) for $\zeta = 1$, compared to that of the SYK model with $J_{ij,kl} \in \mathbb{R}$ (red line). Data are for $N = 14$ fermionic modes at half-filling, and represent ensemble averages over 100(1000) disorder realizations in our proposed system(SYK model). The Heisenberg time $t_{\text{H}} = 2D$(plateau height $1/D$) is indicated by the vertical(horizontal) black dotted line, which shows a very good agreement with the SFF of H_{SYK}. For the effective model, the shades of blue from light to dark correspond to $N_m = 3, 11, 21, 37, 107, 211$. The time axes for the SFFs of the effective model have been rescaled to match the Heisenberg time of H_{SYK}. The upper inset shows the deviation of the ramp time t_{r} of the effective model compared to the real SYK model as a function of the effective number of cavity modes N_m. The ramp times are shown in the main plot by the vertical dashed lines in the same color.

In order to study the many-body chaotic properties of our effective model in more detail, we thus turn to the SFF, which is also sensitive to long-range spectral correlations and thus able to diagnose chaotic behavior already at intermediate times. Figure 6.10 shows the SFF $S(\beta, t) = \left|Z(\beta + it)/Z(\beta)\right|^2$ [where $Z(\beta + it)$ is the analytically-continued partition function] of our proposed Hamiltonian for $\zeta = 1$, compared to the SYK model, at the inverse temperature of $\beta = 0$. The SFF of the SYK model (red curve) is known to exhibit the characteristic features predicted by random matrix theory (RMT) [133, 137–141]: Early time oscillations decaying as t^{-3}, followed by a linear ramp in t, which transitions to a plateau of value $1/D$ at the Heisenberg time $2D$ (D is the Hilbert space dimension). For all values of N_m considered, the SFF of the proposed scheme (blue curves) shows signatures of the dip and ramp and, similar to the OTOCs, the depth of the dip and the temporal range of the ramp approach to that of the SYK model as N_m increases (light to dark blue).

These results highlight the importance of microscopic parameters N_m and ζ for laboratory implementations using cQED. Correctly tuning these parameters (large N_m and $\zeta = 1$) the fast scrambling dynamics (OTOC) and long-range spectral correlations (SFF) of the SYK model are well approximated by our proposed system. Finally, to obtain the results presented, we have considered the speckle correlation length to be matched to the harmonic oscillator length.

6.6 Experimental Requirements and Challenges

Our simulations highlight the key requirements to faithfully approximate the dynamics of H_{SYK}. In the following, we present a list of experimental requirements and state how these can be met using our experimental capabilities. This sets the stage for future developments of our experimental techniques.

6.6.1 Matching of the Disorder, Cavity-Mode and Trap Length Scales

In the simulations, we have shown that the length scale of the disorder patterns and the sizes of the cavity modes must be matched with the size of the motional states ($\zeta = 1$). Otherwise, the rank of the interactions does not scale linearly with the number of cavity-modes and or Trotter steps, but rather saturates.

The multimode cavity approach imposes stringent requirements on the size of the atomic cloud. The cavity installed in our experimental setup has a waist of 13.3 µm. To match this size with the ground-state wave function of ^{6}Li in a harmonic trap, we would need to operate with trap frequencies as low as 5 Hz. This is highly challenging experimentally, as it would significantly slow the preparation process of our atomic samples, which currently have a cycle time of 200 ms. This would lead to a considerable loss of statistics. Therefore, the Trotter approach appears to be more feasible experimentally. The size constraint in this case is between the spot size of the focusing beam (0.52 µm) and the ground state of the atomic motion, which would correspond to trap frequencies of roughly 3 kHz, compatible with our experimental cycle times.

6.6.2 Implementation of Random Interaction using Speckle Pattern

The results of our experimental proposal presented in Section 6.5 suggest that the implementation of random couplings based on the disordered light shift resulting from a speckle pattern is an efficient approach to generate the dynamics of the SYK model. Using a spatial light modulator (see Section 4.1), we were able to generate speckle patterns on the focusing beam at the location of the atoms. Pictures of two different intensity patterns are shown in Figure 6.11. They are generated by projecting patches of random phases on the SLM (see inset).

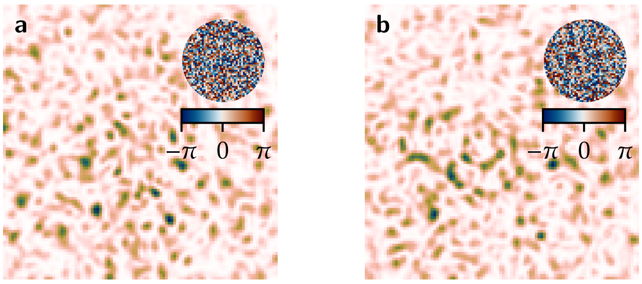

Figure 6.11: **Speckle Patterns in Experiment.** Pictures of two different speckle patterns imaged in the setup. The random phase patterns that were applied to the SLM are shown as an inset.

To implement the Trotter approach, we need to be able to quickly switch between different disorder patterns on the microsecond time scale. This could not be possible with an SLM as usual refresh rates are on the order of tens of milliseconds. This limitation can be lifted if faster optical devices, such as an acousto-optical modulator (AOM), are used for the spatial modulation of light [142].

6.7 Discussion

This chapter demonstrates that it is possible to implement holographic matter in our experiment by considering the Hamiltonian dynamics of the system. However, photon loss through the cavity mirrors and scattering off the atoms introduce incoherent dynamics. An important theoretical question is whether these losses prevent the observation of holographic matter. The dissipation-fluctuation theorem states that cavity photon losses induce randomly fluctuating forces on the atoms. It is challenging to distinguish these forces from the quantum chaotic behavior of holographic matter. Therefore, it is yet to be determined whether there is a defining characteristic of holographic matter that is resistant to random forces caused by photon losses and can be measured with feasible experimental techniques.

Theoretically, there are numerous approaches to incorporate intricate four-point interactions into our cavity QED system. However, each of these techniques requires its own set of experimental conditions (see Section 6.6). It has yet to be determined whether any of the proposed scenarios can be used to implement holographic matter in the laboratory. Even if this is not feasible, having the ability to exercise high control over atom-cavity interactions would be a remarkable advancement, enabling us to explore nonlinear optomechanics with degenerate Fermi gases.

Conclusion and Outlooks

In this thesis, we explored the development of a laboratory apparatus that allows us to control the interaction between fermionic atoms in both space and time. This includes the construction of a cavity-microscope, a device that combines a high-precision cavity with a high-resolution microscope, as well as the necessary infrastructure and techniques to cool, capture and manipulate the optical properties of fermionic ^{6}Li atoms. We provided an overview of the various experimental techniques used to acquire information about the atomic cloud in our experiment and demonstrated how these techniques can be used to gain insight into the structure of the atom-cavity system's eigenstates. Additionally, we demonstrated in proof-of-principle experiments the fast and local control over atom-cavity interactions with our cavity-microscope. This shows one of the many necessary conditions for the experimental realization of holographic quantum matter, as discussed in the last chapter. However, before attempting the quantum simulation of the SYK model many other experimental and theoretical challenges need to be overcome.

In the following, we present a list of problems that need to be overcome in the laboratory in the near future:

Improving Cavity-Microscope to Coherence Times of Cavity-Mediated Interactions. The current cavity-microscope has a low single-atom cooperativity, limiting the coherence times of cavity-mediated interactions. It is uncertain if the next-generation version, with a new batch of super-polished mirrors, will be able to address the mechanical issues of the current cavity-microscope and simultaneously provide improved optical performance. Predictions suggest that single-atom cooperativities of approximately 50 may be attainable with this device, which would be a more than tenfold enhancement compared to the devices currently in our vacuum chamber.

Towards Generating Small Samples of Degenerate Fermi Gases. Another necessary criterion for simulating the SYK model is the preparation of a degenerate Fermi gas with a few atoms of ^{6}Li. In many experiments, efficient evaporative cooling of ^{6}Li around the Feshbach resonance has been demonstrated. In fact, it is not even necessary to go to high magnetic fields to achieve strong interactions between the atoms, and therefore fast thermalization of the atomic cloud. At low magnetic fields, the 1–3 mixture of ^{6}Li can be used to achieve efficient evaporative cooling [143]. Furthermore, using the dimple trap technique, it is possible to generate small samples of tens of atoms in the degenerate quantum regime [11, 12, 144, 145].

At the end of my thesis, we implemented a technique to prepare a 1–3 mixture of ^{6}Li by driving hyperfine transitions $2 \rightarrow 3$ using the RF antenna located in the main chamber of the experiment. Using lattice cancelation techniques, we plan to remove the longitudinal lattice structure of the cavity-enhanced dipole trap (see Section 2.2), allowing us to prepare a connected cloud of atoms. The next steps are to reduce the depth of the dipole trap, start evaporative cooling, and introduce the optical tweezers trap at 780 nm as a dimple.

Controlling Heating Processes in the Floquet Technique. Our proof-of-principle experiments in Chapter 4 demonstrated local control over the atom-cavity coupling but were accompanied by considerable particle losses. This was due to the anti-trapped nature of the $4D$ manifold, the control state $|c\rangle$. These heating effects may forbid any physics related to the SYK model from being observed in experiments based on resonant Floquet driving with an amplitude-modulated control beam. It is yet to be seen whether it is possible to reduce these heating effects by detuning the control beam from the transition or even using them to strengthen the cavity-mediated interactions. As long as the atom does not spontaneously emit a blue photon and decay from the $4D$ manifold, the antitrapping dipole forces remain coherent and could be used to amplify the strength of the cavity-mediated forces.

Once the initial issues with our experimental setup have been addressed, there are still a number of unanswered questions and proof-of-principles experiments that must be done before attempting to create holographic matter in the lab. In the following, we present an outlook on possible future experiments.

Observation of Motional Sidebands. So far, we have conducted experiments with a thermal cloud of atoms. The high temperature and the associated large Doppler effect made it impossible to observe the production of distinct motional sidebands in the cavity field. It is yet to be determined whether reducing the temperature of the cloud with evaporative cooling can enhance the signal-to-noise ratio of our cavity measurements and create the conditions for controlling the motional degree of freedom of the atoms.

Calibration of Motion-Cavity Coupling. The interaction matrices $u_{ij}^{(m)}$ describe how the motion of the atoms is coupled to the optical resonator. Depending on the intensity pattern of the control beam, this coupling term has a different shape (see Section 6.4). In principle, it is possible to calibrate the couplings using the motional sideband on the cavity field. For example, if the shape is quadratic, there should be second-order sidebands to which the cavity field couples. A measurement of the structure of the sidebands as a function of the shape of the control beam would allow for the calibration of $u_{ij}^{(m)}$, the elementary building block of tunable cavity-mediated interactions.

Cavity Cooling with Tunable Atom-Cavity Interactions. The finite cooperativity of cavity QED systems limits the coherence time of the SYK dynamics they generate. However, there are some experiments that require limited coherence times. Cavity cooling is a classic example, the removal of excitations from the system is essential for reducing the temperature. Normally, due to the collective nature of the atom-cavity coupling, it is only the center-of-mass motion that can be effectively cooled [120]. It is worth investigating whether the high-rank structure that is essential for the quantum simulation of the SYK model and allows for rapid scrambling of quantum information, can also facilitate efficient cooling of all the degrees-of-freedom of the atomic cloud.

This brings the list of current issues and upcoming experiments to a close. In summary, the potential to engineer interactions on a scale that is in line with the size of the wave function is a major breakthrough, and there are numerous exciting possibilities for the future of cavity-microscope experiments.

Bibliography

1. Sauerwein, N. *et al.* Engineering random spin models with atoms in a high-finesse cavity. en. *Nature Physics* **19.** Number: 8 Publisher: Nature Publishing Group, 1128–1134. URL: `https://www.nature.com/articles/s41567-023-02033-3` (Aug. 2023) (cit. on pp. v, vi, 79, 94, 96–98).
2. Uhrich, P. *Towards Quantum Simulation of the Sachdev–Ye–Kitaev Model* PhD Thesis (University of Trento, May 2023). URL: `https://iris.unitn.it/retrieve/handle/11572/384269/660659/Philipp_Uhrich_revised_thesis.pdf` (cit. on pp. vi, 56, 86, 87, 97, 113).
3. Zweig, G. An SU3 model for strong interaction symmetry and its breaking; Version 2. URL: `https://cds.cern.ch/record/570209` (1964) (cit. on p. 1).
4. Gell-Mann, M. A schematic model of baryons and mesons. *Physics Letters* **8,** 214–215. URL: `https://www.sciencedirect.com/science/article/pii/S0031916364920013` (Feb. 1964) (cit. on p. 1).
5. Aad, G. *et al.* Observation of a new particle in the search for the Standard Model Higgs boson with the ATLAS detector at the LHC. *Physics Letters B* **716,** 1–29. URL: `https://www.sciencedirect.com/science/article/pii/S037026931200857X` (Sept. 2012) (cit. on p. 1).
6. Collaboration, T. E. H. T. *et al.* First M87 Event Horizon Telescope Results. I. The Shadow of the Supermassive Black Hole. en. *The Astrophysical Journal Letters* **875,** L1. URL: `https://dx.doi.org/10.3847/2041-8213/ab0ec7` (Apr. 2019) (cit. on p. 1).
7. LIGO Scientific Collaboration and Virgo Collaboration *et al.* GW150914: First results from the search for binary black hole coalescence with Advanced LIGO. *Physical Review D* **93,** 122003. URL: `https://link.aps.org/doi/10.1103/PhysRevD.93.122003` (June 2016) (cit. on p. 1).
8. Hartnoll, S. A., Lucas, A. & Sachdev, S. *Holographic Quantum Matter* en. Google-Books-ID: DW9RDwAAQBAJ (MIT Press, Mar. 2018) (cit. on p. 1).
9. Liu, H. & Sonner, J. Quantum many-body physics from a gravitational lens. en. *Nature Reviews Physics* **2,** 615–633. URL: `https://www.nature.com/articles/s42254-020-0225-1` (Nov. 2020) (cit. on p. 1).
10. Sachdev, S. Bekenstein-Hawking Entropy and Strange Metals. *Physical Review X* **5,** 041025. URL: `https://link.aps.org/doi/10.1103/PhysRevX.5.041025` (Nov. 2015) (cit. on p. 1).
11. Zürn, G. *et al.* Fermionization of Two Distinguishable Fermions. en. *Physical Review Letters* **108,** 075303. URL: `https://link.aps.org/doi/10.1103/PhysRevLett.108.075303` (Feb. 2012) (cit. on pp. 1, 121).

12. Holten, M. *et al.* Observation of Cooper pairs in a mesoscopic two-dimensional Fermi gas. en. *Nature* **606,** 287–291. URL: `https://www.nature.com/articles/s41586-022-04678-1` (June 2022) (cit. on pp. 1, 121).

13. Mivehvar, F., Piazza, F., Donner, T. & Ritsch, H. Cavity QED with quantum gases: new paradigms in many-body physics. *Advances in Physics* **70,** 1–153. URL: `https://doi.org/10.1080/00018732.2021.1969727` (Jan. 2021) (cit. on p. 1).

14. Helson, V. *et al.* Density-wave ordering in a unitary Fermi gas with photon-mediated interactions. en. *Nature* **618.** Number: 7966 Publisher: Nature Publishing Group, 716–720. URL: `https://www.nature.com/articles/s41586-023-06018-3` (June 2023) (cit. on pp. 1, 51).

15. Tanji-Suzuki, H. *et al.* in *Advances In Atomic, Molecular, and Optical Physics* (eds Arimondo, E., Berman, P. R. & Lin, C. C.) 201–237 (Academic Press, Jan. 2011). URL: `https://www.sciencedirect.com/science/article/pii/B9780123855084000048` (cit. on pp. 7, 8).

16. Baur, S., Tiarks, D., Rempe, G. & Dürr, S. Single-Photon Switch Based on Rydberg Blockade. *Physical Review Letters* **112.** Publisher: American Physical Society, 073901. URL: `https://link.aps.org/doi/10.1103/PhysRevLett.112.073901` (Feb. 2014) (cit. on p. 7).

17. Poldy, R., Buchler, B. C. & Close, J. D. Single-atom detection with optical cavities. *Physical Review A* **78.** Publisher: American Physical Society, 013640. URL: `https://link.aps.org/doi/10.1103/PhysRevA.78.013640` (July 2008) (cit. on p. 8).

18. Terraciano, M. L. *et al.* Photon burst detection of single atoms in an optical cavity. en. *Nature Physics* **5.** Number: 7 Publisher: Nature Publishing Group, 480–484. URL: `https://www.nature.com/articles/nphys1282` (July 2009) (cit. on p. 8).

19. Goldwin, J., Trupke, M., Kenner, J., Ratnapala, A. & Hinds, E. A. Fast cavity-enhanced atom detection with low noise and high fidelity. en. *Nature Communications* **2.** Number: 1 Publisher: Nature Publishing Group, 418. URL: `https://www.nature.com/articles/ncomms1428` (Aug. 2011) (cit. on p. 8).

20. Yang, D., Vasilyev, D. V., Laflamme, C., Baranov, M. A. & Zoller, P. Quantum scanning microscope for cold atoms. *Physical Review A* **98,** 023852. URL: `https://link.aps.org/doi/10.1103/PhysRevA.98.023852` (Aug. 2018) (cit. on pp. 9, 77).

21. Yang, D., Laflamme, C., Vasilyev, D. V., Baranov, M. A. & Zoller, P. Theory of a Quantum Scanning Microscope for Cold Atoms. *Physical Review Letters* **120,** 133601. URL: `https://link.aps.org/doi/10.1103/PhysRevLett.120.133601` (Mar. 2018) (cit. on pp. 9, 77).

22. Deist, E., Gerber, J. A., Lu, Y.-H., Zeiher, J. & Stamper-Kurn, D. M. Superresolution Microscopy of Optical Fields Using Tweezer-Trapped Single Atoms. *Physical Review Letters* **128,** 083201. URL: `https://link.aps.org/doi/10.1103/PhysRevLett.128.083201` (Feb. 2022) (cit. on pp. 10, 27).

23. *Research | Leonard Lab at TU Wien* en. URL: `https://www.quantuminfo.at/cavity-lab` (cit. on p. 10).

24. Liu, Y. *et al.* Realization of Strong Coupling between Deterministic Single-Atom Arrays and a High-Finesse Miniature Optical Cavity. *Physical Review Letters* **130,** 173601. URL: `https://link.aps.org/doi/10.1103/PhysRevLett.130.173601` (Apr. 2023) (cit. on p. 10).

25. Léonard, J. *A Supersolid of Matter and Light* PhD thesis (ETH Zurich, 2017). URL: `https://www.research-collection.ethz.ch/handle/20.500.11850/262194` (cit. on pp. 10, 20).

26. Ferri, F., Garcia, S., Baghdad, M., Reichel, J. & Long, R. Mapping optical standing-waves of an open-access Fabry–Perot cavity with a tapered fiber. *Review of Scientific Instruments* **91,** 033104. URL: `https://doi.org/10.1063/1.5142709` (Mar. 2020) (cit. on pp. 10, 156).

27. Wipfli, O. *Development of a Cryogenic High-Power Build-up Cavity for Optical Trapping of Ions* en. Doctoral Thesis (ETH Zurich, May 2022). URL: `https://www.research-collection.ethz.ch/handle/20.500.11850/564576` (cit. on pp. 10, 26).

28. Bennett, H. E. & Porteus, J. O. Relation Between Surface Roughness and Specular Reflectance at Normal Incidence. EN. *JOSA* **51.** Publisher: Optica Publishing Group, 123–129. URL: `https://opg.optica.org/josa/abstract.cfm?uri=josa-51-2-123` (Feb. 1961) (cit. on p. 11).

29. Nguyen, C. H., Utama, A. N., Lewty, N. & Kurtsiefer, C. Operating a near-concentric cavity at the last stable resonance. *Physical Review A* **98.** Publisher: American Physical Society, 063833. URL: `https://link.aps.org/doi/10.1103/PhysRevA.98.063833` (Dec. 2018) (cit. on pp. 12, 20).

30. Coyne, D. *LIGO Vaccum Compatible Materials List* tech. rep. (May 2013). URL: `https://dcc.ligo.org/public/0003/E960050/012/E960050-v12%20Vacuum%20Compatible%20Materials%20List.pdf` (cit. on pp. 13, 33).

31. Sauerwein, N. *QuEMS Cavity v2022* en. Oct. 2023. URL: `https://sketchfab.com/models/96facf967c4f42f4a7af5fd0226bbb01/embed?autostart=1` (cit. on p. 14).

32. Reiter, N. *Towards a Cavity-Enhanced Microscope for Cold Atoms: Trapping and Cooling 6Li Atoms in a High-Finesse Cavity* MA thesis (École Polytechnique Fédérale De Lausanne, May 2021) (cit. on pp. 16, 35, 41).

33. *Perkins Precision Optics* URL: `https://www.perkinsprecision.com/` (cit. on pp. 17, 27).

34. *FiveNine Optics – Boulder, Colorado | R > 99.999%* URL: `https://www.fivenineoptics.com/` (cit. on p. 17).

35. *OSLO | Lambda Research Corporation* en. URL: `https://lambdares.com/oslo` (cit. on p. 17).

36. *Asphericon* URL: `https://www.asphericon.com/` (cit. on p. 17).

37. *PI Ceramic* URL: `https://www.piceramic.de/de/` (cit. on pp. 17, 27).

38. *Kompetenz in Keramik | Fraunhofer IKTS* de. URL: `https://www.ikts.fraunhofer.de/de.html` (cit. on p. 17).

39. Sauerwein, N., Cantat-Moltrecht, T., Grigoras, I. T. & Brantut, J.-P. Vibration damping platform for cavity quantum-electrodynamics experiments. *Review of Scientific Instruments* **93,** 033203. URL: `https://doi.org/10.1063/5.0069765` (Mar. 2022) (cit. on p. 19).

40. Aspelmeyer, M., Kippenberg, T. J. & Marquardt, F. Cavity optomechanics. *Reviews of Modern Physics* **86.** Publisher: American Physical Society, 1391–1452. URL: `https://link.aps.org/doi/10.1103/RevModPhys.86.1391` (Dec. 2014) (cit. on pp. 19, 106).

41. LIGO Scientific Collaboration and Virgo Collaboration. Observation of Gravitational Waves from a Binary Black Hole Merger. *Physical Review Letters* **116,** 061102. URL: `https://link.aps.org/doi/10.1103/PhysRevLett.116.061102` (Feb. 2016) (cit. on p. 19).

42. Okano, M. *et al.* Vibration isolation for scanning tunneling microscopy. *Journal of Vacuum Science & Technology A* **5,** 3313–3320. URL: `https://doi.org/10.1116/1.574189` (Nov. 1987) (cit. on pp. 19, 22).

43. Slama, S., Bux, S., Krenz, G., Zimmermann, C. & Courteille, P. W. Superradiant Rayleigh Scattering and Collective Atomic Recoil Lasing in a Ring Cavity. *Physical Review Letters* **98,** 053603. URL: `https://link.aps.org/doi/10.1103/PhysRevLett.98.053603` (Feb. 2007) (cit. on p. 20).

44. Bertoldi, A., Bernon, S., Vanderbruggen, T., Landragin, A. & Bouyer, P. *In situ* characterization of an optical cavity using atomic light shift. EN. *Optics Letters* **35,** 3769–3771. URL: `https://opg.optica.org/ol/abstract.cfm?uri=ol-35-22-3769` (Nov. 2010) (cit. on p. 20).

45. Keßler, H., Klinder, J., Wolke, M. & Hemmerich, A. Optomechanical atom-cavity interaction in the sub-recoil regime. en. *New Journal of Physics* **16,** 053008. URL: `https://dx.doi.org/10.1088/1367-2630/16/5/053008` (May 2014) (cit. on p. 20).

46. Kollár, A. J., Papageorge, A. T., Baumann, K., Armen, M. A. & Lev, B. L. An adjustable-length cavity and Bose–Einstein condensate apparatus for multimode cavity QED. en. *New Journal of Physics* **17,** 043012. URL: `https://dx.doi.org/10.1088/1367-2630/17/4/043012` (Apr. 2015) (cit. on p. 20).

47. Davis, E. J., Bentsen, G., Homeier, L., Li, T. & Schleier-Smith, M. H. Photon-Mediated Spin-Exchange Dynamics of Spin-1 Atoms. *Physical Review Letters* **122.** Publisher: American Physical Society, 010405. URL: `https://link.aps.org/doi/10.1103/PhysRevLett.122.010405` (Jan. 2019) (cit. on pp. 20, 77, 80, 100).

48. Roux, K., Helson, V., Konishi, H. & Brantut, J. P. Cavity-assisted preparation and detection of a unitary Fermi gas. en. *New Journal of Physics* **23,** 043029. URL: `https://dx.doi.org/10.1088/1367-2630/abeb91` (Apr. 2021) (cit. on p. 20).

49. Jaffe, M., Palm, L., Baum, C., Taneja, L. & Simon, J. Aberrated optical cavities. *Physical Review A* **104,** 013524. URL: `https://link.aps.org/doi/10.1103/PhysRevA.104.013524` (July 2021) (cit. on p. 20).

50. Briles, T. C., Yost, D. C., Cingöz, A., Ye, J. & Schibli, T. R. Simple piezoelectric-actuated mirror with 180 kHz servo bandwidth. EN. *Optics Express* **18,** 9739–9746. URL: `https://opg.optica.org/oe/abstract.cfm?uri=oe-18-10-9739` (May 2010) (cit. on p. 20).

51. Notcutt, M., Ma, L.-S., Ye, J. & Hall, J. L. Simple and compact 1-Hz laser system via an improved mounting configuration of a reference cavity. EN. *Optics Letters* **30,** 1815–1817. URL: `https://opg.optica.org/ol/abstract.cfm?uri=ol-30-14-1815` (July 2005) (cit. on p. 20).

52. Chadi, A., Méjean, G., Grilli, R. & Romanini, D. Note: Simple and compact piezoelectric mirror actuator with 100 kHz bandwidth, using standard components. *Review of Scientific Instruments* **84,** 056112. URL: `https://doi.org/10.1063/1.4807859` (May 2013) (cit. on p. 20).

53. Sinclair, L. C. *et al.* Invited Article: A compact optically coherent fiber frequency comb. *Review of Scientific Instruments* **86,** 081301. URL: `https://doi.org/10.1063/1.4928163` (Aug. 2015) (cit. on p. 20).

54. Anderson, E. H., Glaese, R. M. & Neill, D. *A comparison of vibration damping methods for ground based telescopes* in *Ground-based and Airborne Telescopes II* **7012** (SPIE, July 2008), 184–198. URL: `https://www.spiedigitallibrary.org/conference-proceedings-of-spie/7012/70120H/A-comparison-of-vibration-damping-methods-for-ground-based-telescopes/10.1117/12.790195.full` (cit. on p. 20).

55. Ryou, A. & Simon, J. Active cancellation of acoustical resonances with an FPGA FIR filter. *Review of Scientific Instruments* **88,** 013101. URL: https://doi.org/10.1063/1.4973470 (Jan. 2017) (cit. on pp. 20, 24).

56. Hoffman, D., Singh, B. & III, J. H. T. *Handbook of Vacuum Science and Technology* en. Google-Books-ID: HWvo5gKTiv0C (Elsevier, Oct. 1997) (cit. on p. 21).

57. Fu, W. & Chung, D. Vibration Reduction Ability of Polymers, Particularly Polymethylmethacrylate and Polytetrafluoroethylene. en. *Polymers and Polymer Composites* **9,** 423–426. URL: https://doi.org/10.1177/096739110100900607 (Sept. 2001) (cit. on p. 21).

58. Lehnert, R. J., Hendra, P. J., Everall, N. & Clayden, N. J. Comparative quantitative study on the crystallinity of poly(tetrafluoroethylene) including Raman, infra-red and 19F nuclear magnetic resonance spectroscopy. *Polymer* **38,** 1521–1535. URL: https://www.sciencedirect.com/science/article/pii/S0032386196006842 (Mar. 1997) (cit. on p. 21).

59. Rae, P. J. & Dattelbaum, D. M. The properties of poly(tetrafluoroethylene) (PTFE) in compression. *Polymer* **45,** 7615–7625. URL: https://www.sciencedirect.com/science/article/pii/S0032386104008511 (Oct. 2004) (cit. on p. 21).

60. *Ansys® Academic Research Mechanical, Release 19.2.* (cit. on p. 22).

61. Bolognini, G. *Design and assembly of a cavity-microscope system for cold atoms experiments* MA thesis (École Polytechnique Fédérale De Lausanne, June 2023) (cit. on pp. 25, 27, 28).

62. Sauerwein, N. *QuEMS Cavity v2018* en. Oct. 2023. URL: https://sketchfab.com/models/45564251b3074b21a4fdbd6cc4cc4feb/embed?autostart=1 (cit. on p. 25).

63. Rivolta, C. Airy disk diffraction pattern: comparison of some values of f/No. and obscuration ratio. EN. *Applied Optics* **25,** 2404–2408. URL: https://opg.optica.org/ao/abstract.cfm?uri=ao-25-14-2404 (July 1986) (cit. on p. 26).

64. *Laseroptik GmbH* en. URL: https://www.laseroptik.com/ (cit. on p. 27).

65. Kawasaki, A. *Towards spin squeezed 171Yb atomic clock beyond the standard quantum limit* eng. Thesis (Massachusetts Institute of Technology, 2017). URL: https://dspace.mit.edu/handle/1721.1/115002 (cit. on p. 27).

66. Greve, G. P., Luo, C., Wu, B. & Thompson, J. K. Entanglement-enhanced matter-wave interferometry in a high-finesse cavity. en. *Nature* **610,** 472–477. URL: https://www.nature.com/articles/s41586-022-05197-9 (Oct. 2022) (cit. on p. 27).

67. *First Contact Polymer Kits* URL: https://www.photoniccleaning.com/Kits-s/112.htm (cit. on p. 28).

68. Merzlyakov, M., McKenna, G. B. & Simon, S. L. Cure-induced and thermal stresses in a constrained epoxy resin. *Composites Part A: Applied Science and Manufacturing. Internal Stresses in Polymer Composites* **37,** 585–591. URL: https://www.sciencedirect.com/science/article/pii/S1359835X05001910 (Apr. 2006) (cit. on p. 30).

69. Thurn, J. & Hermel-Davidock, T. Thermal stress hysteresis and stress relaxation in an epoxy film. en. *Journal of Materials Science* **42,** 5686–5691. URL: https://doi.org/10.1007/s10853-006-0654-y (July 2007) (cit. on p. 30).

70. Gupta, M. K., Priyadarshi, A. & Khan, Z. Hydrogen in Stainless Steel as Killing Agent for UHV: A Review. *Materials Today: Proceedings. 4th International Conference on Materials Processing and Characterzation* **2,** 1074–1081. URL: https://www.sciencedirect.com/science/article/pii/S2214785315002564 (Jan. 2015) (cit. on p. 33).

71. Hahn, U. & Zapfe, K. *Guidelines for UHV-Components at DESY* Sept. 2010. URL: `https://photon-science.desy.de/facilities/petra_iii/beamlines/p04_xuv_beamline/e265554/e265562/Vacuum_005_DESY_UHV_guidelines_1-5_final_stamp.pdf` (cit. on p. 33).
72. *Eine Metalllegierung wie ein Schwamm | Unsere Forschung | Paul Scherrer Institut (PSI)* de. June 2023. URL: `https://www.psi.ch/de/media/forschung/eine-metalllegierung-wie-ein-schwamm` (cit. on p. 33).
73. Roux, K., Cilenti, B., Helson, V., Konishi, H. & Brantut, J.-P. Compact bulk-machined electromagnets for quantum gas experiments. en. *SciPost Physics* **6,** 048. URL: `https://scipost.org/SciPostPhys.6.4.048` (Apr. 2019) (cit. on pp. 34, 149).
74. Roux, K. E. R. *Cavity Quantum Electrodynamics with strongly correlated fermions* eng. PhD thesis (EPFL, Lausanne, 2022) (cit. on p. 35).
75. Starkey, P. T. *et al.* A scripted control system for autonomous hardware-timed experiments. en. *Review of Scientific Instruments* **84,** 085111. URL: `https://pubs.aip.org/rsi/article/84/8/085111/356680/A-scripted-control-system-for-autonomous-hardware` (Aug. 2013) (cit. on p. 37).
76. Starkey, P. T. *A software framework for control and automation of precisely timed experiments* en. thesis (Monash University, July 2019). URL: `https://bridges.monash.edu/articles/thesis/A_software_framework_for_control_and_automation_of_precisely_timed_experiments/8637200/1` (cit. on p. 37).
77. *Anaysis Plot Panel* URL: `https://lqg-epfl.github.io/analysis_plot_panel/` (cit. on p. 38).
78. *PyQtGraph - Scientific Graphics and GUI Library for Python* URL: `https://www.pyqtgraph.org/` (cit. on p. 38).
79. *QuEMS Interlock* URL: `https://lqg-epfl.github.io/QuEMS_interlock/` (cit. on p. 38).
80. Kramida, A. & Ralchenko, Y. *NIST Atomic Spectra Database, NIST Standard Reference Database 78* en. 1999. URL: `http://www.nist.gov/pml/data/asd.cfm` (cit. on pp. 41, 52).
81. Lee, J., Vrijsen, G., Teper, I., Hosten, O. & Kasevich, M. A. Many-atom–cavity QED system with homogeneous atom–cavity coupling. EN. *Optics Letters* **39,** 4005–4008. URL: `https://opg.optica.org/ol/abstract.cfm?uri=ol-39-13-4005` (July 2014) (cit. on p. 41).
82. Sherson, J. F. *et al.* Single-atom-resolved fluorescence imaging of an atomic Mott insulator. en. *Nature* **467,** 68–72. URL: `https://www.nature.com/articles/nature09378` (Sept. 2010) (cit. on p. 42).
83. Schlederer, M., Mozdzen, A., Lompe, T. & Moritz, H. Single-atom counting in a two-color magneto-optical trap. en. *Physical Review A* **103,** 033308. URL: `https://link.aps.org/doi/10.1103/PhysRevA.103.033308` (Mar. 2021) (cit. on pp. 43, 44).
84. Hume, D. B. *et al.* Accurate Atom Counting in Mesoscopic Ensembles. *Physical Review Letters* **111,** 253001. URL: `https://link.aps.org/doi/10.1103/PhysRevLett.111.253001` (Dec. 2013) (cit. on p. 44).
85. Bhatt, R. P., Kilinc, J., Höcker, L. & Jendrzejewski, F. Stochastic dynamics of a few sodium atoms in presence of a cold potassium cloud. en. *Scientific Reports* **12,** 2422. URL: `https://www.nature.com/articles/s41598-022-05778-8` (Feb. 2022) (cit. on p. 44).
86. Haroche, S. & Raimond, J.-M. *Exploring the Quantum: Atoms, Cavities, and Photons* en. Google-Books-ID: YHC1kQEACAAJ (OUP Oxford, Apr. 2013) (cit. on p. 45).

87. Gehm, M. E. Properties of 6Li. *Jetlab*, URL: `https://jet.physics.ncsu.edu/techdocs/pdf/PropertiesOfLi.pdf` (2003) (cit. on p. 52).

88. Roux, K., Konishi, H., Helson, V. & Brantut, J.-P. Strongly correlated Fermions strongly coupled to light. en. *Nature Communications* **11,** 2974. URL: `https://www.nature.com/articles/s41467-020-16767-8` (June 2020) (cit. on p. 58).

89. Uchino, S., Ueda, M. & Brantut, J.-P. Universal noise in continuous transport measurements of interacting fermions. *Physical Review A* **98,** 063619. URL: `https://link.aps.org/doi/10.1103/PhysRevA.98.063619` (Dec. 2018) (cit. on p. 58).

90. Fuhrmanek, A., Bourgain, R., Sortais, Y. R. P. & Browaeys, A. Light-assisted collisions between a few cold atoms in a microscopic dipole trap. *Physical Review A* **85,** 062708. URL: `https://link.aps.org/doi/10.1103/PhysRevA.85.062708` (June 2012) (cit. on p. 61).

91. Nogrette, F. *et al.* Single-Atom Trapping in Holographic 2D Arrays of Microtraps with Arbitrary Geometries. *Physical Review X* **4,** 021034. URL: `https://link.aps.org/doi/10.1103/PhysRevX.4.021034` (May 2014) (cit. on p. 73).

92. Mockus, J. *Bayesian Approach to Global Optimization: Theory and Applications* en. Google-Books-ID: FknvAAAAMAAJ (Springer Netherlands, Feb. 1989) (cit. on p. 74).

93. Periwal, A. *et al.* Programmable interactions and emergent geometry in an array of atom clouds. en. *Nature* **600.** Number: 7890 Publisher: Nature Publishing Group, 630–635. URL: `https://www.nature.com/articles/s41586-021-04156-0` (Dec. 2021) (cit. on pp. 77, 80).

94. Finger, F. *et al. Spin- and momentum-correlated atom pairs mediated by photon exchange and seeded by vacuum fluctuations* arXiv:2303.11326 [cond-mat, physics:physics, physics:quant-ph]. Oct. 2023. URL: `http://arxiv.org/abs/2303.11326` (cit. on pp. 77, 80).

95. Browaeys, A. & Lahaye, T. Many-body physics with individually controlled Rydberg atoms. en. *Nature Physics* **16,** 132–142. URL: `https://www.nature.com/articles/s41567-019-0733-z` (Feb. 2020) (cit. on p. 77).

96. Bernien, H. *et al.* Probing many-body dynamics on a 51-atom quantum simulator. en. *Nature* **551,** 579–584. URL: `https://www.nature.com/articles/nature24622` (Nov. 2017) (cit. on p. 77).

97. Deist, E. *et al.* Mid-Circuit Cavity Measurement in a Neutral Atom Array. *Physical Review Letters* **129,** 203602. URL: `https://link.aps.org/doi/10.1103/PhysRevLett.129.203602` (Nov. 2022) (cit. on p. 77).

98. Bohnet, J. G. *et al.* A steady-state superradiant laser with less than one intracavity photon. en. *Nature* **484.** Number: 7392 Publisher: Nature Publishing Group, 78–81. URL: `https://www.nature.com/articles/nature10920` (Apr. 2012) (cit. on p. 80).

99. Norcia, M. A., Winchester, M. N., Cline, J. R. K. & Thompson, J. K. Superradiance on the millihertz linewidth strontium clock transition. *Science Advances* **2.** Publisher: American Association for the Advancement of Science, e1601231. URL: `https://www.science.org/doi/10.1126/sciadv.1601231` (Oct. 2016) (cit. on p. 80).

100. Lewis-Swan, R. J. *et al.* Cavity-QED Quantum Simulator of Dynamical Phases of a Bardeen-Cooper-Schrieffer Superconductor. *Physical Review Letters* **126.** Publisher: American Physical Society, 173601. URL: `https://link.aps.org/doi/10.1103/PhysRevLett.126.173601` (Apr. 2021) (cit. on pp. 81, 100).

101. Bychek, A., Hotter, C., Plankensteiner, D. & Ritsch, H. Superradiant lasing in inhomogeneously broadened ensembles with spatially varying coupling. *Open Research Europe* **1.** arXiv:2105.11023 [quant-ph], 73. URL: `http://arxiv.org/abs/2105.11023` (Sept. 2021) (cit. on pp. 81, 100).

102. Leroux, I. D., Schleier-Smith, M. H. & Vuletić, V. Implementation of Cavity Squeezing of a Collective Atomic Spin. *Physical Review Letters* **104.** Publisher: American Physical Society, 073602. URL: `https://link.aps.org/doi/10.1103/PhysRevLett.104.073602` (Feb. 2010) (cit. on p. 85).

103. Engelsen, N. J., Krishnakumar, R., Hosten, O. & Kasevich, M. A. Bell Correlations in Spin-Squeezed States of 500 000 Atoms. *Physical Review Letters* **118.** Publisher: American Physical Society, 140401. URL: `https://link.aps.org/doi/10.1103/PhysRevLett.118.140401` (Apr. 2017) (cit. on p. 85).

104. Baghdad, M. *et al.* Spectral engineering of cavity-protected polaritons in an atomic ensemble. en. *Nature Physics* **19.** Number: 8 Publisher: Nature Publishing Group, 1104–1109. URL: `https://www.nature.com/articles/s41567-023-02035-1` (Aug. 2023) (cit. on p. 88).

105. Dubail, J., Botzung, T., Schachenmayer, J., Pupillo, G. & Hagenmüller, D. Large random arrowhead matrices: Multifractality, semilocalization, and protected transport in disordered quantum spins coupled to a cavity. *Physical Review A* **105.** Publisher: American Physical Society, 023714. URL: `https://link.aps.org/doi/10.1103/PhysRevA.105.023714` (Feb. 2022) (cit. on pp. 88, 94, 98, 99).

106. Brantut, J. P. *et al.* Light-shift tomography in an optical-dipole trap for neutral atoms. *Physical Review A* **78.** Publisher: American Physical Society, 031401. URL: `https://link.aps.org/doi/10.1103/PhysRevA.78.031401` (Sept. 2008) (cit. on p. 90).

107. Lipkin, H. J., Meshkov, N. & Glick, A. J. Validity of many-body approximation methods for a solvable model: (I). Exact solutions and perturbation theory. *Nuclear Physics* **62,** 188–198. URL: `https://www.sciencedirect.com/science/article/pii/002955826590862X` (Feb. 1965) (cit. on p. 96).

108. Makhalov, V. *et al.* Probing Quantum Criticality and Symmetry Breaking at the Microscopic Level. *Physical Review Letters* **123.** Publisher: American Physical Society, 120601. URL: `https://link.aps.org/doi/10.1103/PhysRevLett.123.120601` (Sept. 2019) (cit. on p. 96).

109. Muniz, J. A. *et al.* Exploring dynamical phase transitions with cold atoms in an optical cavity. en. *Nature* **580.** Number: 7805 Publisher: Nature Publishing Group, 602–607. URL: `https://www.nature.com/articles/s41586-020-2224-x` (Apr. 2020) (cit. on pp. 96, 100).

110. Richardson, R. W. A restricted class of exact eigenstates of the pairing-force Hamiltonian. *Physics Letters* **3,** 277–279. URL: `https://www.sciencedirect.com/science/article/pii/0031916363902592` (Feb. 1963) (cit. on p. 96).

111. Gaudin, M. Diagonalisation d'une classe d'hamiltoniens de spin. fr. *Journal de Physique* **37.** Publisher: Société Française de Physique, 1087–1098. URL: `http://dx.doi.org/10.1051/jphys:0197600370100108700` (Oct. 1976) (cit. on p. 96).

112. Dukelsky, J., Pittel, S. & Sierra, G. Colloquium: Exactly solvable Richardson-Gaudin models for many-body quantum systems. *Reviews of Modern Physics* **76.** Publisher: American Physical Society, 643–662. URL: `https://link.aps.org/doi/10.1103/RevModPhys.76.643` (Aug. 2004) (cit. on p. 96).

113. Botzung, T. *et al.* Dark state semilocalization of quantum emitters in a cavity. *Physical Review B* **102.** Publisher: American Physical Society, 144202. URL: `https://link.aps.org/doi/10.1103/PhysRevB.102.144202` (Oct. 2020) (cit. on pp. 98, 99).

114. Buccheri, F., De Luca, A. & Scardicchio, A. Structure of typical states of a disordered Richardson model and many-body localization. *Physical Review B* **84.** Publisher: American Physical Society, 094203. URL: `https://link.aps.org/doi/10.1103/PhysRevB.84.094203` (Sept. 2011) (cit. on p. 99).

115. Kelly, S. P., Thompson, J. K., Rey, A. M. & Marino, J. Resonant light enhances phase coherence in a cavity QED simulator of fermionic superfluidity. *Physical Review Research* **4.** Publisher: American Physical Society, L042032. URL: `https://link.aps.org/doi/10.1103/PhysRevResearch.4.L042032` (Nov. 2022) (cit. on p. 100).

116. Gopalakrishnan, S., Lev, B. L. & Goldbart, P. M. Frustration and Glassiness in Spin Models with Cavity-Mediated Interactions. *Physical Review Letters* **107.** Publisher: American Physical Society, 277201. URL: `https://link.aps.org/doi/10.1103/PhysRevLett.107.277201` (Dec. 2011) (cit. on p. 100).

117. Habibian, H., Winter, A., Paganelli, S., Rieger, H. & Morigi, G. Bose-Glass Phases of Ultracold Atoms due to Cavity Backaction. *Physical Review Letters* **110.** Publisher: American Physical Society, 075304. URL: `https://link.aps.org/doi/10.1103/PhysRevLett.110.075304` (Feb. 2013) (cit. on p. 100).

118. Kim, J., Cao, X. & Altman, E. Low-rank Sachdev-Ye-Kitaev models. *Physical Review B* **101,** 125112. URL: `https://link.aps.org/doi/10.1103/PhysRevB.101.125112` (Mar. 2020) (cit. on pp. 102, 103, 113).

119. Uhrich, P. *et al. A cavity quantum electrodynamics implementation of the Sachdev–Ye–Kitaev model* arXiv:2303.11343 [cond-mat, physics:hep-th, physics:quant-ph]. Mar. 2023. URL: `http://arxiv.org/abs/2303.11343` (cit. on pp. 108, 113).

120. Schleier-Smith, M. H., Leroux, I. D., Zhang, H., Van Camp, M. A. & Vuletić, V. Optomechanical Cavity Cooling of an Atomic Ensemble. *Physical Review Letters* **107.** Publisher: American Physical Society, 143005. URL: `https://link.aps.org/doi/10.1103/PhysRevLett.107.143005` (Sept. 2011) (cit. on pp. 109, 122).

121. Wertheim, G. K., Butler, M. A., West, K. W. & Buchanan, D. N. E. Determination of the Gaussian and Lorentzian content of experimental line shapes. *Review of Scientific Instruments* **45,** 1369–1371. URL: `https://doi.org/10.1063/1.1686503` (Nov. 2003) (cit. on p. 114).

122. Chen, A., Ilan, R., de Juan, F., Pikulin, D. I. & Franz, M. Quantum Holography in a Graphene Flake with an Irregular Boundary. *Physical Review Letters* **121,** 036403. URL: `https://link.aps.org/doi/10.1103/PhysRevLett.121.036403` (July 2018) (cit. on p. 113).

123. Wei, C. & Sedrakyan, T. A. Optical lattice platform for the Sachdev-Ye-Kitaev model. *Physical Review A* **103,** 013323. URL: `https://link.aps.org/doi/10.1103/PhysRevA.103.013323` (Jan. 2021) (cit. on p. 113).

124. Krajewski, T., Laudonio, M., Pascalie, R. & Tanasa, A. Non-Gaussian disorder average in the Sachdev-Ye-Kitaev model. *Physical Review D* **99,** 126014. URL: `https://link.aps.org/doi/10.1103/PhysRevD.99.126014` (June 2019) (cit. on p. 114).

125. Cao, Y., Zhou, Y.-N., Shi, T.-T. & Zhang, W. Towards quantum simulation of Sachdev-Ye-Kitaev model. *Science Bulletin* **65,** 1170–1176. URL: `https://www.sciencedirect.com/science/article/pii/S2095927320301808` (July 2020) (cit. on p. 114).

126. García-García, A. M., Jia, Y., Rosa, D. & Verbaarschot, J. J. M. Sparse Sachdev-Ye-Kitaev model, quantum chaos, and gravity duals. *Physical Review D* **103,** 106002. URL: `https://link.aps.org/doi/10.1103/PhysRevD.103.106002` (May 2021) (cit. on p. 114).

127. Tezuka, M., Oktay, O., Rinaldi, E., Hanada, M. & Nori, F. Binary-coupling sparse Sachdev-Ye-Kitaev model: An improved model of quantum chaos and holography. *Physical Review B* **107,** L081103. URL: `https://link.aps.org/doi/10.1103/PhysRevB.107.L081103` (Feb. 2023) (cit. on p. 114).

128. Danshita, I., Hanada, M. & Tezuka, M. Creating and probing the Sachdev–Ye–Kitaev model with ultracold gases: Towards experimental studies of quantum gravity. *Progress of Theoretical and Experimental Physics* **2017,** 083I01. URL: `https://doi.org/10.1093/ptep/ptx108` (Aug. 2017) (cit. on p. 114).

129. Maldacena, J. & Stanford, D. Remarks on the Sachdev-Ye-Kitaev model. *Physical Review D* **94,** 106002. URL: `https://link.aps.org/doi/10.1103/PhysRevD.94.106002` (Nov. 2016) (cit. on p. 114).

130. Alexei, K. *A simple model of quantum holography* KITP, Apr. 2015. URL: `https://www.youtube.com/watch?v=wFH1huu9Jcs` (cit. on p. 114).

131. Kobrin, B. *et al.* Many-Body Chaos in the Sachdev-Ye-Kitaev Model. *Physical Review Letters* **126,** 030602. URL: `https://link.aps.org/doi/10.1103/PhysRevLett.126.030602` (Jan. 2021) (cit. on p. 114).

132. Gharibyan, H., Hanada, M., Shenker, S. H. & Tezuka, M. Onset of random matrix behavior in scrambling systems. en. *Journal of High Energy Physics* **2018,** 124. URL: `https://doi.org/10.1007/JHEP07(2018)124` (July 2018) (cit. on p. 114).

133. Cotler, J. S. *et al.* Black holes and random matrices. en. *Journal of High Energy Physics* **2017,** 118. URL: `https://doi.org/10.1007/JHEP05(2017)118` (May 2017) (cit. on pp. 114, 117).

134. Fu, W. & Sachdev, S. Numerical study of fermion and boson models with infinite-range random interactions. *Physical Review B* **94,** 035135. URL: `https://link.aps.org/doi/10.1103/PhysRevB.94.035135` (July 2016) (cit. on p. 114).

135. Brody, T. A. *et al.* Random-matrix physics: spectrum and strength fluctuations. *Reviews of Modern Physics* **53,** 385–479. URL: `https://link.aps.org/doi/10.1103/RevModPhys.53.385` (July 1981) (cit. on p. 116).

136. You, Y.-Z., Ludwig, A. W. W. & Xu, C. Sachdev-Ye-Kitaev model and thermalization on the boundary of many-body localized fermionic symmetry-protected topological states. *Physical Review B* **95,** 115150. URL: `https://link.aps.org/doi/10.1103/PhysRevB.95.115150` (Mar. 2017) (cit. on p. 116).

137. Del Campo, A., Molina-Vilaplana, J. & Sonner, J. Scrambling the spectral form factor: Unitarity constraints and exact results. *Physical Review D* **95,** 126008. URL: `https://link.aps.org/doi/10.1103/PhysRevD.95.126008` (June 2017) (cit. on p. 117).

138. Cotler, J., Hunter-Jones, N., Liu, J. & Yoshida, B. Chaos, complexity, and random matrices. en. *Journal of High Energy Physics* **2017,** 48. URL: `https://doi.org/10.1007/JHEP11(2017)048` (Nov. 2017) (cit. on p. 117).

139. Sonner, J. & Vielma, M. Eigenstate thermalization in the Sachdev-Ye-Kitaev model. en. *Journal of High Energy Physics* **2017,** 149. URL: `https://doi.org/10.1007/JHEP11(2017)149` (Nov. 2017) (cit. on p. 117).

140. Altland, A. & Bagrets, D. Quantum ergodicity in the SYK model. *Nuclear Physics B* **930,** 45–68. URL: `https://www.sciencedirect.com/science/article/pii/S0550321318300609` (May 2018) (cit. on p. 117).

141. Altland, A., Bagrets, D., Nayak, P., Sonner, J. & Vielma, M. From operator statistics to wormholes. *Physical Review Research* **3,** 033259. URL: `https://link.aps.org/doi/10.1103/PhysRevResearch.3.033259` (Sept. 2021) (cit. on p. 117).

142. Liu, X., Braverman, B. & Boyd, R. W. Using an acousto-optic modulator as a fast spatial light modulator. EN. *Optics Express* **31,** 1501–1515. URL: `https://opg.optica.org/oe/abstract.cfm?uri=oe-31-2-1501` (Jan. 2023) (cit. on p. 119).

143. O'Hara, K. *Optical Trapping and Evaporative Cooling of Fermionic Atoms* PhD Thesis (Duke University, 2000). URL: `https://jet.physics.ncsu.edu/theses/pdf/OHara.pdf` (cit. on p. 121).

144. Viverit, L., Giorgini, S., Pitaevskii, L. P. & Stringari, S. Adiabatic compression of a trapped Fermi gas. en. *Physical Review A* **63,** 033603. URL: `https://link.aps.org/doi/10.1103/PhysRevA.63.033603` (Feb. 2001) (cit. on p. 121).

145. Raizen, M. G., Wan, S.-P., Zhang, C. & Niu, Q. Ultrahigh-fidelity qubits for quantum computing. en. *Physical Review A* **80,** 030302. URL: `https://link.aps.org/doi/10.1103/PhysRevA.80.030302` (Sept. 2009) (cit. on p. 121).

146. Neuhaus, L. *et al. PyRPL (Python Red Pitaya Lockbox) — An open-source software package for FPGA-controlled quantum optics experiments* in *2017 Conference on Lasers and Electro-Optics Europe & European Quantum Electronics Conference (CLEO/Europe-EQEC)* (June 2017), 1–1. URL: `https://ieeexplore.ieee.org/document/8087380` (cit. on p. 148).

147. Gases, E. L. f. Q. *rp_out_amp* original-date: 2021-02-01T16:05:04Z. Sept. 2023. URL: `https://github.com/LQG-EPFL/rp_out_amp` (cit. on p. 148).

148. GmbH, C. O. G. *O-ring calculator* en-GB. URL: `https://www.cog.de/en/products/all-about-o-rings/o-ring-calculator,https://www.cog.de/en/products/all-about-o-rings/o-ring-calculator` (cit. on p. 150).

149. ewadmin. *Vacuum Bagging Basics - Epoxyworks* en-US. Oct. 2019. URL: `https://www.epoxyworks.com/index.php/vacuum-bagging-basics/,https://www.epoxyworks.com/index.php/vacuum-bagging-basics/` (cit. on p. 152).

Appendix **A**

Layout of Experiment

In this chapter, we give a detailed description of the laboratory layout and infrastructure.

A.1 Layout of the Room

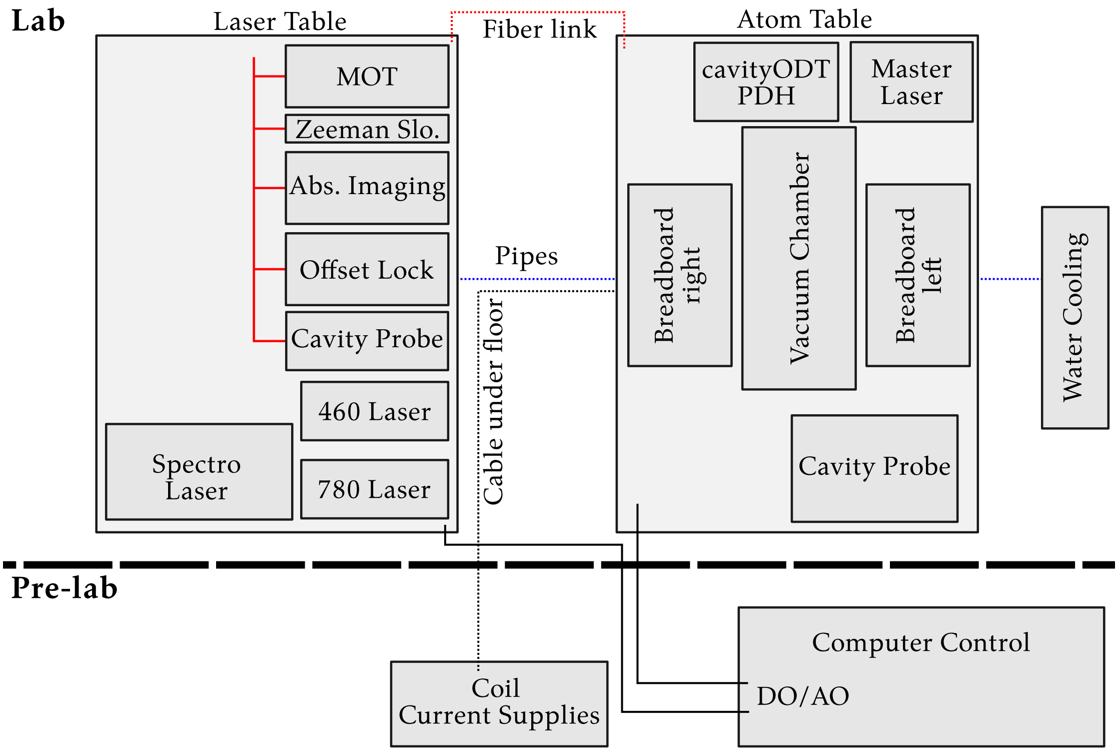
Lab
Laser Table
MOT
Zeeman Slo.
Abs. Imaging
Offset Lock
Cavity Probe
460 Laser
Spectro Laser
780 Laser
Fiber link
Pipes
Cable under floor
Atom Table
cavityODT PDH
Master Laser
Breadboard right
Vacuum Chamber
Breadboard left
Cavity Probe
Water Cooling
Pre-lab
Coil Current Supplies
Computer Control
DO/AO

Figure A.1: **Layout of Laboratory.**

Our laboratory is divided into two sections: the prelab and the lab (see Figure A.1). The two rooms are separated by two sliding doors. The laboratory is where the lasers and vacuum systems are located and is the site of the atom experiment. The lasers and radio-frequency devices are managed from the prelab. During normal operations (not when the lasers are adjusted), the experimenter sits in front of the control computer in the prelab. This minimizes thermal variations when entering the room and also improves laser safety. Both the laser and the vacuum systems are installed on two large damped optical tables (2 m × 3 m): the laser table and the atom table. Both tables are placed in their own air-conditioned compartments in the lab. To access the laser beams during alignment, the front panels of the enclosures are removed.

We send both optical and electrical signals between the two optical tables. This is achieved through optical fibers (fiber link in Figure A.1) and coaxial cables. Under each optical table we have constructed a rack where different electrical devices are placed (RF drivers for AOMs and EOMs, PID electronics, RF antenna driver, etc.). The RF amplifiers are placed on water-cooled metal plates, which reduces the heat load on the air-conditioning system and improves stability. A water distribution system, located in the laboratory, enables the regulation of water flow to the various devices. The water pipes are pulled under the floor of the laboratory. Most of the heat is generated by the MOT coils that surround the primary chamber of the experiment. In this area, water cooling is of utmost importance, as even slight alterations in the temperature of the vacuum chamber can cause misalignment of the cavity.

The current that flows through the coils is created by power supplies located in a rack in the prelab. The heat produced by the power supplies is dispersed in the prelab by cooling fans. Large cables (150 mm^2 for the MOT coils) running under the floor transport the current from the prelab to the coils. The H-bridge, which allows us to switch from a quadruple to a dipole configuration of the MOT coils, is located under the atom table.

A.2 Layout of Laser System

In this section, we provide a comprehensive outline of the laser system. A concise overview of the laser system, including all essential components, is provided in Section 2.1.3 of the main text.

The laser system is distributed over two optical tables (see Figure A.1). On the 'laser table' is where most of the lasers are located. The only laser that is on the atom table is the master laser, as it needs to be locked to the cavity with high bandwidth, and therefore the distance to the cavity matters. This is due to the time the signals travel through the cables.

We start our discussion of the layout of the laser system around the vacuum chamber. Then it is clear where all the beam lines are needed and what they are used for. Then we will go through all of the different setups marked in Figure A.1 in chronological order, meaning that we start with the laser source and then end up at the atoms.

A.2.1 Laser Beam Setup around Vacuum Chamber

There are three levels of optical tables that surround the vacuum chamber. The bottom layer, which is the top of the optical table, is used to distribute MOT and Zeeman slower light, as well as house the absorption imaging camera. The top layer is used to distribute the absorption imaging light. The middle layer is the most important, as it allows access to the cavity microscope.

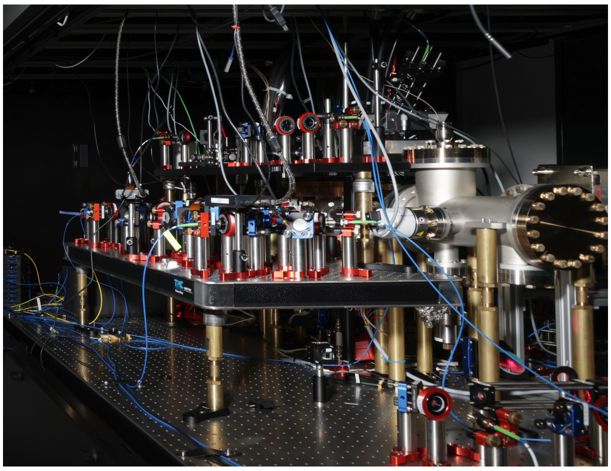

Figure A.2: **Picture of Experiment.** The pictures shows the vacuum chamber and the tree different layers of optics around it. The bottom layer a large optical table. The middle layers are two damped stainless steel breadboards and on the top we have two light aluminum breadboards.

Bottom Layer

As can be seen in Figure A.2, there are significantly fewer optical elements in the bottom layer. Ultimately, this surface was only used to separate the vertical and horizontal MOT beams and to create the Zeeman slower beam that is sent from the bottom into the chamber*. Finally, the camera used for absorption imaging is situated on the bottom layer.

Middle Layer

A map of the middle layer is presented in Figure A.3.

---

*There is a mirror in the pumping cross that reflects this beam (see Figure 2.1**a**). This design prevents the viewport from being covered with lithium evaporated from the oven.

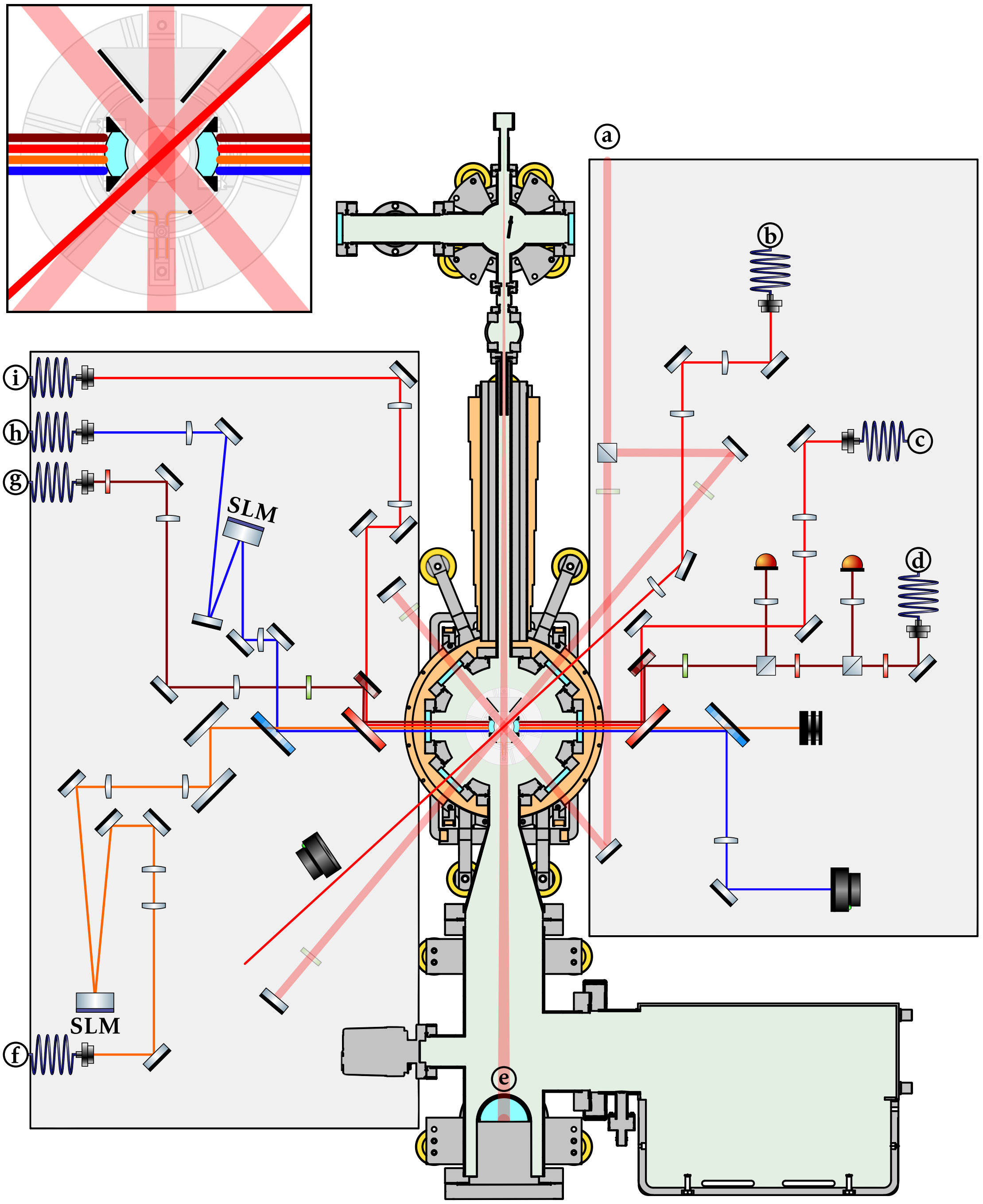

Figure A.3: **Map of Laser Beams around Vacuum Chamber (middle layer).** A magnified view of the cavity is displayed in the top left corner.

Most of the beams that couple to the cavity are injected from the left breadboard. This leaves enough space for the microscope optics, which includes the spatial light modulators (SLM) for

460 nm and 780 nm on the right. In the following, we will go through all of the beam lines:

a: MOT beams We transfer the cooler and repumper light from the laser table to the atom table in a fiber with crossed polarization. The fiber output is located in the bottom layer of the atom table, where it is divided into a vertical beam and a horizontal beam. The horizontal beam is then brought to the middle layer using a periscope, arriving on the left breadboard (see Figure A.3**a**) with a diameter of 1 cm. The beam is divided into two equal parts that are sent at an angle of 50° with respect to the cavity axis through the main chamber with circular polarization. On the other side of the chamber (right breadboard), the beams go through a quarter-wave plate and are reflected back. The two beams intersect at the center of the cavity, the place of the MOT. They pass between the cavity mirrors, the RF antenna, and the shield which protects the mirrors from the lithium emitted from the oven (see the inset in Figure A.3).

b: Sidepump beam The sidepump beam is used to send light onto atoms directly without passing through the resonator. The beam is focused on the cloud location with a waist of 60 µm. We have used this beam for our cavity cooling and Raman cooling experiments (see Section 3.3.4).

c, i: Cavity probe beam and single-photon counter Light is brought from the cavity probe setup to the left breadboard using a fiber (see Figure A.3**c**). We adjust the beam size to match the TM_{00} mode of the cavity with high efficiency. The light coupling out at the other side of the cavity (right breadboard) is injected into a fiber (see Figure A.3) which is plugged into a fiber-coupled single-photon counter located on the bottom layer of the atom table. This setup allows for cavity transmission and reflection spectroscopy (see Section 2.4).

d, g: PDH lock and dipole trap beam After being phase modulated in a free space EOM, the cavity lock light is coupled to a fiber and brought to the left breadboard (as seen in Figure A.3**d**). This beamline is shared with the counterpropagating dipole trap light (as seen in Figure A.3**g**). At the cavity, the dipole trap light and the PHD light are circularly polarized but in orthogonal directions. The back-reflected PHD light is detected on the photo diode closest to the cavity, while the dipole trap power is measured on the other photo diode. Since the dipole trap and the PHD lock operate on two different transverse modes of the cavity, no interference is observed at low frequency between the beams. The lenses in the beam path are adjusted to ensure the highest degree of compatibility with the cavity mode.

e: Zeeman slower beam The Zeeman slower beam is extracted from a fiber at the bottom layer of the atom table and then directed up to the middle layer through a viewport (as seen in Figure A.3**e**). Once in the vacuum chamber, the beam is deflected 90° into the horizontal direction using a gold-coated in-vacuum mirror made of stainless steel. This mirror was crafted and polished in-house, as the optical flatness is not a major factor for this beam. The Zeeman slower beam then travels orthogonally through the cavity (see inset in Figure A.3) and directly into the oven. A lens located at the bottom layer of the atom table focuses the beam into the oven.

f: Optical tweezers beam The light from the laser table is transmitted through a fiber and then out-coupled onto the right breadboard (as seen in Figure A.3**f**). The beam is then reflected off a spatial light modulator (SLM) and directed into the cavity lens. Two telescopes (two pairs of lenses) are placed before and after the SLM to adjust the size of the beam to the SLM and the cavity lens. After passing through the cavity microscope, the beam is absorbed in a beam dump.

h: Control beam The blue control beam, which is out-coupled from a fiber, is reflected off an SLM in a manner similar to the tweezers beam. Contrary to tweezers beams, since the focal length of the cavity lenses is not half of the cavity length for 460 nm, the beam must be defocused before entering the cavity lens, with the distance between the focus and lens being 26 cm. This configuration is shown in Figure A.4.

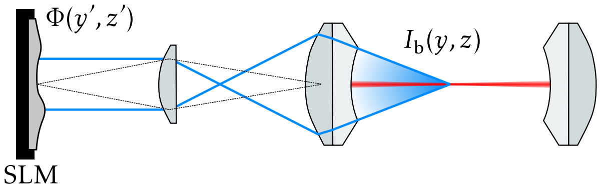

Figure A.4: **SLM Setup.**

The control beam is focused when it reaches the SLM. A lens between the SLM and the cavity lens is used to compensate for the shorter focal length. The compensation lens projects the SLM surface onto the cavity lens, guaranteeing that all rays that hit the SLM pass through the cavity lens. More details on how the SLM setup was used to remove aberrations from the cavity lens and carry out a scanning microscopy of the atomic cloud can be found in Chapter 4.

Top Layer

Here is a list of setups located on the top layer:

- **MOT beam:** A mirror is situated at the top of the breadboard, causing the vertical MOT beam to be reflected back.
- **Absorption beam preparation:** The absorption beam is taken out of a fiber and expanded to the appropriate size for imaging. A unique feature of this setup is the mask, which is a SNOM tip placed in the path of the absorption beam. This is used to shorten the length of the atomic cloud by expelling the edges with resonant light (see Section 2.2). The tip is incorporated into a two-lens telescope so that its shadow is projected onto the atoms. The tip is placed on a 3D translation stage for precise alignment with the atomic cloud.
- **Fluorescence imaging:** A camera situated on the uppermost breadboard was utilized to capture an image of the center of the chamber. This was especially useful at the start of the experiment as it aided in the positioning of the MOT with the cavity center.

A.2.2 Master Laser: From the Source to the Atoms

The master laser is located on the atom table (see Figure A.1), as close to the cavity as possible. This reduces delays in the feedback loop and allows for higher locking bandwidth. The optical setup is illustrated in Figure A.5.

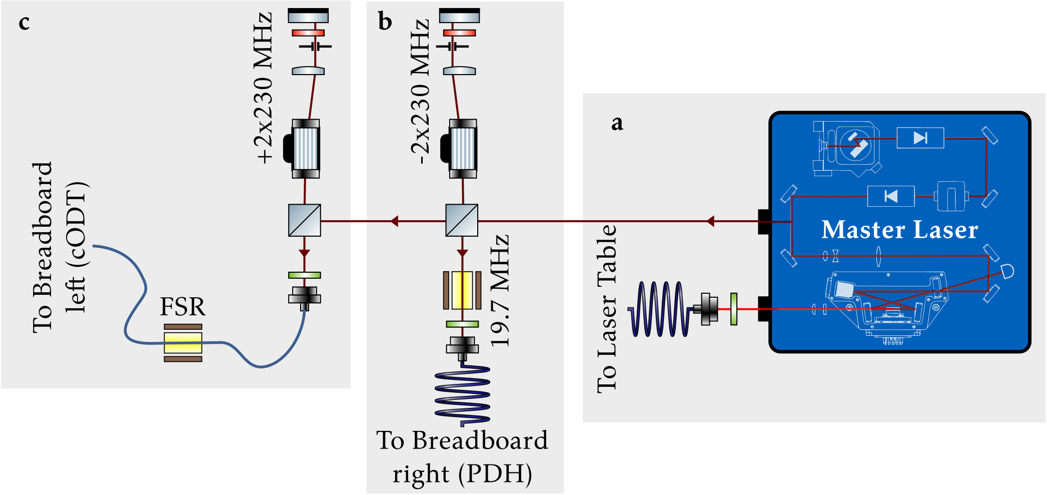

Figure A.5: **Master laser setup.**

A diode laser emitting at 1342 nm is amplified to 1.8 W and then frequency-doubled in a cavity to generate 1 W of red light, which is coupled into a fiber and sent to the laser table (see Figure A.5**a**). A variable beam splitter is used to extract some light after the amplifier (roughly 50 mW). This light is divided into two double-pass AOMs. The first double-pass AOM (illustrated in Figure A.5**b**) reduces the laser frequency by 460 MHz and outputs it into a free space EOM (QuBig) operating at 19.7 MHz. This light is then injected into a fiber and sent to the left breadboard (**d** in Figure A.3) where it is used to implement a PDH lock. The second double-pass acousto-optic modulator (shown in Figure A.5**c**) increases the frequency of the laser by 460 MHz, which is then transmitted to the right breadboard via a fiber (see Figure A.3**g**) where it is used for the dipole trap.

The red light at 671 nm that is transmitted to the laser table is used for the MOT, the Zeeman slower, the cavity probe and to stabilize the length of the cavity. The main beamline is illustrated in Figure A.6.

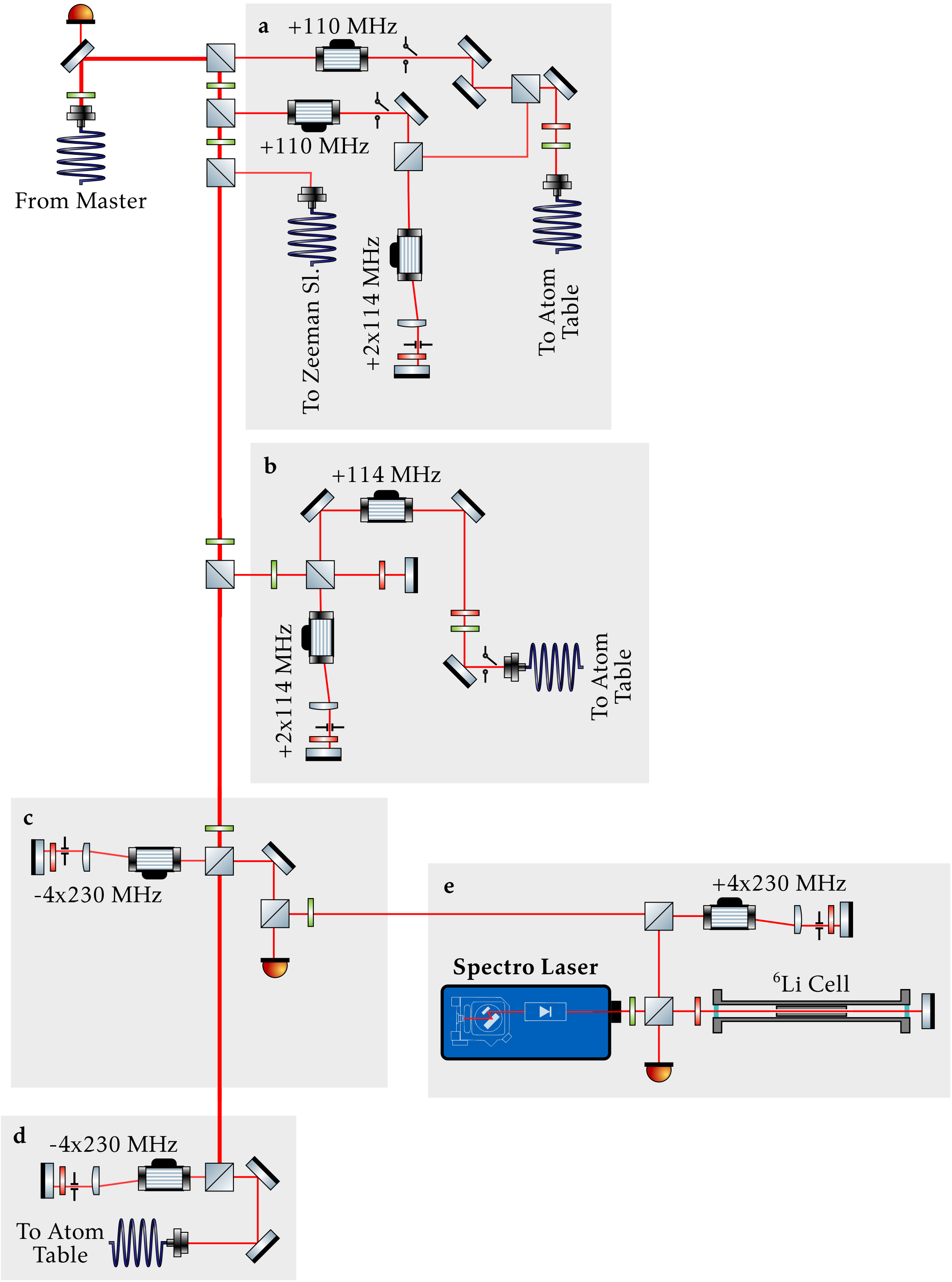
From Master
a
+110 MHz
+110 MHz
To Zeeman Sl.
+2x114 MHz
To Atom Table
b
+114 MHz
+2x114 MHz
To Atom Table
c
-4x230 MHz
d
-4x230 MHz
To Atom Table
e
+4x230 MHz
Spectro Laser
^{6}Li Cell

Figure A.6: **Layout of master beamline.**

In the following, we go through each setup:

a: MOT and Zeeman slower setup We require light at three different frequencies for the MOT and Zeeman slower setup. The Zeeman slower is red-shifted from the MOT cooler by 110 MHz and the repumper is blue-shifted from the MOT cooler by the hyperfine splitting of 228 MHz. A polarizing beam splitter is used to branch off the Zeeman slower light from the master beamline and inject it into a fiber. A shutter is placed in front of the fiber input to enable the Zeeman slower light to be switched. The cooler beam is branched off the main beamline and passes through a blue-shifting acousto-optic modulator (AOM) operating at 110 MHz. This AOM can be used for fast switching and power setting. The repumper setup is similar, but the beam also passes through a double-pass AOM bridging the hyperfine splitting of ^{6}Li. Both beamlines are equipped with a mechanical shutter (SRS) to completely remove light during the experiment (after loading the MOT). The two beams are combined on a polarizing beam splitter with orthogonal polarization and then injected into a fiber that brings them to the bottom layer of the atom table.

b: Imaging setup This setup is used to prepare light for absorption imaging. We also use it to project a mask, which helps to reduce the size of the atomic cloud in the cavity direction. Generally, imaging setups only use one frequency of light, and the MOT beams can be used for repumping. However, this is not suitable for our setup since it would mean that the part that is shielded by the mask would also be illuminated with light. Therefore, we opt for a two-colored imaging scheme, which combines cooler and repumper light in the same fiber. Essentially, the imaging setup is a replica of the MOT setup, with the order reversed. That is, after the two beams are combined, they go through a single-pass AOM, changing their frequency. Then, the beams are transferred to the top layer on the atom table in the same fiber with crossed polarization. Additionally, there is a mechanical shutter to be able to completely shut the beam off when not needed.

c, e: Frequency offset lock between the master and the spectro laser We use a beating lock between the spectroscopy laser and the master laser to maintain the cavity length, as described in Section 2.1.3. This is demonstrated in Figure A.6, parts **c** and **e**. The light emitted by the spectro-laser passes through a spectroscopy cell containing a hot lithium vapor. A mirror after the spectro cell reflects the beam back. A quarter-wave plate is placed in front of the spectroscopy cell, which rotates the polarization of the back-reflected light by 90°, causing it to be deflected by a polarizing beam splitter onto a photo diode. This enables us to detect the saturated absorption signal on the photodiode. To lock the spectro-laser to the crossover, the current of the laser diode is modulated and the signal on the photodiode is demodulated to generate the error signal. The master beamline and the spectro-laser emit light which is shifted in frequency in opposite directions by two second-order double-pass AOMs operating at 230 MHz. The beams are then combined in a 50:50 beam splitter and sent to a high-bandwidth fiber-based photodetector (Thorlabs DX12CF). This produces an electrical beating signal between the lasers, which is used to maintain the frequency difference between them.

d: Cavity probe frequency shifter The majority of the cavity probe system is located on the atom table, while the second-order broadband double-pass AOM used for frequency sweeps of the cavity probe light is situated on the laser table (see Figure A.6**d**). An optional fiber-EOM can be inserted into the cavity probe beamline, allowing us to probe multiple longitudinal cavity modes spaced by multiple free-spectral ranges at the same time. This has been used to measure the temperature of the cloud (see Section 3.3.3).

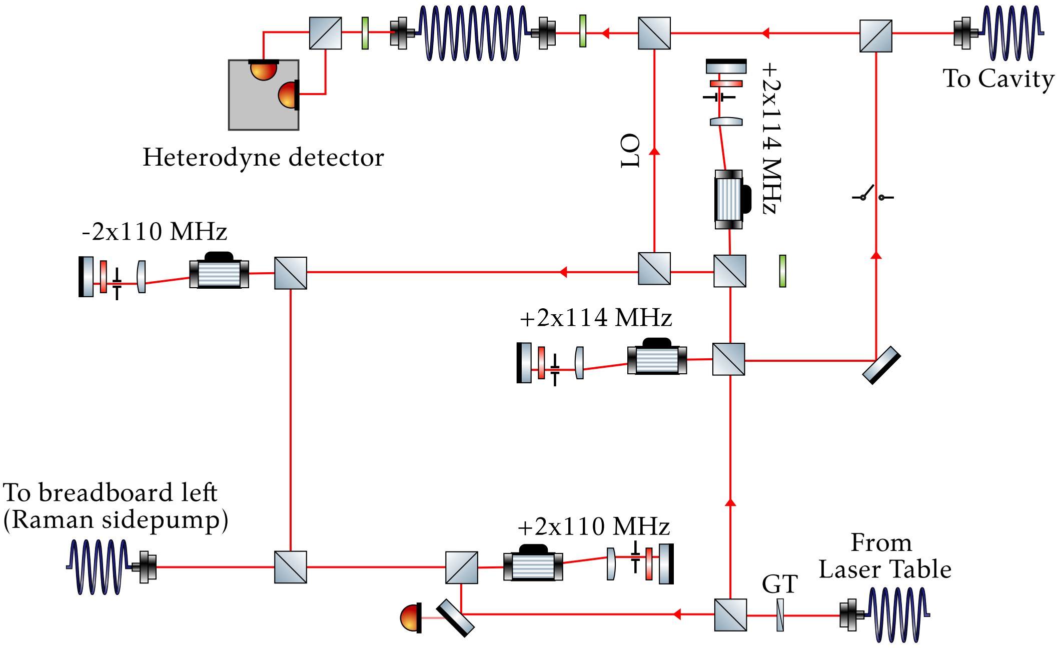

Figure A.7: **Cavity probe setup.**

The beamline of the cavity probe is shown in Figure A.7. It consists of the cavity probe beam, a heterodyne detector, and three different beamlines to direct light onto the atoms from the side, one vertical and two horizontal. This setup has been used for cavity cooling and Raman cooling experiments. The light is transmitted from the laser table to the atom table via a fiber. A Glan–Thompson polarizer is placed after the fiber to ensure that the polarization of the light in the cavity probe is linear and constant. The light is then divided into two beams, one for the cavity probe and heterodyne and the other for all the sidepumps. A photodiode placed after a mirror monitors the power of light arriving at the cavity probe setup. This signal is used to stabilize the power during frequency sweeps of the cavity probe.

A.3 Layout of Imaging Setup

In total, four cameras are installed. Here, we provide an overview of their locations.

- **Blue camera:** The camera used to capture the blue control beam is situated on the left breadboard of the middle layer (see Figure A.3). It is utilized to calibrate the SLM's operation and to carry out two-photon imaging (see Section 2.3).

- **Top fluorescence:** This camera is situated on the uppermost layer and is utilized to capture images of the MOT. Specifically, it is used to determine the relative position of the MOT and the cavity.

- **Side fluorescence:** This camera is situated on the right side of the middle layer breadboard (see Figure A.3). It is used to measure the position and size of the MOT, and the images in Figure 2.10**a,b** were taken with it.

- **Absorption camera:** This camera is situated at the lowest level. We utilize it to capture the cloud with a beam originating from the top. The image in Figure 2.10**c** was taken with this camera. Additionally, the calibration of the light shift Figure 5.8 was performed using this camera.

A.4 PID Loops in the Experiment

This section provides an overview of the feedback loops used in our experiment. A list of the loops can be found in Appendix A.4.1. The red pitaya, which is used for most of the feedback loops in the lab, is discussed in Appendix A.4.2. Finally, Appendix A.4.3 explains the feed-forward scheme that enables us to rapidly adjust the atom-cavity detuning during the sequence.

A.4.1 Detailed Overview of Feedback Systems

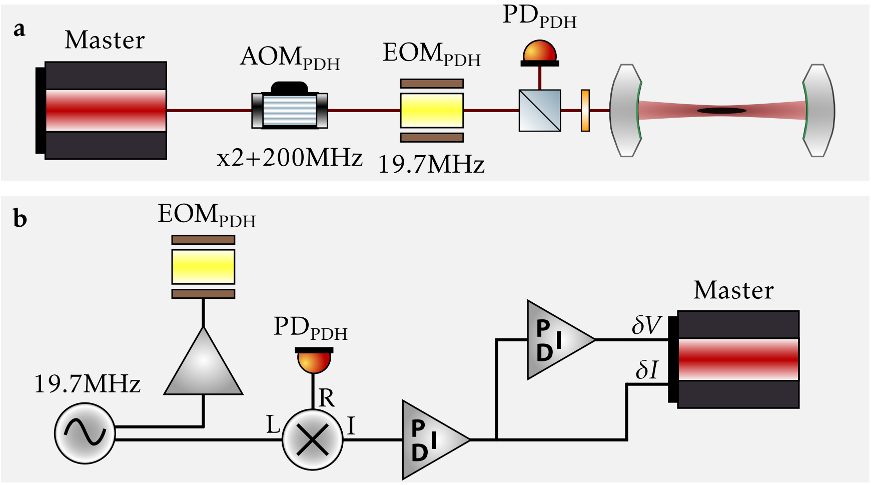

Figure A.8: **Map of feedback loops.**

Cavity Lock The cavity lock ensures that the master laser is in precisely resonance with the cavity. To do this, we have implemented a PDH locking scheme. Figures A.5**b** and A.3**d** show the optical setup. The feedback loop is electrically implemented with a fast analog lockbox (Toptica's Falc pro) combined with a FPGA (Red Pitaya). The Falc produces the error signal by demodulating the photodiode signal in phase with the EOM modulation and implements a fast PID circuit, whose output is connected to the DC port of the laser diode current. This allows quick corrections of the laser frequency (1.8 MHz bandwidth). The Red Pitaya takes the output signal of the Falc as input and implements a second integrator that acts on the piezo of the laser.

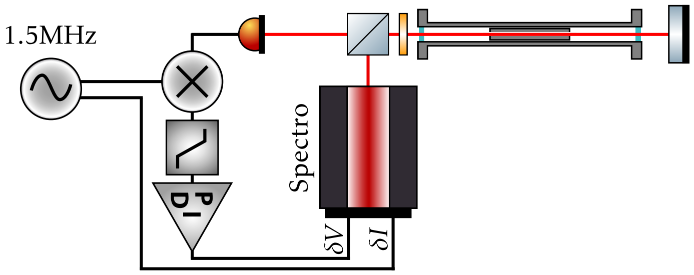

Figure A.9: **Map of feedback loops.**

Spectro Lock The spectro laser is locked to the crossover lying between the two hyperfine ground states of ^{6}Li. A Red Pitaya is used to implement the feedback loop. The error signal is created by modulating the laser current and demodulating the spectroscopy signal obtained from saturated-absorption spectroscopy. The feedback has a bandwidth below 1 kHz.

Beating Lock

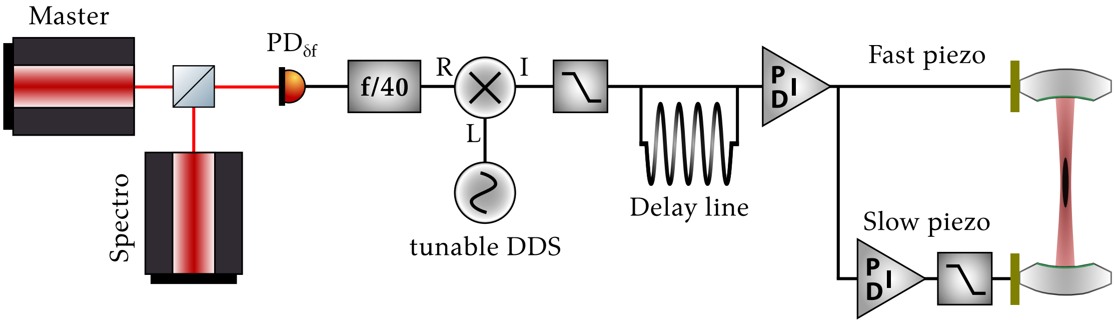

Figure A.10: **Map of feedback loops.**

Spectro Lock The beating lock stabilizes the relative frequency detuning between the master and spectro lasers. This is done optically by having both lasers interfere on a fast fiber-coupled photodiode, as shown in Figure A.6**c**. We reduce the output frequency of the amplified photodiode by a factor of 40 using a frequency divider (Pasternack PE88D40000). This enables us to measure beating frequencies ranging from 100 MHz to 12 GHz with regular RF electronics. The downscaled signal is then mixed with a tunable reference frequency. The output signal is filtered with a lowpass filter and fed into an analog frequency discriminator based on a delayed self-heterodyne technique. This generates an error signal that is used adjust the cavity length by acting of the cavity piezos. Similarly to the cavity lock, we implement a feedback loop based on two PIDs. A fast integrator acting on the fast cavity piezo and a slow double integrator removing slow drifts of the cavity length due to temperature fluctuations in the laboratory.

Cavity-enhance Optical Dipole Trap Power Regulation The intensity noise in the dipole trap leads to heating of the atoms that are trapped. Consequently, power stabilization is required. Figure A.11 displays a schematic of lock stabilizing our cavity-enhanced optical dipole trap. In summary, we inject light into the cavity and measure the transmitted power. To control the power of the dipole trap, we adjust the RF power sent to a double-pass AOM on the cODT path (see Figure A.5**c**).

The complexity of locking the dipole trap is largely due to the thermal Kerr effect, which causes the resonance frequency of the trap to be dependent on the power. This is largely corrected by the PDH cavity lock. However, since our cavity is near-concentric, its transverse mode spacing also depends on the intensity of the dipole trap. Therefore, the frequency difference between the dipole trap beam and the PDH beam must be stabilized (AOM in Figure A.6**b,c**). This was accomplished by using a dither lock on the dipole trap beam to act on the frequency of the PDH double-pass AOM. By acting on the PDH frequency while keeping the offset frequency between the master laser and the dipole trap constant, a fixed frequency relation between the master laser and the TM$_0$0 modes of the cavity is established. As a result, the relative frequency stability between the doubled 671 nm light and the 671 nm TM$_0$0 cavity mode is improved.

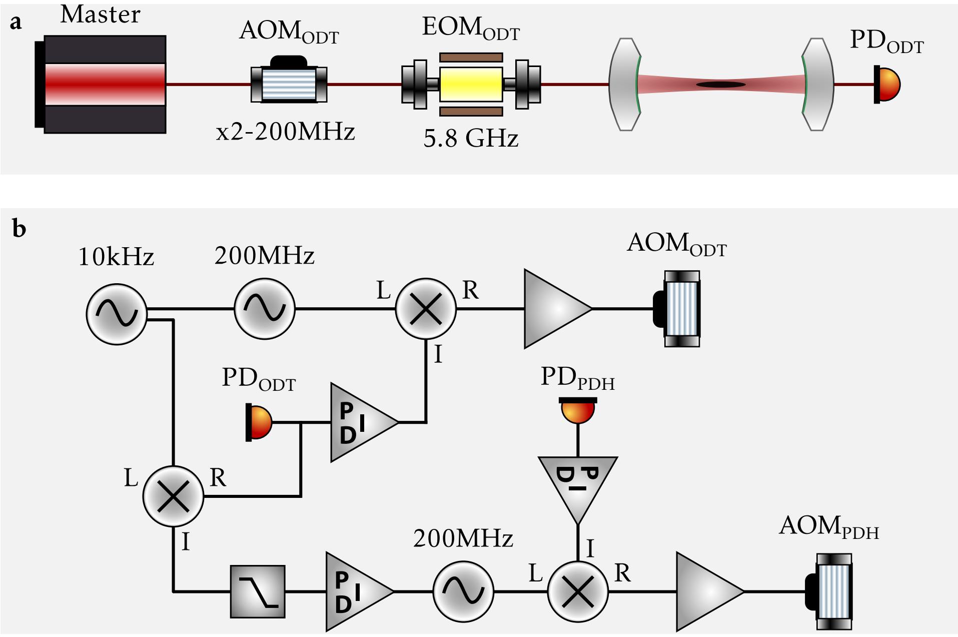

Figure A.11: **Map of feedback loops.**

Cavity Probe Power Regulation For our experiment, we need a consistent power of the cavity probe. Especially when the frequency of the cavity probe is altered, the power can vary as a result of changes in the efficiency of the double-pass AOM. We measure the power of light that reaches the atom table using a photodiode that collects the light that passes through a mirror (see Figure A.7). A PID loop based on a Red Pitaya is employed to regulate the RF power sent to the double-pass AOM located on the laser table (see Figure A.6**d**) in order to maintain the monitored laser power constant.

PDH Power Regulation The gain of the PDH feedback look is directly proportional to the power of light that reaches the photodiode. Since fiber couplings can drift over time, this power can change and therefore the lock can become less optimal. Therefore, we implemented a power lock that acts on the PF power sent to the double-pass AOM (see Figure A.5**b**). This PID is implemented using a Red Pitaya.

Bottom Flange Temperature Stabilization Our cavity system is very sensitive to temperature changes. Therefore, the temperature of our vacuum chamber was regulated to ensure the long-term stability of our experiment. This was done with a Peltier element that was connected to the chamber. The hot side was cooled by a standard CPU cooler. To prevent the fan from influencing the cavity, it was removed from the CPU cooler and mounted on an optical post on the optical table. Temperature stabilization was electrically implemented with a Peltier controller from Meerstetter Engineering GmbH.

A.4.2 RedPitaya for PIDs

The red pitaya is a test and measurement board that is powered by a fast FPGA. It has two analog inputs and two analog outputs. By using pyRPL, a Python-based library created by Leonard Neuhaus [146], it can be used as a lockbox, lock-in amplifier, oscilloscope, spectrum, network analyzer, and many other combinations. We have also developed an analog amplifier to reduce noise at the red pitaya output [147].

A.4.3 Feed-forward Scheme

In the course of each experimental sequence, we must alter the atom-cavity detuning. This requires us to adjust both the cavity length and the laser frequency in order to keep the cavity dipole trap constant and the atoms confined. Although the laser and cavity can be locked to each other with high bandwidth, relying on the feedback loop for changes in the configuration is not stable and fast enough, as it would require a very large dynamic range. Therefore, we opt for a feedforward scheme. By using an analog signal that is divided into three signals with different gain acting on the cavity piezo, the laser piezo, and the variable reference frequency of the beating lock, we can synchronously change the cavity length and the laser frequency so that they remain close to resonance. Precision fine-tuning is achieved with the PID feedback loops mentioned above. Electrically, the splitting and amplification of the signals is realized with a custom electrical device based on analog multipliers, whose gain can be adjusted using potentiometers on the front panel.

Appendix B

Design and Construction of the MOT coils

Our MOT coils are based on a design of compact bulk-machined electromagnets that was published by our group [73]. In this Section, we will explain the construction steps. We will also emphasize the distinctions between our design and the one that was published.

B.1 Design of Coils

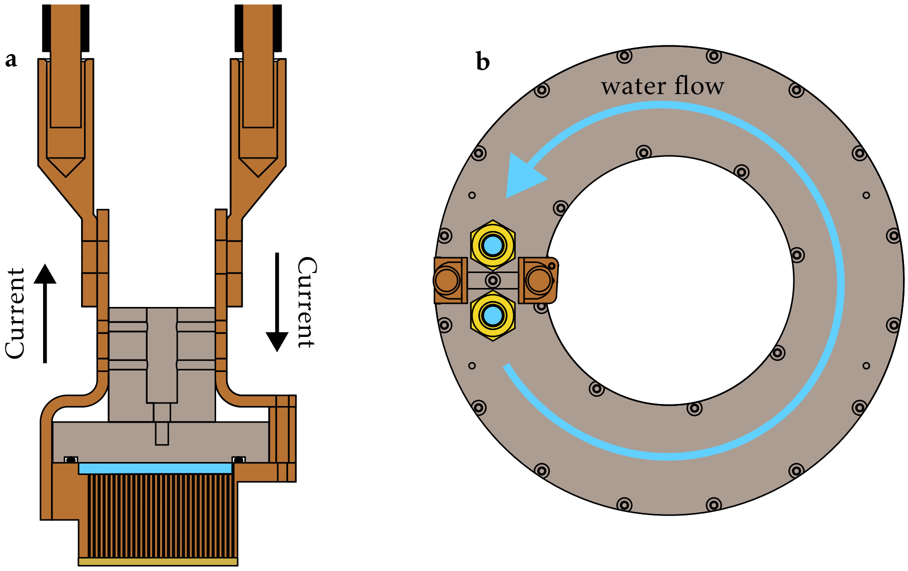

Figure B.1: **Schematic Drawing of Coil Design.**

Our coils are composed of two distinct components: a copper coil with cut windings and a plastic cap (PEEK). A water channel between the cap and the copper allows for direct cooling of the windings. The copper coil has a T-shaped cross section, with a thick center part where the windings are cut out and narrower wings forming the first and last windings. The first and last windings act as a flange with tapped holes, which are used to attach the PEEK cap to the coil and guarantee a watertight seal. The grooves in the PEEK cap determine the position of the o-rings that are outside of the narrow windings, ensuring their effective water cooling. There are several online tools that help you dimension the grooves for a precise seal [148].

B.2 Difference to Published Design

Our MOT coils are constructed around the primary chamber, which eliminates the spatial restrictions posed by the reentrant viewport discussed in the paper. As a result, the complexity of the assembly is reduced. Specifically, our design does not require drilling into the copper windings to secure the Peek cap or provide the current. Furthermore, all the coils windings are cooled with direct contact to cooling water, something that was not achievable in the prior design as the sealing surface where the o-ring touches was at a smaller radius than the last winding.

B.2.1 Assembly Procedure

The assembly procedure used to manufacture the our MOT coils is summarized in this section.

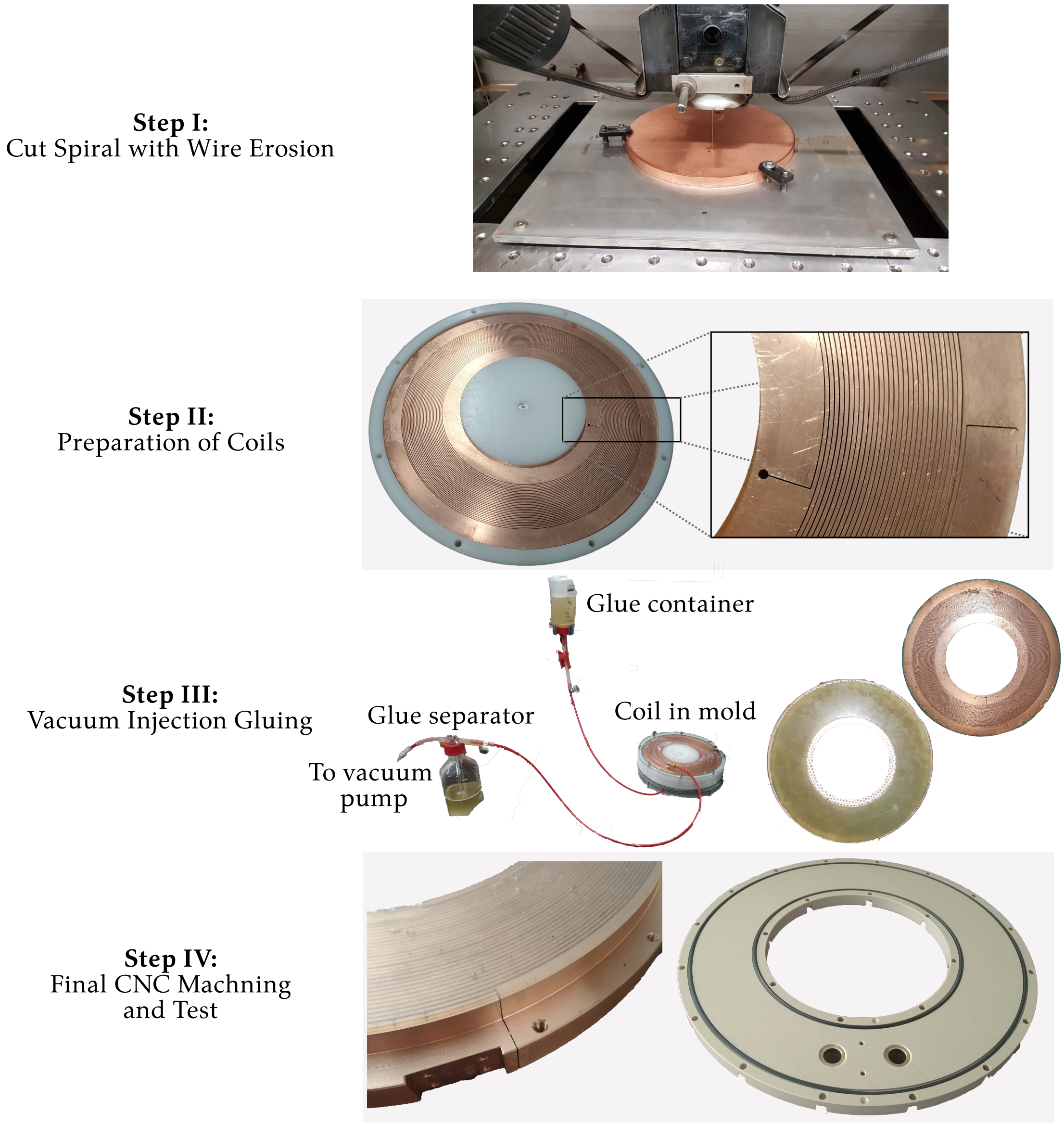
Step I:
Cut Spiral with Wire Erosion
Step II:
Preparation of Coils
Step III:
Vacuum Injection Gluing
Glue container
Glue separator
Coil in mold
To vacuum pump
Step IV:
Final CNC Machning and Test

Figure B.2: **Assembly procedure for the coils.**

Step I: Wire Erosion of the Copper Disk The fabrication process begins with the cutting of a spiral into an OFHC copper disk. For this, the disk was mounted on a wire erosion machine with a special aluminum adapter (see Figure B.2**I**). The holes were drilled in the disk before wire erosion, through which the wire was fed. It is essential to not cut the disk all the way to the edge, as this would make assembly and alignment much more challenging. When handling the coil after wire erosion, we made sure to transport it on a plate to prevent the copper from bending.

Step II: Preparation of Mold and Coil After cutting the spiral into the copper disk, it was washed with industrial soap to remove any residue of grease and oil from the surface. We then submerged the coil in a 50 % acidic acid solution for a few hours until the entire oxide layer was removed. After cleaning, the coil was heated at 90 °C in a vacuum for the entire night. We were careful to handle the coil only with gloves, as fingerprints can easily be left on the exposed copper. At the same time, we applied FormulaFive Mold Release to the mold. After baking, we inserted the coil into the mold and placed chips of size 23 × 10 mm cut from a thin sheet of glass fiber epoxy into the spiral gap. We visually inspected the windings to make sure that the copper was not touching. This process was very laborious as we had to place more than 100 spacers in the coil. The final product can be seen in Figure B.2**II**

Step III: Vacuum Injection Gluing The most essential part of the assembly process is the adhesion of the coils using epoxi glue. The glue was mixed with glass fibers and the bubbles were removed under vacuum. It is imperative to have an airtight mold for this assembly step. In our experiment, we neglected to check the mold before using it, which caused bubbles to form during injection. It is suggested to test if the chamber can maintain a vacuum for a prolonged period. In the same way as the vacuum bagging technique [149], the glue is injected from the container into the bottom of the mold and then extracted from the top. The exhaust is then filtered through a separator to stop the glue from entering the pump. After it has cured, the coil can be removed from the mold. It is essential to consider the removal process in advance, as it could require a lot of effort if the mold is not designed properly.

Step IV: Final CNC Machining and Test In the last step, the coil was given its final form. We used CNC milling to remove excess glue and free the spiral. This is also when the tapped holes and electrical connections were established. The PEEK cap, which seals the water channel, was also created with CNC milling. Examples of the finished product can be seen in Figure B.2**IV**. After attaching the PEEK cap to the copper coil, we tested it for water leaks under 1 bar pressure. To ensure a good seal, it is important to polish the surface of the coil where the o-ring touches. If a leak is detected (as was the case for one of our coils), a sheet of epoxy-infused glass fiber mesh can be glued to the bottom part of the coil, which solved the problem. At the last stage, we coated the exterior of the copper coil with an electrically insulating transparent varnish. This helps to protect the coil from oxidation and reduces the possibility of short circuits. Before installing the coils in the setup, the electrical performance was evaluated. We mapped out the magnetic field and gauged the heating of the coils at the highest current, which enabled us to determine the least amount of water flow needed.

B.3 Mistakes and Possible Improvements of the Design

- Make sure that the mold is vacuum-tight before gluing.
- Reduce the time before mixing of glue and gluing, as fibers tend to separate from the glue because of gravity.
- Design the mold so that the coil can be easily removed.

Appendix C

Assembly of the Optically-Contacted Cavity Microscope

In this section more details of the assembly procedure shown in Figure 1.8 are given.

C.1 Step I: Optical Contact Between Mirror and Lens

The cavity mirror and the aspherical lens were fixed together using optical contact. To do this, the two optical elements were aligned, and then a drop of water was inserted between them. This caused the two components to bond directly to each other. To achieve good optical contact, the lens and mirror surfaces were repeatedly cleaned using the drag-wipe technique and then inspected under a microscope to ensure that no contaminants remained. The two elements were then mounted on custom mirror mounts that allowed them to touch each other.

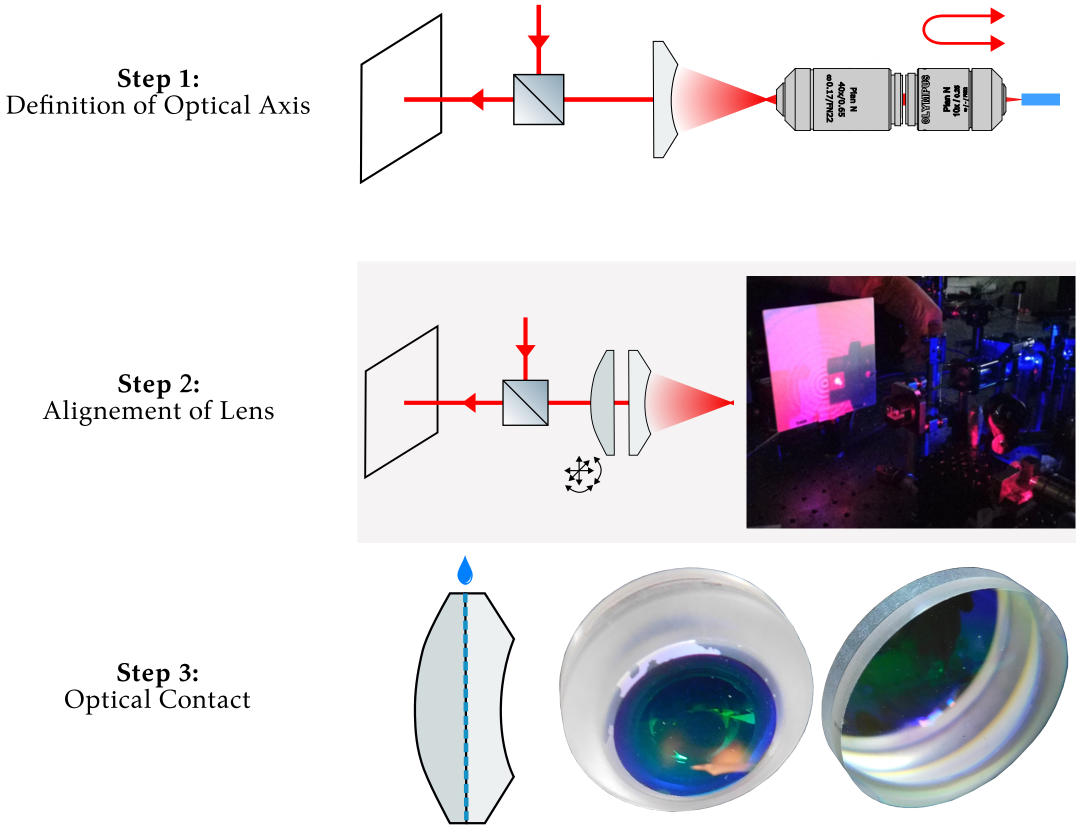

Figure C.1: **Assembly Procedure for Optically Contacted Cavity Lens.**

In the following, we will detail the alignment and optical contact procedure. A schematic view of the most important steps is shown in Figure C.1.

The laser beam is reflected off the mirror to form an optical axis. We ensure the beam is aligned to the mirror by overlapping the back reflections from the flat and spherical surfaces. On the opposite side of the mirror, two achromatic objectives are combined to backcouple light into a fiber. If the focus of the second objective coincides with the spherical surface of the mirror, the reflection is coupled back into the fiber. We use the back-reflection signal to detect any movement of the mirror. Additionally, blue light was sent through the fiber to evaluate the optical performance of the cavity lens.

In the second step, the lens is aligned with the optical axis using a 5-axis stage. The tip-tilt combination is very critical for good optical contact. We have aligned it by mechanically pressing the lens onto the mirror and then clamping it on the mount. We were able to align the lens by overlapping the different back reflections with the optical axis on a screen (see the picture in Figure C.1).

Once the two components were arranged in the correct position, we increased the space between them and added a drop of water. We then pushed them back together and left them for the night. After that, we removed the cavity lens from the setup and heated it to 70 °C for 1 h under a vacuum. A picture of the final assembly can be seen in Figure C.13.

C.2 Step IV: Cavity Alignment

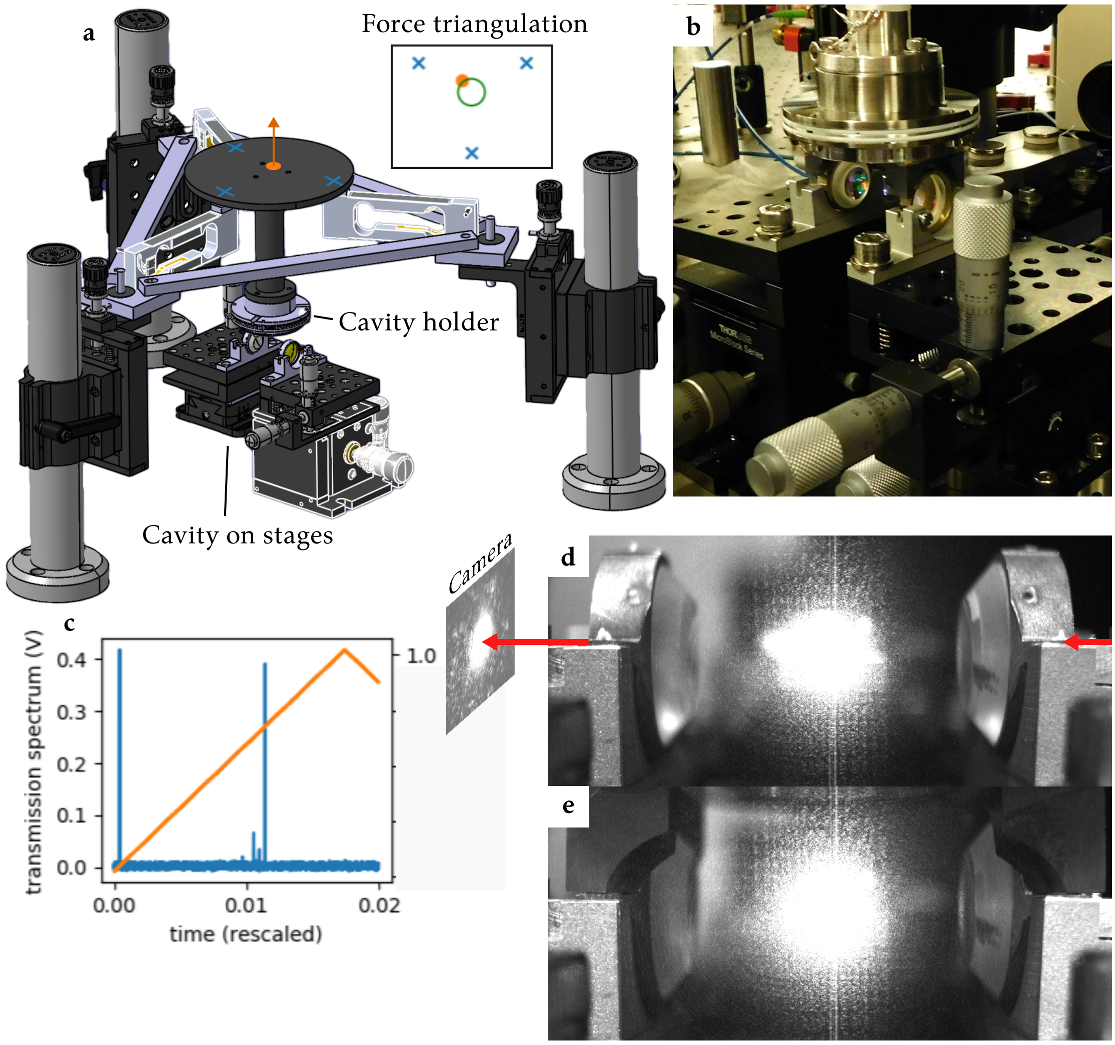
a
Force triangulation
b
Cavity holder
Cavity on stages
Camera
c
d
e
transmission spectrum (V)
0.4
0.3
0.2
0.1
0.0
1.0
0.00
0.01
0.02
time (rescaled)

Figure C.2: **Setup for Alignment and Gluing of Cavity.** **a**, Rendering of the setup. **b**, Picture of the setup. **c**, Graph of cavity transmission when laser is swept. **d**, Picture of side-view camera when glue is applied. **e**, Picture of side-view camera when holder is lowered.

The experimental setup for cavity alignment and gluing, as shown in Figure C.2**a**,**b**, consists of two components: a pair of five- and six-axis stages to precisely position the mirrors and a construction of six linear stages and force sensors to accurately position the cavity support before gluing.

The cavity assembly is divided into two stages: initially, the two mirrors are adjusted to align with each other, and then the holder is placed and secured with a vacuum-compatible adhesive.

The cavity and lenses required two alignment requirements. We wanted the cavity mode to be accurately centered in the mirror, and the lenses to image the center of the cavity where the atoms are held. Due to the geometry of the cavity lenses (focus coincides with the center of the mirror), these two conditions were connected. We decided to use the imaging capability of the setup to align the cavity. This was done by injecting 460 nm light into a tapered fiber tip, which is usually used for scanning near field optical microscopy (SNOM), and using it as a point source. As in [26], the fiber tip was placed in the center of the cavity. When the lenses were correctly aligned, the image of the tip would coincide with the cavity mode transmitted through the cavity. The cavity transmission was monitored on a photodiode and a camera. The peaks in the photodiode signal (see Figure C.2**c**) were from the different modes of the cavity. The spacing of the peaks enabled us to precisely adjust the cavity length.

Once we were convinced of the correct alignment of the cavity, we applied glue to the wings of the mirror (see Figure C.2**d**) and lowered the cavity holder onto the mirrors (see Figure C.2**e**). We used force sensors to measure the force at the points marked by the blue crosses in Figure C.2**a**. By triangulating the forces, we can estimate the force vector applied to the cavity support due to pressing on the mirrors (orange arrow). With the help of the pictures taken from two cameras on both sides, we were able to position the holder on the mirrors (see Figure C.2**d**). It took 24 h before the glue had completely cured. After that we were able to release the mirrors from the states. Then the cavity is held by the holder from above. We confirmed that the mode of the cavity was still aligned. The final cavity was then placed in a dust-free box for storage.

The cavity was misaligned after being heated during the initial bakeout of the vacuum chamber, so the process had to be repeated. To ensure success on the second attempt, we only exposed the cavity to a dry atmosphere with nitrogen. This enabled us to achieve a good vacuum in the main chamber without having to go through the bakeout process again.

CURRICULUM VITAE

NICK SAUERWEIN

PhD Student in Laboratory for Quantum Gases, EPFL

German ☎ +41 78 740 96 54 @ nicksauerwein@hotmail.de ✉ Avenue de Milan 28, 1007 Lausanne
in https://www.linkedin.com/in/nick-sauerwein-313a36b7/

EXPERIENCE

Doctoral Assistant

EPFL Lausanne

11/18 - ongoing Lausanne, Switzerland

in the group LQG of Prof. J.-P. Brantut working on the microscope experiment.
Skills: quantum optics, ultra cold atom physics, vacuum technology, laser technology

Research Assistant

EPFL Lausanne

01/18 - 10/18 Lausanne, Switzerland

in the group LPQM of Prof. T. J. Kippenberg, working on the project of circuit optomechanics.
Skills: Superconducting microwave circuits, cryogenics, web applications

Research Internship

École Polytechnique, Laboratoire Leprince-Ringuet, CNRS, CEA

09/16 - 02/17 Paris, France

"Theory and Experimental Test of Electron Spectrometers for Laser Wakefield Accelerators",
Supervised by Dr. A. Specka.
Skills: Electron optics, numerical regularization, image recognition

Research Internship

Paul-Scherer-Institute

06/16 - 09/16 Villigen, Switzerland

"Laser-based Electron Acceleration by an Intense Thz Pulse from a Needle Cathode",
Supervised by Dr. C. Hauri.
Skills: CPA, nonlinear optics, adaptive optics, FEM simulations, vacuum technology

Teaching Assistant

ETH Zürich

03/13 - 06/17 Zürich, Switzerland

- Numerical Methods (*Dr. V. Gradinaru*)
- Mathematical Methods for Physics I & II (*Prof. Dr. G. Felder*)
- Calculus II (*Prof. Dr. M. Einsiedler*)

"Jugend-forscht" Project

ThermoSolar AG

09/11 - 04/13 Ziar nad Hronom, Slovakia

"Thermal Hybrid Solar Systems"
Skills: organic rankine cycles, industrial control systems, heating systems

LANGUAGES

German
Mother tongue

English
Fluent

French
Good speaking and writing skills

Swiss German
Good understanding

Croatian
Beginner

SOFTWARES

Python Django HTML
MatLab C C++ Linux
GNU LaTex Mathematica
Microsoft Office Solidworks
Catia OpenFoam Ansys
Comsol

HOBBYS

Skiiing, sailing, swimming, mountain biking, canoeing, rowing, running, movies, dancing

PUBLICATIONS

Journal Articles

- Sauerwein, Nick et al. “Engineering random spin models with atoms in a high-finesse cavity”. In: *Nature Physics* (Mar. 2023).
- – “Vibration damping platform for cavity quantum-electrodynamics experiments”. In: *Rev. Sci. Inst.* 93.3 (Feb. 2022), p. 033203.
- Joshi, Yash J. et al. “Automated wide-ranged finely tunable microwave cavity for narrowband phase noise filtering”. In: *Review of Scientific Instruments* 92.3 (Feb. 2021), p. 034710.
- Shomroni, Itay et al. “Two-Tone Optomechanical Instability and Its Fundamental Implications for Backaction-Evading Measurements”. In: *Phys. Rev. X* 9 (4 Oct. 2019), p. 041022.
- Adelmann, Andreas et al. “Real-Time Tomography of Gas-Jets with a Wollaston Interferometer”. In: *Applied Sciences* 8.3 (Mar. 2018), p. 443. ISSN: 2076-3417.
- Eichenberger, Michael et al. “Deformable mirror for wavefront shaping of infrared radiation”. In: *Optics Letters* 43.9 (May 2018), p. 2062. ISSN: 0146-9592.

AWARDS & PRICES

- EPFL Teaching Award 2022
- ETH Medal for Master Thesis 2018
- ETH / VMP Teaching Assistant Award 2016

EDUCATION

MSc Physics with Honours

ETH Zürich

Fall 2015 - Spring 2018

Master Thesis: *"Beam Characterization of Low Energy Electrons from a Laser Wakefield Accelerator"*,
Supervised by Dr. A. Adelmann (ETH & PSI) and Dr. R. Ischebeck (PSI).
Average grade 5.9 (pass: 4, top grade: 6)

Exchange Semester

University of Toronto

Fall 2014

BSc in Physics with Honours

ETH Zürich

Fall 2012 - Spring 2015

Proseminar Thesis: *"Topological Phases of Matter and Majorana Modes"*,
Supervised by Prof. O. Zilberberg and Dr. R. Chitra.
Average grade 5.8 (pass: 4, top grade: 6)

EXTRACURICULAR ACTIVITIES

Canoe Racing

SSKC Aschaffenburg

2006 - 2012 Aschaffenburg, Germany

Achievements: Bavarian champion in 5000 m single (2011), 8th on German Canoe Marathon (2011)

European Travels with my Donkey

Summer 2012 Germany, Switzerland and Italy

1000 km hiking trip with a donkey and my good friend Sven Wang through Europe. The trip was funded by busking with the accordion on the way.